Novel RF Slow-Wave Coupled-Line Circuits and Antennas for Compact Wireless Systems

BY

HAIJIANG MA
B.S.E.E., Zhejiang University, Hangzhou, China, 2004
M.S.E.E., Zhejiang University, Hangzhou, China, 2006

DISSERTATION

Submitted as partial fulfillment of the requirements
for the degree of Doctor of Philosophy in Electrical and Computer Engineering
in the Graduate College of the
University of Illinois at Chicago, 2012

Chicago, Illinois

Defense Committee:

Hung-Yu David Yang, Chair and Advisor
Danilo Erricolo
Piergiorgio Uslenghi
Siddhartha Ghosh
Nick Buris, NEBENS LLC

This dissertation is dedicated to my respected parents for their immense love, endless encouragement, and unwavering support without which I would not have accomplished the doctoral degree. They have instilled me with senses of confidence, resolution, assiduity, persistence, pride, and gratitude that continue to richly bless my life in the journey of chasing dreams.

ACKNOWLEDGMENTS

First of all, I would like to thank my advisor, Professor H. Y. David Yang, for his invaluable inspiration, guidance, and patience throughout the completion of this dissertation. It is my honor to conduct research under his experienced supervision and support. I am also very grateful to all the members on my defense committee for their keen advice and recommendations. I appreciate the staffs in Department of Electrical and Computer Engineering at UIC for their kindly help and assistances to my studies throughout the pursuit of my Ph.D. degree in the past five more years.

Secondly, I gratefully acknowledge measurement assistances with Andrew Electromagnetics Lab in B017 ERF, Mr. George Ashman in the teaching lab (4255 SEL), Dr. Ntsanderh Christian Azenui in Broadcom, as well as Prof. William J. Chappell and Dr. Xiaoguang Liu in Purdue University.

In addition, I am thankful to my fellow lab members, classmates, and friends for their friendship during my Ph.D. studies, especially Dr. Chengzhi Zhou, Dr. Jing Liang, and Dr. Yanyan Zhang for cheerful and helpful discussions I had with them. I also wish to thank all of my teachers, instructors, professors, mentors, and advisors for their significant contributions to my education from elementary school until graduate college.

Last but not least, I have immense appreciations to my father You Xiang Ma and my mother Tiao Xian Zhang for their persistent love, encouragements, and supports through my growing up. I would like to express special gratitude to them for their care, understanding, and dedications since I left my beloved hometown after high school.

HM

TABLE OF CONTENTS

CHAPTER **PAGE**

TABLE OF CONTENTS (Continued)

CHAPTER **PAGE**

TABLE OF CONTENTS (Continued)

CHAPTER **PAGE**

LIST OF TABLES

LIST OF FIGURES

FIGURE **PAGE**

LIST OF FIGURES (Continued)

FIGURE **PAGE**

LIST OF FIGURES (Continued)

FIGURE **PAGE**

LIST OF FIGURES (Continued)

FIGURE **PAGE**

LIST OF FIGURES (Continued)

FIGURE **PAGE**

LIST OF FIGURES (Continued)

FIGURE **PAGE**

LIST OF ABBREVIATIONS

BPF	Band-Pass Filter
CF	Coupling Factor
CMRR	Common-Mode Rejection Ratio
CPW	Coplanar Waveguide
CRLH	Composite Right/Left-Handed
CTF	Compressed, Twisted, Fragmented
DC	Direct Current
DGS	Defected Ground Structure
EBG	Electromagnetic Band-Gap
EM	Electromagnetic/Electromagnetism
EMC	Electromagnetic Compatibility
ESA	Electrically Small Antenna
FBW	Fractional BandWidth
FEM	Finite Element Method
GPS	Global Positioning System
IC	Integrated Circuit
IL	Insertion Loss
ISM	Industrial, Scientific, Medical
ITR	Impedance Transformation Ratio
LH	Left-Handed
LTCC	Low-Temperature Co-fired Ceramics
MEMS	Micro-Electro-Mechanical Systems
MOM	Method Of Moment

LIST OF ABBREVIATIONS (Continued)

MPE	Modal Phase-velocity Equalization
MSC	Mode-Selection Characteristics
MW	Microwave
PCB	Printed Circuit Board
PSR	Power Splitting Ratio
RF	Radio Frequency
RFI	Radio-Frequency Interference
RFID	Radio-Frequency Identification
RH	Right-Handed
RL	Return Loss
SIW	Substrate Integrated Waveguide
SNR	Signal-to-Noise Ratio
SWF	Slow-Wave Factor
TEM	Transverse Electromagnetic
TL	Transmission Line
VSWR	Voltage Standing Wave Ratio
WLAN	Wireless Local Area Network
3D	Three Dimention/Dimensional

SUMMARY

Recently, the demand for small RF front ends has been ever increasing for modern compact versatile wireless systems. It brings new design challenges to RF engineers, as the dimensions of antennas and passive circuits are proportional to a guided wavelength. Coupled-line circuits still remain the bottleneck for miniaturization due to their more complexity over other passive circuits.

In this thesis, novel slow-wave coupled line circuits and antennas are proposed to address the above-mentioned bottleneck. Initially, a complete theoretical study is conducted on both right-handed and left-handed artificial coupled transmission lines. Design criteria and tradeoffs are illustrated for right-handed slow-wave coupled lines through guided-wave characteristics in terms of propagation constants, line impedances, slow-wave factors, and cut-off frequencies under even- and odd-mode excitations. High-density 3D metallization on multilayer substrate can help to enrich inductive and capacitive effects periodically within a small unit cell. New slow-wave coupled and isolated lines are designed with least dispersion and attenuation based on the three-layer inverse mushroom topology.

In succession, high-performance miniaturized coupled line circuits with DC isolation are demonstrated with over 80% planar area reduction, in contrast to their conventional microstrip counterparts. Apart from directional coupler, two low-order coupled line band-pass filters are presented in both regular and folded configurations. A Marchand balun is shown with an impedance transformation ratio of 1:3 from source to load impedances. A novel coupled line 180^{o} hybrid coupler is developed with equal power splitting and excellent isolation at outputs. In addition, circuit architectures, analyses, and syntheses are provided.

Finally, miniaturized printed folded helical dipole and monopole antennas at GSM1800/1900 bands are investigated as two examples of electrically small antennas with self resonance, sufficient bandwidth, and self impedance matching. Their radiation *Q*-factor reductions of about 40% and 62% are observed, respectively, over their non-folded helix counterparts.

1 INTRODUCTION

Over the past century, there had been major shifts in the worldwide electronics industry as it responded to the emerge of wireless communications with emphasis on portability that requires the communication system to be of small size, light weight, multi-functionalities, power saving, and low cost. Typical applications include, but not limited to, mobile phones, pagers, global positioning system (GPS), wireless local area network (WLAN), cordless computer peripherals (mouse, keyboard, printer), implantable wireless biomedical devices, RF identification (RFID) tags, wireless gaming, etc. These wireless electronic products not only have yielded marvelous revolutions, but also continue to show far-reaching impact on our daily work and life.

Meanwhile, with the explosion in growth of wireless market in recent years, an unprecedentedly ever-increasing demand for smaller, lighter, and more versatile handheld wireless products presents a challenge to the relatively cumbersome RF front end that should be well suited in an entire compact system. Nowadays, functional integration and size reduction play an important role and are usually regarded as a key to success in the highly competitive wireless market, thereby inspiring many engineers to attempt substantial efforts to win this miniaturization campaign.

Now questions are: 1) where is miniaturization technology headed, 2) what kind of techniques shall we choose for specific applications, and 3) how can we embrace this intriguing area? Answers to these questions would lead to the dissertation topic: *Novel RF Slow-Wave Coupled-Line Circuits and Antennas for Compact Wireless Systems.*

1.1 Motivation

As mentioned above, one can benefit much from high-performance miniaturized wireless electronic devices. Hence it is quite natural for engineers to arouse an enthusiasm for advancing miniaturizing wireless products further to cater to consumers' demands. Our investigations reveal, as

for RF engineers, that considerable research efforts could be placed on coupled-line passive components that have been not yet extensively explored in RF and microwave society.

Wireless communication systems are composed primarily of digital and analog/RF parts. As silicon-based IC technology evolves dynamically over the past several decades in semiconductor industry, Moore's law has continued to make effective for device density in digital world: the number of transistors integrated on a single chip doubles approximately every two years. It makes possible to integrate digital functions into a tiny module for compact electronic systems. Nevertheless, the efficiency of present 'so-called' high-density packaging, which is defined as the ratio of the area of IC chips to that of the underneath printed circuit board (PCB), still remains very low (around 10%). A possible way to dramatically raise packaging efficiency is to miniaturize RF and microwave passive components and integrate them on the PCB substrate. But RF/microwave engineers made very little advances on miniaturizing passive devices, in particular, which have not kept pace with their digital counterparts in wireless communication systems.

Obviously, even with today's microelectronics technology and high-density packaging, antennas and RF/microwave passive components still occupy significant area in RF front-end systems, for their sizes are proportional to the guided wavelength. Recently, the maturity of multi-layer IC technology has enabled the high-density three-dimensional (3D) metallization on common substrates, which help to implement at low cost slow-wave transmission lines, regardless of right-handed (EBG) or left-handed metamaterials, with large slow-wave factors. Consequently, very small passive circuits are achieved due to the much reduced guided wavelength of artificial uncoupled transmission lines [1-4].

In addition to isolated lines, signals can also be guided by coupled transmission lines. Coupled lines are used widely as basic circuit elements for directional coupler, Marchand balun, bandpass filters (BPF), and other various useful circuits that are critical components in distributed RF and microwave passive community. Owing to inhomogeneous dielectric medium topology, conventional

coupled microstrip lines exhibit different phase velocities of two dominant propagating modes. As excitation signal on a coupled line is a superposition of such two modes in general, considerable discrepancy between propagation velocities is often undesirable for signal fidelity, which often deteriorates the performance of coupled-line components. For example, directional couplers suffer poor directivity from this nonsynchronous feature.

Moreover, it is of importance to have coupled-line balanced configuration to transfer/yield differential signals with the feature of its immunity to external noise by rejecting the intrinsic common-mode interference in balanced environments. This is beneficial to noise-sensitive active circuits in RF front-end systems. In addition, differential signals are preferred to suppress electromagnetic emission in IC interconnects, as compared to common-mode signals, from the perspective of electromagnetic compatibility (EMC).

However, in sharp contrast to the widely investigated slow-wave isolated transmission lines, artificial coupled transmission lines have not gained comparable attention so far. Coupled-line components still remain the bottleneck for miniaturization of high-performance microwave passive devices. Therefore, it is of great significance and practical importance in both academia and industry to address artificial coupled transmission lines, especially for slow-wave coupled lines leading to miniaturized devices.

In summary, we intend to address the dilemma between the bottleneck of RF/microwave passives miniaturization and huge demand for modern compact wireless communication systems.

1.2 Problem Statement

Microwave passive circuits are evolved from guided-wave structures where RF signals are carried by isolated or coupled transmission lines. At first, our goal is for device miniaturization to consolidate more functionalities on small-size circuit boards or chips for compact wireless systems. Later, as we

investigate further on artificial coupled transmission lines, we find some new features in addition to slow-wave effects.

Principles of Artificial (Isolated & Coupled) Transmission Lines. Periodical structures loaded with reactive elements exhibit basic pass-band and stop-band characteristics, and could be capable of supporting slow-wave propagations (slower phase velocity than unloaded line). When the periodicity is very small compared with a wavelength, electromagnetic (EM) wave does not perceive significant discontinuities as it travels along periodical structures. Under such homogeneity condition, it is possible to synthesize artificial transmission lines by cascading electrically small unit cells to mimic conventional distributed counterparts in certain frequency domain of interest. By employing the intuition inferred from lumped-circuit theory, dispersion characteristics and characteristic impedances can be engineered by means of distributed inductors and capacitors within each unit cell for artificial transmission lines.

1) **Isolated Transmission Line.** If a line is loaded or cascaded periodically with series inductive and/or shunt capacitive elements, it is frequently referred to as dominant right-handed metamaterial transmission line. If it is loaded or cascaded periodically with series capacitive and/or shunt inductive elements, it is often called dominant left-handed metamaterial transmission line. The word ‘dominant’ originates from parasitic reactive effects which usually need to be taken into account in practical implementations. Dispersion property and characteristic impedance are investigated for the fundamental mode (propagating wave in pass-band and evanescent wave in stop-band) in the whole frequency range. The emphasis is placed on slow-wave effects of metamaterial transmission line leading to isolated-line circuit miniaturization. The right-handed case has low dispersion over a broad frequency range and hence it is more favored in slow-wave applications at low frequencies.

2) **Coupled Transmission lines**. Similarly, reactive loadings could also be applied periodically on coupled lines. In contrast to the isolated line case, a combination of considerable electric and magnetic couplings has to be taken into account. Depending on reactive the loadings and coupling reactance (inductance and/or capacitance) between two closely-placed lines, such artificial coupled lines can be regarded as dominant right-handed or left-handed metamaterial coupled transmission lines. Due to electromagnetic coupling, coupled lines exhibit different field patterns corresponding to two fundamental modes of propagation: in-phase and anti-phase waves (common and differential modes). These two modes present different characteristic impedances, and in general have unequal propagation velocities in inhomogeneous dielectric medium topology. Dispersion characteristics of a metamaterial coupled line are not only controlled by distributed self inductances and capacitances, but also can be altered significantly by coupling capacitance and inductance. In contrast to the isolated-line case, the design of metamaterial coupled transmission lines involves more variables with additional degrees of freedom.

3) **Symmetric Coupled Line**. Symmetric artificial coupled transmission lines are made of two identical lines adjacent to each other. Placing magnetic and electric wall in the symmetry plane, respectively, yields even- and odd-mode half circuits. Consequently, a four-port coupled line is reduced to two simple two-port circuits. Based on the previous analysis for the artificial isolated line case, it is quite straightforward to obtain dispersion curves and characteristic impedances for the fundamental even and odd modes, respectively, with equivalent mode parameters.

A goal of this study is to provide guidelines and criteria for designing large-SWF artificial coupled lines featuring equal phase velocities of two fundamental propagating modes, as well as offering enhanced coupling level over conventional uniform coupled microstrip lines. It aims at developing

high-performance miniaturized coupled-line components. Design tradeoffs will be illustrated in terms of guided-wave characteristics, including propagation constants, line impedances, slow-wave factors, and cut-off frequencies, under common- and differential-mode excitations.

1.3 Technical Approach

Nowadays, the sophisticated multi-layer IC technology has enabled the standardization of three-dimensional (3D) fabrication of metallic components within common dielectric or semiconductor substrates in a millimeter, micron, or even nano scale, which leads to cost-effective implementation of artificial transmission lines. Compressed, twisted, or fragmented (CTF) metallic strips/plates are spread out three dimensionally into multi-layer substrate structure to serve electrically as distributed inductors and capacitors (quasi-lumped elements) within each unit cell. High-density 3D substrate metallization are favored to enhance large slow-wave effects. As for artificial coupled transmission lines, a great portion of attention must be directed to synthesizing modest mutual inductance and coupling capacitance to alter dispersion characteristics to achieve desired phase velocities of two fundamental propagation modes, as well as to produce significant discrepancy between the two normalized mode impedances to yield substantial power coupling between two adjacent coupled lines.

2 BACKGROUND OVERVIEW

In this chapter, we will present a background overview of miniaturizing RF/microwave passive devices utilizing artificial slow-wave isolated or coupled transmission lines for modern wireless systems. Before introducing the concept of artificial electromagnetic material, we are going to review briefly various aspects of wireless communications and systems in section 2.1. A couple of typical miniaturization techniques will be summarized in section 2.2. Finally, coupled-line applications will be reviewed in section 2.3.

2.1 Wireless Communication

Why Radio Frequency or Microwave (RF/MW)?

In principle, wireless transmission can be achieved by means of electromagnetic waves propagating through space at any possible frequency. The group of all possible frequencies constitutes the electromagnetic spectrum, as illustrated in Figure 1. An interesting question arises naturally: *why RF/MW range is favored among all frequency pieces for today's prevailing wireless communications?*

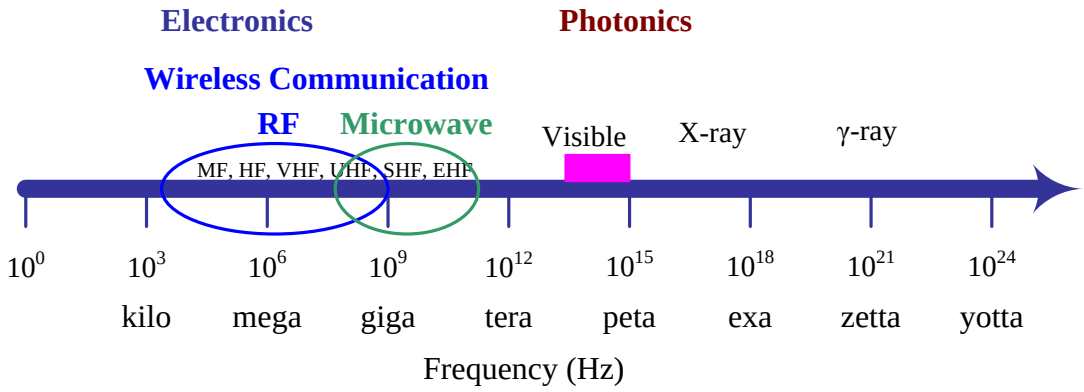

Figure 1: Electromagnetic Spectrum

Traditionally, radio frequency is defined from a few kHz (3 kHz) to roughly 1 GHz (1 cm), and microwave spans over a frequency window from 300 MHz (1 m) to 300 GHz (1 mm). The boundary is ambiguous between RF and microwave, which often leads to confusions to many electrical engineers. One may consider microwave as part of RF for radio spectrum to cover the full frequency range from 3 kHz to 300 GHz where a majority of present wireless communications are located. Nevertheless, a combinational term '*RF/MW*' (radio frequency or microwave) can be used to describe such frequency window more exactly. Regular band divisions within this window are illustrated in Table I.

TABLE I: RF/MW BANDS

Frequency	Wavelength	Band
30-300 Hz	10^4-10^3 km	ELF (extremely low frequency)
300-3000 Hz	10^3-10^2 km	VF (voice frequency)
3-30 kHz	100-10 km	VLF (very low frequency)
30-300 kHz	10-1 km	LF (low frequency)
0.3-3 MHz	1-0.1 km	MF (medium frequency)
3-30 MHz	100-10 m	HF (high frequency)
30-300 MHz	10-1 m	VHF (very high frequency)
300-3000 MHz	100-10 cm	UHF (ultra-high frequency)
3-30 GHz	10-1 cm	SHF (super-high frequency)
30-300 GHz	10-1 mm	EHF (extremely high frequency)

Now we are going to answer the aforementioned question. In general, the operation frequency of a wireless system is designated considering a variety of tradeoffs among system size and cost, space wave propagation efficiency, signals' immunity to noise/interference/impairments, transmission date

rates, etc. *RF/MW* constantly reaches a good compromise among these factors for most wireless communications.

Antennas are essential for wireless systems, and are usually around half- or quarter-wavelength in practice resulting from their resonance principle. If a wireless system operates at extremely low frequency, let's take 300 Hz for example, its antenna dimension corresponds to around 500 km or 250 km, which keeps it from practical applications. In addition, intrinsic features of low data rates and poor immunity to noise are not desirable at low frequency.

Above 300 GHz entering terahertz window, waves attenuate quickly due to substantiate absorption as propagating in atmosphere (particularly wet weather) which becomes opaque effectively to terahertz radiation. Fortunately, atmosphere turns back transparent in infrared and optical regions. Although infrared signals can offer considerable date rates, but they would be blocked easily by small obstacles, which confines to short-range indoor applications (local data links and remote controllers). Moreover, optical signals can provide even higher data rates, but they would be blocked by very tiny obstacles (such as dust and fog in air) and hence usually require line-of-sight propagation that is infeasible for wireless communication in public environment, in particular, urban area. Furthermore, losses become intolerable for too high frequency signals in circuit boards in systems.

RF/MW signals can present modest data rates, wide bandwidth, high propagation efficiency, good immunity to interference, along with the ability to penetrate from tiny obstacles to even buildings. Therefore, *RF/MW* is often preferred in various modern wireless communications.

2.2 Typical Miniaturizaiton Techniques

In this section, a brief review of typical miniaturization techniques involved in planar integrated microwave passive circuits and antennas is provided. By its name, miniaturization is meant to those process/methods leading to *electrically small* components whose dimensions, areas, or occupied

volumes are very small compared to their operating wavelengths. It is meaningless to say “small” or “large” judging only by their physical size without operational frequency taken into account.

Considering that miniaturization of RF/MW passives plays an extremely important role and imposes a far-reaching impact on compact mobile wireless systems, we summarize various size reduction techniques to offer a comprehensive perspective in this field.

2.2.1 High Dielectric-Constant Material

The dielectric constant is a relative measure of how much electric flux can be confined in a dielectric medium, and reflects its ability to transmit an applied electric filed to some degree. Rapid advances in material engineering since late 1970s had enabled high dielectric-constant ε_r, temperature-stable (for frequency stability), low-loss dielectric material in microwave region [5-7], which are critical to the miniaturization of both base-station and mobile-terminal wireless systems.

It is well-known that dielectric materials can be utilized as substrates for printed circuits such as microstrip, stripline, and coplanar waveguide (CPW). As the component dimension is inversely proportional to the square root of effective dielectric constant ε_{eff} (e.g. microstrip) in general [8], high dielectric-constant substrates can be employed to achieve device miniaturization [9-11]. In addition, tightly bound fields can help reduce undesired radiation loss into space and capture most energy stored in the dielectric medium, which yields high quality factor Q that is usually preferred in microwave circuitry, but with relatively narrow bandwidth.

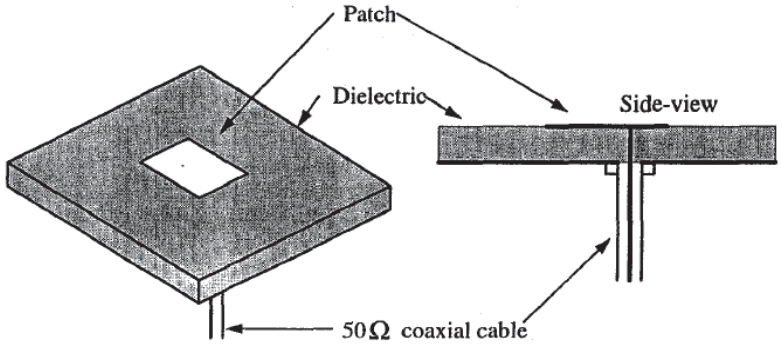

Figure 2: Miniature patch antenna on high dielectric-constant substrate. (Source: reference [12] Fig. 1.)

High dielectric-constant material may be also used to realize small planar printed antennas. One miniaturization example of rectangular patch antenna [12] is implemented on the high dielectric constant substrate (barium titratitanate) for 900 MHz frequency band. However, antenna designer desires loosely bound fields to render low energy stored in dielectric and the radiation into space as much as possible. Hence super-high dielectric-constant material may not be a proper candidate for antenna miniaturization applications where low Q, high radiation efficiency, and large bandwidth are favored constantly.

2.2.2 LTCC Multi-Layer 3D Structure

It is fairly well known that series inductor and shunting capacitor could be distributed to imitate conventional transmission line and further to achieve slow-wave effects, leading to miniaturization of passive devices. For standard PCB technology, this approach is often limited by the fabrication constraints, such as the number of layers, line width, line spacing, and via size. Nevertheless, as for LTCC or microelectronics technology, such constraints are addressed dramatically [13-17]. Inductance and capacitance can be deposited into vertical direction, and hence 3D substrate metallization can be implemented in very high density, as shown in Figure 3 (a). Moreover, front-end

module, including both passive and active parts, could also be integrated into LTCC multi-layer 3D structure, as illustrated in Figure 3 (b).

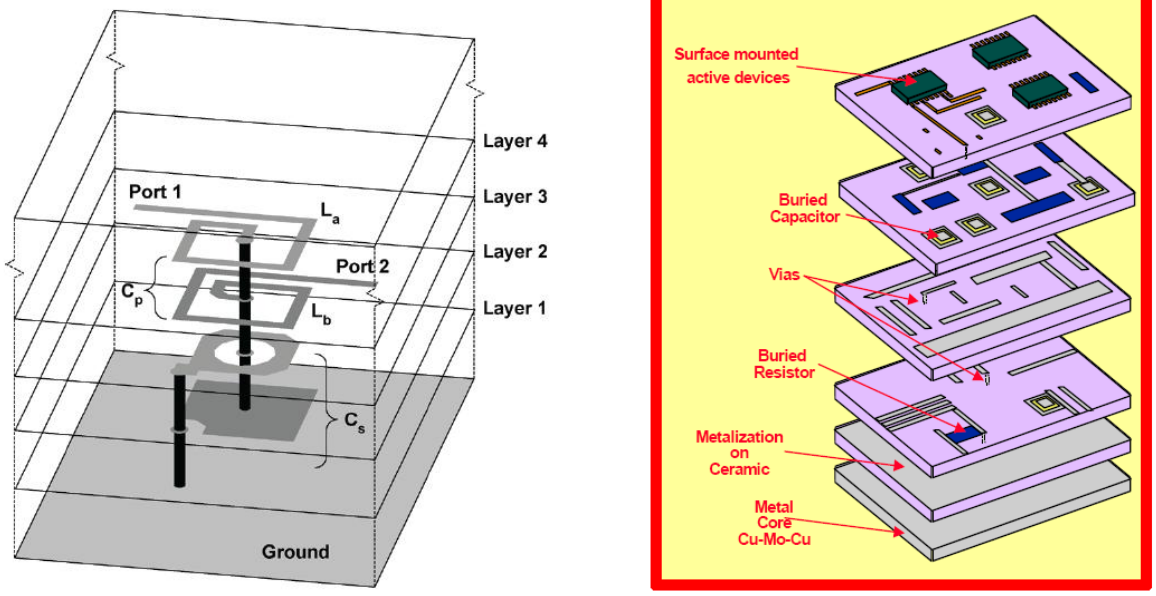

(a) LTCC quasi-lumped element (b) RF front end in LTCC

Figure 3: LTCC multi-layer structure for miniaturization. (Source: reference [14, 17])

2.2.3 Geometry Optimization

Passive circuits and antennas require certain physical dimensions to achieve a desired amount of phase shift, resonating, coupling, radiation, etc. Many efforts have been attempted to modify the shape and geometry of microwave passives to utilize the available space efficiently as well as to improve their performances [18-22]. Some miniaturized examples are shown in Figure 4 of circuit applications by meander-shaped lines.

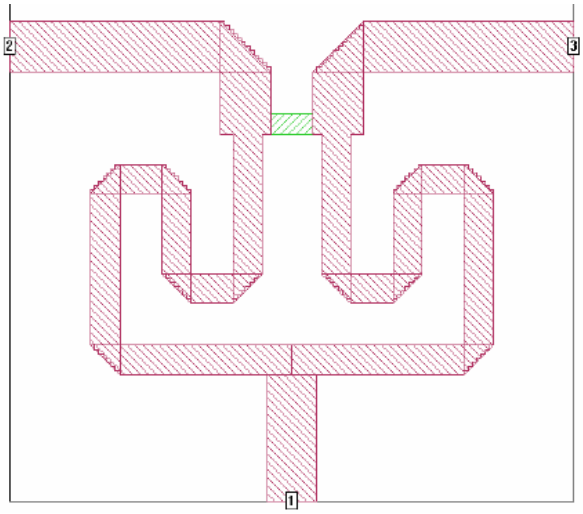

(a) Meander line Wilkinson power divider. (Source: reference [22] Fig. 2.)

(b) CMOS 3dB directional coupler using meander edge-coupled synthetic transmission lines. (Source: reference [21] Fig. 1.)

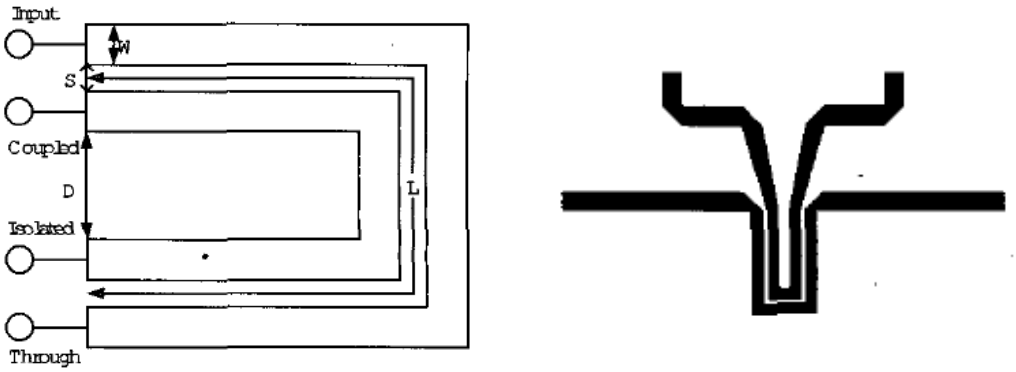

(c) Meandered microstrip parallel coupler with high directivity. (Source: reference [24] Fig. 1.)

Figure 4: Miniaturized microwave passive circuits using meandered lines.

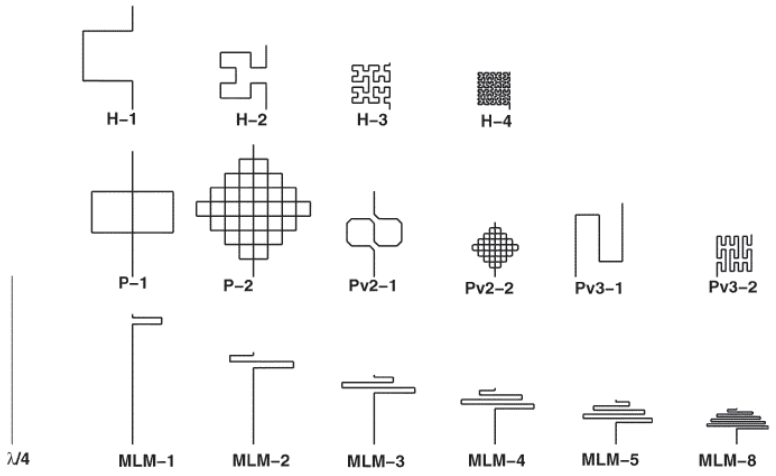

Figure 5: Bi-dimensional space-filling curves for potential antenna miniaturizations. First row: Hilbert monopoles; Second row: Peano monopoles; Third row: standard λ/4 monopole and meandered monopole. (Source: reference [23])

In addition, geometry optimization can also be applied to electrical small antenna (ESA) design. The basic idea is to render the antenna occupy the available volume as much as possible within the small radiansphere. Space-filling curves (as shown in Figure 5) could be employed to achieve high miniaturization in planar antenna design [23]. However, high quality factor and low radiation efficiency make this approach not so interesting or efficient, since much energy is stored in near fields confined in complicated structure and large ohmic loss stems from long wire lengths. Moreover, genetic algorithm (GA) optimization was reported to attain both antenna miniaturization and good radiation performance [24-25].

2.2.4 Artificial Slow-Wave Structures

The propagation behaviors of electromagnetic wave are fundamentally governed by the Maxwell's equations, and are usually characterized by their propagation constants, including both attenuation and phase constants. Phase and group velocities can be derived from the phase constant. Group

velocity is a measure of dispersion of wave propagation. Guide-wave structures (waveguides or transmission lines) are referred to as artificial/metamaterial slow-wave structures if they can support wave propagation with phase velocities less than attainable values of the original host structures. Slow-wave structures, which provide large slow-wave factors, low attenuation, and little dispersion in the frequency region of interest, are usually preferred for practical applications.

Periodically disturbed lines loaded with distributed inductors and/or capacitors are often regarded as left-handed or right-handed metamaterial transmission lines. They support slow-wave propagations and can find many applications in passive circuit miniaturization. A 3GHz miniaturized branch-line coupler was developed with 70% size reduction based on slow-wave structure on three-layer Rogers RO4003C substrate [3]. By employing four-layer FR4 substrate, the branch-line coupler was further miniaturized with 86% size reduction and scaled down to 2.4GHz [4]. They are shown in Figure 6.

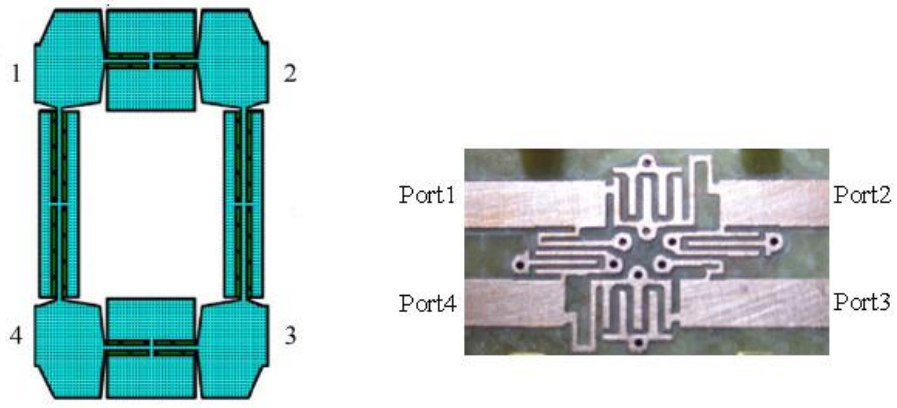

(a) Three-layer Rogers RO4003C
(Source: reference [3] Fig. 13.)

(b) Four-layer FR4
(Source: reference [4] Fig. 6.)

Figure 6: Slow-wave miniaturized branch-line couplers.

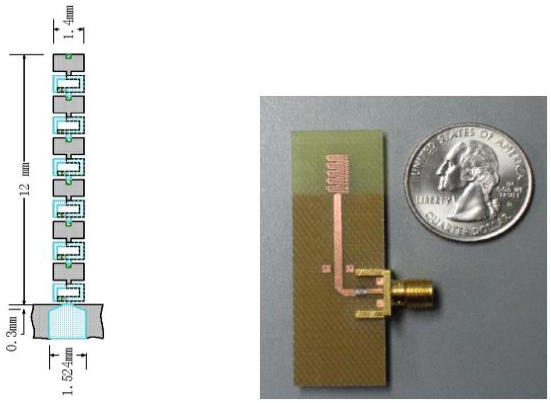

(a) (b)

Figure 7: Slow-wave miniaturized printed wire antennas: (a) Double-layer FR4; (Source: reference [2] Fig. 5.). (b) Three-layer FR4. (Source: reference [26] Fig. 3.).

Slow-wave transmission line can also be employed for printed wire antenna design. As shown in Figure 7, a 2.4GHz monopole antenna was developed on double-layer FR4 with about 50% size reduction [2], and it was further miniaturized on three-layer FR4 with 70% size reduction [26]. Actually, one layer (ground layer) was removed underneath the radiating part from their original slow-wave structures.

In addition, other miscellaneous techniques could also be applied to RF/microwave passive miniaturization, such as high-permeability substrate [27-28] and scaling up to higher frequency (e.g. 60 GHz).

2.3 Applications of Coupled Transmission Lines

It is well known that RF/microwave signals are usually guided by *single isolated* or *coupled* transmission lines (as well as waveguides) in *RF/MW* circuits. Transmission lines are utilized in two ways normally: 1) to transfer information or power from one point to another; or 2) to behave as circuit elements for passive circuits, for example, branch-line coupler, Wilkinson power divider, impedance transformer, balun, directional coupler, filter, DC blocks, etc. Here, we pay attention only

to coupled transmission lines. Coupled transmission lines are able to transfer differential signal with its advantage of noise immunity/suppression in balanced circuit environments, from which subsequent noise-sensitive active circuits could benefit much.

More commonly, coupled-line structures can be employed to develop various microwave passive devices [29]. Coupling mechanism was intuitively discussed previously in chapter 1 and will be examined further in later chapters. In this section, we discuss some of their applications, and introduce briefly some typical microwave passive components using symmetric coupled lines. We wish to miniaturize passive components by using artificial slow-wave coupled transmission lines. Other applications are still under investigation.

2.3.1 Coupled-Line Circuits with Equal Modal Phase Velocities

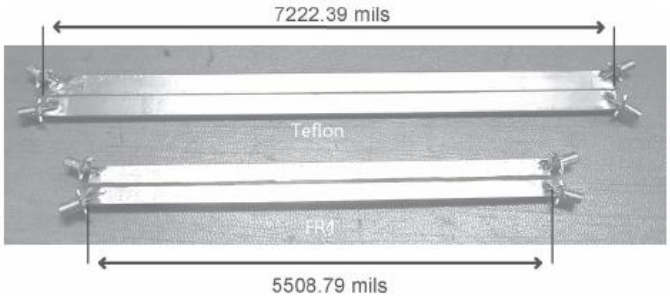

(a) Directional coupler on Teflon and FR4 substrate. (Source: reference [30] Fig. 3.)

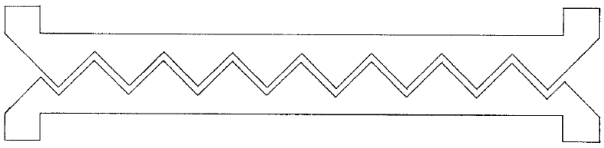

(b) Typical Wiggly line coupler. (Source: reference [31] Fig. 1.)

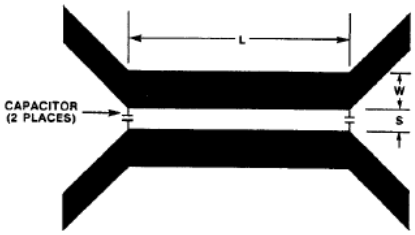

(c) Capacitively loaded directional coupler. (Source: reference [32] Fig. 1.)

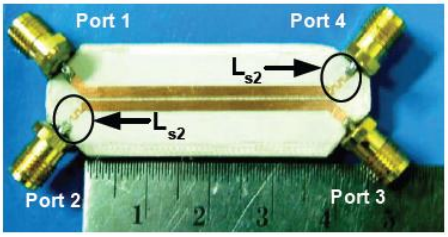

(d) Inductively loaded directional coupler. (Source: reference [33] Fig. 5.)

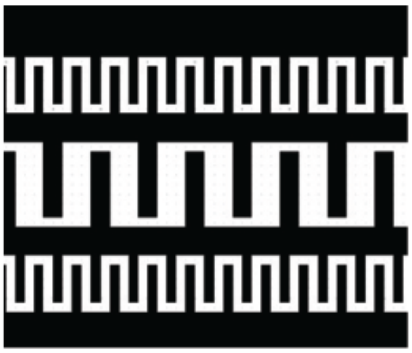

(e) Coplanar waveguide (CPW) slow-wave coupler. (Source: reference [34] Fig. 7.)

Figure 8: λ/4 coupled lines as directional couplers and phase compensations.

Directional Coupler. A quarter-wave long symmetric coupled line section could be used as a directional coupler. Equalization of even- and odd-mode phase velocities is crucial to its performance in terms of directivity. Conventional microstrip directional coupler (Figure 8a) [30] often suffers poor directivity from its significant discrepancy in modal phase velocities. A couple of techniques were proposed to compensate the phase differences, including Wiggly line (Figure 8b) [31], capacitor loading (Figure 8c) [32], and inductor loading (Figure 8d) [33]. Recently, a slow-wave coupled transmission line was implemented by coplanar waveguide (CPW) with interdigital capacitor loading to attempt miniaturization of coupler (Figure 8e) [34]. However, its performance is not exceptional.

Actually, quarter-wavelength coupled line section not only can be used as a directional coupler, but also as basic building blocks to construct other coupled-line circuits. Hence it is of significance to design a proper λ/4 coupled line section.

Marchand Balun. Two λ/4 coupled line sections can be cascaded together to form a conventional Marchand balun. Among all kinds of baluns, the Marchand balun has become one of the most popular forms to yield a balanced signal since it was first introduced in 1944 [35]. Moreover, it provides DC isolation between input and outputs. Its performance relies on the coupling level and directivity of each directional coupler element. Conventional microstrip Marchand balun (Figure 9a) suffers narrow bandwidth from the low coupling factor of each coupled line section, owing to the standard cost-effective PCB fabrication constraints. Two same Marchand baluns can be connected parallel (Figure 9b) to efficiently improve the operational bandwidth [36]. Equalization of even- and odd-mode phase velocities is crucial to the phase balance of output signals. Therefore, a quarter-wavelength coupled-line section shows great significance with high coupling level and equal modal phase velocities.

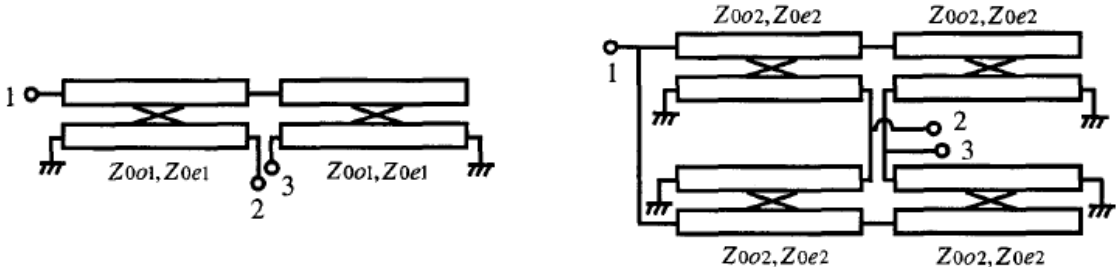

(a) Conventional Marchand balun. (b) Parallel connected Marchand balun.

Figure 9: Planar Marchand balun configurations. (Source: reference [36] Fig. 1.)

Power Divider/Combiner. λ/4 coupled line sections can also be applied to power divider design. Two-way Wilkinson power dividers could be realized by using one λ/4 coupled line section [37] for single-band (Figure 10a) or together with isolated line [38] for dual-band applications (Figure 10b). What's more, coupled line sections can be employed to adjust a three-way Wilkinson power divider from three- to two-dimensional configuration (Figure 11), as well as to offer DC block [39].

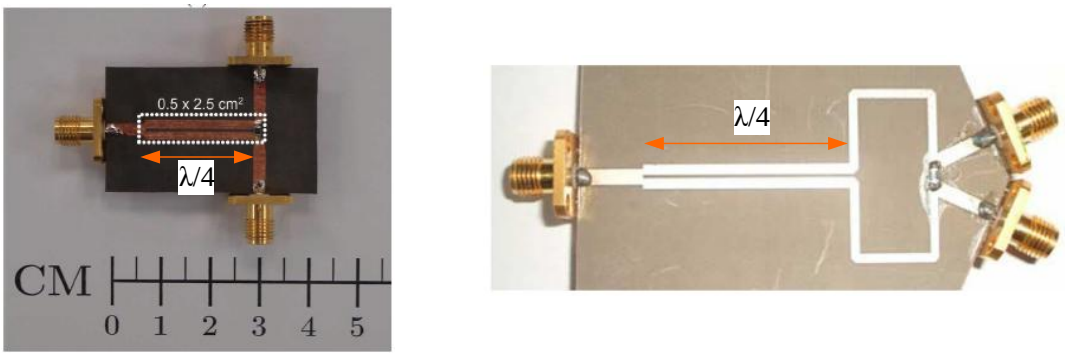

(a) Single band. (Source: reference [37] Fig. 6.) (b) Dual band. (Source: reference [38] Fig. 5.)

Figure 10: Coupled-line two-way Wilkinson power dividers.

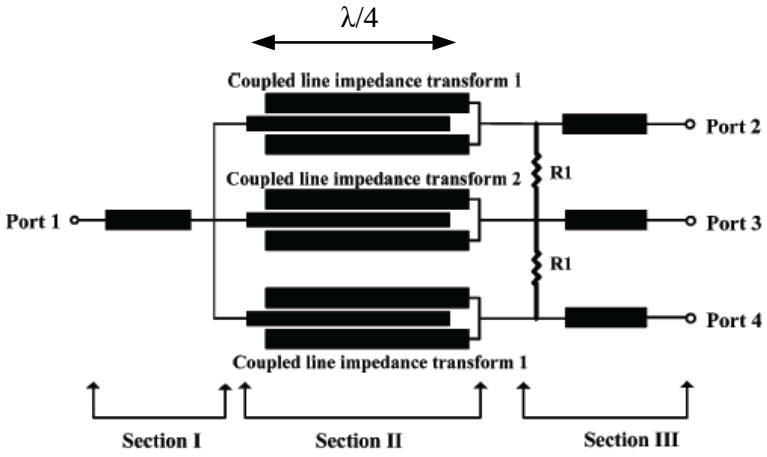

Figure 11: Coupled-line three-way power divider. (Source: reference [39] Fig. 1.)

180^o Hybrid Coupler. Recently, it was reported that λ/4 coupled line sections could be employed to construct 180^o hybrid coupler [40-41]. Two quarter-wave coupled line sections and one isolated line section are used (Figure 12a). A three-layer layout example was implemented on LTCC multilayer structure for 24GHz applications (Figure 12b) [41]. Again, coupling factor and equal modal phase velocities of the coupled line sections play an important role in the hybrid's performance, for example, in-phase or out-of-phase characteristics between outputs and coupling level at coupled outputs.

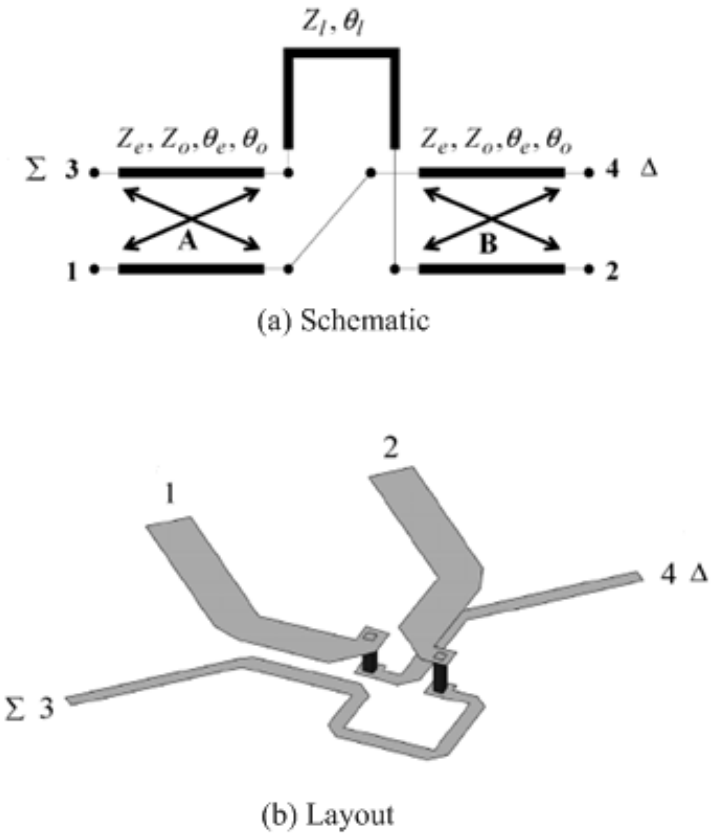

Figure 12: Coupled-line 180^o hybrid coupler on LTCC. (Source: reference [41] Fig. 3&4.)

2.3.2 Coupled-Line Circuits with Different Modal Phase Velocities

Quadrature Hybrid Coupler. We may also find some useful applications based on the symmetric coupled line with desired different even- and odd-mode phase velocities. A compact 90° hybrid coupler was developed to mimic conventional branch-line coupler based on artificial coupled transmission lines with interdigital capacitor loaded between two main lines (Figure 13) [42]. The mutual coupling between two lines is attributed primarily to the loaded mutual capacitance, which leads to different modal phase velocities. Inductive coupling could be ignored here. The condition for quadrature hybrid coupler is that: 1) even-mode characteristic impedance is matched; 2) even-mode electrical length is quarter wavelength and odd-mode electrical length is half wavelength. Certain class of coupled-line filters utilized large modal velocity ratio of inhomogeneous coupled-line structure [43-44].

$$z_{ce} = 1 \qquad \beta_e d = \pi/2 \qquad \beta_o d = \pi$$

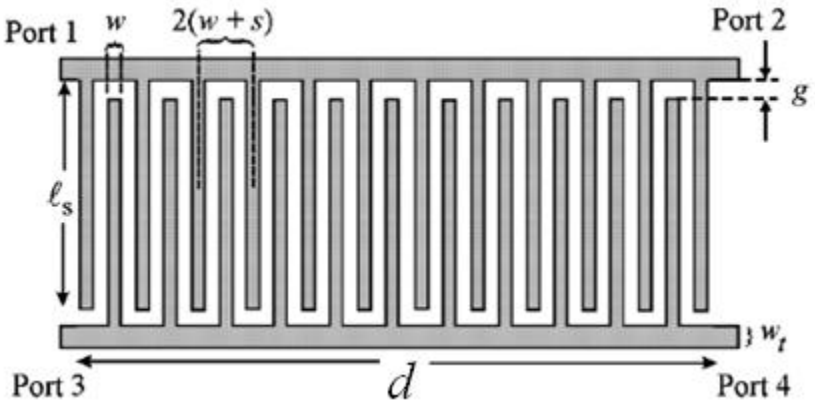

Figure 13: Coupled-line 90° hybrid coupler. (Source: reference [42] Fig. 1.)

3 THEORY OF ARTIFICIAL SYMMETRIC COUPLED TRANSMISSION LINES

In this chapter, we are going to introduce the concept of *artificial coupled transmission lines*, mainly based on right-handed or left-handed symmetric coupled-line configurations. An intensive theoretical analysis in both pass-band and stop-band is examined for both cases. A design example will be provided in chapter 4 on slow-wave right-handed coupled lines with equal even-/odd-mode phase velocities over a broad frequency range in pass-bands and its application in a 2.4 GHz miniaturized directional coupler.

3.1 Introduction

When two transmission lines are placed in proximity close enough, there are electromagnetic couplings between two lines with field patterns disrupted in contrast with those of isolated lines. A portion of signal excited on one line will appear on another line. This feature may be *desirable* in microwave coupled-line components whose primary objective is to transfer power between lines [45-48]. However, it may be *undesirable* and is often referred to as *crosstalk* or *interference* in printed or IC interconnects where the main objective is to propagate signal on the individual line alone. In general, the former is investigated in frequency domain, whereas the later often in time domain from the angle of *signal integrity* (*SI*) in *electromagnetic compatibility or interference* (*EMC*/EMI) [49].

Transmission lines are such an old subject that had been widely investigated over the past century. But they have renewed interests since metamaterial concept was introduced recently, and particularly matematerial single isolated transmission lines had attracted tremendous attention [1-4, 50-52] at the beginning of this new century.

Likewise, coupled transmission lines could gain renewed and even more interests by incorporating the metamaterial concept. Compared to its metamaterial isolated-line counterparts, *artificial coupled*

transmission lines have additional degrees of freedom on engineering electrical characteristics and hence yields many unique *features* such as:

1) Slow wave of even and/or odd modes [34];
2) Equal even- and odd-mode phase velocities in pass-band [34];
3) Different even- and odd-mode phase velocities [42];
4) Mode-selection characteristics [53];
5) Fast wave of even and/or odd modes [54-55];
6) Evanescent wave tunneling of even and/or odd modes in stop-band.

Based on the above features, one can envision that sections of metamaterial coupled lines could function as basic building blocks to yield small and high-performance coupled-line devices, such as directional coupler, balun, filter, dc block, etc. Moreover, apart from the slow-wave effects, artificial coupled transmission lines enable the possibility of certain novel passive components which might have not been explored so far. In principle, metamaterial coupled lines could help synthesize desired coupled-line properties.

For simplicity, theoretical study utilizes the model of artificial *symmetric* coupled transmission lines. Symmetric coupled lines consist of two identical signal lines with respect to the common ground reference and both alone have the same line characteristic impedances and propagation constants in the absence of each other. Theoretical analysis provides the understanding of both dispersion characteristics and characteristic impedance tailored by the coupling mechanism of metamaterial coupled transmission lines under even- and odd-mode excitations. Emphasis is placed on the pass-band characteristics, while stop-band characteristics are also examined. Closed-form equations are provided to serve as design guidelines for practical implementation later.

3.2 Right-handed Coupled Transmission Line

Conventional planar coupled transmission lines, in the form of microstrip, stripline, or coplanar waveguide (CPW) implementation (Figure 14), are fundamental low-pass right-handed structures with distributed series inductive and shunt capacitive elements. The incremental equivalent circuit model of an infinitesimal coupled-line section is shown in Figure 15. In contrast to the isolated-line case, both electric (capacitive) and magnetic (inductive) couplings should be taken into account for coupled transmission lines.

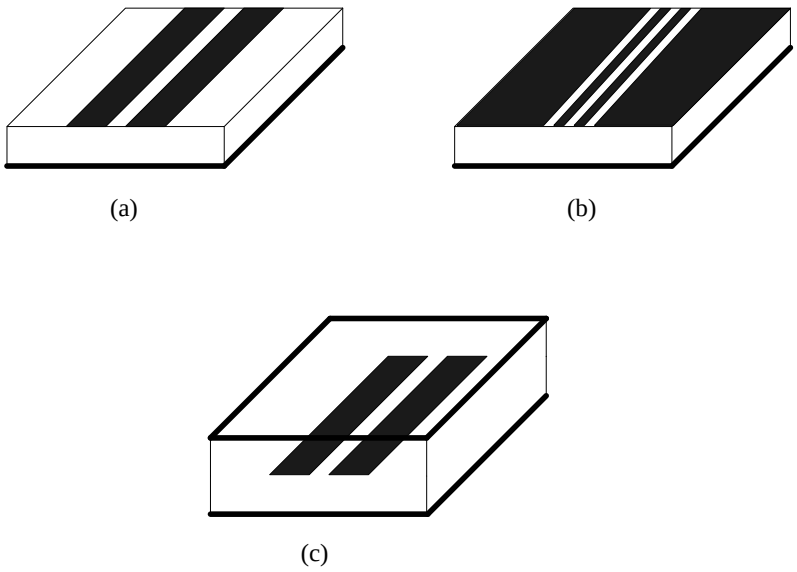

Figure 14: Conventional planar coupled lines. (a) coupled microstrip lines; (b) coupled CPW; (c) coupled stripline.

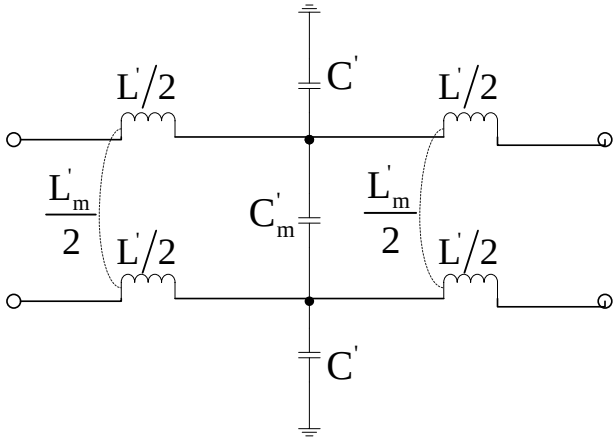

Figure 15: Equivalent *lumped* circuit model of an infinitesimal section of conventional coupled transmission lines in Figure 14. (Here $L^{'}$ and $C^{'}$ are per-unit-length parameters: H/m, F/m).

3.2.1 Equivalent Quasi-Lumped Circuit Model

Artificial coupled lines are fundamentally a four-port component. In contrast to conventional coupled transmission lines, reactive loadings are applied periodically to construct metamaterial symmetric right-handed coupled lines. The equivalent *quasi-lumped* circuit of a unit cell with finite length d is shown in Figure 16 (a). For simplicity, loss issues are not considered here. By placing magnetic or electric wall in the symmetry plane, the four-port symmetric circuit can be decomposed into even- or odd-mode two-port half circuits, respectively, as shown in Figure 16 (b) and (c). Under homogeneity condition that the periodicity is small compared to a wavelength, cascade of unit cells (Figure 16 (d)) forms an even- or odd-mode transmission line (Figure 16 (e)) with characteristic impedances $Z_{e,o}$ and propagation constants $\lambda_{e,o} = \alpha_{e,o} + j\beta_{e,o}$, where "*e*" and "*o*" stand for even and odd modes, respectively. Note that even- or odd-mode line is modeled as a regular right-handed transmission line with series inductance L_e or L_o and shunt capacitance C_e or C_o within a unit cell.

Furthermore, based on the images due to electric and magnetic walls, one could find that

$$L_e = L + L_m \,, \tag{3.1a}$$

$$C_e = C \,, \tag{3.1b}$$

$$L_o = L - L_m \,, \tag{3.1c}$$

and

$$C_o = C + 2C_m \,. \tag{3.1d}$$

where L and C are self inductance and capacitance of each isolated signal line (in the absence of the other signal line) with respect to ground, L_m and C_m are mutual inductance and coupling capacitance accounting for electric and magnetic couplings between coupled lines, L_e/L_o and C_e/C_o denote the effective series inductance and shunt capacitance of the decomposed even- or odd-mode line. All those circuit parameters are Henry and Farad in units within a unit cell of finite length d.

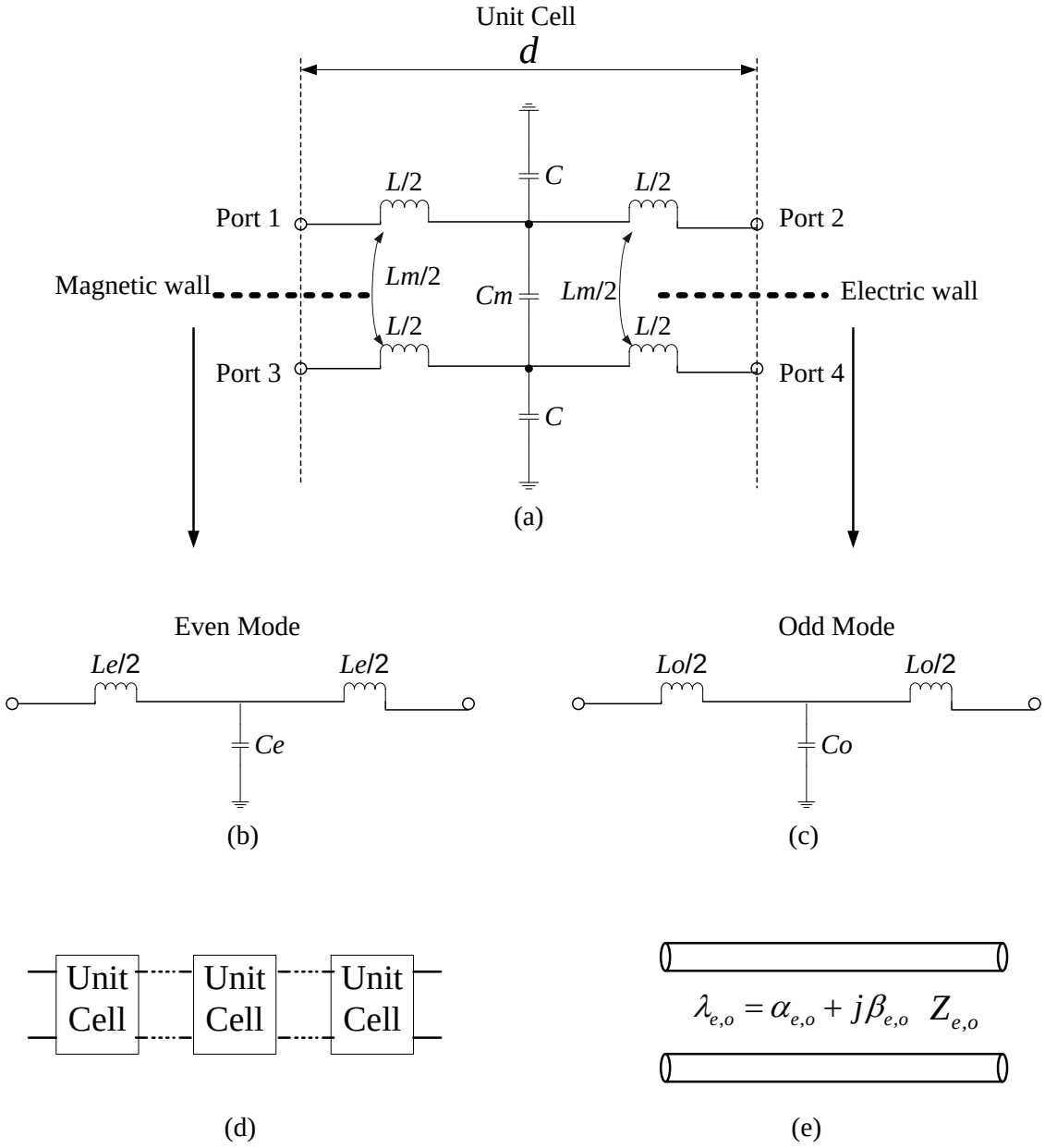

Figure 16: Unit cell equivalent *quasi-lumped* circuit of metamaterial symmetric *right-handed* coupled-line periodic structure and its corresponding even-/odd-mode half circuits. (Here *L* and *C* are H and F in units deposited in unit cell with finite length *d*).

3.2.2 Dispersion Characteristics Under Even-Mode Excitation

Based on Figure 16, the theoretical analysis of two-port LC circuits can be employed to study the characteristics of metamaterial symmetric coupled lines. By replacing L and C with L_e/L_o and C_e/C_o, characteristic impedances and propagation constants of metamaterial coupled lines can be obtained straightforwardly under even- or odd-mode excitations.

From Figure 16 (b), the even-mode line is basically a low-pass structure with cut-off frequency

$$f_{ce} = \frac{1}{\pi\sqrt{L_0 C_0}} \cdot \frac{1}{\sqrt{1+k_L}} \tag{3.2}$$

where k_L is the inductive coupling coefficient defined as $k_L = L_m / L_0$.

In the pass-band $f \le f_{ce}$, the propagation constants on the even-mode line is

$$\alpha_e = 0, \tag{3.3a}$$

$$\beta_e = \frac{2}{d} \arcsin\left(\sqrt{1+k_L}\, \frac{\omega\sqrt{L_0 C_0}}{2} \right), \tag{3.3b}$$

and characteristic impedance is

$$Z_{ce} = \sqrt{1+k_L} \cdot \sqrt{\frac{L_0}{C_0}} \cdot \sqrt{1-(1+k_L)\frac{\omega^2 L_0 C_0}{4}}, \tag{3.4}$$

In the stop-band $f > f_{ce}$, the propagation constant and characteristic impedance of the even-mode line are

$$\alpha_e = \frac{2}{d} \arccos h\left(\sqrt{1+k_L}\, \frac{\omega\sqrt{L_0 C_0}}{2} \right), \tag{3.5a}$$

$$\beta_e = \frac{\pi}{d}, \tag{3.5b}$$

$$Z_{ce} = j\sqrt{1+k_L}\cdot\sqrt{\frac{L_0}{C_0}}\cdot\sqrt{\frac{\omega^2 L_0 C_0}{4}\left(1+k_L\right)-1}\,. \tag{3.6}$$

Assuming lossless (no resistor in circuit model), *evanescent wave* exists in the stop-band and encounters π phase shift across a unit cell.

3.2.3 ***Dispersion Characteristics Under Odd-Mode Excitation***

Similarly, from Figure 16 (c), odd-mode line also exhibits low-pass guided-wave characteristics with cut-off frequency

$$f_{co} = \frac{1}{\pi\sqrt{L_0 C_0}}\cdot\frac{1}{\sqrt{1-k_L}}\cdot\frac{1}{\sqrt{1+2k_c}}\,. \tag{3.7}$$

where $k_c = C_m/C_0$ is the capacitive coupling coefficient.

In the pass-band $f \le f_{co}$, the propagation constants and characteristic impedances are

$$\alpha_o = 0\,, \tag{3.8a}$$

$$\beta_o = \frac{2}{d}\arcsin\left(\frac{\omega\sqrt{L_0 C_0}}{2}\sqrt{1-k_L}\sqrt{1+2k_c}\right), \tag{3.8b}$$

$$Z_{co} = \sqrt{\frac{1-k_L}{1+2k_c}}\sqrt{\frac{L_0}{C_0}}\sqrt{1-\frac{\omega^2 L_0 C_0}{4}\left(1-k_L\right)\left(1+2k_c\right)}\,. \tag{3.9}$$

In the stop-band $f > f_{co}$, the dispersion characteristics are

$$\alpha_o = \frac{2}{d}\arccos h\left(\frac{\omega\sqrt{L_0 C_0}}{2}\sqrt{1-k_L}\sqrt{1+2k_c}\right), \tag{3.10a}$$

$$\beta_o = \frac{\pi}{d}, \tag{3.10b}$$

$$Z_{co} = j\sqrt{\frac{1-k_L}{1+2k_c}}\sqrt{\frac{L_0}{C_0}}\sqrt{\frac{\omega^2 L_0 C_0}{4}\left(1-k_L\right)\left(1+2k_c\right)-1}\,. \tag{3.11}$$

Similarly, *evanescent wave* also exists in the stop-band with π phase shift over the coupled-line unit cell under odd-mode excitation.

*3.2.4 **Modal Phase-Velocity Equalization Condition***

It is well known that equal even- and odd-mode phase velocities are frequently desirable for signal fidelity when waves propagate on the coupled lines, as excitation signal is a superposition of even and odd modes in general. Equal modal phase velocities are often necessary to achieve good performance in many coupled-line components, such as directional coupler and Marchand balun.

In this section, *modal phase-velocity equalization condition* is derived in pass-bands where most circuits operate for practical purpose.

According to equations 3.1, even- and odd-mode phase velocities would be equal if

$$L_e C_e = L_o C_o \tag{3.12}$$

for periodic symmetric coupled lines.

Alternatively, the *modal phase-velocity equalization condition* can also be expressed in terms of inductive and capacitive coupling coefficients. From equations (3.3b) and (3.8b), the equalization of even- and odd-mode phase velocities ($\beta_e d = \beta_o d$) in pass-bands requires that

$$\sqrt{1+k_L} = \sqrt{1-k_L}\sqrt{1+2k_c}\ ,$$

thus we have

$$k_L = \frac{k_c}{1+k_c}, \tag{3.13a}$$

or

$$k_c = \frac{k_L}{1-k_L}. \tag{3.13b}$$

Expression either (3.12) or (3.13) is the *modal phase-velocity equalization condition* for right-handed coupled lines. Obviously, odd-mode phase equals even-mode phase if $k_L = \frac{k_c}{1+k_c}$, which is referred to as *balanced capacitive/inductive coupling*; odd-mode phase *leads* even mode if $k_L < \frac{k_c}{1+k_c}$ which is called *dominant capacitive coupling;* or odd-mode phase *lags* even mode if $k_L > \frac{k_c}{1+k_c}$ which is called *dominant inductive coupling* here.

Example 1: *Balanced* capacitive and inductive couplings $k_L = \frac{k_c}{1+k_c}$ would lead to the equalization of even- and odd-mode phase velocities. (e.g. L=2.9nH, C=0.96pF, k_L=0.3, k_c=0.43).

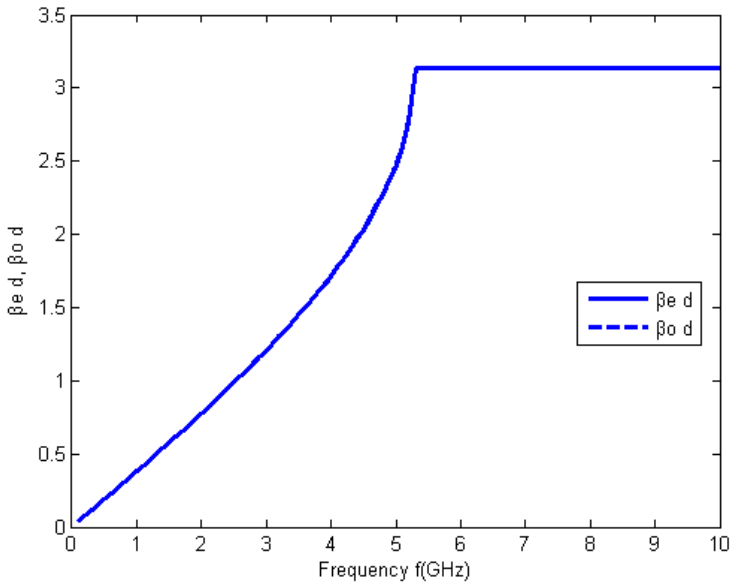

(a) Even- and odd-mode phase constants

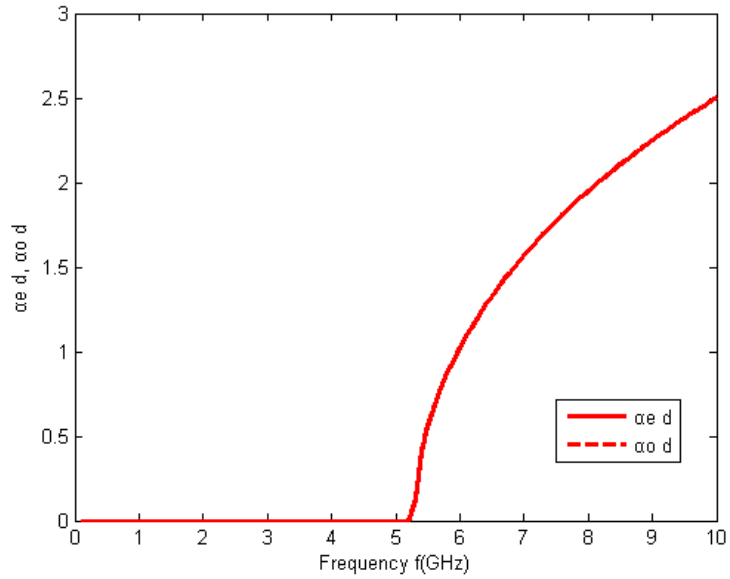

(b) Even- and odd-mode attenuation constants

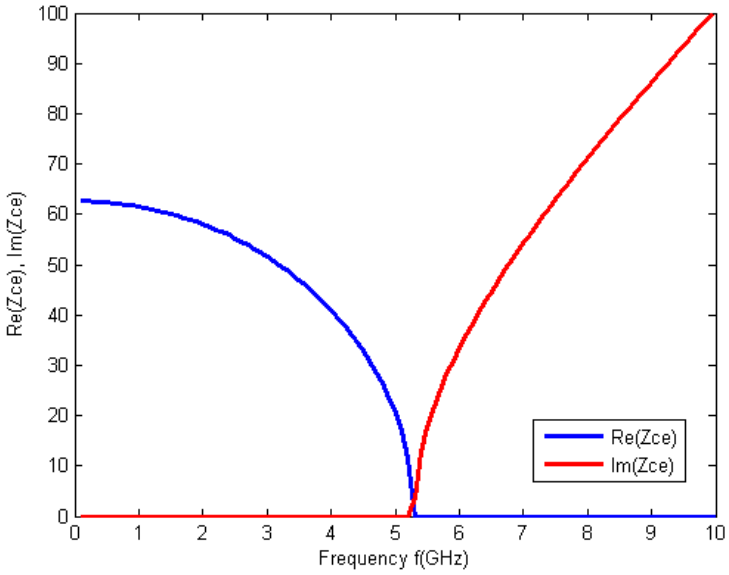

(c) Even-mode characteristic impedance

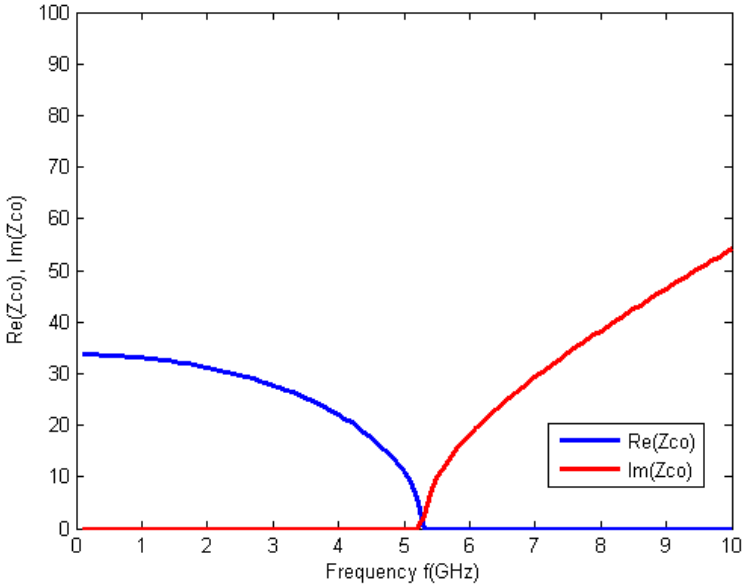

(d) Odd-mode characteristic impedance

Figure 17: Propagation constants and characteristic impedances of RH coupled lines under mode-phase equalization condition (L=2.9nH, C=0.96pF, k_L=0.3, k_c=0.43).

Example 2: *Dominant* capacitive coupling ($k_L < \frac{k_c}{1+k_c}$, or $k_c > \frac{k_L}{1-k_L}$) would result that odd-mode phase *leads* that of even mode (e.g. L=2.9nH, C=0.96pF, k_L=0.3, k_c=0.8)

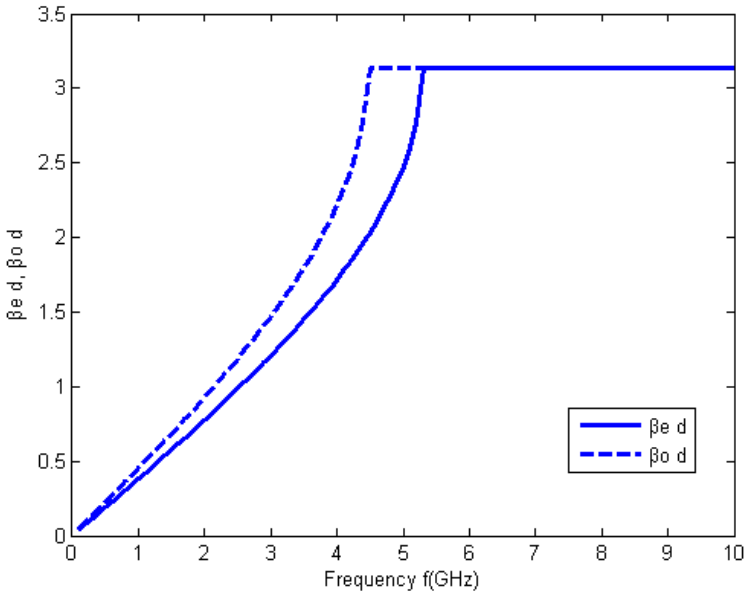

Figure 18: Even- and odd-mode phases of RH coupled line with dominant capacitive coupling (L=2.9nH, C=0.96pF, k_L=0.3, k_c=0.8).

Example 3: *Dominant* inductive coupling ($k_L > \frac{k_c}{1+k_c}$, or $k_c < \frac{k_L}{1-k_L}$) would result that odd-mode phase *lags* that of even mode (e.g. L=2.9nH, C=0.96pF, k_L=0.3, k_c=0.2)

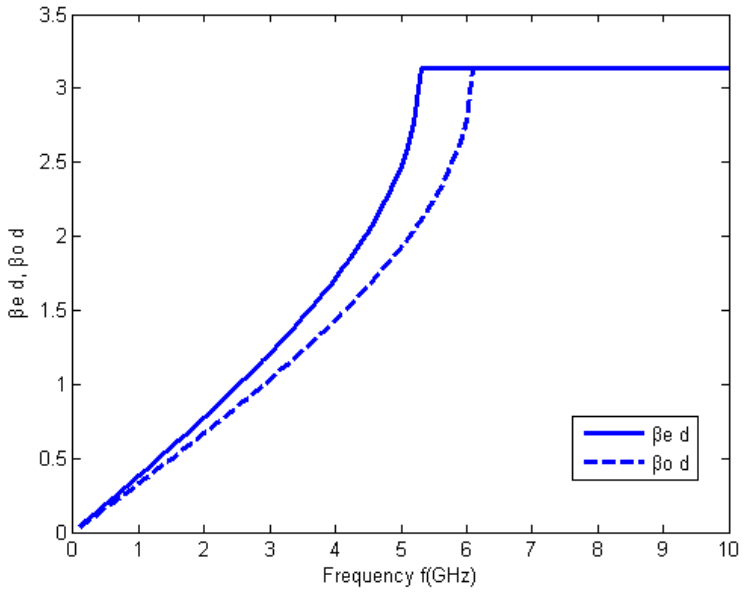

Figure 19: Even- and odd-mode phases of RH coupled line with dominant inductive coupling (L=2.9nH, C=0.96pF, k_L=0.3, k_c=0.2).

3.3 Left-handed Coupled Transmission Line

In contrast to the above-mentioned right-handed case, a theoretical study is proposed on the artificial symmetric left-handed coupled transmission lines in this section. Dispersion characteristics are investigated in both pass-band and stop-bands of left-handed coupled lines under even- and odd-mode excitations. It is found that the modal phase-velocity equalization is not possible to achieve over a broad frequency range, but it may (instead of always) exist at only a single frequency point in pass-band. *Mode-selection characteristics* are a prominent feature in this case.

3.3.1 Equivalent Quasi-Lumped Circuit Model

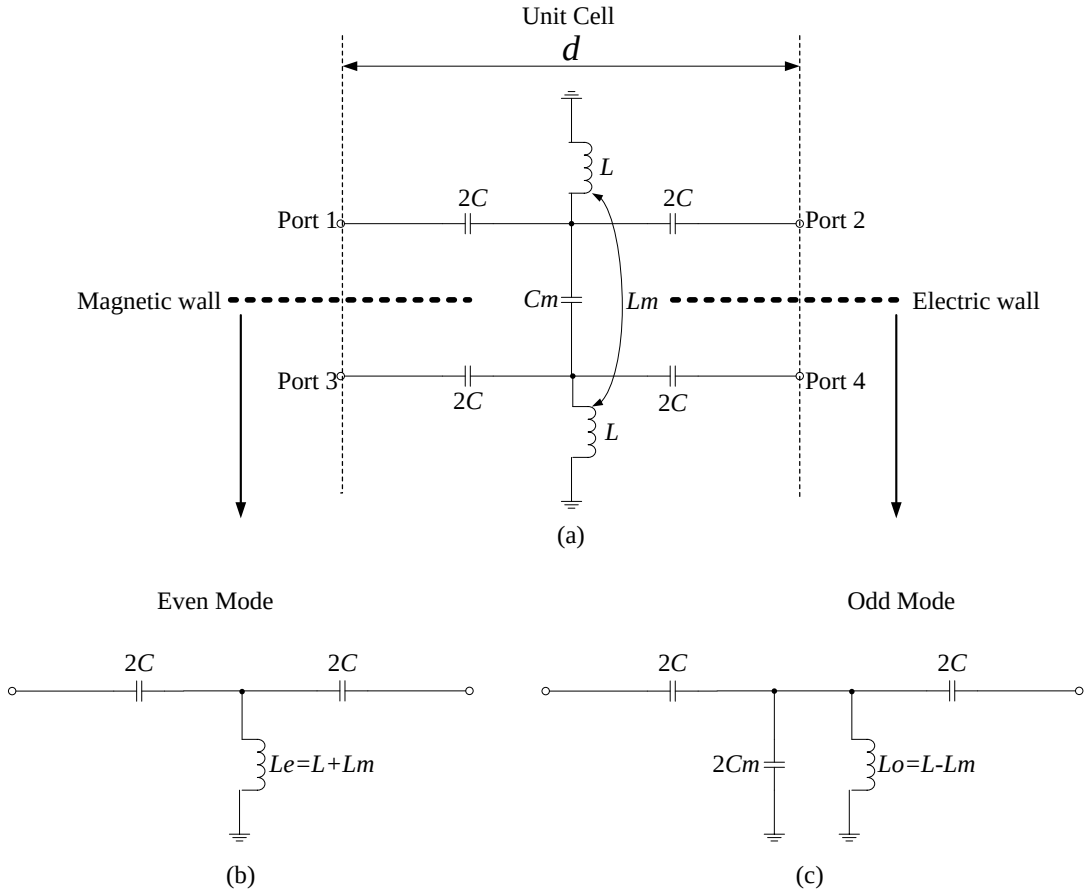

Figure 20: Unit cell equivalent *quasi-lumped* circuit of metamaterial symmetric *left-handed* coupled-line periodic structure and its decomposed even-/odd-mode half circuits. (Here *L* and *C* are H and F in units deposited in a unit cell with finite length *d*).

C and *L* are self series capacitance and shunt inductance; C_m and L_m are mutual capacitance and inductance accounting for the coupling effect of left-handed coupled lines. $k_c = C_m / C$ denotes capacitive coupling coefficient and $k_L = L_m / L$ for inductive coupling coefficient, respectively.

3.3.2 Dispersion Characteristics Under Even-Mode Excitation

From Figure 20 (b), left-handed coupled line exhibits *high-pass* characteristic under even-mode excitation with cut-off frequency

$$f_{ce} = \frac{1}{4\pi\sqrt{L_0 C_0}} \cdot \frac{1}{\sqrt{1+k_L}} . \tag{3.14}$$

In the pass-band $f \geq f_{ce}$, the propagation constant on the even-mode line is

$$\alpha_e = 0, \tag{3.15a}$$

$$\beta_e = -\frac{2}{d} \arcsin\left[\frac{1}{2\omega\sqrt{L_0 C_0}} \cdot \frac{1}{\sqrt{1+k_L}} \right], \tag{3.15b}$$

and characteristic impedance is

$$Z_{ce} = \sqrt{1+k_L} \cdot \sqrt{\frac{L_0}{C_0}} \cdot \sqrt{1 - \frac{1}{4\omega^2 L_0 C_0 \left(1+k_L\right)}} . \tag{3.16}$$

In the stop-band $f < f_{ce}$, the propagation constant and characteristic impedance of the even-mode line are

$$\alpha_e = \frac{2}{d} \arccos h\left[\frac{1}{2\omega\sqrt{L_0 C_0}} \cdot \frac{1}{\sqrt{1+k_L}} \right], \tag{3.17a}$$

$$\beta_e = -\frac{\pi}{d}, \tag{3.17b}$$

$$Z_{ce} = \pm j\sqrt{1+k_L} \cdot \sqrt{\frac{L_0}{C_0}} \cdot \sqrt{\frac{1}{4\omega^2 L_0 C_0 \left(1+k_L\right)} - 1} . \tag{3.18}$$

Evanescent wave appears in the stop-band and experiences $-\pi$ phase shift over a unit cell under an even-mode excitation.

3.3.3 Dispersion Characteristics Under Odd-Mode Excitation

From the simple circuit topology in Figure 20 (c), left-handed coupled lines present *band-pass* characteristics under an odd-mode excitation with two boundary frequencies:

lower cutoff frequency $$f_{lco} = \frac{1}{4\pi\sqrt{L_0 C_0}} \frac{1}{\sqrt{\left(1+\frac{k_c}{2}\right)\left(1-k_L\right)}}, \tag{3.19a}$$

and upper cutoff frequency $$f_{hco} = \frac{1}{2\sqrt{2}\pi} \frac{1}{\sqrt{L_0 C_0}} \frac{1}{\sqrt{k_c\left(1-k_L\right)}}. \tag{3.19b}$$

In the pass-band $f_{lco} \le f \le f_{hco}$, the propagation constants and characteristic impedances are

$$\alpha_o = 0, \tag{3.20a}$$

$$\beta_o = -\frac{2}{d}\arcsin\left[\frac{1}{2\omega\sqrt{L_0 C_0}}\sqrt{\frac{1-2\omega^2 L_0 C_0 k_c\left(1-k_L\right)}{1-k_L}}\right], \tag{3.20b}$$

$$Z_{co} = \sqrt{\left(1+\frac{k_c}{2}\right)\left(1-k_L\right)}\sqrt{\frac{L_0}{C_0}}\sqrt{\frac{1-1\Big/\left[4\omega^2 L_0 C_0\left(1+\frac{k_c}{2}\right)\left(1-k_L\right)\right]}{1-2\omega^2 L_0 C_0 k_c\left(1-k_L\right)}}. \tag{3.21}$$

In the lower stop-band $f < f_{lco}$, propagation constants and characteristic impedance are

$$\alpha_o = \frac{2}{d}\arccos h\left[\frac{\sqrt{1-2\omega^2 L_0 C_0 k_c\left(1-k_L\right)}}{2\omega\sqrt{L_0 C_0}\sqrt{1-k_L}}\right], \tag{3.22a}$$

$$\beta_o = -\frac{\pi}{d}, \tag{3.22b}$$

$$Z_{co} = \pm j\sqrt{\left(1+\frac{k_c}{2}\right)\left(1-k_L\right)}\sqrt{\frac{L_0}{C_0}}\sqrt{\frac{1\Big/\left[4\omega^2 L_0 C_0\left(1+\frac{k_c}{2}\right)\left(1-k_L\right)\right]-1}{1-2\omega^2 L_0 C_0 k_c\left(1-k_L\right)}}. \tag{3.23}$$

Evanescent wave exists in the lower stop-band with $-\pi$ phase shift over a unit cell under an odd-mode excitation.

In the upper stop-band $f > f_{hco}$, the propagation constants and characteristic impedance are

$$\alpha_o = \frac{2}{d}\operatorname{arcsin} h\left[\frac{\sqrt{2\omega^2 L_0 C_0 k_c (1-k_L)-1}}{2\omega\sqrt{L_0 C_0 (1-k_L)}}\right], \tag{3.24a}$$

$$\beta_o d = 0 \quad (2n\pi), \tag{3.24b}$$

$$Z_{co} = \pm j\sqrt{\left(1+\frac{k_c}{2}\right)(1-k_L)}\sqrt{\frac{L_0}{C_0}}\sqrt{\frac{1-1\Big/\left[4\omega^2 L_0 C_0\left(1+\frac{k_c}{2}\right)(1-k_L)\right]}{2\omega^2 L_0 C_0 k_c (1-k_L)-1}}. \tag{3.25}$$

Evanescent wave exist in upper stopband with ***zero*** phase shift over a unit cell for odd-move wave.

3.3.4 Mode-Selection Characteristics

In practice, there usually exists a nonzero potential between two signal lines (differential mode), along with a nonzero potential on the pair of signal lines with respect to ground (common mode), as illustrated in Figure 21. Signals guided by coupled lines are actually *mixed modes* which have both common- and differential-mode components.

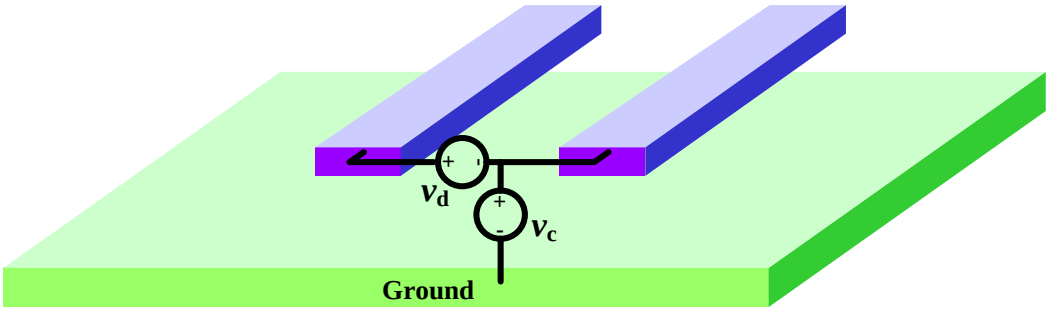

Figure 21: Mixed-mode signals on coupled lines. (v_c: common-mode voltage; v_d: differential-mode voltage.)

Differential signals have an interesting feature of their immunity to external noises in order to maintain high *signal-to-noise ratio (SNR)* over a long transmission path. They are often favored in active components in RF front end and baseband digital circuits, where noises are rather sensitive, in wireless communication systems. Moreover, differential signals are also preferred to suppress electromagnetic emissions from the perspective of *electromagnetic compatibility* (EMC) or *electromagnetic interference* (EMI).

Common-mode signals might be beneficial to enhance the electromagnetic radiation in some antenna applications.

Artificial/metamaterial coupled lines could be employed to block the common-mode (or differential) signals to refine differential (or common-mode) signals, which helps to improve *common-mode rejection ratio* (CMRR).

Left-handed coupled transmission lines exhibit high-pass and band-pass features, respectively, under even- and odd-mode excitations. Relative locations of three cutoff frequencies (f_{ce}, f_{lco}, f_{hco}) yields *mode-selection characteristics* over the whole frequency range. In certain frequency windows, left-handed coupled lines *block*/suppress even (common) and/or odd (differential) mode waves, which behave as a mode-selection filter in addition to frequency selectivity. Note that it is not a balun, because it does not perform the *transformation* from single-ended signal to differential signal, or vice versa.

Strictly, the mode-selection feature may also be present in right-handed coupled lines, depending on even- and odd-mode cutoff frequencies. Nevertheless, it is more distinct in left-handed case due to more flexibility in two (lower and upper) cutoff frequencies of its odd-mode band-pass nature. We discuss it here in detail for the left-handed case.

According to equations (3.14) and (3.19), we can obtain

$$k_c = \frac{4k_L}{1-k_L}, \quad \text{or } k_L = \frac{k_c}{k_c+4} \qquad \text{for } f_{ce} = f_{lco}; \tag{3.26a}$$

and

$$k_c = \frac{2(1+k_L)}{1-k_L}, \text{ or } k_L = \frac{k_c-2}{k_c+2}, \ (k_L<1) \quad \text{for } f_{ce} = f_{hco}. \tag{3.26b}$$

Depending on the relative locations of one even-mode and two odd-mode cutoff frequencies, five cases arise to characterize the *mode-selection feature* of metamaterial left-handed coupled transmission lines, as illustrated in Table II.

TABLE II: MODE-SELECTION CHARACTERISTICS OF METAMATERIAL LEFT-HANDED COUPLED TRANSMISSION LINES.

Cases	**Conditions**	**Modes exist from low to high freq.**	**Examples**
1: $f_{ce} < f_{lco}$	$k_c < \frac{4k_L}{1-k_L}$, or $k_L > \frac{k_c}{k_c+4}$	No-Even-Even & Odd-Even	$k_L = 0.2, k_c = 0.6$
2: $f_{ce} = f_{lco}$	$k_c = \frac{4k_L}{1-k_L}$, or $k_L = \frac{k_c}{k_c+4}$	No-Even & Odd-Even	$k_L = 0.2, k_c = 1$
3: $f_{lco} < f_{ce} < f_{hco}$	$\frac{4k_L}{1-k_L} < k_c < \frac{2(1+k_L)}{1-k_L}, (k_L<1)$	No-Odd-Even & Odd-Even	$k_L = 0.2, k_c = 2$
4: $f_{ce} = f_{hco}$	$k_c = \frac{2(1+k_L)}{1-k_L}, (k_L<1)$	No-Odd-Even	$k_L = 0.2, k_c = 3$
5: $f_{ce} > f_{hco}$	$k_c > \frac{2(1+k_L)}{1-k_L}, (k_L<1)$	No-Odd-No-Even	$k_L = 0.2, k_c = 5$

For all cases, both even and odd modes are prohibited at low frequencies, only an even mode is permitted at high frequency, and either an even mode or odd mode is present in other certain frequency window. For the cases 1 to 3, even and odd modes appear simultaneously in the overlap

frequency range of their corresponding pass-bands. Obviously, mode-selection feature is evident in all cases.

Now we examine the *modal phase-velocity equalization condition* for *left-handed* coupled lines in passbands. By inspecting equations (3.15b) and (3.20b), even- and odd-mode phases are equal ($\beta_e d = \beta_o d$) if

$$\frac{1}{\sqrt{1+k_L}} = \sqrt{\frac{1-2\omega^2 L_0 C_0 k_c \left(1-k_L\right)}{1-k_L}}$$

which requires

$$\omega = \frac{1}{\sqrt{L_0 C_0}} \sqrt{\frac{k_L}{k_c \left(1-k_L^2\right)}} .$$

Therefore, *left-handed* coupled lines have to satisfy the following three conditions for *modal phase-velocity equalization (MPE)* in pass-bands:

1) Even and odd modes are present simultaneously in certain frequency windows (this is true at low frequencies for artificial *right-handed* coupled lines with low-pass characteristics)

$$k_c < \frac{2\left(1+k_L\right)}{1-k_L}, \left(k_L < 1\right); \tag{3.27a}$$

2) The equalization of even- and odd-mode phase velocities occurs at a *single* frequency point

$$f_{MPE} = \frac{1}{2\pi\sqrt{L_0 C_0}} \sqrt{\frac{k_L}{k_c \left(1-k_L^2\right)}} ; \tag{3.27b}$$

3) This frequency point f_{MPE} is located within the above-mentioned frequency window (the overlap of even- and odd-mode pass-bands)

$$\max\left\{ f_{ce},\ f_{lco} \right\} < f_{MPE} < f_{hco} . \tag{3.27c}$$

Based on the above three conditions, mode-phase equalization always exist in **CASE 1**. Now we can conclude that the *modal phase-velocity equalization condition* of metamaterial *left-handed* coupled lines is

$$k_c < \frac{4k_L}{1-k_L}, \tag{3.28a}$$

or

$$k_L > \frac{k_c}{k_c+4} \tag{3.28b}$$

and phase-velocity equalization occurs at a ***single*** frequency point f_{MPE} in pass-band.

Furthermore, *mode-selection feature* and *modal phase-velocity equalization* are to be illustrated through some examples corresponding to Table II.

Example 1: Case 1 $f_{ce} < f_{lco}$

In this case, even-mode cut-off frequency arrives earlier than the lower odd-mode cut-off frequency. Odd mode exhibits band-pass characteristics and its upper cut-off frequency is located within the pass band of even mode which presents high-pass feature. Hence there is always an intersection point between even- and odd-mode dispersion curves within the overlap of their pass bands, which corresponds to the *modal phase-velocity equalization (MPE)* point (Figure 22 (a)).

There exists no mode when frequency is lower than the even-mode cut-off frequency. Only even mode exist between even-mode and lower odd-mode cut-off frequencies. Both even and odd modes are present between lower and upper odd-mode cut-off frequencies. However, above upper odd-mode cut-off frequency, odd mode enters stop band and only even mode could propagate on the coupled lines.

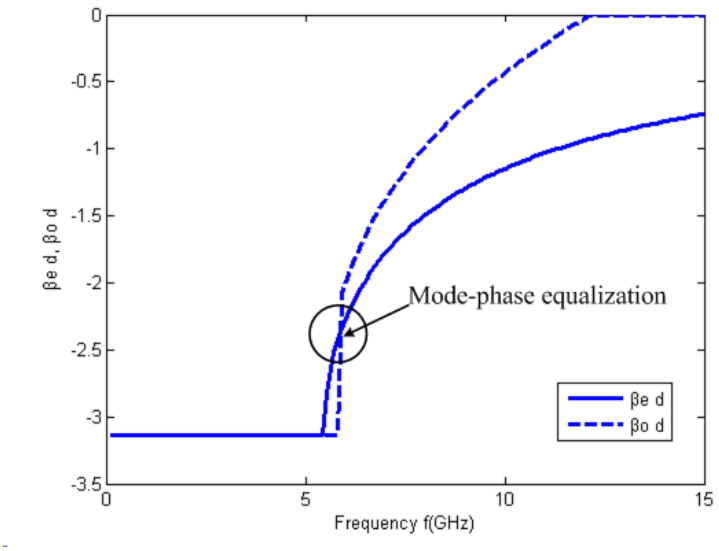

(a) Even- and odd-mode propagation constants.

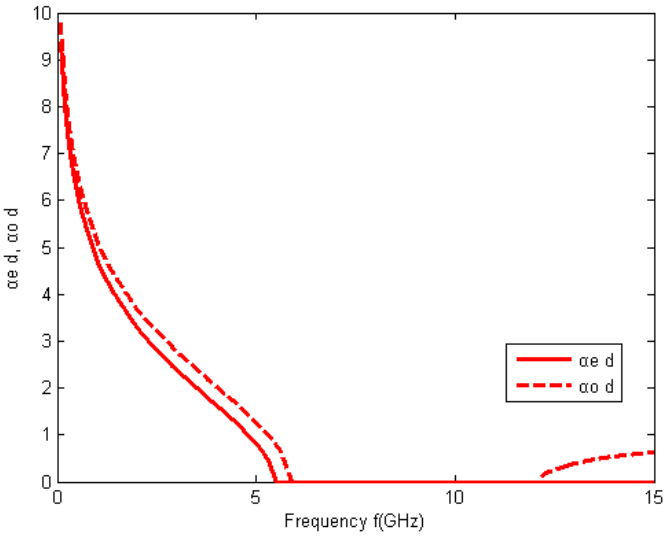

(b) Even- and odd-mode attenuation constants.

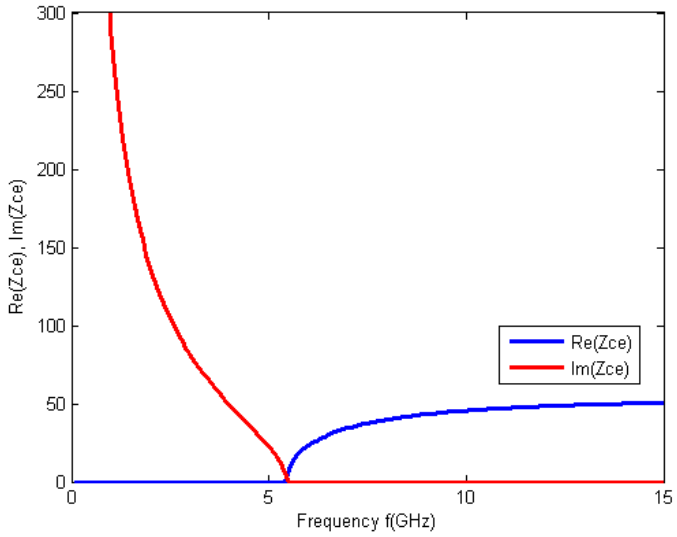

(c) Even-mode characteristic impedance.

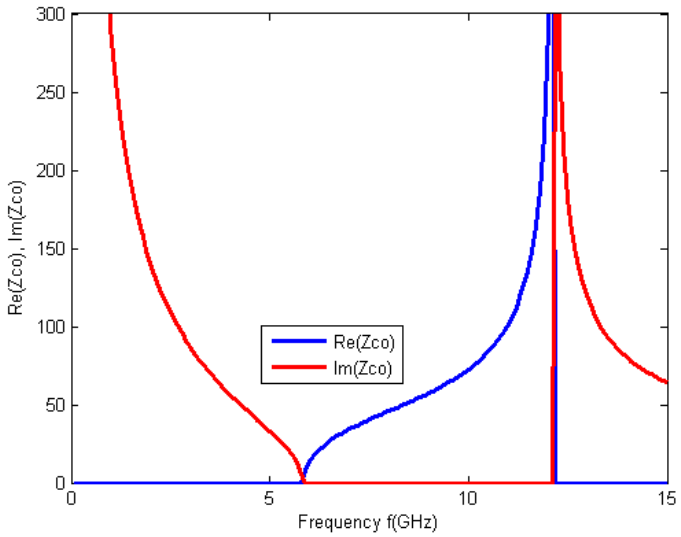

(d) Odd-mode characteristic impedance.

Figure 22: Propagation constants and characteristic impedances of LH coupled line under modal phase-velocity equalization condition. (**Case 1**: C=0.27pF, L=0.6631nH, k_L=0.2, k_c=**0.6**)

Example 2: Case 2 $f_{ce} = f_{lco}$

In this example, even-mode and lower odd-mode cut-off frequencies arrive simultaneously. There exists no mode prior to this point. Both even and odd modes are present between lower and upper odd-mode cut-off frequencies, since their pass bands overlap. Nevertheless, only even mode exists above upper odd-mode cut-off frequency. It is impossible to achieve modal phase-velocity equalization, since even- and odd-mode dispersion curves cannot intersects within pass bands in this case and followings.

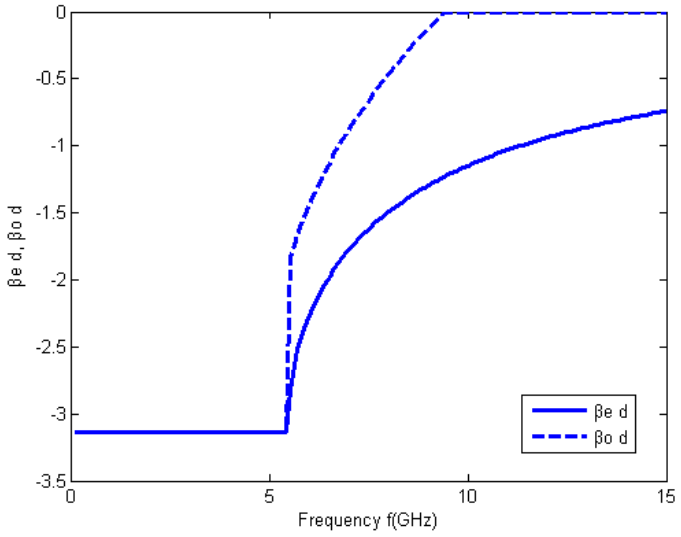

Figure 23: Even- and odd-mode phases of LH coupled line (**Case 2**: C=0.27pF, L=0.6631nH, k_L=0.2, k_c=**1**).

Example 3: Case 3 $f_{lco} < f_{ce} < f_{hco}$

In this example, the even-mode cut-off frequency arrives between lower and upper odd-mode cut-off frequencies. There exists no mode prior to the lower odd-mode cut-off frequency. Only odd exists between the lower odd-mode cut-off frequency and even-mode cut-off frequency. Both even and odd modes are present between the even-mode and upper odd-mode cut-off frequencies. Again, only even mode can exist above the upper odd-mode cut-off frequencies.

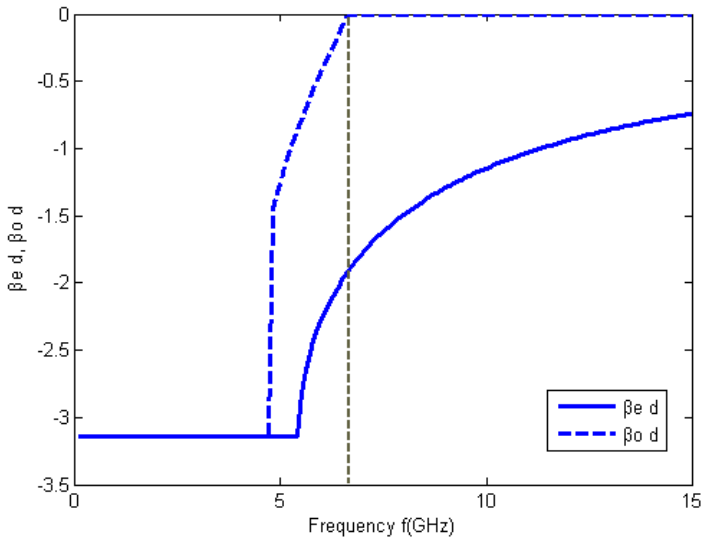

Figure 24: Even- and odd-mode phases of LH coupled line (**Case 3**: C=0.27pF, L=0.6631nH, k_L=0.2, k_c=**2**).

Example 4: Case 4 $f_{ce} = f_{hco}$

In this example, even-mode cut-off frequency arrives later than the lower odd-mode cut-off frequency and comes with the upper odd-mode cut-off frequency simultaneously. Prior to the lower odd-mode cut-off frequency, there exists no mode. Only odd mode is present between the lower odd-mode cut-off frequency and even-mode cut-off frequency (or upper odd-mode cut-off frequency). Above the even-mode cut-off frequency, even mode enters the pass band, while odd mode enters the stop band.

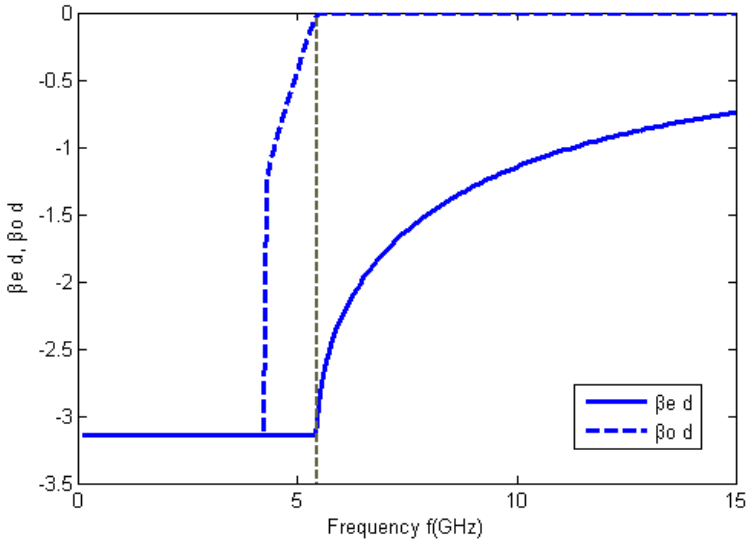

Figure 25: Even- and odd-mode phases of LH coupled line (**Case 4**: C=0.27pF, L=0.6631nH, k_L=0.2, k_c=**3**).

Example 5: Case 5 $f_{ce} > f_{hco}$

In this example, the even-mode cut-off frequency arrives later than the upper odd-mode cut-off frequency. There exists no mode prior to the lower odd-mode cut-off frequency. Only odd mode is present between lower and upper odd-mode cut-off frequencies. Again, there exists no mode between the upper odd-mode cut-off frequency and even-mode cut-off frequency. Above even-mode cut-off frequency, only even mode is present since it enters the pass band.

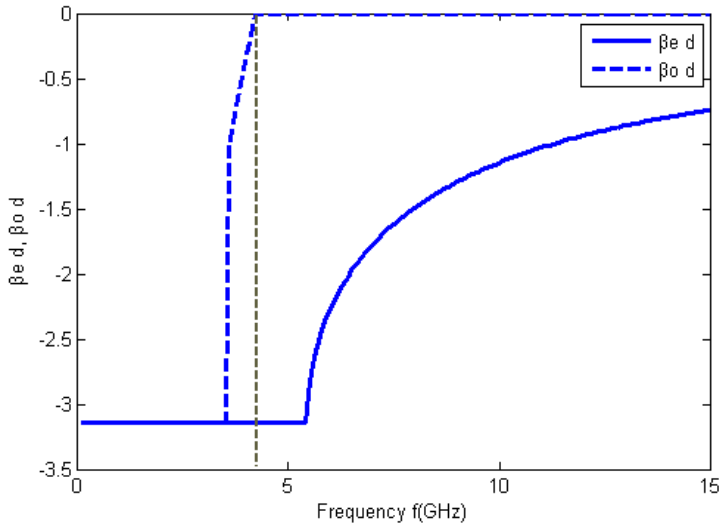

Figure 26: Even- and odd-mode phases of LH coupled line (**Case 5**: C=0.27pF, L=0.6631nH, k_L=0.2, k_c=**5**).

An initial layout example of left-handed coupled-line unit cell (shown in Figure 27) is used to illustrate the mode-selection feature and modal phase-velocity equalization point (shown in Figure 28) in *Case* 1 for the metamaterial left-handed coupled transmission lines.

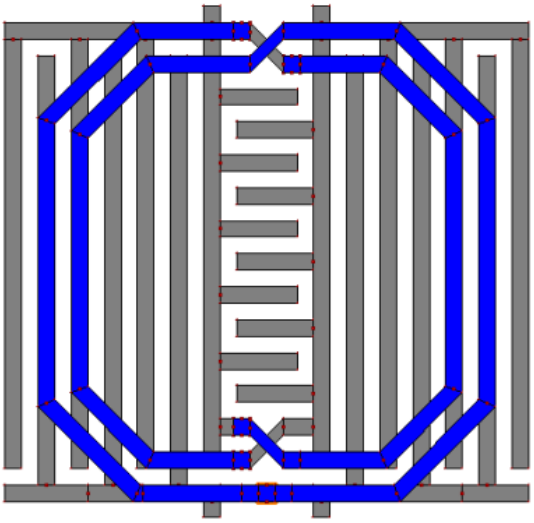

Figure 27: A layout unit cell of metamaterial LH coupled line with shunt coupled sipral inductors to ground and series inter-digital capacitors.

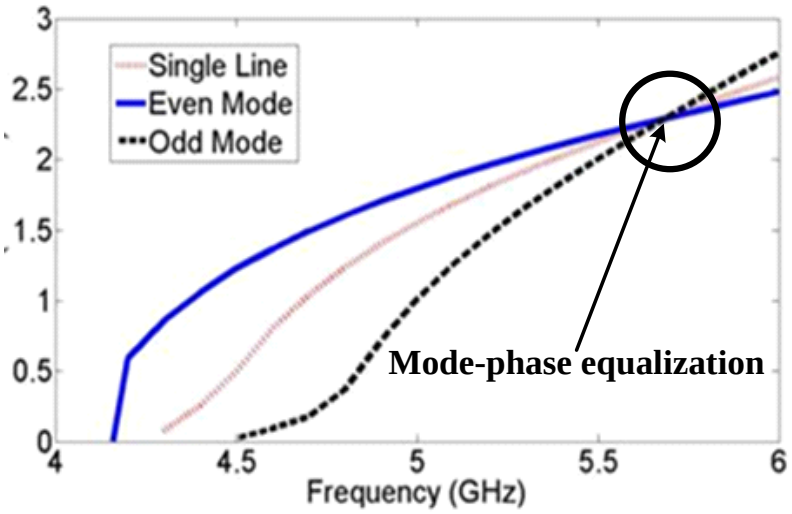

Figure 28: IE3D simulation of even- and odd-mode phases of LH coupled-line layout unit cell.

So far, mode-selection characteristics have been clearly illustrated by circuit Examples 1 ~ 5 in Figures 22 ~ 26 for metamaterial left-handed coupled transmission lines. It is shown that *modal phase-velocity equalization* occurs only in Case 1 (Figure 22 in Example 1) at a single frequency point, while it does not happen in other cases. Furthermore, a left-handed coupled-line layout example (Figure 27) is designed and simulated to demonstrate the *mode-selection feature* and *modal phase-velocity equalization* point in Figure 28. Novel left-handed coupled-line structures with proper performances are still ongoing.

4 DESIGN CRITERIA AND EXAMPLE OF SLOW-WAVE COUPLED LINES

Theoretical study in chapter 3 offers a good understanding of guided-wave characteristics over the whole frequency range of both artificial right-handed and left-handed *coupled* transmission lines. In this chapter, design criteria and guidelines are proposed specifically for *right-handed slow-wave* coupled lines as they dominate coupled-line applications in practice. As an illustration example, we present a slow-wave coupled-line structure providing large slow-wave factors, equal even- and odd-mode phase velocities, as well as comparable coupling level of conventional coupled microstrip lines.

This slow-wave coupled-line structure consists mainly of two inter-wound right-handed artificial (EBG) transmission lines. The basic approach is to compress, twist, and fragment (CTF) metal strips or discs periodically in a multi-layer substrate to form a four port structure that carries the features of large slow-wave factors (SWF). Design tradeoffs are illustrated in terms of guided-wave characteristics, including propagation constants, line impedances, SWFs, and cutoff frequencies, under even (common) and odd (differential) mode excitations. The proposed coupled-line structure is developed based upon three-layer microstrip implementation on the cost-effective FR4 substrate. It is fabricated and tested finally. The measured results of slow-wave factors and line impedances are in good agreement with those of simulated results.

Potential applications are also discussed. As a proof-of-concept demonstration, a directional coupler is developed at 2.4GHz as an application example with both dramatic 80% size reduction and comparable performances of the normal microstrip counterpart. Experimental results validate the simulation, and further substantiate our methodology. In addition, high-performance miniaturized coupled-line circuits will be presented in detail in chapters 5, 6, and 7.

4.1 Introduction of Microstrip Coupled Lines

It is well known that *isolated* transmission lines could find many applications in various microwave circuits, including monopole antenna, phase shifter, power divider/combiner, branch-line hybrid, etc. Nevertheless, other microwave devices comprising coupled lines remain frequently utilized in prevailing communication modules nowadays. Coupled planar transmission lines are basic circuit elements for directional coupler, Marchand balun, and bandpass filter which are critical components in distributed RF and microwave passive community [29]. *Conventional coupled microstrip lines* were widely investigated for more than 30 years, and sophisticated techniques had been developed to yield a variety of microstrip coupled-line devices.

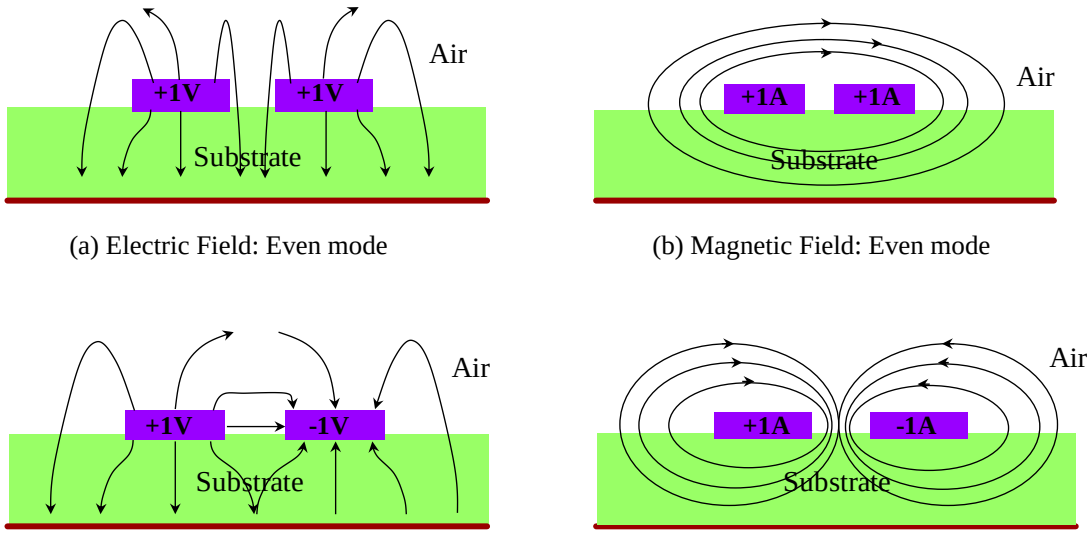

(a) Electric Field: Even mode

(b) Magnetic Field: Even mode

(c) Electric Field: Odd mode

(d) Magnetic Field: Odd mode

Figure 29: Electric and magnetic field patterns of conventional coupled microstrip lines under even- and odd- mode excitations.

However, one major *drawback* associated with conventional coupled microstrip lines is their *unequal even- and odd-mode phase velocities* due to the inhomogeneous dielectric medium (air-substrate) topology (Figure 29). The interactions of electromagnetic fields render the coupled-line system characteristics dependent on field patterns. As shown in Figure 29 (a) and (c), even and odd modes have different percentages of the total electric fields fringing through air above the substrate, resulting in different effective dielectric constants. As we know, phase velocity is related directly to the effective dielectric constant in form of $v_p = c/\sqrt{\varepsilon_e}$. Hence the coupling between microstrip lines gives rise to noticeable variations in propagation velocities of two distinct modes, which are undesirable for signal fidelity, since excitation signal on a coupled line is a superposition of even and odd modes in general. They often deteriorate the performance of coupled-line components. For example, microstrip directional couplers suffer poor directivity from such a non-synchronous feature. In addition, the considerable discrepancy between modal phase velocities would incur substantial crosstalk noise at far ends of the transmission path from the viewpoint of signal integrity.

Playing an important role in coupled-line system performances, equalization of modal phase velocities has gained substantial attention and efforts in microwave society. Several techniques were proposed to compensate the unequal even- and odd-mode phase velocities in parallel edge-coupled microstrip lines, such as Wiggly line [31], meander line [22], anisotropic substrate [56], dielectric overlay [57-58], capacitive loading [32, 59-60], and inductive loading [33, 60-61].

Other drawbacks of coupled-line devices by conventional microstrip implementation include, but not limited to:

1) significant planar area;
2) weak edge coupling based on present fabrication constraints of standard PCB technology;
3) limited (narrow) operational bandwidth;
4) spurious harmonic-response interference especially degrading filter's stopband characteristics.

The poor-coupling issue and its enhancement technique will be explored later through another novel coupled-line structure in Chapter 5.

In order to overcome some or all of the above-mentioned disadvantages of conventional uniform coupled microstrip lines, the concept of artificial/metamaterial *slow-wave coupled* transmission lines is proposed correspondingly. The theoretical analysis in the previous chapter can be employed as design guidelines and criteria for such symmetric periodic coupled lines. We will demonstrate the design methodology by introducing an example of slow-wave right-handed coupled-line structure which benefits much from two inter-wound inductors. Large modal slow-wave factors, equalization of modal phase velocities, and modest coupling level will be achieved for the proposed artificial coupled line. Finally, a 2.4 GHz directional coupler with 80% planar area saving will be designed as an example to demonstrate its application in device miniaturizations. Other possible miniaturized RF/microwave coupled-line components will also be discussed based on the proposed structure.

4.2 Design Criteria for Right-Handed Slow-Wave Coupled Lines

In general, both even- and odd-mode dispersion diagrams and characteristic impedances of artificial coupled lines can be tailored not only by self inductance L_0 and capacitance C_0 of each line, but also by coupling capacitance C_m and mutual inductance L_m between two interacted lines that are usually placed in close proximity. Based on theoretical analysis in Chapter 3, here we investigate the effects of electromagnetic couplings on the design criteria specifically for *periodic symmetric right-handed slow-wave coupled transmission lines* in terms of even- and odd-mode cutoff frequencies, slow-wave factors, equalization of modal phase velocities, line impedances, as well as coupling level in pass-bands.

The *cutoff frequencies* are, respectively, for even and odd modes

$$f_{ce} = \frac{1}{\pi\sqrt{L_e C_e}} = \frac{1}{\pi\sqrt{(L_0 + L_m)C_0}} \cdot = \frac{1}{\pi\sqrt{L_0 C_0}} \cdot \frac{1}{\sqrt{1+k_L}}, \tag{4.1a}$$

$$f_{co} = \frac{1}{\pi\sqrt{L_o C_o}} = \frac{1}{\pi\sqrt{(L_0 - L_m)(C_0 + 2C_m)}} = \frac{1}{\pi\sqrt{L_0 C_0}} \cdot \frac{1}{\sqrt{1-k_L}} \cdot \frac{1}{\sqrt{1+2k_c}}. \tag{4.1b}$$

Obviously, mutual inductance would lower the even-mode cutoff frequency while increase odd-mode cutoff frequency if mutual inductance is positive. This condition is true under the modal phase-velocity equalization condition, which will be stated later. This impact would be reversed for the negative mutual inductance case. Nevertheless, coupling capacitance would lower the odd-mode cutoff frequency, but does not affect the even-mode cutoff frequency (coupling capacitance is always positive).

The *slow-wave factors* (SWFs) are, respectively, for even and odd modes in pass-bands

$$SWF_e = \frac{\beta_e}{k_0} = \frac{c}{\pi f d}\arcsin\left(\pi f\sqrt{L_e C_e}\right) = \frac{c}{\pi f d}\arcsin\left(\pi f\sqrt{L_0 C_0}\sqrt{1+k_L}\right), \tag{4.2a}$$

$$SWF_o = \frac{\beta_o}{k_0} = \frac{c}{\pi f d}\arcsin\left(\pi f\sqrt{L_o C_o}\right) = \frac{c}{\pi f d}\arcsin\left(\pi f\sqrt{L_0 C_0}\sqrt{1-k_L}\sqrt{1+2k_c}\right). \tag{4.2b}$$

Apparently, both self inductance and capacitance contribute mainly to enhancing slow-wave factors for even and odd modes. Besides, positive mutual inductance could increase even-mode SWF_e but decrease odd-mode SWF_o; coupling capacitance only helps increase odd-mode SWF_o.

Modal phase-velocity equalization (MPE) condition can be expressed in the form of either equation (3.12) or (3.13), and was illustrated by equation (3.13) in detail through several examples in terms of capacitive and inductive *coupling coefficients* in Section 3.2.4. Now we illustrate such condition alternatively by equation (3.12)

$$L_e C_e = L_o C_o \text{ or } (L_0 + L_m)C_0 = (L_0 - L_m)(C_0 + 2C_m) \tag{4.3}$$

by means of self and mutual inductance and capacitance for convenience of practical implementation on PCB board.

This condition implies that in order to achieve equal even/odd- mode phase velocities over a broad frequency range of interest in the pass band, one should design self and mutual capacitances and inductances carefully. Coupling capacitance C_m can increase the phase constant of an odd mode while it has no impact on even-mode phase constant. Mutual inductance can enhance even-mode phase constant and reduce odd-mode phase constant if $L_m > 0$. *Therefore, equal modal phase velocity is possible only if* L_m *is positive.* This condition corresponds to the requirement that the *inductive coupling coefficient* k_L must be positive in equation (3.13).

As shown in Figure 29, two parallel wires with the *same* current direction (even mode) enhance the *magnetic flux* linkage contributing to the increase of effective inductance, while the opposite is true for two wires with *opposite* current flow directions. And two parallel wires with the *opposite potentials* (odd mode) enhance the *electric flux* linkage contributing to the increase of effective capacitance (coupling capacitance) between two wires.

The *characteristic line impedances* are, respectively, for even and odd modes

$$Z_{ce} = \sqrt{\frac{L_0 + L_m}{C_0}} \sqrt{1 - \frac{\omega^2 \left(L_0 + L_m\right) C_0}{4}} = \sqrt{1 + k_L} \cdot \sqrt{\frac{L_0}{C_0}} \cdot \sqrt{1 - \pi^2 f^2 L_0 C_0 \left(1 + k_L\right)}, \tag{4.4a}$$

$$Z_{co} = \sqrt{\frac{L_0 - L_m}{C_0 + 2C_m}} \sqrt{1 - \frac{\omega^2 \left(L_0 - L_m\right)\left(C_0 + 2C_m\right)}{4}} = \sqrt{\frac{1 - k_L}{1 + 2k_c}} \sqrt{\frac{L_0}{C_0}} \sqrt{1 - \pi^2 f^2 L_0 C_0 \left(1 - k_L\right)\left(1 + 2k_c\right)}$$

. (4.4b)

At low frequencies where unit cells are electrically small with slight dispersions, *positive* mutual inductance can help increase even-mode characteristic impedances (larger than that of a single *isolated* line) but decrease odd-mode impedance; while coupling capacitance could only help decrease odd-mode characteristic impedance (smaller than that of a single *isolated* line). One could

find that even-mode line characteristic impedance should be larger than the odd-mode line impedance in the entire frequency domain under/around the modal phase-velocity equalization (*MPE*) condition, or at low frequencies with releasing the *MPE* condition, for the case of *positive* mutual inductance.

Coupling level is another important measure of coupled-line performances, and reflects the content of power transferred across two interacted lines. The maximum *voltage coupling coefficient* (usually at design frequency) is generally defined as [62]

$$C_{V\max} = \frac{Z_{ce} - Z_{co}}{Z_{ce} + Z_{co}}, \tag{4.5a}$$

which occurs at a quarter wavelength or its odd multiples on coupled lines. In other words, the percentage difference between modal line impedances conveys how much coupling can be achieved at most for coupled transmission lines. Substantial coupling is usually desirable for coupled-line components in the microwave community.

Under the *modal phase-velocity equalization* (MPE) condition (4.3), the maximum *voltage coupling coefficient* defined for coupled lines becomes accordingly

$$C_{V\max} = \frac{k_c}{1 + k_c} = k_L \tag{4.5b}$$

by substituting even- and odd-mode characteristic impedances (4.4) into (4.5a). Now it is clear that the attainable coupling level depends explicitly on inductive and capacitive coupling coefficients for symmetric right-handed coupled transmission lines with equal modal phase velocities. In turn, equation (4.5b) can also be used to evaluate inductive/capacitive coupling coefficients by judging the maximum coupling level (*S31* for port configurations in Figure 16) for coupled lines with equal or similar even- and odd-mode propagation velocities.

So far, it is quite clear that mutual inductance and coupling capacitance could tailor the even- and odd-mode dispersion diagrams and characteristic impedances as well as the coupling level of coupled lines. The modal cutoff frequencies and propagation constants determine the coupled-line itself

intrinsic propagation characteristics. However, modal characteristic line impedances mainly determine the coupled-line performance in response to external environment (e.g. port termination impedances), apart from the coupling level or 'crosstalk' between coupled lines.

4.3 Design Example of Slow-Wave Coupled Transmission Lines With Equal Modal Phase Velocities

4.3.1 Unit Cell Topology Based on Quasi-Lumped Setup

The basic idea of slow-wave coupled line structure herein is described as follows. Compressed, twisted, or fragmented (CTF) metallic strips/plates are spread out three dimensionally into multilayer substrate structure to serve electrically as distributed self inductors and capacitors (quasi-lumped elements) within each unit cell to enhance slow-wave effects. In the meantime, a great portion of attention must be directed to synthesizing proper mutual inductance and coupling capacitance to alter dispersion characteristics to achieve equal modal propagation velocities, as well as to produce significant discrepancy between two normalized modal impedances to yield substantial power coupling between coupled lines.

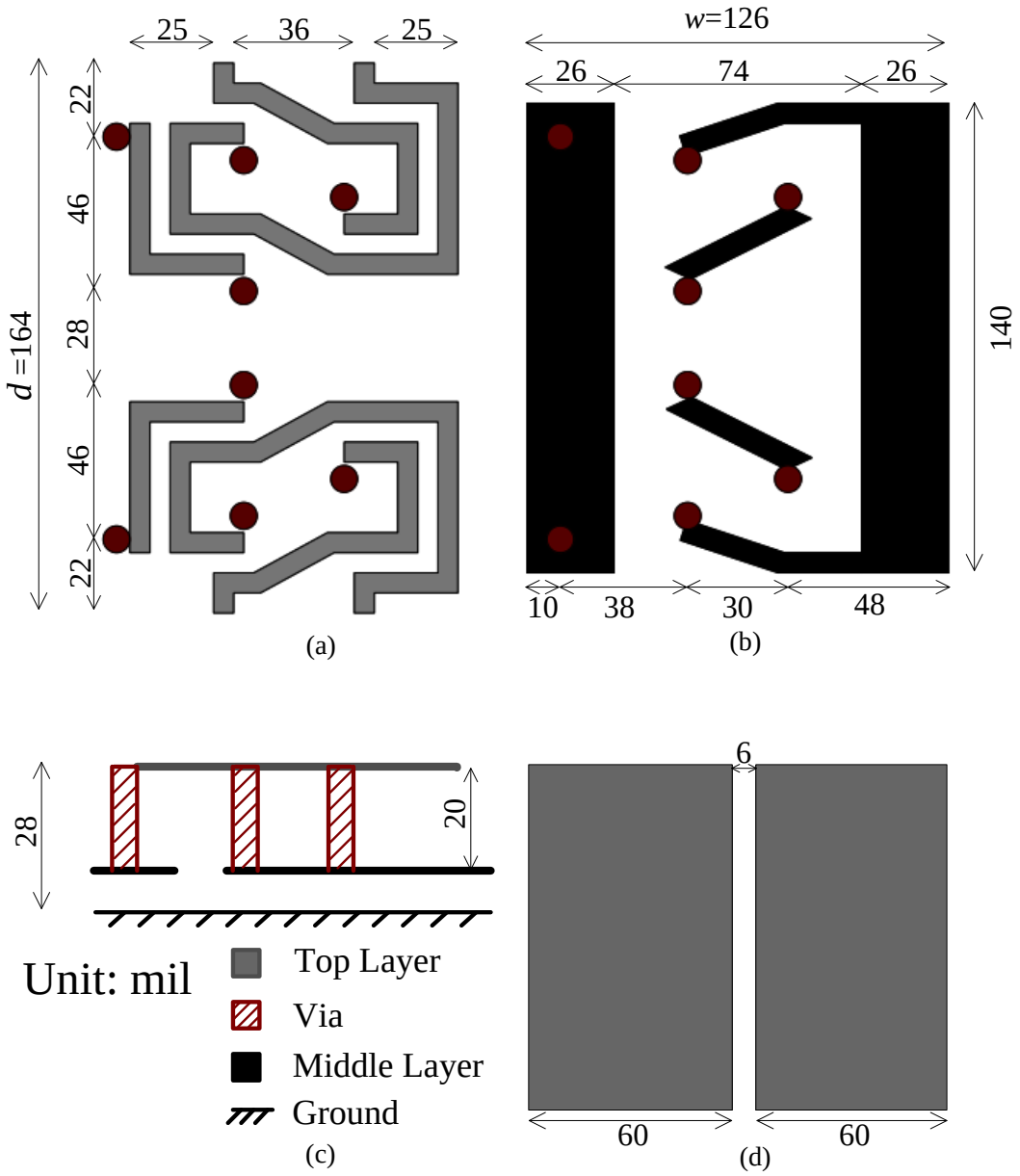

Figure 30: Unit cell of three-layer periodic structure of slow-wave coupled line based on quasi-lumped setup. (a) Top layer. (b) Middle layer. (c) Side view. (d) Conventional uniform coupled microstrip lines on the same substrate for comparison.

An example of right-handed slow-wave coupled lines is designed based on three-layer FR4 (ε_r=4.2, tanδ =0.02) substrate of 28mil total thickness. The middle layer is 8 mils above the ground and the top layer is 20 mils above the middle layer. Its periodically repeated unit cell is illustrated in Figure 30 with the period d=164mil and width w=126mil. Loops are used on the top layer to increase series self inductances. Rectangular patches are used on the middle layer to form parallel plate capacitors with respect to the ground to enhance shunting self capacitances. The slight couplings between these two patches could be neglected.

The two series loop inductors are inter-wound together in such a way (slightly non-symmetric) to form coupled inductors to ensure significant and positive mutual inductance that is a necessary condition to equalize odd- and even-mode phase velocities. Such inductive coupling coefficient depends on the spacing between coupled inductors, which is limited by the manufacture constraints in standard PCB fabrication process. In addition, their close proximity also helps enhancing the coupling capacitance. Both minimum trace width (loop inductor) and minimum spacing are 6 mils in our design here.

The 8mil-diameter circular via-holes serve as inter-layer interconnects, and are surrounded by 6mil-width annular rings (not shown in Fig. 4.2) which provide electrical connections to top-layer inductors and middle-layer capacitors. Small strips are on the middle layer to serve as bridge interconnects for the top layer coupled inductors. Dimensions of inductors, spacing, and patches are required to be chosen very carefully. Full-wave simulations (based on IE3D) are utilized to fine tune various parameters. Specific dimensions are labeled in the figure.

Two sets of coupled inductors are arranged as one reflection of the other (see Figure 30) in order to improve the symmetry along the signal propagation direction to ensure optimal transmission. So the unit-cell structure is symmetric along the horizontal plane bisecting it, and each half could be used as a unit cell alternatively. The purposes of this configuration are: 1) to avoid introducing additional

such vias (and bridges) for connections between adjacent cells in order to further reduce size/area; 2) to reduce the imaginary part of characteristic impedances, which is true for symmetric *LC* circuit topology, in contrast to an asymmetric topology along signal flow direction.

For purpose of comparison, two 50Ω microstrip lines are placed closely with 6mil spacing to form conventional uniform coupled microstrip lines on the same substrate as shown in Figure 30 (d).

4.3.2 Experimental Verification

This design example of slow-wave coupled lines is fabricated on the cost-effective FR4 epoxy substrate with 0.5oz copper cladding for each metal layer. SMA connectors are used for testing such a tiny slow-wave coupled line structure, which requires the feeding line extension at each port. The photograph of a fabricated unit cell is shown in Figure 31.

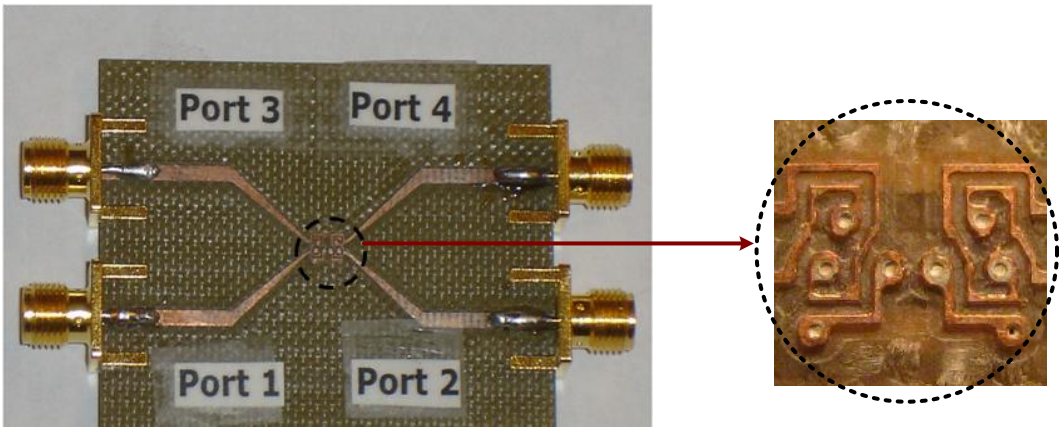

(a) (b)

Figure 31: Fabrication prototype: (a) with feeding line extensions, (b) unit cell.

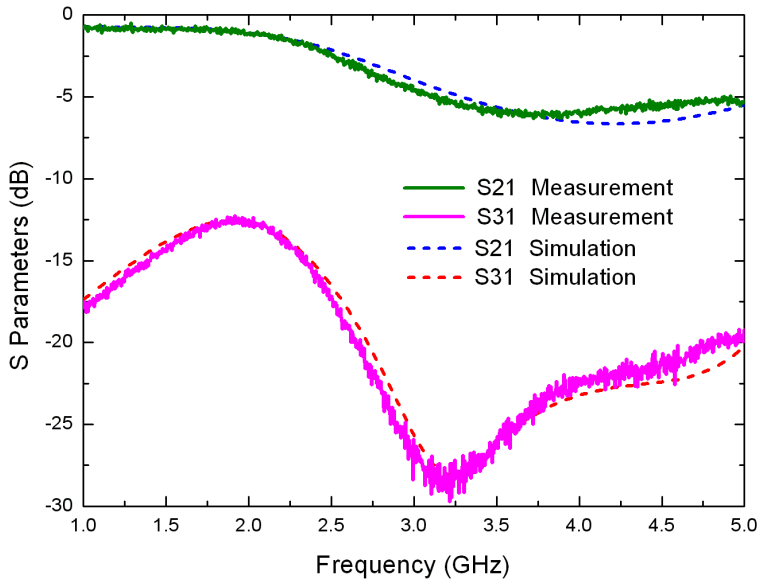

(a)

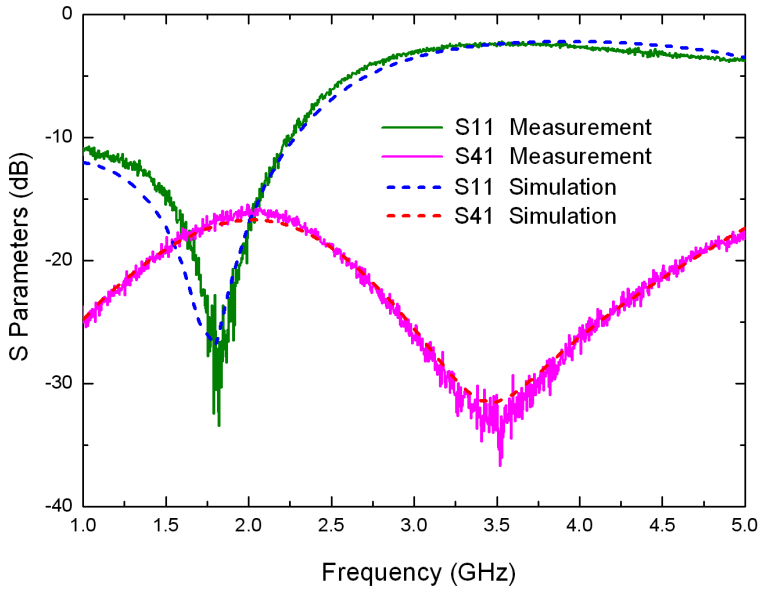

(b)

Figure 32: Experimental verification of simulation in terms of S-parameter comparison of the 4-port coupled-line circuit shown in Figure 31 (a).

Figure 32 shows the S-parameter comparison between simulation and measurement. Here, both simulation and measurement results are based on the slow-wave coupled-line unit cell (shown in Figure 31 (a)) including the feeding line extension effects. Full-wave electromagnetic simulations are run by the IE3D package (method-of-moment solver) from Zeland Software, Inc., Fremont, CA. The four-port circuit with SMA connectors was measured by Agilent Technologies, E5071B network analyzer. The reference plane is about 5mm beyond the board edge after the cable and connector calibration is made.

As illustrated in Figure 32, the measurement shows very good agreement with simulation results, which substantiates the validity of IE3D simulation on our coupled line structure.

4.3.3 Even- and Odd-Mode Propagation Constants

Coupled lines are fundamentally a four-port circuit. Its four-port S parameters are converted to common- and differential-mode two-port S parameters, which can be done in commercial simulation software such as Agilent's ADS or Zeland's Modua. The resulting two-port circuits (for both even and odd modes) are treated as the usual single isolated transmission line circuits. Subsequently, the complex propagation constants and characteristic impedances are extracted from those two-port even-/odd-mode S parameters [63].

$$e^{j\gamma_i L} = \frac{1 - S_{i11}^2 + S_{i21}^2 + \sqrt{\left(1 + S_{i11}^2 - S_{i21}^2\right)^2 - \left(2S_{i11}\right)^2}}{2S_{i21}} \tag{4.6a}$$

$$Z_{ci} = Z_0 \sqrt{\frac{\left(1 + S_{i11}\right)^2 - S_{i21}^2}{\left(1 - S_{i11}\right)^2 - S_{i21}^2}} \tag{4.6b}$$

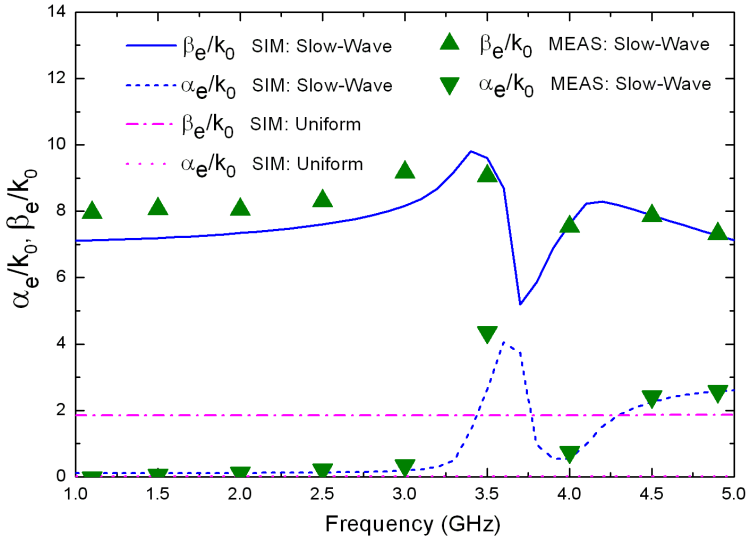

(a) Even mode

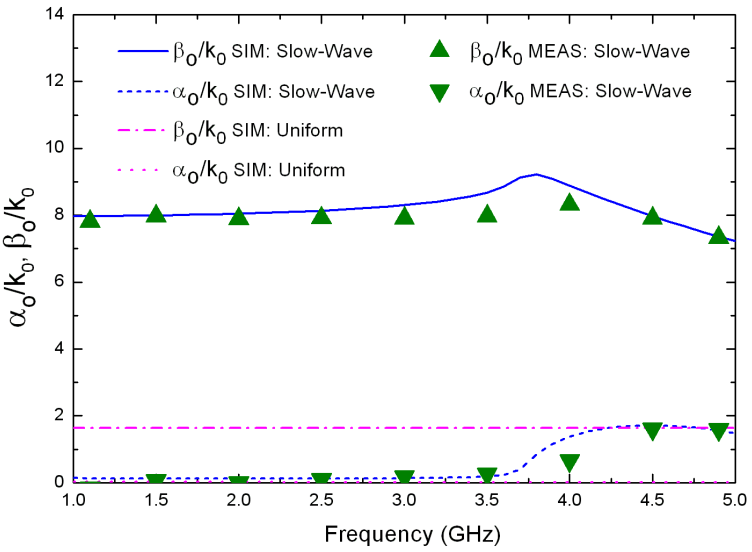

(b) Odd mode

Figure 33: Normalized propagation constants: (a) Even mode, and (b) Odd mode.

Figure 33 shows the comparison between simulation (*SIM*) and measurement (*MEAS*) of even- and odd-mode propagation constants for the designed *slow-wave* periodic coupled line. Due to substrate dielectric and metal losses, propagation constants are complex valued, including both attenuation and phase constants (SWFs). It is found the comparison is very good between simulation and measurement. Here, conventional *uniform* coupled microstrip lines (whose layout was shown in Figure 30 (d)) are also demonstrated for comparison.

From the simulation, cutoff frequencies of both even and odd modes are around 3.5GHz (more specifically, 3.3GHz for even mode and 3.6GHz for odd mode), above which evanescent waves dominate in the stop bands (low-pass characteristics). For the slow-wave coupled lines, even- and odd-mode SWFs are 7.54 and 8.12 at the design frequency of 2.4GHz, corresponding to the normalized percentage difference $|\beta_e - \beta_o| / |\beta_e + \beta_o|$ of about 3.70%, which is rather good in phase equalization. In sharp contrast, the conventional uniform coupled microstrip line exhibits stable even-mode SWF of only 1.85 and odd-mode SWF of only 1.64 at 2.4GHz, corresponding to the percentage difference of 6.02%.

4.3.4 Even- and Odd-Mode Characteristic Impedances

Comparison is shown in Figure 34 between simulation (*SIM*) and measurement (*MEAS*) of even- and odd-mode line characteristic impedances for the designed right-handed *slow-wave* periodic coupled lines. Both real and imaginary parts are included for a comprehensive view. It demonstrates a very good agreement between simulation and measurement. Similarly, for the purpose of comparison, conventional *uniform* coupled microstrip lines are also shown in the figure.

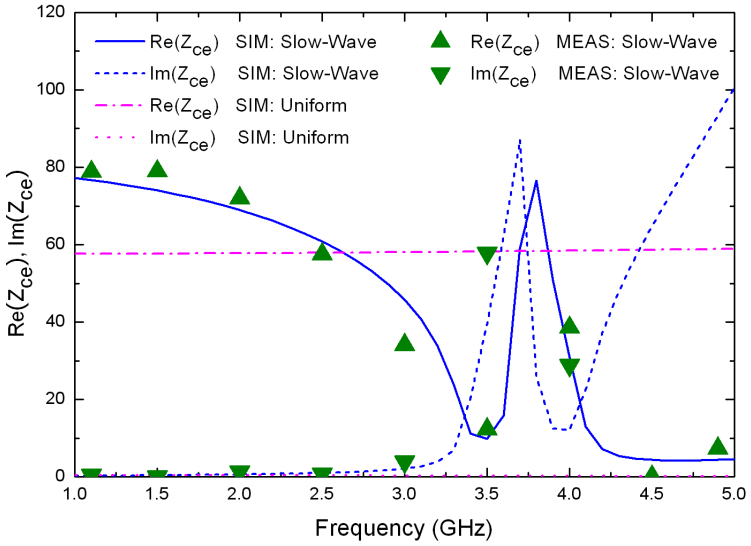

(a) Even mode

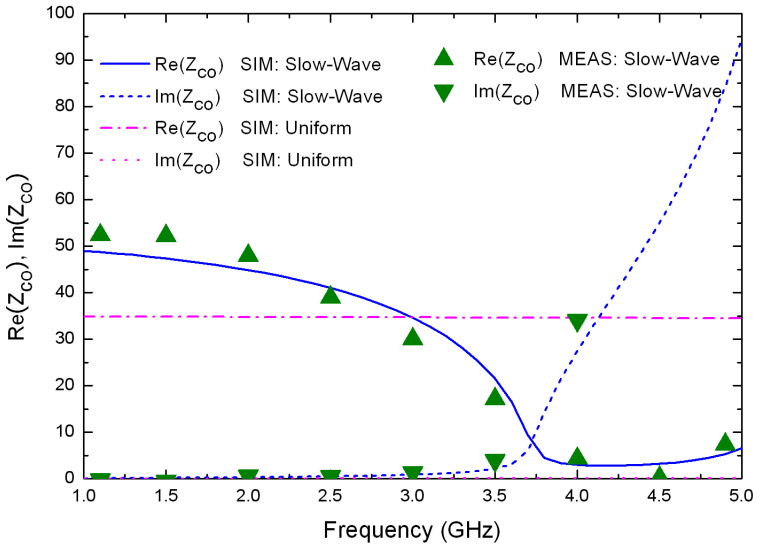

(b) Odd mode

Figure 34: Characteristic impedances: (a) Even mode, and (b) Odd mode.

It is found from the simulation that Z_{ce}=62.8Ω and Z_{co}=41.9Ω at the design frequency of 2.4GHz, corresponding to the normalized percentage difference $|Z_{ce} - Z_{co}|/|Z_{ce} + Z_{co}|$ of 20.0%, for the slow-wave coupled lines. In contrast, the conventional uniform coupled microstrip line presents Z_{ce}=57.8Ω and Z_{co}=34.7Ω, corresponding to percentage difference of 25.0% at 2.4GHz. As indicated in the expression (4.5a), the coupling level of this slow-wave coupled lines is almost comparable to that of the normal coupled microstrip lines.

In conclusion, it demonstrates a new slow-wave coupled line structure that is much smaller than normal coupled microstrip lines (size reduction by a factor of 4.5), at the same time, with similar modal phase velocities and modest coupling level. It is conceivable that many useful RF components could be evolved from such a compact planar coupled line structure in integrated circuits. For example, a quarter-wave length of the coupled line with port 3 short and port 4 open can be designed as a low-pass filter. Also, quarter-wave long coupled lines with ports 2 and 3 open (or short) are a band-pass filter. The cascade of such quarter-wave coupled lines could be applied to the Marchand balun design. A directional coupler will be developed as a miniaturization example in next section. Other high-performance coupled-line circuit applications in miniaturization will be developed in next chapter .

It is worthwhile to note that the designed periodic unit cell, as shown in Figure 30, is not strictly symmetric along the vertical plane bisecting the coupled line. For multilayer implementation within a small area, vias and bridges have often to be utilized for layer-to-layer interconnection. They complicate the design configuration and somewhat disturb the symmetry of artificial coupled lines. However, it offers reasonable approximation of common and differential modes to even and odd modes.

4.4 A 2.4 GHz Miniaturized Directional Coupler

A coupled-line directional coupler consists generally of two transmission lines (quarter-wave long) that are placed together closely nearby, and is illustrated in Figure 35. All ports are assumed terminated with a match load. The input power is routed to separate destinations. Part of input power is transferred along a transmission line to the '*Through*' output port 2, while another prescribed amount of input power is coupled via electromagnetic interactions to another line to the *auxiliary* '*Coupled*' output port 3 and ideally no power reaches the '*Isolation*' output port 4. Usually, the power splitting between '*Through*' and '*Coupled*' ports differs from the 1:1 ratio considerably, and only a small portion of input power reaches the *'Coupled'* port.

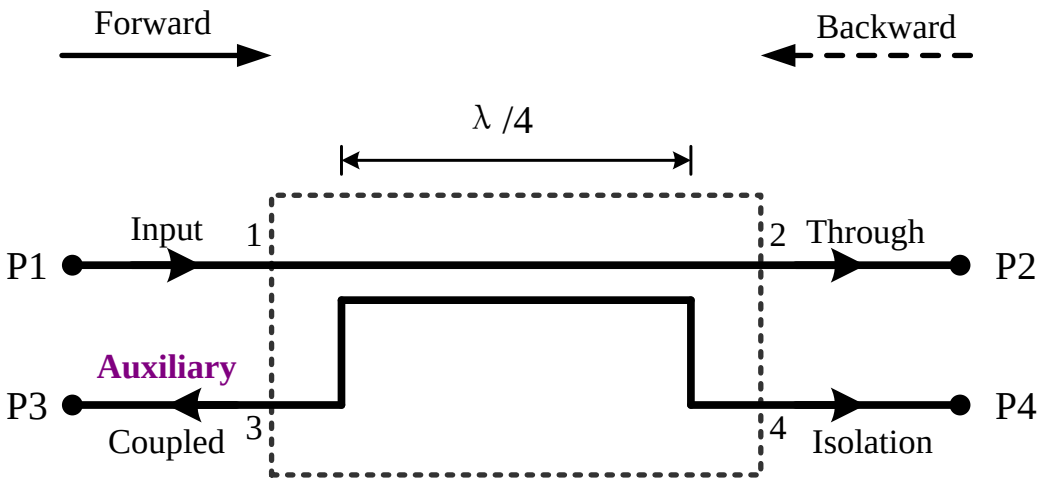

Figure 35: Coupled-line backward-wave directional coupler.

*4.4.1 **Design Concerns of Coupled-Line Coupler***

Let's denote the incident power as P1 at port 1, output powers as P2, P3, and P4 at ports 2, 3, and 4, respectively. As for a directional coupler, figures of merit are coupling factor (*CF*), isolation (*I*), directivity (*D*), and insertion loss (*IL*). They can be defined as

$$CF\ (\mathrm{dB}) = 10\log_{10}\mathrm{P1/P3} = -20\log_{10}|S31|, \tag{4.6a}$$

$$I\ (\mathrm{dB}) = 10\log_{10}\mathrm{P1/P4} = -20\log_{10}|S41|, \tag{4.6b}$$

$$D\ (\mathrm{dB}) = 10\log_{10}\mathrm{P3/P4} = -20\log_{10}\left(|S41|/|S31|\right), \tag{4.6c}$$

$$IL\ (\mathrm{dB}) = 10\log_{10}\mathrm{P1/P2} = -20\log_{10}|S21|. \tag{4.6d}$$

Obviously, *D* (dB) = *I* (dB) – *CF* (dB). Ideally, both directivity (*D*) and isolation (*I*) should be infinite. Note: all of those parameters are defined as positive quantities intentionally.

The insertion loss relies on the coupling factor of a coupler. Intuitively, the more power is coupled to the auxiliary port, the less power is transferred to the through port. Ideally, for a *lossless* coupler with all ports properly terminated and perfect isolation, P2 = P1 – P3, that is, P2/P1 = 1 – P3/P1. Hence the insertion loss could be derived as

$$IL\left(\mathrm{dB}\right) = -10\log_{10}\frac{\mathrm{P2}}{\mathrm{P1}} = -10\log_{10}\left(1-10^{-CF/10}\right). \tag{4.7}$$

where the coupling factor *CF* is in dB value. Apparently, the larger the coupling factor *CF*, the smaller the insertion loss *IL* (all quantities are positive). A few typical values of the coupling factor and insertion loss are listed in Table III. Usually, as the coupling factor exceeds 15 dB, the insertion loss is attributed primarily to parasitic metal loss, substrate dissipation, or emission loss, instead of the coupling loss, for practical couplers.

TABLE III: THE RELATIONSHIP BETWEEN INSERTION LOSS AND COUPLING FACTOR OF AN IDEAL COUPLER.

Coupling Factor *CF* (dB)	**Insertion Loss *IL* (dB)**
3	3
6	1.25
9	0.58
12	0.28
15	0.14
20	0.044
30	0.0043

For the directional coupler constructed from quarter-wavelength coupled transmission lines with equal modal velocities (which is usually assumed for directional coupler analysis), the coupling factor and insertion loss can be expressed in terms of inductive or capacitive coupling coefficients

$$CF\,(\mathrm{dB}) = -20\log_{10} k_L\,, \tag{4.8a}$$

$$IL\,(\mathrm{dB}) = -10\log_{10}\left(1-k_L^2\right). \tag{4.8b}$$

where $k_L = \dfrac{k_c}{1+k_c}$ under the modal phase-velocity equalization (MPE) condition. *Design tradeoffs* are clearly illustrated in Figure 36 about coupling factor, insertion loss, and inductive (or capacitive) coupling coefficient, for an ideal lossless equal-velocity coupled-line coupler with all ports terminated properly. This chart is useful for coupled-line coupler design.

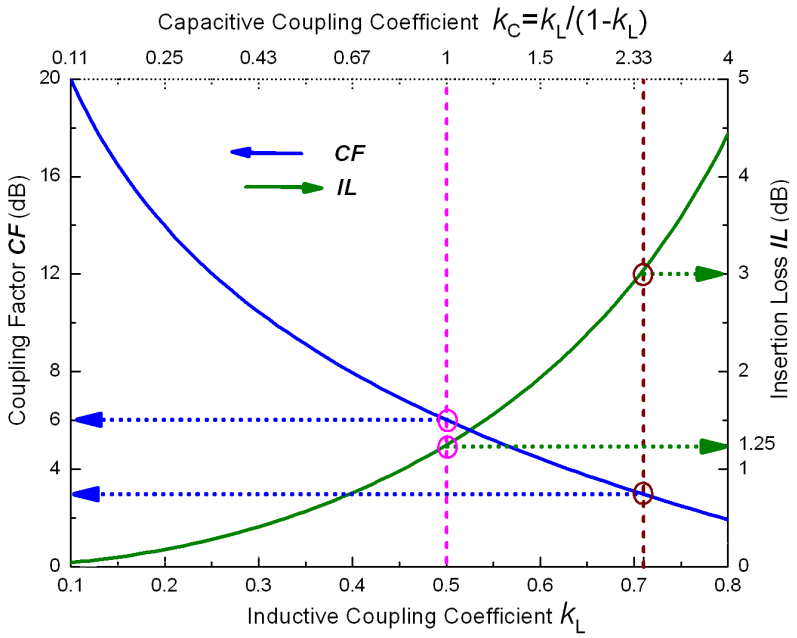

Figure 36: Design tradeoffs on coupling factor, insertion loss, and inductive coupling coefficient for an ideal coupled-line coupler.

Based on the low-cost standard PCB fabrication constraints (6mil spacing), conventional coupled microstrip directional coupler presents loose coupling whose coupling factor *CF* might be typically around 12~14 dB. Directivity might be about 10~15 dB, resulting from the significant discrepancy between even- and odd-mode phase velocities.

4.4.2 Performances of the Miniaturized Directional Coupler

A slow-wave right-handed coupled line was developed in the section 4.3. As inferred from the dispersion characteristics (shown in Figures 33 and 34), this coupled-line structure shows great significance. It gains a large average slow wave factor of around 7.83 at design frequency, which is 4.5 times of the average SWF of about 1.74 for normal coupled microstrip lines. In addition, such a large SWF is achieved with no expense of extra line width (it has the same width as the normal

coupled microstrip line). So the designed slow-wave coupled line has an attractive feature of saving up to 78% of either length or planar area on PCB surface.

Moreover, it presents its advantage to balance propagation velocities of two dominant propagating modes, which helps to maintain signal fidelity on coupled lines. Furthermore, it also offers modest coupling level which is comparable to the conventional uniform coupled microstrip lines.

The slow-wave coupled-line unit cell is of 90-degree electrical length at 2.4 GHz with very small dispersion. Hence one unit cell of the coupled line section can be actually employed as a 2.4GHz miniaturized directional coupler. Its layout and fabricated prototype were shown in Figures 30 and 31, respectively, based on the cost-effective FR4 substrate. For testing such tiny directional coupler by the usual SMA connectors, feeding line extensions are required at each port. Four-port S parameters were measured by Agilent's E5071B network analyzer. By proper de-embedding, the feeding line extension effects could be removed to extract S parameters of the embedded miniaturized directional coupler.

Figure 37 shows the comparison between measurement and simulation of four-port S parameters of the miniaturized directional coupler. It demonstrates a good agreement between simulation and measurement results. The slight difference may be attributed to fabrication tolerance as well as the unaccounted parasitics associated with SMA connectors soldered at each port.

At the design frequency of 2.4GHz, we can find that return loss RL = 33dB, insertion loss IL = 0.39dB, coupling factor CF = 14dB, isolation I = 26dB, and directivity $D = I - CF$ = 12dB from the simulation results. According to equation (4.7), coupling loss contributes 0.18dB to the insertion loss, and the remaining part originates primarily from the parasitic metal and dielectric losses. Note that the developed 2.4GHz directional coupler occupies only 22% area of the conventional microstrip counterpart, but it exhibits comparable performances.

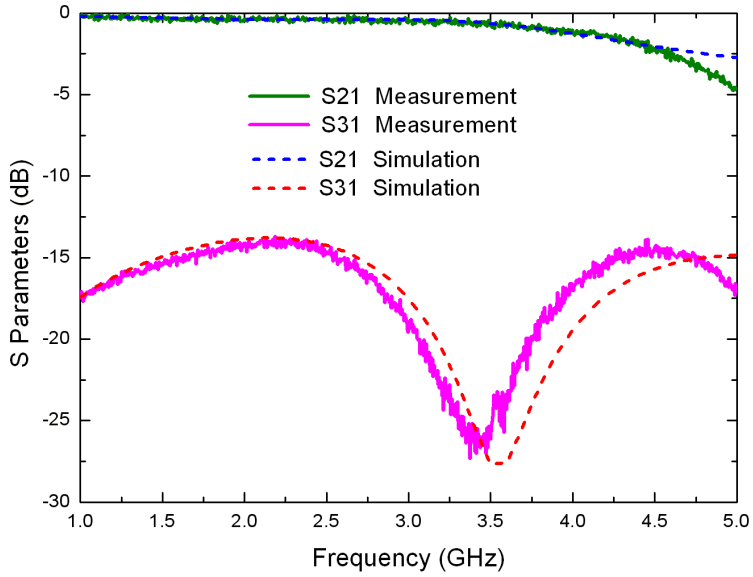

(a)

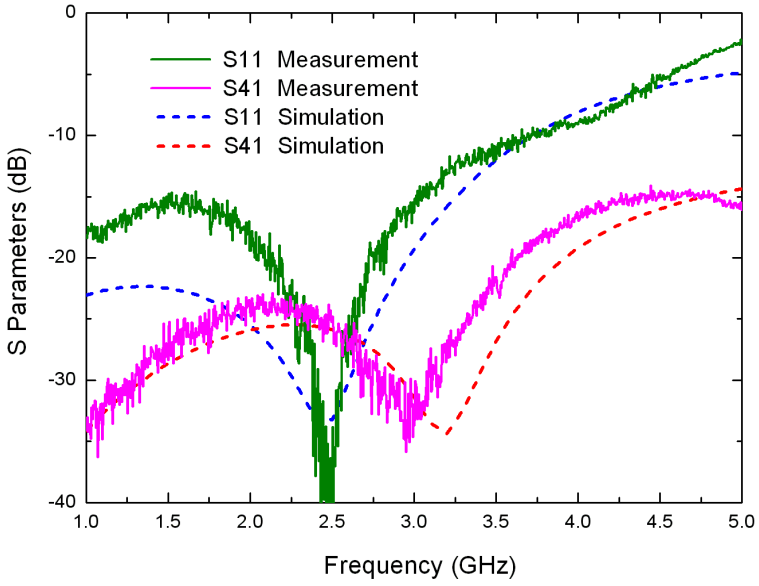

(b)

Figure 37: S-parameter comparison between simulation and measurement of the miniaturized directional coupler shown in Figure 31 (b).

5 NOVEL SLOW-WAVE COUPLING-ENHANCED COUPLED LINES AND APPLICATIONS

In the previous chapter, a slow-wave coupled-line structure was demonstrated to show large SWFs and similar even- & odd-mode phase velocities, but it presented a relatively 'low' coupling level that is simply comparable to conventional microstrip coupled lines. In addition to equal modal phase velocities, *coupling level* plays an important role in many coupled-line microwave circuits, which had been illustrated through several examples in the last section of chapter 2.

Balanced capacitive and inductive couplings (Equation 3.13) are necessary for the equalization of even- and odd-mode phase velocities. As for the parallel edge-coupled lines under modal phase-velocity equalization condition, the effective coupling level is limited mainly by the *inductive coupling coefficient*, which usually cannot be enhanced dramatically based on the cost-effective PCB fabrication process. Nevertheless, it is possible to achieve large *capacitive coupling coefficient* (even $k_c > 1$) with the same PCB technology, for example, using multi-layer interdigital capacitors.

In this chapter, we are going to develop a novel coupled-line structure which provides significant slow-wave factors and equal modal phase velocities, more importantly, it also presents an *enhanced* coupling level on the common PCB fabrication technology. The inductive coupling could be enhanced substantially and it is fundamentally different from the previous edge coupling. The proposed coupling-enhanced slow-wave coupled transmission lines are illustrated in detail in terms of guided-wave characteristics under common- and differential-mode excitations. Furthermore, this novel structure successfully demonstrates its intriguing applications to *high-performance miniaturized coupled-line circuits*, including directional couplers, coupled-line band-pass filters, Marchand balun, and coupled-line 180^o hybrid coupler.

5.1 Introduction

Nowadays, sophisticated multi-layer integrated-circuit (IC) technology has enabled the standardization of three-dimensional (3D) fabrication of metallic components within common dielectric or semiconductor substrates at a millimeter, micron, or even nano scale. It leads to the cost-effective implementation of artificial right- or left-handed transmission lines. Since dispersion characteristics can be tailored, many research activities [50, 64-65] have advocated such artificial electromagnetic materials in recent years. Of their various applications, slow wave is of particular interest in miniaturization of RF and microwave passive components in modern compact wireless systems.

However, most of the previous efforts were focused on single isolated transmission lines [3, 66]. But coupled lines are widely used in RF and microwave systems especially since the differential operation has become the preferred choice for its salient feature of immunity to the environmental noise. Typical coupled-line applications include, but not limited to, directional couplers, filters, baluns, transformers, and DC blocks [29].

Common microstrip coupled lines (shown in Figure 38 (a)) are basically a four-port structure comprising two closely-spaced coplanar parallel microstrip lines with electromagnetic (EM) interactions between each other. Nevertheless, circuit applications are usually limited by their weak edge coupling on printed circuit boards (PCB). Further improvement is often prohibited by the constraint on minimum spacing between traces in conventional PCB fabrication where at present 0.15mm (6mil) line width/spacing are considered as limit to implement circuits at low cost. In addition, the two dominant modes (even and odd) exhibit considerable discrepancy in phase velocities due to the inhomogeneous dielectric medium topology (air-substrate) [32]. By the way, coupling enhancement by placing coupled two lines in *closer* proximity usually render the odd-mode propagation velocity deviate further from that of even mode. It is undesirable for signal fidelity and

often degrades circuit performances. Moreover, the common microstrip coupled-line circuits occupy relatively large planar area as their physical dimensions are proportional to a guided wavelength.

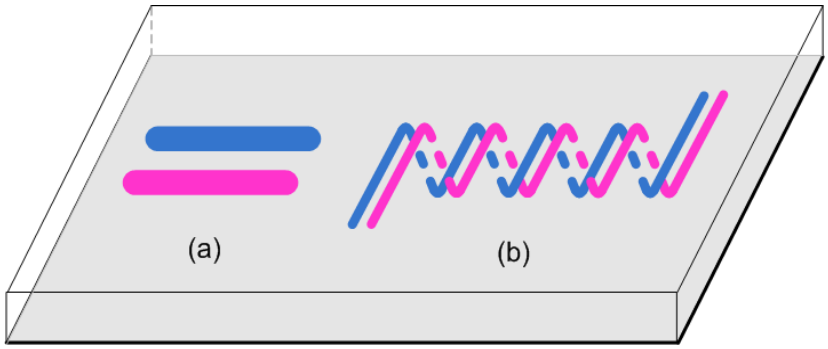

Figure 38: Coupled lines based on microstrip implementation on a common substrate: (a) conventional, and (b) proposed structure (dashed lines embedded in substrate) .

Recently, artificial right-handed coupled transmission lines were proposed to overcome the above-mentioned drawbacks of conventional coupled microstrip lines. Inter-digital open-circuited stubs were loaded between the coupled two lines [34, 42] to enhance capacitive coupling through fringing electric fields. Nevertheless, either unequal modal phase velocities [42] or relatively weak effective coupling [34] was reached. Spiral-type planar coupled inductors [67] were proposed in Chapter 4 to attain large slow-wave factors as well as similar modal phase velocities, but it yields a coupling level simply comparable to that of conventional coupled microstrip lines. Coupling had been improved dramatically through techniques of the ground plane aperture, defected ground structure (DGS) [68-70], or floating ground-plane conductor [71]. However, slow-wave effects or modal phase-velocity equalization were not achieved substantially. Besides, ground plane perturbations are usually not favored for implementation or integration with other circuits on the same circuit board in practical applications.

In this chapter, by employing a novel coupling mechanism that enhances magnetic coupling significantly, a new slow-wave coupled-line structure (shown in Figure 38 (b)) is proposed to achieve equal phase velocities of even and odd modes. The new structure consists of two layers of parallel metal strips interconnected through high density of vias. The two arrays of vias resemble fence walls in a substrate integrated waveguide (SIW). But they serve here to enhance the magnetic coupling coefficient for interleaved periodic coupled lines.

Guided-wave characteristics are illustrated in terms of transmission line effective distributed parameters, including characteristic impedances, propagation constants, slow-wave factors, and cut-off frequencies, under common- and differential-mode excitations. Good agreement between full-wave EM simulations and equivalent circuit model helps to verify our theoretical analyses and to illustrate design criteria for the artificial right-handed coupled transmission lines presented in previous chapters. It shows about 80% planar area reduction and 3-4dB coupling enhancement, in contrast to conventional coupled microstrip lines on the same substrate.

Dispersion characteristics of the proposed coupled-line structure are rather interesting. It is found that this new structure possesses the figures of merit as follows:

1) significant slow-wave factors,

2) equal even- and odd-mode phase velocities,

3) proper modal characteristic impedances, and

4) *enhanced* coupling level.

By taking advantage of the features above, *high-performance miniaturized coupled-line circuits* are developed accordingly in the frequency range of interest, e.g., directional coupler, band-pass filters, Marchand balun, and coupled-line 180^{o} hybrid. As proof-of-concept demonstrations, prototypes of those application examples are eventually designed and fabricated on the Rogers RO4003C microwave substrate based upon three-layer microstrip implementation. Measured performances

agree quite well with those of simulations. Excellent agreements help to validate the full-wave EM simulations, design methodology, as well as theoretical analyses.

The remainder of this chapter is organized as follows. Section II shows the coupling-enhanced slow-wave coupled-line structure, full-wave EM simulations, equivalent circuit model with extracted *LC* parameters, and dispersion characteristics of coupled lines. Theoretical results based on ideal circuit model are compared with full-wave simulations. Section III develops an application example of miniaturized directional couplers evolved from the proposed slow-wave coupled-line structure. Miniaturization applications to coupled-line band-pass filters in both regular and folded configurations are demonstrated in section IV. Measurement results are presented and compared with simulations in sections III-IV. Finally, a conclusion is summarized in section V.

5.2 Novel Slow-Wave Coupled Lines With Enhanced Coupling

5.2.1 Design Tradeoffs

Theoretical analyses were formulated in chapter 3 for periodic symmetric coupled lines, but it also reveals the basic design methodology. Correspondingly, design criteria were elaborated in detail in chapter 4 for right-handed slow-wave coupled lines. In general, apart from self inductance and capacitance, coupling capacitance and mutual inductance can also help tailor the even- and odd-mode dispersion diagrams and characteristic impedances as well as the coupling level of artificial coupled lines. As for practical circuit applications, proper line impedances are necessary for circuits to work functionally in response to external terminations.

TABLE IV: DESIGN TRADEOFFS AMONG CUTOFF FREQUENCIES, SLOW-WAVE FACTORS, LINE IMPEDANCES, AND COUPLING LEVEL AS A FUNCTION OF THE CIRCUIT PARAMETERS FOR PERIODIC SLOW-WAVE SYMMETRIC COUPLED LINES*.

Parameters		L_m	C_m	L	C
$f_{ce,o}$	even	↓	⊗	↓	↓
	odd	↑	↓	↓	↓
$SWF_{e,o}$	even	↑	⊗	↑	↑
	odd	↓	↑	↑	↑
$Z_{e,o}$	even	↑	⊗	↑	↓
	odd	↓	↓	↑	↓
C_{Vmax}		↑	↑	\	\
MPE		$(L+L_m)\,C = (L-L_m)\,(C+2C_m);\ L_m > 0$			

* (Symbol meanings: ↑ increase; ↓ decrease; ⊗ don't care; \ not determined)

Surely, the more comprehensive the analyses are, the more accurate the statements would be. In this section, however, we are going to simplify the analyses and preserve the minimum complexity for our goal here is to acquire direct design insights, based on the equivalent circuit model.

Therefore, analyses are reduced to render it appropriate for the design approach, especially for slow-wave coupled lines operating much below cut-off frequencies to have little dispersion and small attenuation. Trade-offs are summarized in Table IV for the impacts of equivalent circuit components on effective distributed transmission-line parameters of coupled lines. 'L' and 'C' denote *self* inductance and capacitance, while 'L_m' and 'C_m' represent *mutual* inductance and *coupling* capacitance. Symbols of '↑', '↓', '⊗', and '\' indicate the verbal meanings of '*increase*', '*decrease*', '*don't care*', and '*not determined*', respectively (the concept of '*don't care*' is borrowed from Karnaugh map in digital circuits). They are briefly interpreted as follows.

1. Equalization of even- and odd-mode phase velocities requires synthesizing proper self and coupling inductances and capacitances with *positive* mutual inductance, satisfying the *MPE* condition (3.12) or (3.13);
2. Self inductance L helps to increase even- and odd-mode slow-wave factors and characteristic impedances, but it decreases cut-off frequencies of both even and odd modes;
3. Self capacitance C helps to increase even/odd-mode slow-wave factors, but it decreases even/odd-mode characteristic impedances. It reduces both even- and odd-mode cut-off frequencies;
4. Mutual inductance L_m helps to increases even-mode slow-wave factor and characteristic impedance as well as odd-mode cut-off frequency, but it decreases odd-mode slow-wave factor and characteristic impedance as well as even-mode cut-off frequency;
5. Coupling capacitance C_m helps to increase odd-mode slow-wave factor while it decreases odd-mode characteristic impedance and cut-off frequency. But it does not affect much the even-mode parameters which *don't care* about C_m;
6. Both mutual inductance L_m and coupling capacitance C_m could enhance the coupling level, but balanced inductive and capacitive couplings help the modal phase-velocity equalization.

5.2.2 Design Example

A. Layout Realization

From the design point of view, specific layout guidelines could be provided below for the slow-wave structure of coupled lines with coupling enhancement. Compressed, twisted, or fragmented (CTF) metal strips are periodically spread out three-dimensionally into a multilayer dielectric substrate. High-density distributed metallic elements can help synthesize significant quasi-lumped

inductors and capacitors within small unit cells. It gives rise to slow-wave effects and proper impedances of each line. Multi-layer 3D-folded inductors are inter-wound together to form coupled inductors and to progress in parallel. In addition to regular parallel-edge capacitive and inductive couplings, magnetic fields are confined and guided in a way to have more magnetic flux linkage between coupled inductors. Inductive coupling is enhanced dramatically, so is the total effective coupling level. Balanced inductive and capacitive couplings also facilitate the equalization of even- and odd-mode phase velocities.

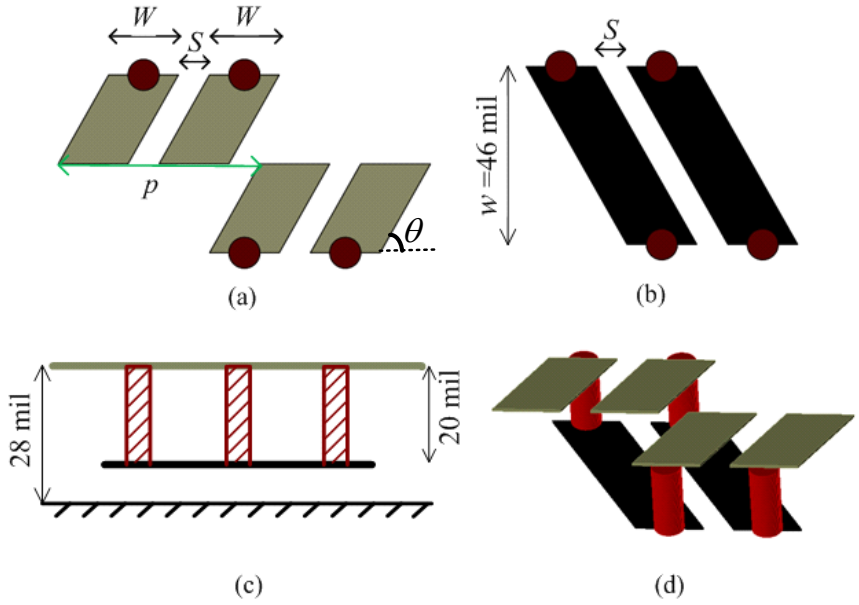

Figure 39: Unit cell layout of periodic structure of slow-wave coupled lines based on a three-layer setup. (a) top layer, (b) middle layer, (c) side view, and (d) 3-D view (ground not shown). (1 mil = 25.4 μm)

A layout design example of a unit cell is depicted in Figure 39 for the periodic structure of slow-wave coupled lines based upon a three-layer setup on the Rogers substrate comprising the upper RO4003C core laminate and lower RO4450B prepreg. The bottom metal layer serves as the ground plane. Middle and top metal layers are 8 and 28 mils above the ground, respectively. Parallel strips

are interleaved three-dimensionally onto top and middle layers through circular vias of 8mil diameter with 5mil-width annular ring as contact pads providing inter-layer interconnects. Middle-layer traces mainly form parallel plate shunt capacitors to the ground plane along with parasitic inductance, while top-layer traces serve primarily as series inductors. High density of vias are used to enhance their inductive effects. The two 3D-folded traces progress and inter-wind together in parallel to ensure the significant enhancement of positive inductive coupling.

Both trace width and spacing should be kept larger than 6 mils (0.15mm) which are considered the minimum requiremens of many standard PCB fabrication houses. The tilting angle θ cannot be too small to ensure the spacing above 6 mils. Commercial Full-wave EM solver (HFSS) is employed to fine tune various dimensions for proper performances.

B. Parametric Analyses

Parametric analyses are run by full-wave simulations to find out the right geometry dimensions of this structure for certain objectives. The analysis complexity depends on the number of dimension variables under consideration. Apparently, simpler structure involves fewer variables which would lead to less complexity. As for the proposed structure, the total coupled line width of 64 mils (w=46mil plus via sizes) is intentionally kept the same as that of a single *isolated* 50ohm *uniform* microstrip line on the same substrate. Therefore, benefiting from the simple nature of this structure, only two variables (strip width W and spacing S) are left for parametric analyses.

HFSS provides the convenience of simulations under common- and differential-mode excitations for multi-conductor transmission lines. By taking advantage of the symmetry of proposed coupled-line structure, common and differential modes are well reduced to conventional even and odd modes, which will be confirmed in a subsection later. After obtaining even/odd-mode two-port S parameters of coupled lines, the modal propagation constants and characteristic impedances can be extracted from those 2-port S parameters by using Equation (4.6).

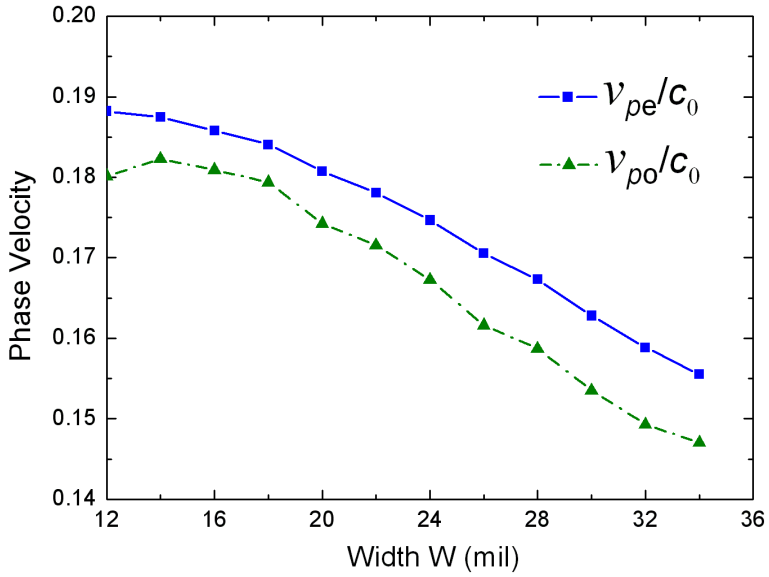

(a)

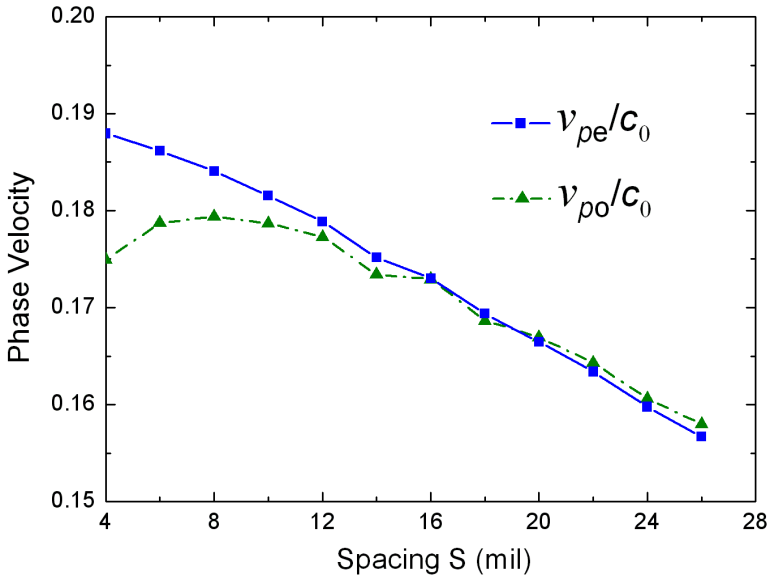

(b)

Figure 40: Normalized even- and odd-mode phase velocities versus: (a) strip width *W*, and (b) spacing *S* (unit: mil).

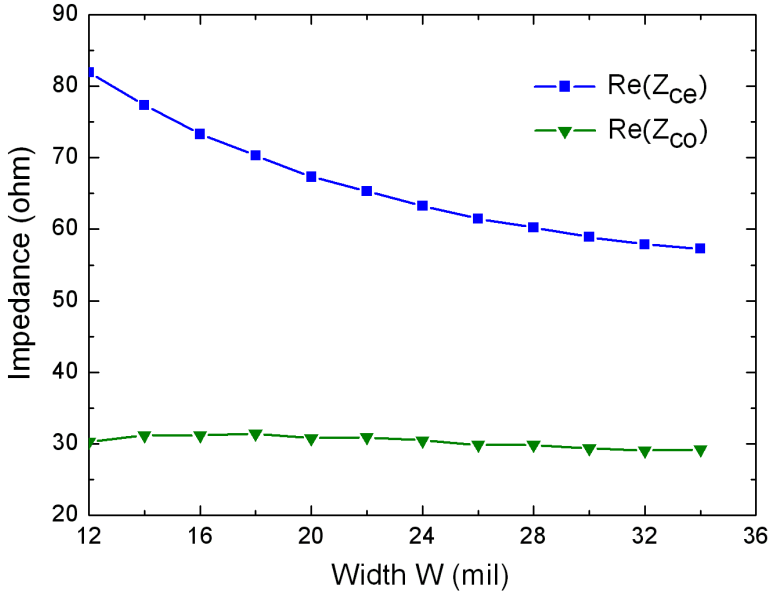

(a)

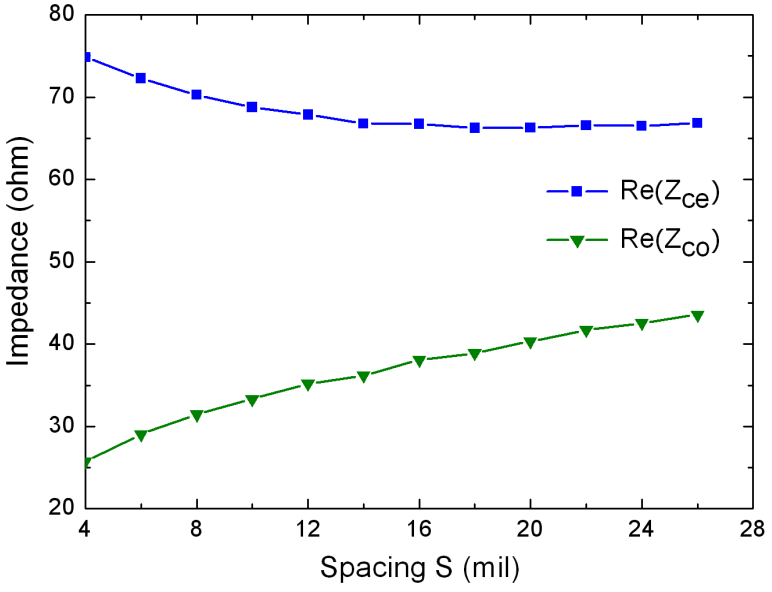

(b)

Figure 41: Even- and odd-mode impedances versus: (a) strip width *W*, and (b) spacing *S* (unit: mil).

Phase velocity can be calculated from the extracted phase constant since they bear the relationship $v_p = \omega/\beta$. Even- and odd-mode phase velocities are normalized to the speed of light c_0 in vacuum, and they are illustrated in Figure 40 versus the strip width *W* and spacing *S*, respectively, in unit of mils. As indicated in the Expressions (3.3) and (3.8), increasing strip width *W* boosts the self capacitance, which reduces the phase velocities of both even and odd modes. Enlarging the spacing *S* increases the self inductance due to narrower and longer trace path, which decreases the even- and odd-mode phase velocities generally. But odd-mode phase velocity does not change monotonically because of the decrease of both inductive and capacitive couplings, which can be inferred from Expression (3.8).

Characteristic impedances of even and odd modes are shown in Figure 41 versus the strip width *W* and spacing *S* in mils. Again, increasing the strip width *W* leads to the increase of self capacitance, which reduces the even-mode impedance substantially. However, the coupling capacitance remains significant and constant, which makes the odd-mode impedance a little bit stable. Expanding the spacing *S* reduces both inductive and capacitive couplings, which results in the decrease of even-mode impedance and increase of odd-mode impedance. The change rate of the former is not as fast as the later, since coupling capacitance dose not impose substantial affects on even-mode impedance. All of above explanations can be found in Expressions (3.4)/(4.4a) and (3.9)/(4.4b).

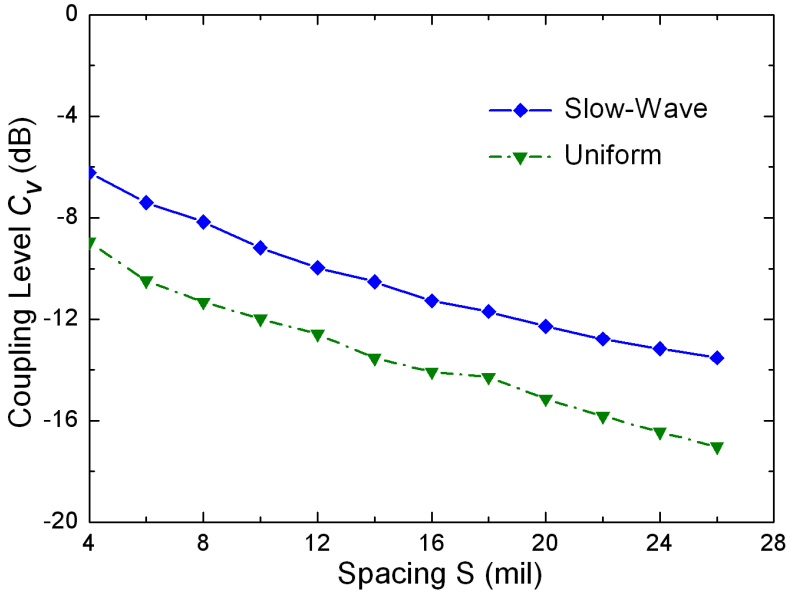

Figure 42: Comparison of the attainable coupling levels between proposed slow-wave coupled lines and conventional uniform coupled microstrip lines.

Attainable coupling level of proposed coupled lines versus spacing *S* is presented in Figure 42 as well as its comparison with conventional uniform coupled lines on the same substrate. The effective coupling level falls as the spacing *S* increases which gives rise to reduced capacitive and inductive couplings due to more electric and magnetic flux leakage. It will be shown later that it prefers to have coupling level above/around -8 dB for proper coupled-line circuit applications, which is necessary for coupled-line 180^{o} hybrid with equal power splitting at outputs.

Physically, two factors should be taken into account for choosing values for variables: 1) strip width and spacing cannot be too small due to practical PCB fabrication constraints, and 2) they should not be large for a small unit cell to enhance slow-wave effects. Here, our emphases are placed on the trade-offs among modal phase-velocity equalization, proper line impedances, and coupling enhancement. Finally, strip width *W* and spacing *S* are, respectively, assumed 18 and 8 mils for this

structure. As a result, equal phase velocities and slow-wave effects of even and odd modes can be realized in normalized phase velocities. The proposed coupled-line structure should work properly for standard 50ohm systems. It is capable of 3-4dB coupling enhancement over conventional uniform coupled microstrip lines on the same substrate.

C. S-Parameter Conversion

Differential structures are widely employed in RF, microwave, and high-speed circuits for its intrinsic feature of suppressing the external noises. It is well known that coupled lines involve two interacted lines with four ports providing the backbone of many differential circuits in microwave community. Combined common- and differential-mode (***m****ixed-****m****ode*) *S* parameters $[\boldsymbol{S}]_{mm}$ are well adapted to characterize those differential structures. More importantly to us, it can also be used to investigate the coupled-line dispersion characteristics, which will be illustrated later. By the way, it might be possible to utilize common mode to study electromagnetic emission/radiation phenomenon of coupled lines.

To convert from the standard single-ended four-port S parameters $[\boldsymbol{S}]_{std}$ to the mixed-mode S parameters $[\boldsymbol{S}]_{mm}$, a simple matrix transformation [72-73] is performed in Equation (5.1).

$$
\begin{aligned}
S_{mm} &= \begin{bmatrix} [S_{dd}]_{2\times 2} & [S_{dc}]_{2\times 2} \\ [S_{cd}]_{2\times 2} & [S_{cc}]_{2\times 2} \end{bmatrix} = \begin{bmatrix} \begin{bmatrix} S_{d1d1} & S_{d1d2} \\ S_{d2d1} & S_{d2d2} \end{bmatrix} & \begin{bmatrix} S_{d1c1} & S_{d1c2} \\ S_{d2c1} & S_{d2c2} \end{bmatrix} \\ \begin{bmatrix} S_{c1d1} & S_{c1d2} \\ S_{c2d1} & S_{c2d2} \end{bmatrix} & \begin{bmatrix} S_{c1c1} & S_{c1c2} \\ S_{c2c1} & S_{c2c2} \end{bmatrix} \end{bmatrix} \\
&= \frac{1}{2} \cdot \begin{bmatrix} \begin{bmatrix} S_{11}-S_{13}-S_{31}+S_{33} & S_{12}-S_{14}-S_{32}-S_{34} \\ S_{21}-S_{23}-S_{41}+S_{43} & S_{22}-S_{24}-S_{42}+S_{44} \end{bmatrix} & \begin{bmatrix} S_{11}+S_{13}-S_{31}-S_{33} & S_{12}+S_{14}-S_{32}-S_{34} \\ S_{21}+S_{23}-S_{41}-S_{43} & S_{22}+S_{24}-S_{42}-S_{44} \end{bmatrix} \\ \begin{bmatrix} S_{11}-S_{13}+S_{31}-S_{33} & S_{12}-S_{14}+S_{32}-S_{34} \\ S_{21}-S_{23}+S_{41}-S_{43} & S_{22}-S_{24}+S_{42}-S_{44} \end{bmatrix} & \begin{bmatrix} S_{11}+S_{13}+S_{31}+S_{33} & S_{12}+S_{14}+S_{32}+S_{34} \\ S_{21}+S_{23}+S_{41}+S_{43} & S_{22}+S_{24}+S_{42}+S_{44} \end{bmatrix} \end{bmatrix}
\end{aligned}
\tag{5.1}
$$

where: 1) subscripts '*c*' and '*d*' denote the common and differential modes, respectively; 2) $\boldsymbol{S}_{cc}/\boldsymbol{S}_{dd}$ are common/differential-mode two-port S parameters, and 3) $\boldsymbol{S}_{dc}/\boldsymbol{S}_{cd}$ are mode conversion two-port S parameters when differential/common-mode measured under common/differential-mode excitation. Note that the port ordering is arranged as shown in Figure 16.

D. Discussions on Symmetry

In practice, there always exist a superposition of common and differential signals on general coupled lines due to imperfect common/differential-mode excitations (illustrated in Figure 21) or the inevitable perturbations on the symmetry nature, even for symmetric coupled lines. In this subsection, we would like to evaluate the symmetry feature of the proposed coupled-line structure itself.

Simulations are run by HFSS to obtain single-ended four port S parameters of a coupled-line section with three unit cells. Feeding line extensions are used to suppress high-order modes at discontinuities around coupled-line terminals which could also disturb the symmetry a little bit. Reference planes are imposed to remove effects from the feeding line extensions. Although one may encounter difficulties in simulation environment, the EM modeling setup is not depicted here for limited space. As for perfectly symmetric coupled lines, mode-conversion S parameters should vanish in principle.

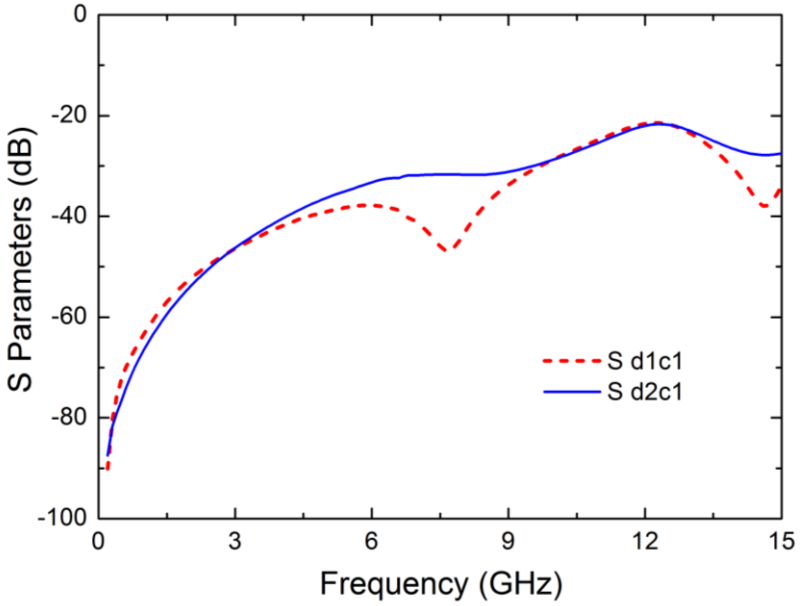

(a)

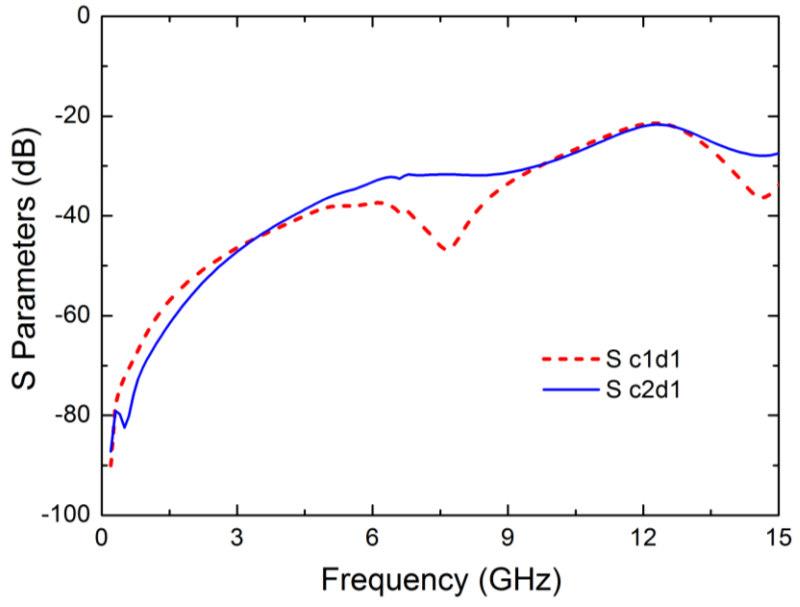

(b)

Figure 43: Mixed-mode *S* parameter of novel slow-wave coupled lines: (a) common to differential-mode conversion, and (b) differential to common-mode conversion.

The standard single-ended 4-port ***S*** matrix can be transformed to mixed-mode *S* parameters by Equation (5.1). Shown in Figure 43 are the mode-conversion *S* parameters between common and differential modes. They are about the same. Both S_{d1c1} (or S_{c1d1}) and S_{d2c1} (or S_{c2d1}) are below -20dB over a broad frequency range up to 15 GHz, which reveals that little reflections or transmissions occurs for both common-to-differential and differential-to-common conversions. It means that mode conversions are suppressed enough to be ignored, especially in the frequency range of interest (0 ~ 4 GHz) where *S* parameters are far below -40dB. Therefore, symmetry is well guaranteed both physically and electrically for the proposed coupled-line structure. The general common and differential modes could be reduced to well-known even and odd modes for analysis.

E. Circuit-Parameter Extraction

So far, it already demonstrated the validity to use symmetric equivalent circuit model for analysis. The component values in the equivalent circuit model can be extracted by Agilent ADS through curve fitting based on HFSS full-wave electromagnetic simulations of the novel coupled lines comprising three unit cells. The *S* parameter comparison between full-wave EM simulation and equivalent circuit model is presented in Figure 44. Good agreements are found to prove the extraction procedure, especially below cut-off frequencies.

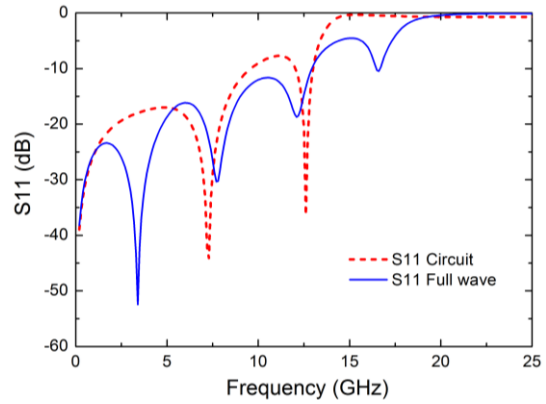

(a) Magnitude of S11

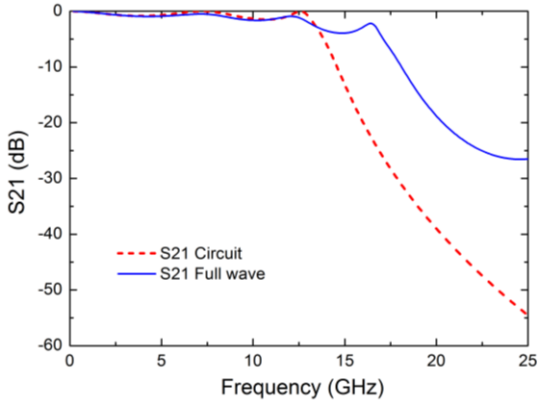

(b) Magnitude of S21

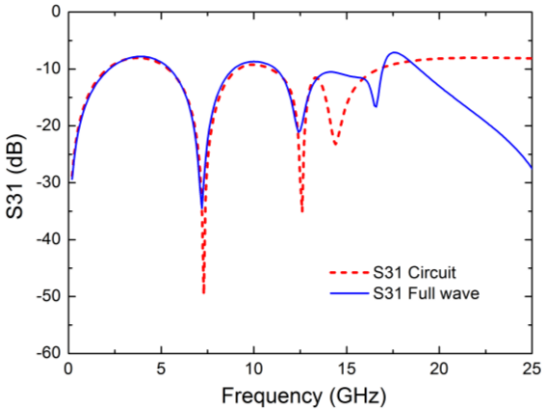

(c) Magnitude of S31

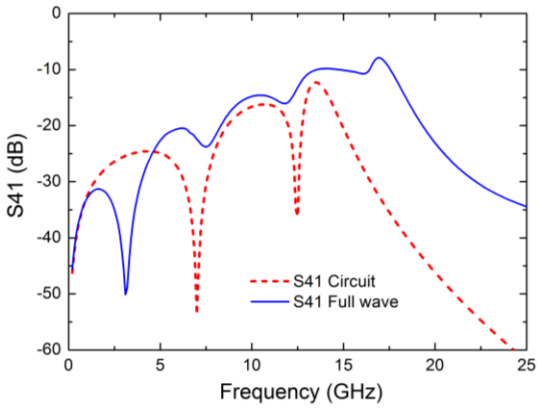

(d) Magnitude of S41

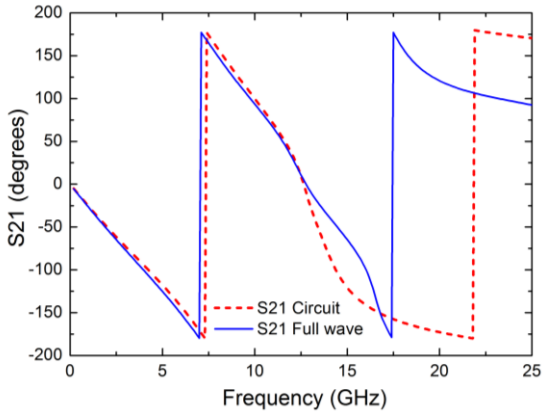

(e) Phase of S21

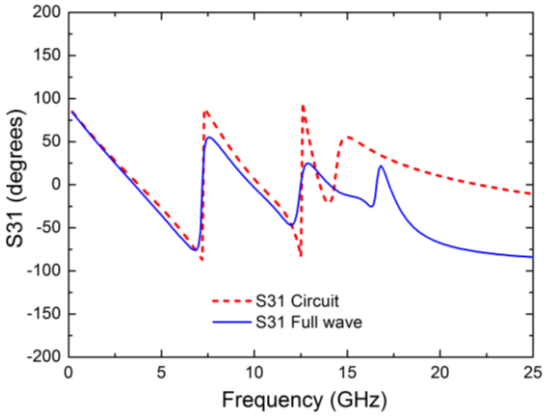

(f) Phase of S31

Figure 44: S-parameter comparison between full-wave EM simulation (HFSS) and extracted equivalent circuit model (ADS) of slow-wave coupled lines with three unit cells.

The extracted values of circuit parameters of slow-wave couple-line *unit cell* are reported in Table V. It is found that the condition of modal phase-velocity equalization (MPE) is satisfied very well, as described in Equation (3.13) or (4.3). This scenario will be confirmed soon in dispersion characteristics of the proposed coupled-line structure in next section.

TABLE V: EQUIVALENT CIRCUIT MODEL PARAMETERS OF SLOW-WAVE COUPLED-LINE UNIT CELL*.

Parameter	L (nH)	C (fF)	L_m (nH)	C_m (fF)	k_L	k_C
Value	1.05	320	0.42	220	0.4	0.6875

* MPE condition is satisfied: $(L+L_m)\,C = (L-L_m)\,(C+2C_m)$, or $k_L = k_C/(1+k_C)$

5.2.3 Dispersion Characteristics

In general, dispersion refers to transmission lines with phase velocities dependent on frequency in microwave society. As a signal with more than one frequency component in its phase propagates down the dispersive transmission line, the original phase relationship cannot be maintained for the 'faster' wave would lead to 'slower' wave in phase, resulting in signal distortion. In this section, dispersion characteristics are going to be investigated for the novel slow-wave coupling-enhanced coupled lines.

Dispersion diagrams, attenuation and phase constants, as well as characteristic impedances of the proposed coupled-line structure are presented in Figures 45, 46, and 48, respectively, under even- and odd-mode excitations. The curves corresponding to full-wave simulations using HFSS are extracted from two-port *S* parameters of coupled lines with three unit cells to take into account both intra- and inter-cell couplings. A comparison is provided with the informative and insightful ideal circuit model

of Figure 16 (a). For simplicity, the slight couplings between adjacent cells could be approximately attributed to those within unit cells. In addition, the curves for equivalent circuit model are calculated from Equations (3.2-3.11, and 4.2) using the extracted unit-cell circuit parameters, instead of obtaining from its 2-port *S* parameters using Equation (4.6), to further verify the proposed theory of artificial coupled transmission lines in Chapter 3. As illustrated in Figures 45-48, dispersion characteristics of the proposed slow-wave coupled-line structure are rather interesting.

Even- and odd-mode dispersion diagrams of the slow-wave coupled-line *unit cell* are shown in Figure 45 (a) and (b), respectively, over a broad frequency range up to 25GHz with fast-wave and slow-wave regions on the left- and right-hand sides of air line. They are quite similar, which can be inferred from Equations (3.3) and (3.8) under the MPE condition (3.13) $k_L = k_C/(1+k_C)$. It is clear that this structure supports slow waves for both even and odd modes below cut-off frequencies. For both even and odd modes, the coupled-line theory based on equivalent circuit model predicts the cut-off frequencies of about 15 GHz, while HFSS full-wave simulations give rise to around 17 GHz. Good agreements are maintained between theory and full-wave simulations for the fundamental mode of operation until 13 GHz. Beyond that point, noticeable discrepancies are observed since significant distributed parasitics are taken into account in the full-wave electromagnetic simulations at high frequencies especially approaching cut-off frequencies, while they are not considered in theory.

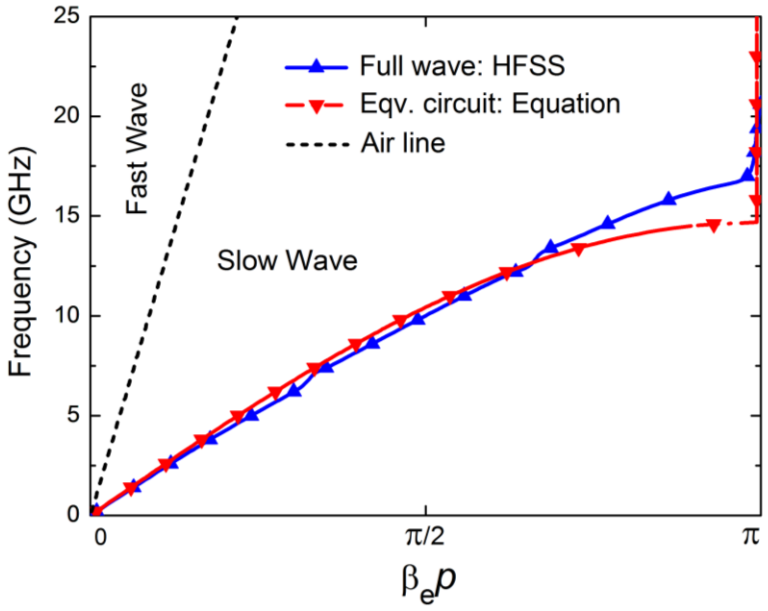

(a) Even mode

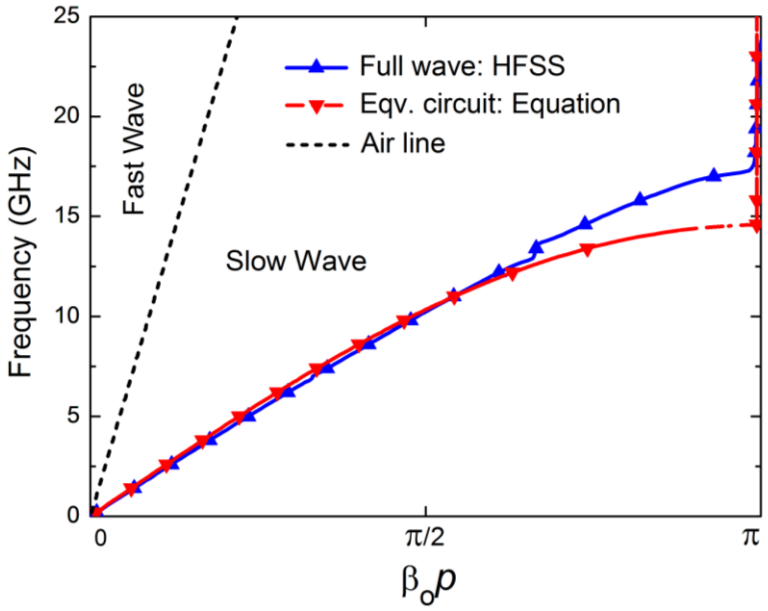

(b) Odd mode

Figure 45: Even- and odd-mode dispersion diagrams of the slow-wave coupled-line unit cell.

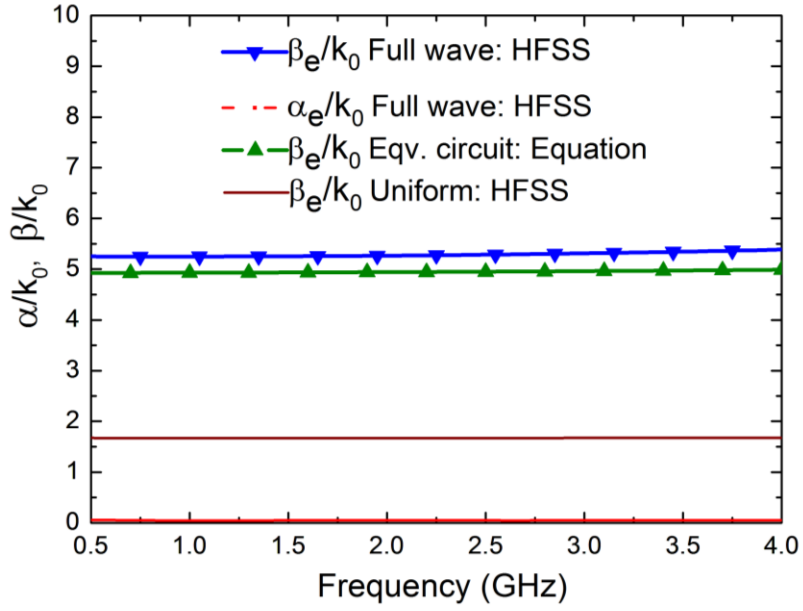

(a) Even mode

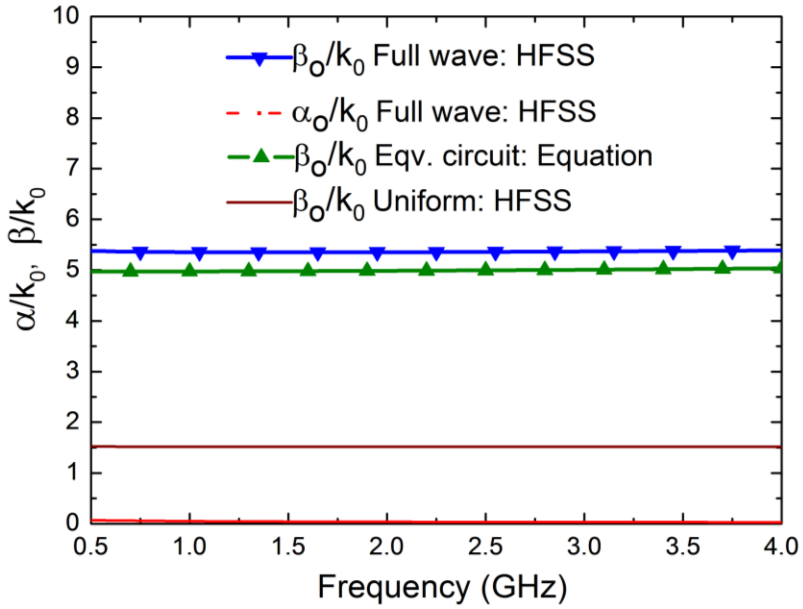

(b) Odd mode

Figure 46: Normalized attenuation and phase constants of even and odd modes in the frequency range of interest.

Figure 45 exhibits a linear dispersion curve over a very broad frequency range starting from DC up to around 13 GHz under both even- and odd-mode excitations. It is much preferred for least-dispersive transmission lines. More details are going to be inspected on propagation constants and characteristic impedances in the frequency range of interest from 0.5 to 4 GHz, because a few miniaturization examples of coupled-line circuit applications at 2.4GHz will be developed in subsequent sections and chapters based on the novel slow-wave coupling-enhanced coupled-line structure.

Normalized phase and attenuation constants of the slow-wave coupled-line structure are shown in Figure 46 (a) and (b), respectively, under even- and odd-mode excitations in the frequency range of interest. The comparisons of phase constants are good between full-wave simulation (blue solid line with downward triangles) and theory based on equivalent circuit model (green dash dot line with upward triangles) for both even and odd modes. It is observed that phase constants are very stable over the whole frequency region, indicating little dispersion occurs. Moreover, the curves (red dash line) for normalized attenuation constants stay at the bottom, which means that losses could be negligible. In contrast, modal phase constants (wine solid line) of the conventional uniform coupled microstrip lines on the same substrate are also provided based on HFSS full-wave simulations.

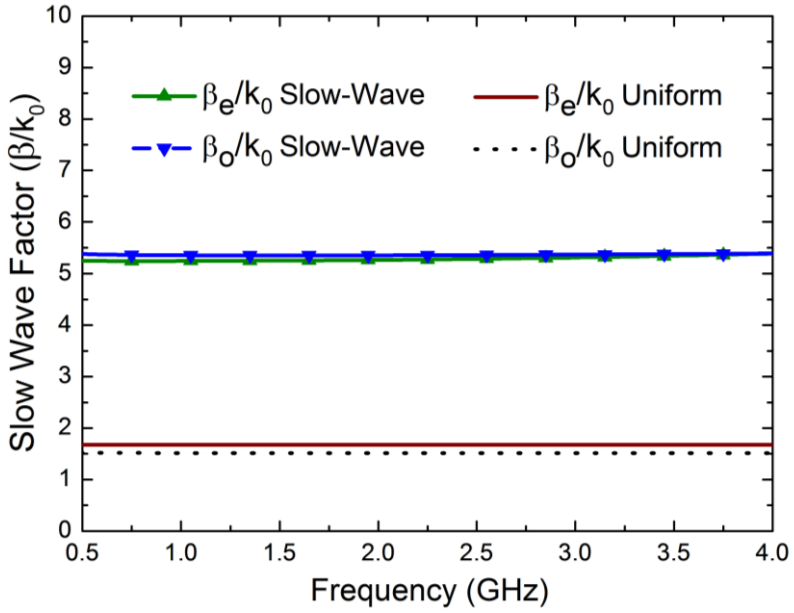

Figure 47: Even- and odd-mode slow-wave factors based on full-wave simulations in the frequency range of interest.

From full-wave simulations, the slow-wave coupled lines exhibit slow-wave factors (normalized phase constant) of 5.281 and 5.358 for even and odd modes, respectively, at design frequency of 2.4 GHz. They are much greater than those (1.672 and 1.515) of the uniform coupled microstrip lines. As defined by $|\beta_e - \beta_o|/|\beta_e + \beta_o|$, the normalized percentage difference of modal phase constants of the slow-wave structure presents about 0.72% over 4.93% for the uniform coupled-line counterpart. Therefore, the proposed slow-wave coupled lines achieve the equalization of even- and odd-mode phase velocities very well. This is clearly illustrated in Figure 47 for a straightforward comparison between even- and odd-mode cases.

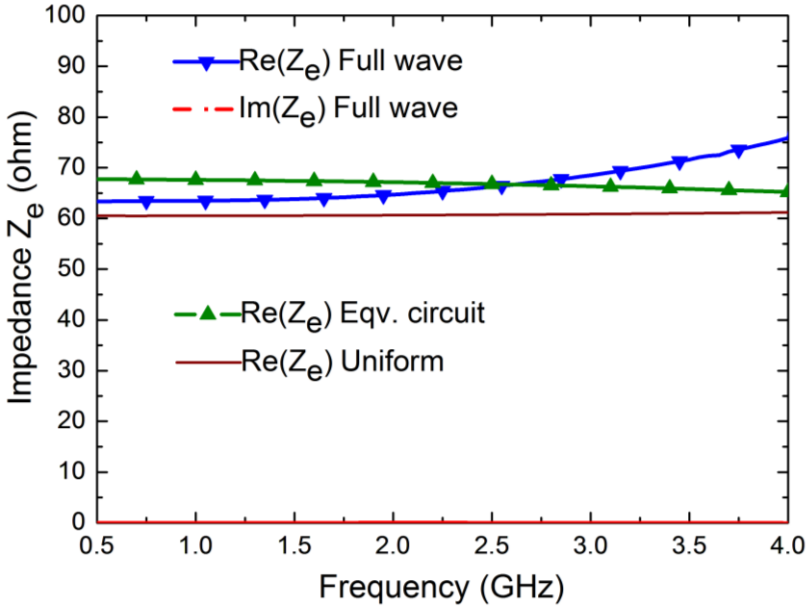

(a) Even mode

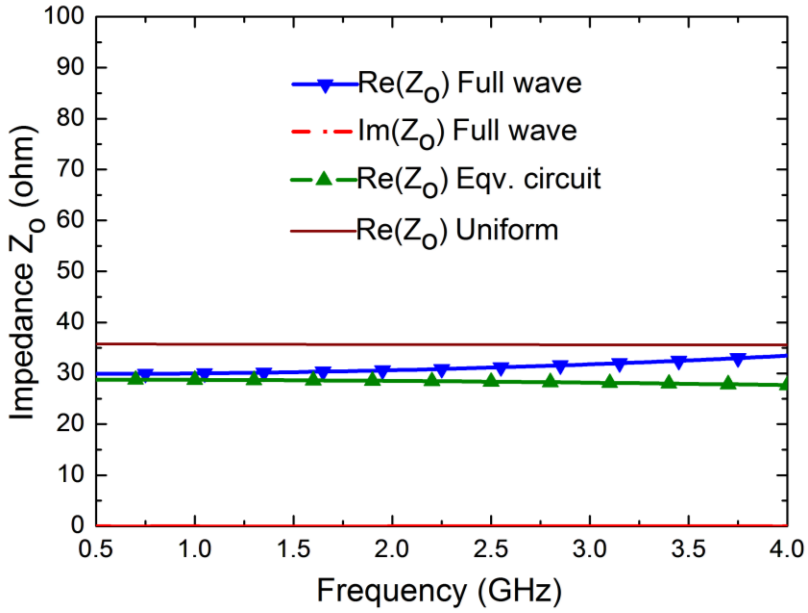

(b) Odd mode

Figure 48: Even- and odd-mode impedances in the frequency range of interest.

In practice, proper line impedances are necessary for transmission-line circuits to maintain certain functionality in response to external impedance terminations. Figure 48 shows the characteristic impedances of slow-wave coupled lines under even- and odd-mode excitations, respectively. Good agreements are observed between full-wave simulations (blue solid line with downward triangles) and theoretical equations using extracted circuit parameters (green dash dot line with upward triangles). The real parts of even- and odd-mode impedances are about 66 and 31 ohms at design frequency (2.4GHz) from full-wave simulation results. Their imaginary parts (red dash line) could be negligible. In contrast, simulated modal impedances (wine solid line) are also shown in figures for the uniform coupled lines consisting of two 50ohm microstrip lines with 6mil spacing. Even-mode impedance of the proposed coupled lines is larger than that of its uniform counterpart, while the opposite is observed for odd-mode impedance. It conveys the enhancement of coupling level (defined by Equation (4.5a)) over uniform microstrip coupled lines, which was illustrated in previous Figure 42.

It is worthwhile to mention empirically that the accuracy of extracting impedance from two-port S parameters using Equation (4.6b) falls gradually as transmission line's electrical length increases and exceeds quarter wavelength, especially around half wavelength where jumps may occur.

5.2.4 Potential Circuit Applications

The previous subsections present a new slow-wave structure of coupled lines with least dispersion and loss over a broad frequency range of interest. 3D-folded coupled inductors are proposed for a novel magnetic coupling mechanism. It allows synthesizing artificial periodic coupled transmission lines: 1) the equalization of even- and odd-mode phase velocities, 2) large slow-wave factors, 3) proper line impedances; and 4) coupling enhancement.

Benefiting from above features which provide a glimpse into potential of circuit applications, this novel coupled-line structure seems very intriguing. One can envision that many high-performance miniaturized coupled-line circuits could be evolved from such compact structure. For instances, a

quarter-wave section can be used to construct a miniaturized directional coupler with both enhanced coupling and improved directivity. Coupled-line band-pass filters could be enabled with lower orders. Marchand balun can be developed by directly cascading two quarter-wave coupled-line sections to have good amplitude and phase balances as well as impedance transformation. Novel coupled-line 180^{o} hybrid coupler could be innovated by comprising two quarter-wave coupled-line sections with a half-wave isolated-line section in between.

All of aforementioned compact coupled-line circuits offer DC isolation since their functionalities originate from the mechanism of electromagnetic couplings which would fail to take effect at DC. It is well-known that DC isolations are preferred for circuits in RF front ends where DC signal components always exist due to DC biasing, even-order nonlinearities, self-mixing, etc, in wireless communication systems.

In addition, it appeals to us that the proposed theory and design methodology can be applied to circuit implementations on printed circuit board (PCB), but also on low temperature co-fired ceramic (LTCC), silicon IC microelectronics, or other advanced processes. In this dissertation, all circuit examples are developed based on the low-cost standard PCBs without stringent requirements only for purpose of demonstration. More advanced fabrication processes with fine line/spacing resolutions could be employed for circuits with better performances or at very high frequency bands.

5.3 Miniaturized Directional Coupler With Improved Coupling and Directivity

As mentioned above, a quarter-wavelength coupled-line section can be utilized to construct a directional coupler. In general, conventional microstrip parallel edge coupled lines can only provide a weak coupling level of about 11~14 dB based on standard low-cost PCB implementation. It can be improved by placing two coupled lines closer with finer spacing at increasing fabrication cost. However, it also gives rise to more discrepancy between modal phase velocities, thereby deteriorating its directivity. In addition, distributed microstrip directional couplers usually occupy large board area.

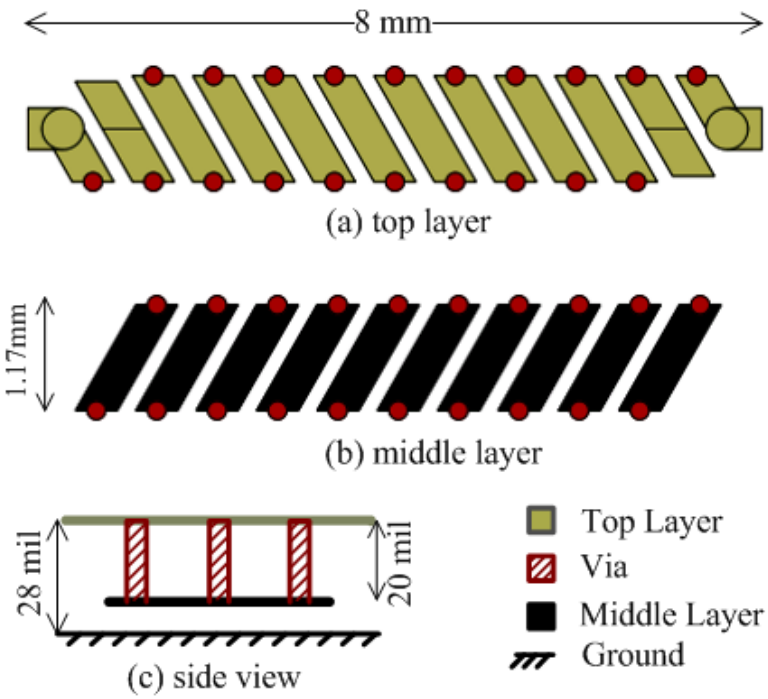

Figure 49: Layout of the miniaturized directional coupler based on a three-layer setup. (a) top layer, (b) middle layer, (c) side view.

Slow-wave effects, equal modal phase velocities, and enhanced coupling of our proposed artificial coupled lines can, respectively, contribute to the compactness, isolation, and coupling level of its evolved directional coupler. Proper even- and odd-mode impedances would make the coupler circuit suitable for a 50Ω system. To validate and reinforce the above statements, a miniaturized directional coupler is designed by using a quarter-wave section of the novel coupled-line structure on Rogers substrate. Figure 49 depicts the top- and middle-layer layouts of the directional coupler along with its side view. Bottom layer is a regular ground plane and its layout is not shown here. The quarter-wave coupling section comprises five unit cells with small extra traces added at ports for terminal connections to facilitate measurement in standard 50Ω system. Physical dimensions are labeled on the figure.

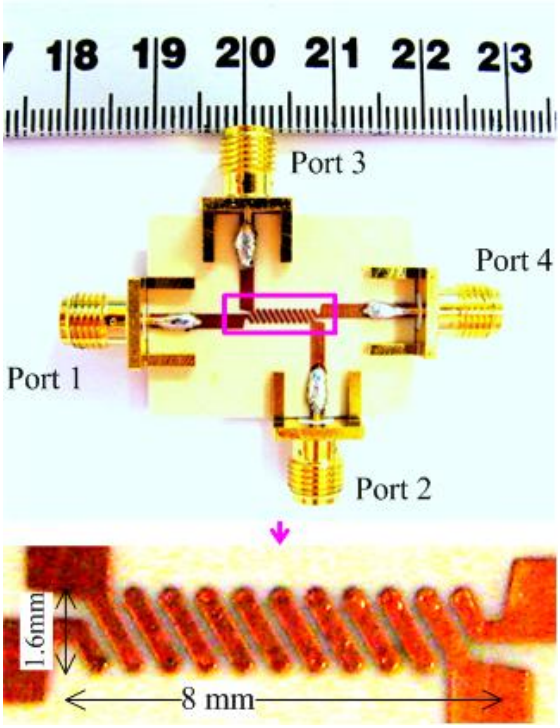

Figure 50: Photograph of the fabricated miniaturized directional coupler.

As a proof-of-concept demonstration, a PCB prototype is fabricated on the Rogers microwave substrate composed of the uppper RO4003C core laminate (ε_r=3.38, tanδ=0.0021) and lower RO4450B prepreg (ε_r=3.54, tanδ=0.004) with 1oz copper cladding on each metal layer. Its photograph is shown in Figure 50. The finished directional coupler occupies a compact planar area of 8mm by 1.6mm (including via sizes), or equivalently, $0.064\lambda_0$ by $0.0128\lambda_0$ at 2.4 GHz where λ_0 is the free-space wavelength. Feeding lines are used to extend coupler ports to board edges for testing using 50Ω SMA connectors. The four-port circuit is measured by Agilent Technologies N5230C PNA-L network analyzer, while full-wave simulations are run by HFSS. Proper calibration and de-embedding are performed to remove effects from cables, connectors, and feeding lines. Its performances are presented in Figures 51 and 52.

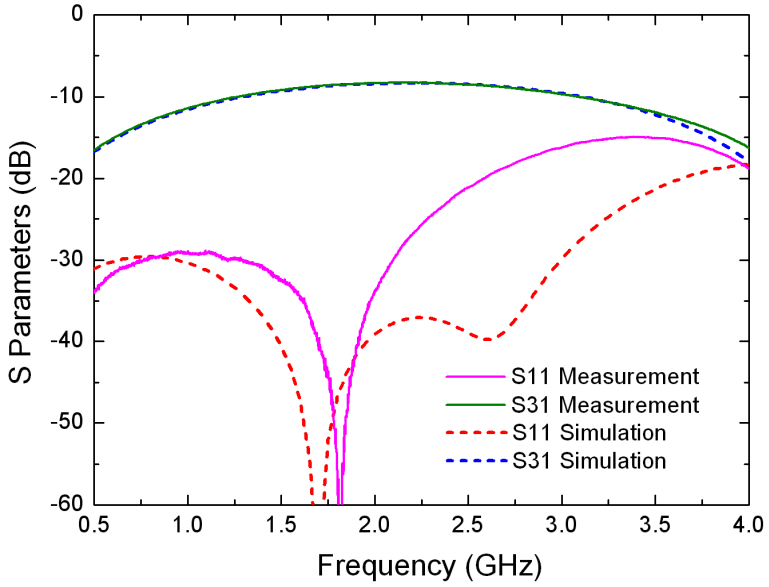

(a)

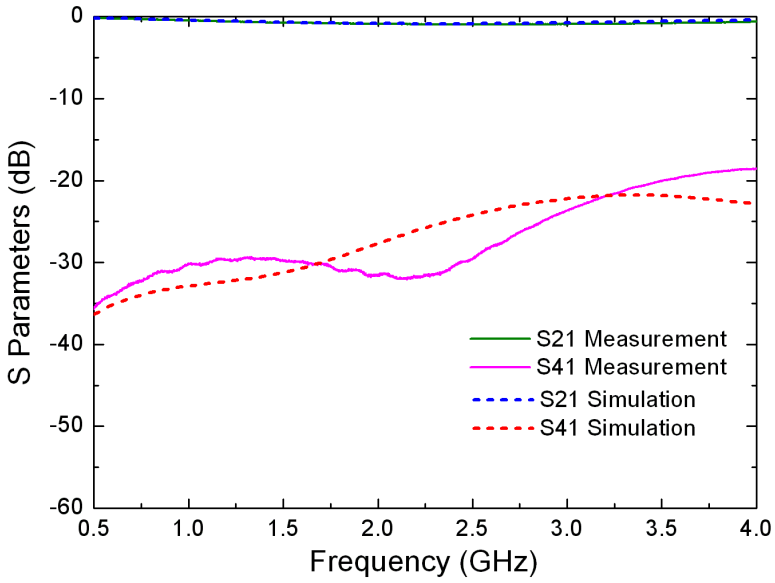

(b)

Figure 51: Measured (solid lines) and simulated (dashed lines) *S*-parameters of the designed directional coupler. (a) reflection $|S_{11}|$ and coupling $|S_{31}|$; (b) through $|S_{21}|$ and isolation $|S_{41}|$.

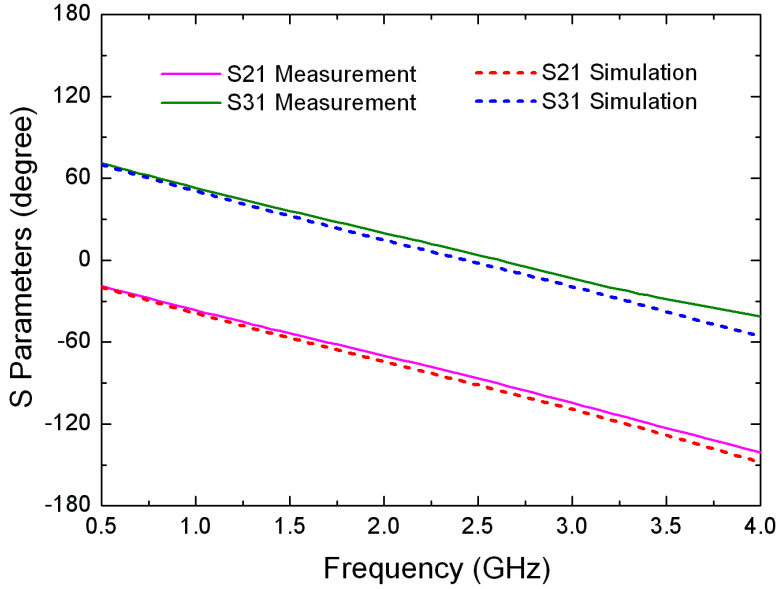

(a) Phases of S_{21} and S_{31}

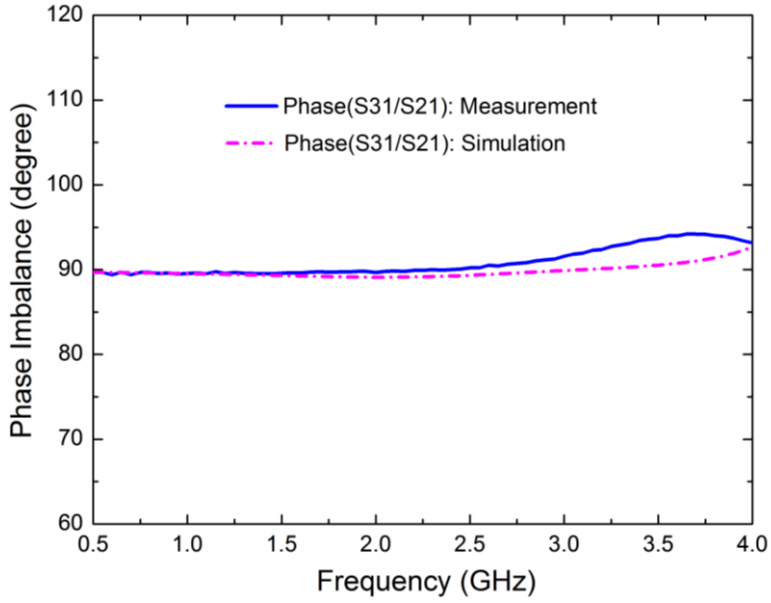

(b) Quadrature phase imbalance

Figure 52: Phases and their imbalance at through and coupled ports of the designed directional coupler. (a) Phases of S_{21} and S_{31}; (b) Quadrature phase imbalance.

Both measured and simulated magnitudes of the four-port scattering parameters are shown in Figure 51 for the miniaturized directional coupler. From measurement results, the return loss and isolation are, respectively, better than 15dB and 20dB over the entire frequency range from 0.5 to 4 GHz under investigation. It confirms the theoretical prediction of wideband characteristics for coupled-line coupler circuits in terms of impedance matching at terminations and isolation between ports. The highest coupling level of -8.3dB occurs at the operation frequency around 2.2 GHz where the corresponding measured directivity is about 23.5 dB. The return loss dip shifts from the operating frequency a little bit, perhaps mainly because the reference impedance of designed coupled lines is slightly different from standard 50Ω termination impedances.

The phase characteristics of the coupler are illustrated in Figure 5.52 for through and coupled signals. Measured results show that the phase difference is 89.9^{o} at center frequency and quadrature phase balance is achieved very well within $90^{o} \pm 5^{o}$ over entire frequency region under investigation. It further demonstrates the wideband phase feature of the coupled-line directional coupler.

5.4 Miniaturized Coupled-Line Band-Pass Filters

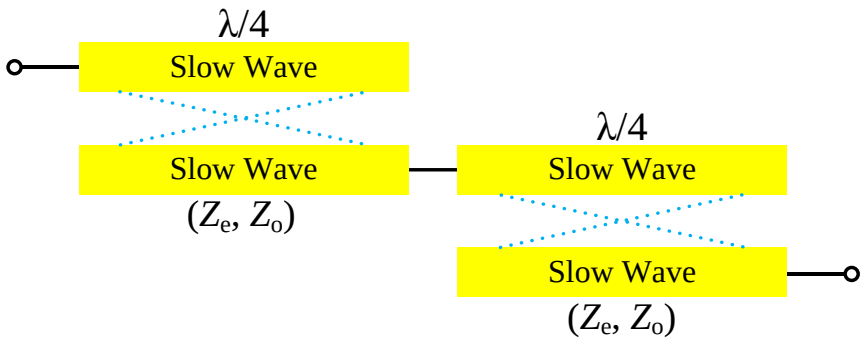

(a) Regular configuration

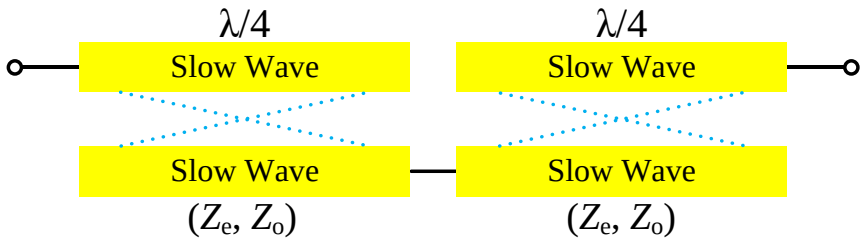

(b) Folded configuration

Figure 53: Schematic diagrams of compact bandpass filters using slow-wave coupled lines. (a) Regular configuration. (b) Folded configuration to save more area.

In general, coupled lines are a four-port passive network. A two-port circuit can be constructed by terminating two of four ports in form of either open or short circuits. Different combinations would lead to various frequency responses of the two-port circuits [62]. Among them, bandpass filters are favored in most practical applications. One of main reasons is that open-circuit terminations are easier to be implemented than short circuits on printed circuit boards. Narrowband bandpass filters can be developed by cascading $N + 1$ coupled line sections, where N is considered the order in the cases of Chebyshev and Butterworth filters. Coupled line sections are about a quarter-wavelength long at center frequency of the bandpass response. Detailed theoretical analyses are described in the reference [62].

5.4.1 Regular Configuration

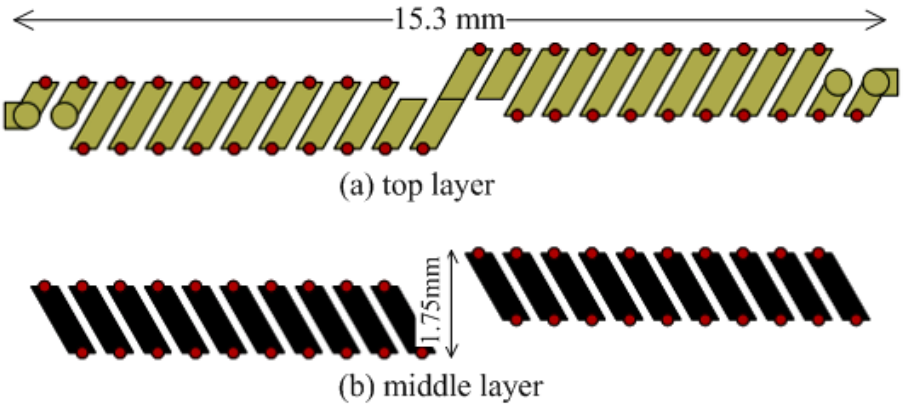

Figure 54: Layout of the miniaturized coupled-line bandpass filter in *regular* configuration. (a) Top layer. (b) Middle layer. (Bottom ground plane is not shown)

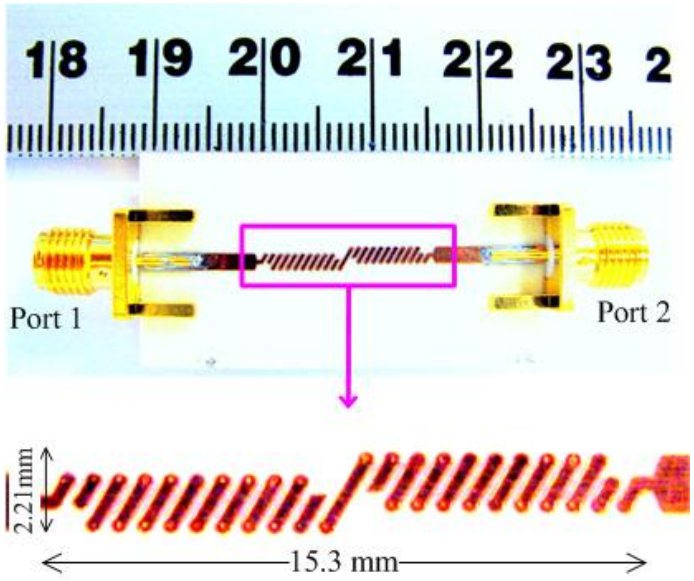

Figure 55: Prototype photograph of the *regular* miniaturized coupled-line bandpass filter.

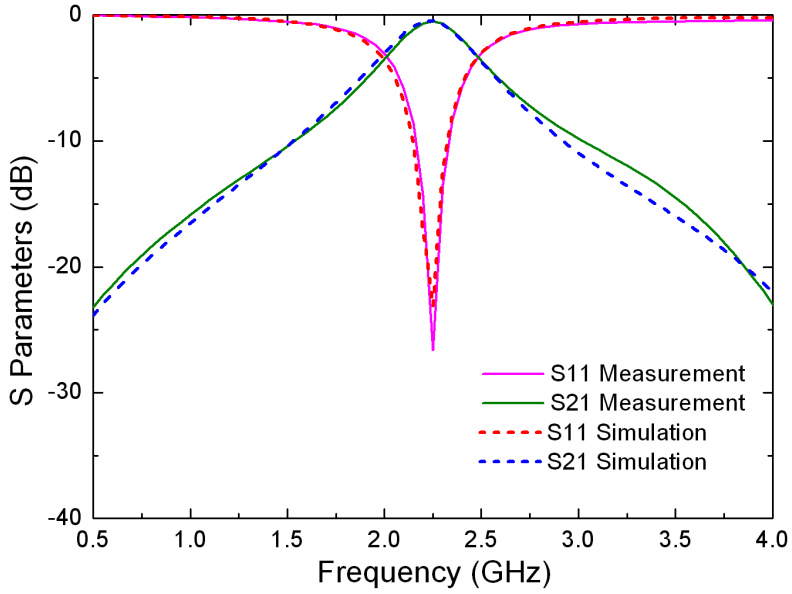

(a)

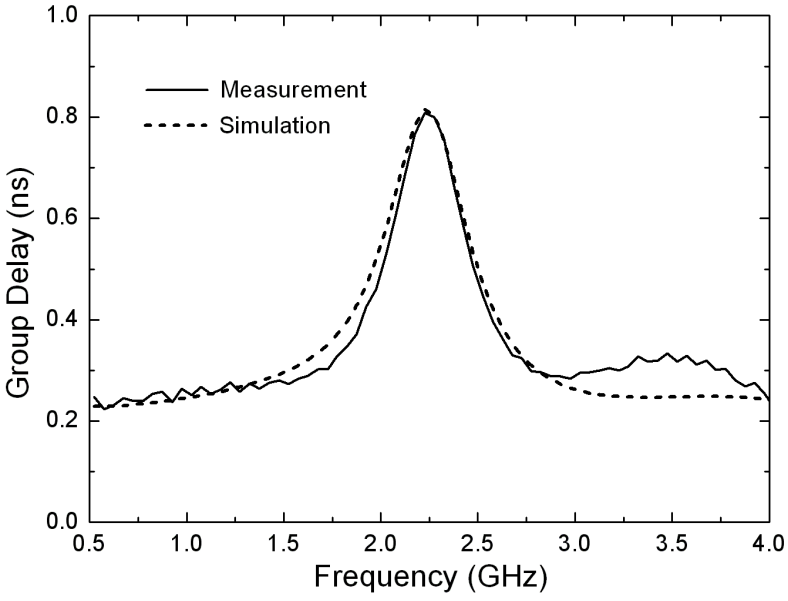

(b)

Figure 56: Measured (solid lines) and simulated (dashed lines) results of the miniaturized bandpass filter in *regular* configuration. (a) Scattering parameters. (b) Group delay.

The novel slow-wave coupled-line structure with enhanced coupling proposed in Section 5.2 can be employed to develop many types of small filters. Two configurations of compact coupled-line bandpass filters with order of only one are schematically depicted in Figure 53. Both two-port filter circuits are composed of two identical quarter-wave sections of parallel coupled lines, while one is folded to further reduce rectangular planar board area, in contrast to another circuit in the regular configuration. Their operation principles are fundamentally the same, thereby being expected to gain same performances.

To demonstrate the proposed schemes of bandpass filters, two layout examples are designed and implemented on Rogers microwave substrate by using the novel slow-wave coupled lines in both regular and folded configurations. They are shown in Figures 54 and 57, respectively, with key dimensions labeled. Two quarter-wave sections each with five unit cells are cascaded together with two remaining ports open circuited. Detailed unit cell structure was depicted previously in Figure 39. Both filter prototypes are fabricated on the same three-layer printed circuit board as the miniaturized directional coupler in Section 5.3. Similar statements could be made to layouts and fabrication processes, and hence are omitted here for conciseness.

The photographs of both fabricated prototypes are presented in Figures 55 and 58. The finished coupled-line bandpass filter in a regular configuration occupies a compact planar area of 15.3mm by 2.21mm (including via sizes), or equivalently, $0.1148\lambda_0$ by $0.0166\lambda_0$ at the center frequency around 2.25 GHz, where λ_0 is the free-space wavelength. In contrast, the rectangular planar dimensions of the finished folded coupled-line filter are 15.9mm by 1.6mm, or equivalently $0.1193\lambda_0$ by $0.012\lambda_0$ at 2.25 GHz, with extra 25% area reduction. In addition, this folded filter has the same width as a 50Ω microstrip line on the same substrate. It looks like a 50Ω line with bandpass transmission characteristics. Again, the EM simulations are performed by full-wave solver HFSS, while filter

circuits are measured by Agilent Technologies N5230C PNA-L network analyzer along with proper calibration and de-embedding. Their performances are shown in Figures 56 and 59.

5.4.2 Folded Configuration

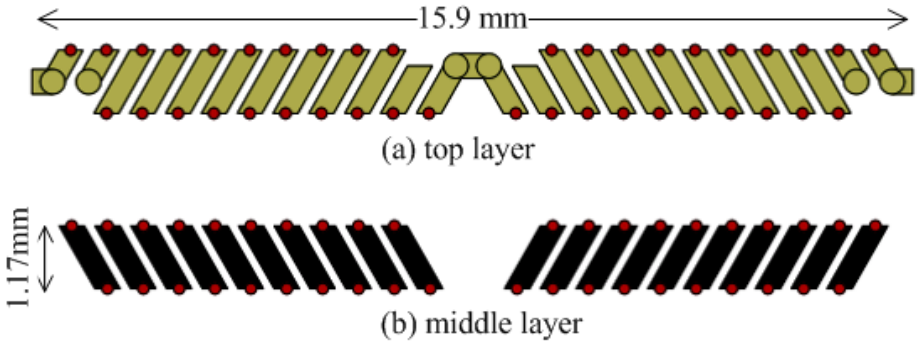

Figure 57: Layout of the miniaturized coupled-line bandpass filter in *folded* configuration. (a) Top layer. (b) Middle layer. (Bottom ground plane is not shown)

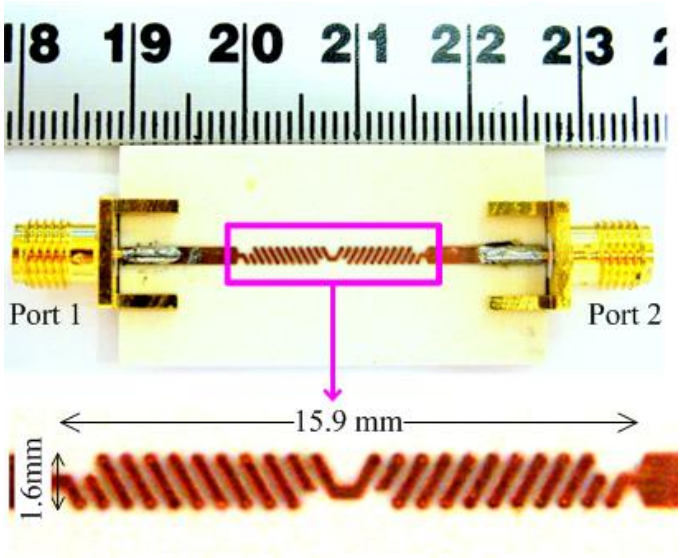

Figure 58: Prototype photograph of the *folded* miniaturized coupled-line bandpass filter. (extra 25% saving of rectangular planar area)

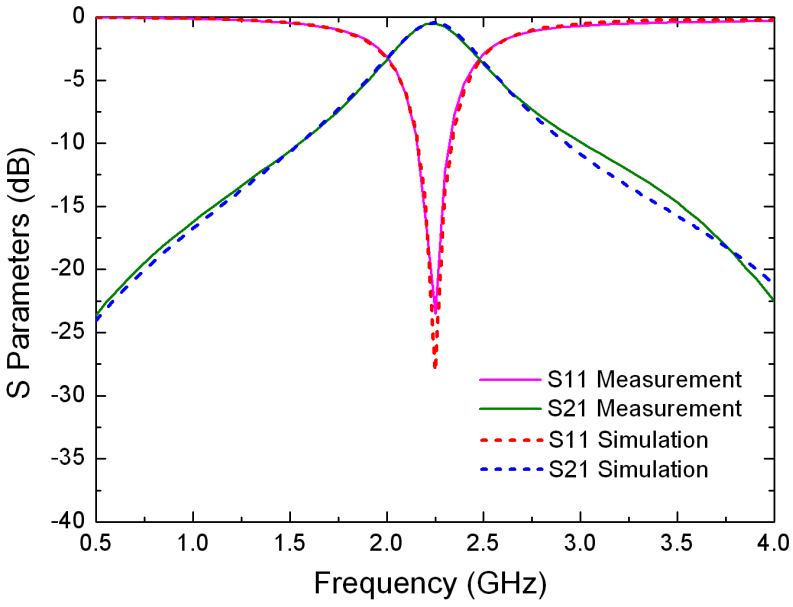

(a)

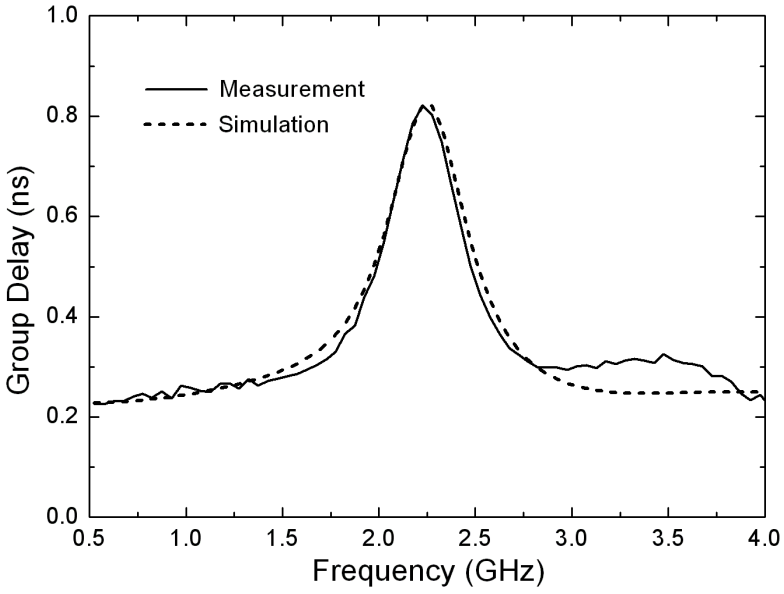

(b)

Figure 59: Measured (solid lines) and simulated (dashed lines) results of the developed bandpass filter in *folded* configuration. (a) Scattering parameters. (b) Group delay.

The measured (solid lines) and simulated (dashed lines) results of both regular and folded compact coupled-line bandpass filters are illustrated in Figures 56 and 59, respectively. As expected, it is found that both filters exhibit about the same performances. From measurement results, the center frequencies around 2.25 GHz are observed with a minimum insertion loss of about 0.57 dB and maximum return loss of about 25 dB. The 3dB fractional bandwidth of insertion loss is 23.1% from 1.99 to 2.51 GHz where the group delay variation is less than 0.4 ns.

In addition, as for both directional coupler and filters, the agreements between measured and simulated results are good enough to validate full-wave EM simulations. Slight differences might be attributed to discontinuities between soldered SMA connectors and feeding lines on the circuit board and other parasitics associated with connectors as well as fabrication tolerances, etc. It is worthwhile to mention that the operating center frequency of 2.25GHz deviates a little bit from the initial design frequency of 2.4GHz, owing to that the requested fabrication processes were misused in PCB house. Revisions had already been made in simulation setups accordingly. The overall experimental performances have verified the proposed concepts of such compact slow-wave coupled-line coupler and bandpass filters.

5.5 Concluding Remarks

In this Chapter, a new slow-wave structure of coupled lines is proposed by employing 3D-folded coupled inductors for a novel magnetic coupling mechanism. It exhibits linear dispersion relationship with respect to frequency over a very broad frequency range with high cut-off frequencies (around 17 GHz) under both even- and odd-mode excitations. Even- and odd-mode phase constants are stable and their phase velocities achieve equalization very well over a broad frequency region of interest where little dispersion and attenuation are observed. Proper modal impedances are synthesized to work for practical circuits with enhanced coupling to improve their performances. In contrast to conventional uniform coupled microstrip lines on the same substrate, this new structure is half

coupled-line width and slow-wave factors of about 5.3, both of which contribute to planar area saving of above 80% over its uniform counterpart.

The theory and design criteria based on the ideal circuit model of right-handed artificial coupled lines are validated by their excellent agreements with full-wave electromagnetic simulations. Novel miniaturized coupled-line circuits could be evolved from such intriguing slow-wave structure. A quarter-wave section can be used to construct a miniaturized directional coupler with improved coupling level and directivity. Two compact coupled-line bandpass filters are enabled with low order in regular and folded configurations. As proof-of-concept demonstrations, PCB prototypes are designed, fabricated, and tested. Experimental results help to substantiate full-wave EM simulations. Other high-performance miniaturized coupled line circuits will be discussed and developed in next chapters based on the presented novel slow-wave coupled lines herein.

6 MINIATURIZED IMPEDANCE-TRANSFORMING MARCHAND BALUN

6.1 Introduction

In modern wireless communication systems, differential operations are favored for their salient feature of suppressing environmental noises. It is well known that ***balun*** performs the signal transformation from ***bal***anced to ***un***balanced modes, or vice versa. Hence they are essential components in balanced/differential circuit topologies, such as double balanced mixers [74], frequency doublers/multipliers [75-76], push-pull power amplifiers [77-79], and antenna feeding network [80-83], as shown in Figure 60. In addition to single-ended to differential conversion, it would be beneficial if the balun is also capable of impedance transformations between non-50ohm transistor/diode impedance and standard 50ohm external terminations.

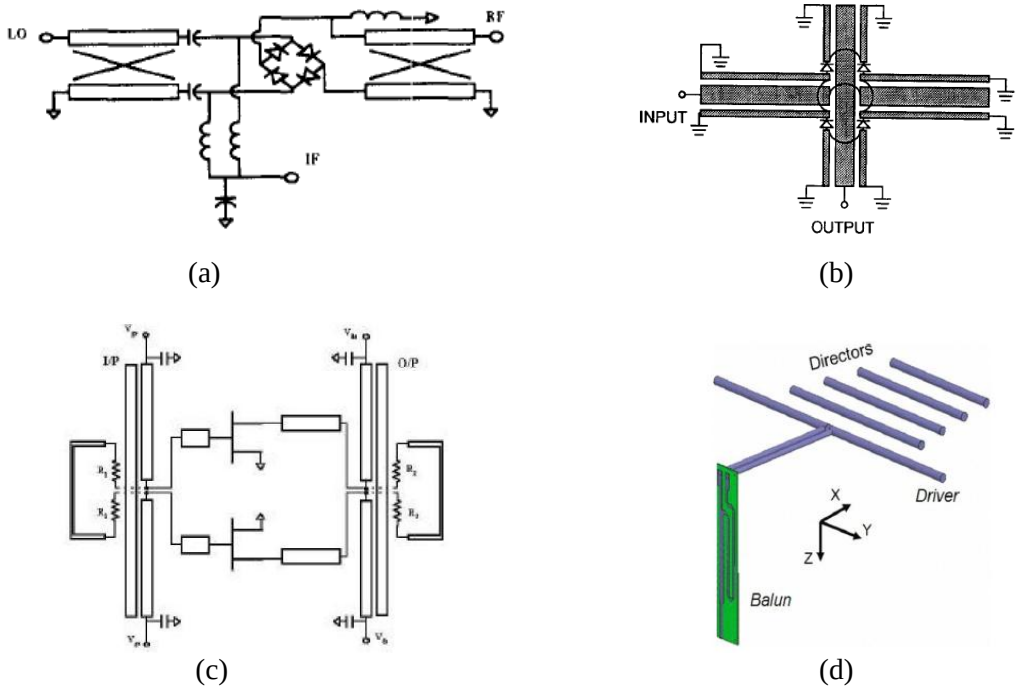

(a) (b)

(c) (d)

Figure 60: Balun applications: (a) Double balanced mixer; (Source: reference [74] Fig. 1.). (b) Diode frequency doubler; (Source: reference [75] Fig. 2.). (c) Push-pull power amplifier; (Source: reference [77] Fig. 3.). (d) Yagi-Uda antenna (Source: reference [82] Fig. 1.).

So far, a wealth of balun configurations have been reported for extensive RF/microwave applications. Among them, Marchand balun is perhaps one of the most popular ones since its concept was first introduced by Marchand in 1944 [35], because of its design simplicity, easy implementation, and wide-band performance. There have been considerable advances in planar Marchand balun and its variations [84-86]. Basically, it can be symmetrically constructed by cascading two identical quarter-wavelength sections of coupled transmission lines. Its performances, in terms of bandwidth, amplitude/phase imbalances, and impedance transformation ratio, depend on the coupling factor and directivity of each directional coupler. In addition, microstrip implementation is preferred for its easy integration with other components or modules on the same circuit board. However, conventional microstrip Marchand baluns suffer poor performances from the weak parallel-edge coupling level and unequal even/odd-mode phase velocities of coupled lines based on the present standard cost-effective PCB fabrication constraints.

Moreover, the main disadvantage associated with distributed Marchand baluns is their bulky sizes especially at low microwave frequencies, because their dimensions are determined by the operating frequency. Surface-mounted lumped elements were employed to miniaturize the distributed baluns on PCB [87-88], but this approach may not be appropriate for applications at very high frequencies where the intrinsic parasitics of lumped elements become significant to deteriorate their performances. Other efforts on miniaturization of Marchand baluns were reported in literature by using low temperature co-fired ceramic (LTCC) technology [89], coplanar waveguide (CPW) [90], multilayered stripline structure [91], or a combination of microstrip/CPW broadside coupling mechanism [92].

In this chapter, our goal is to develop a miniaturized impedance-transforming planar Marchand balun through microstrip implementations on a three-metal-layer setup using the common cost-effective printed circuit board (PCB) fabrication process without stringent requirements. The concept is illustrated in Figure 61. It is evolved from two quarter-wavelength sections of the proposed novel

slow-wave coupled lines with interleaved periodic structure consisting two layers of parallel metal strips interconnected through high density of vias. The artificial coupled transmission lines feature equal even- and odd-mode phase velocities, significant slow-wave factors, and proper line impedances as well as coupling enhancement. They benefit the miniaturized Marchand balun with excellent electrical properties.

As a proof-of-concept demonstration, a PCB prototype is designed and fabricated on the Rogers RO4003C microwave substrate. It shows above 80% planar area reduction, in contrast to the conventional microstrip counterpart on the same board. Measurement data show very good agreement with full-wave simulations. It exhibits broad return-loss bandwidth, good in-band amplitude and phase balances, and an impedance transformation ratio of 1:3.

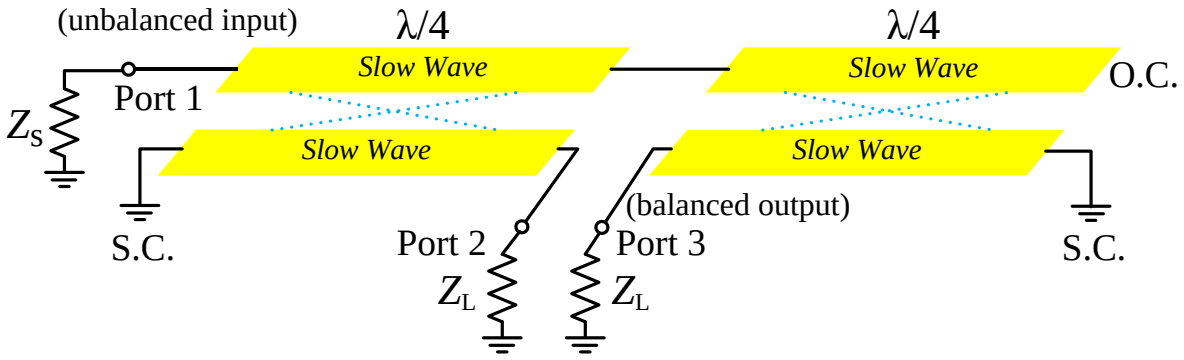

Figure 61: Conceptual miniaturized Marchand balun using artificial slow-wave coupled lines.

6.2 Analysis and Synthesis

6.2.1 Analysis of Marchand Balun

It is well-known that an ideal lossless passive balun would have the three-port *S* parameters in single-ended configuration

$$S_{11} = 0 \tag{6.1a}$$

$$|S_{21}| = |S_{31}| = \frac{1}{\sqrt{2}} \tag{6.1b}$$

$$S_{21} = -S_{31} \tag{6.1c}$$

for optimum balun performances: perfect matching at the unbalanced input and minimum insertion losses (-3dB) to two balanced outputs with equal amplitudes and opposite phases.

Marchand baluns gain their popularity and hence attract many research efforts. Their analysis and characteristics have been well investigated [76, 85-87]. A conventional Marchand balun consists of two identical quarter-wavelength sections of coupled lines, as shown in Figure 61. In general, the source and load impedances (Z_s and Z_L) are different. Therefore, in addition to balanced outputs, it requires the balun to perform an extra impedance transformation between source and loads for practical applications.

An effective approach was proposed in [86] to reduce the design of Marchand balun to ideal directional coupler with certain voltage coupling factor C_V. It helps to reveal the mystery of balun operation principles. Hence it is briefly described here to offer keen insights into the design of impedance-transforming Marchand balun. The 3-port *S* parameters normalized to each termination impedances (Z_s and Z_L) are given below

$$[\mathbf{S}]_{3\times3}=\begin{bmatrix} \dfrac{1-C_V^2\left(2Z_L/Z_s+1\right)}{1+C_V^2\left(2Z_L/Z_s-1\right)} & j\dfrac{2C_V\sqrt{1-C_V^2}\sqrt{Z_L/Z_s}}{1+C_V^2\left(2Z_L/Z_s-1\right)} & -j\dfrac{2C_V\sqrt{1-C_V^2}\sqrt{Z_L/Z_s}}{1+C_V^2\left(2Z_L/Z_s-1\right)} \\ j\dfrac{2C_V\sqrt{1-C_V^2}\sqrt{Z_L/Z_s}}{1+C_V^2\left(2Z_L/Z_s-1\right)} & \dfrac{1-C_V^2}{1+C_V^2\left(2Z_L/Z_s-1\right)} & j\dfrac{2C_V^2\sqrt{Z_L/Z_s}}{1+C_V^2\left(2Z_L/Z_s-1\right)} \\ -j\dfrac{2C_V\sqrt{1-C_V^2}\sqrt{Z_L/Z_s}}{1+C_V^2\left(2Z_L/Z_s-1\right)} & j\dfrac{2C_V\left(Z_L/Z_s\right)}{1+C_V^2\left(2Z_L/Z_s-1\right)} & \dfrac{1-C_V^2}{1+C_V^2\left(2Z_L/Z_s-1\right)} \end{bmatrix}. \quad (6.2)$$

So there is always equal power splitting at balanced outputs with opposite phases, no matter what coupled-line coupling factor and source/load termination impedances are. In order to ensure the optimum balun performances, Equations (6.1) has to be satisfied, which leads to the following two relationships.

1) For given source and load impedances, the voltage coupling factor of each quarter-wave coupled-line section is

$$C_V=\frac{1}{\sqrt{2Z_L/Z_s+1}}. \quad (6.3)$$

2) In turn, for a given coupling factor, the impedance transformation ratio (*ITR*) of source to load impedances (Z_s/Z_L) can be obtained

$$ITR=\frac{Z_S}{Z_L}=\frac{2C_V^2}{1-C_V^2}. \quad (6.4)$$

When condition (6.3) or (6.4) is satisfied, the 3-port ***S*** matrix of a Marchand balun reduces to

$$[\mathbf{S}]_{3\times3}=\begin{bmatrix} 0 & \dfrac{j}{\sqrt{2}} & -\dfrac{j}{\sqrt{2}} \\ \dfrac{j}{\sqrt{2}} & \dfrac{1}{2} & \dfrac{1}{2} \\ -\dfrac{j}{\sqrt{2}} & \dfrac{1}{2} & \dfrac{1}{2} \end{bmatrix}. \quad (6.5)$$

It confirms the lossless balun with optimum properties of null reflections at the unbalanced input and -3dB insertion losses to two balanced outputs with equal power splitting and 180 degrees out of phase.

However, it is also observed that there exist -6dB for both output return losses and isolation between balanced outputs. This phenomenon is quite similar to Wilkinson power divider/combiners which have to employ a resistor between outputs to improve output return losses and isolation. It could be inferred from the fundamental principles of a general three-port passive network [62] which cannot be lossless, reciprocal, and matched at all ports simultaneously.

6.2.2 Circuit Synthesis

The coupling level of coupled transmission lines plays an important role in the impedance transformation of Marchand balun which could be reduced to design proper directional couplers under assumption of infinite directivity. The even- and odd-mode characteristic impedances of coupled lines can be obtained below to ensure optimum impedance matching [62]

$$Z_e = Z_0\sqrt{\frac{1+C_V}{1-C_V}} \tag{6.6a}$$

$$Z_o = Z_0\sqrt{\frac{1-C_V}{1+C_V}} \tag{6.6b}$$

where Z_0 is the system reference impedance for directional coupler and usually chosen as 50ohm.

Based on Equations (6.3), (6.4) and (6.6), it is clear how one should synthesize a Marchand balun circuit for a given impedance transformation ratio (*ITR*). Design curves are plotted in Figure 62 for the coupling level (C_V) of coupled lines along with its even- and odd-mode characteristic impedances. It is found the impedance transformation ratio of a balun circuit depends on the coupling level of coupled lines.

A few typical values of design parameters are listed in Table VI for the synthesis of a Marchand balun circuit. The highlighted data in the table with coupled-line parameters (C_V of -8.45 dB, Z_e of 74.4 Ω, and Z_o of 33.6 Ω) will be realized by our novel slow-wave coupled line structure. It

corresponds to an impedance transformation ratio (*ITR*) of 1:3 from source to load terminations in a single-ended configuration.

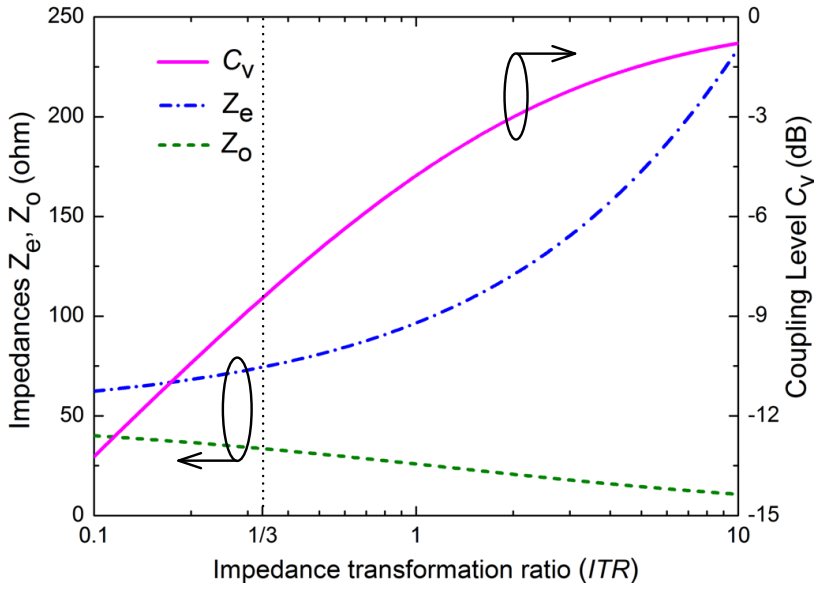

Figure 62: Circuit synthesis of coupled lines for Marchand balun as a function of the impedance transformation ratio (Z_0 =50Ω). (Semi-log plot with a logarithmic scale on the *x*-axis)

TABLE VI: TYPICAL VALUES OF COUPLED-LINE CIRCUIT PARAMETERS FOR THE SYNTHESIS OF AN IDEAL MARCHAND BALUN WITH GIVEN IMPEDANCE TRANSFORMATION RATIOS(Z_0 =50Ω).

ITR	C_V (dB)	Z_e (Ω)	Z_o (Ω)
2:1	-3.01	120.7	20.7
1:1	-4.77	96.5	25.9
1:2	-6.99	80.9	30.9
1:3	-8.45	74.4	33.6
1:4	-9.54	70.7	35.4

6.3 Layout Implementation

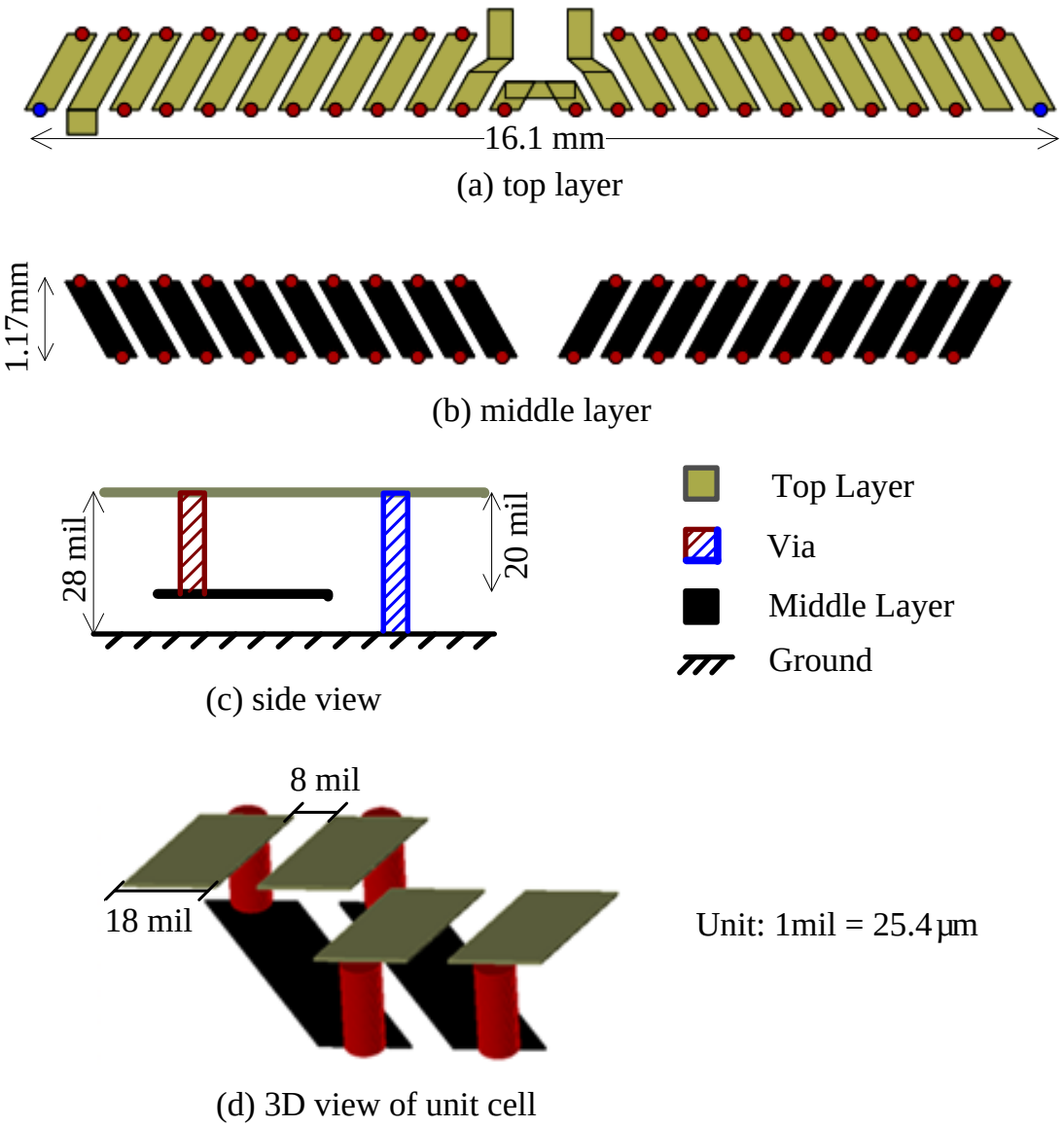

Figure 63: Layout of the miniaturized Marchand balun based on a three-metal-layer setup. (a) top layer, (b) middle layer, (c) side view, (d) enlarged 3D view of coupled line unit cell (ground plane not shown).

A circuit layout example of miniaturized impedance-transforming Marchand balun is depicted in Figure 63 based on a three-metal-layer setup. The bottom metal layer serves as the ground plane. Middle and top metal layers are 8 and 28 mils above the ground, respectively. The balun is composed of two identical sections of artificial slow-wave coupled transmission lines with small adjustments. Each section is composed of five unit cells. Two grounded through-hole vias are used to make short circuited at both leftmost and rightmost ends where blue circular spots mark the location of vias. A metal connection strip is inserted on the top layer due to the physical separation between two balanced outputs. A tuning and optimizing process is necessary while integrating the Marchand balun from coupled line sections. Ideally, for optimum balun performances with specified impedance transformation ratio, a certain coupling level and quarter-wave electrical lengths should be synthesized for the artificial coupled line sections at design frequency of 2.4GHz. Finally, the balun layout exhibits compact planar dimensions with length of 16.1mm and width of 1.17mm (via sizes are not included).

Figure 63 (d) illustrates an enlarged 3D view of a unit cell with dimensions labeled for slow-wave coupled lines. Top-layer metal traces serve electrically as series inductors, while middle-layer metal traces work together with ground plane to primarily form parallel-plate shunt capacitors along with parasitic inductance. Those high-density distributed metallic elements help to enrich inductive and capacitive effects as self inductance and capacitance to enhance slow-wave effects for transmission lines. In addition, parallel traces are folded and interleaved on top and middle layers three-dimensionally (3D) through high density of vias providing inter-layer interconnections, in order to enable more magnetic and electric flux linkages. Accordingly, balanced inductive and capacitive couplings are enhanced significantly to improve the coupling level and equalization of fundamental modal phase velocities for coupled transmission lines. Moreover, proper even- and odd-mode characteristic impedances are purposely synthesized as well.

HFSS full-wave electromagnetic simulator is employed to determine the specific dimensions. Coupled-line standard four-port ***S*** matrix is converted to mixed-mode *S* parameters. Symmetry is guaranteed very well so as for even/odd-mode analysis to be applied. Propagation constants and characteristic impedances can be extracted from the even/odd-mode two-port *S* parameters. Preliminary results of slow-wave coupled lines were presented before. They are shown in Table VII for both convenience and completeness. Attenuation constant and imaginary part of characteristic impedances are negligible.

TABLE VII: FULL-WAVE SIMULATED CHARACTERISTIC PARAMETERS OF THE SLOW-WAVE COUPLED LINES @ 2.4 GHz*.

Z_e	Z_o	Z_0	C_V	ε_{effe}	ε_{effo}	SWF_e	SWF_o
69 Ω	31 Ω	46 Ω	-8.4 dB	27.9	28.7	5.28	5.36

* ε_{eff}: effective dielectric constant; SWF: slow-wave factor

As for Marchand balun, its impedance transformation ratio (*ITR*) and terminal matching depends on even- and odd-mode characteristic impedances of coupled lines. From full-wave simulation results, the coupling factor is about -8.4 dB, close to the theoretical value indicating *ITR* of 1:3 in Table VI. In addition, the coupled-line even- and odd-mode phase velocities reach equalization very well, which can be revealed from their effective dielectric constants (ε_{eff}) or slow-wave factors (SWF). It infers that good amplitude and phase balances should be achieved at two balanced outputs for an *ideal* Marchand balun.

6.4 Measured Results and Discussions

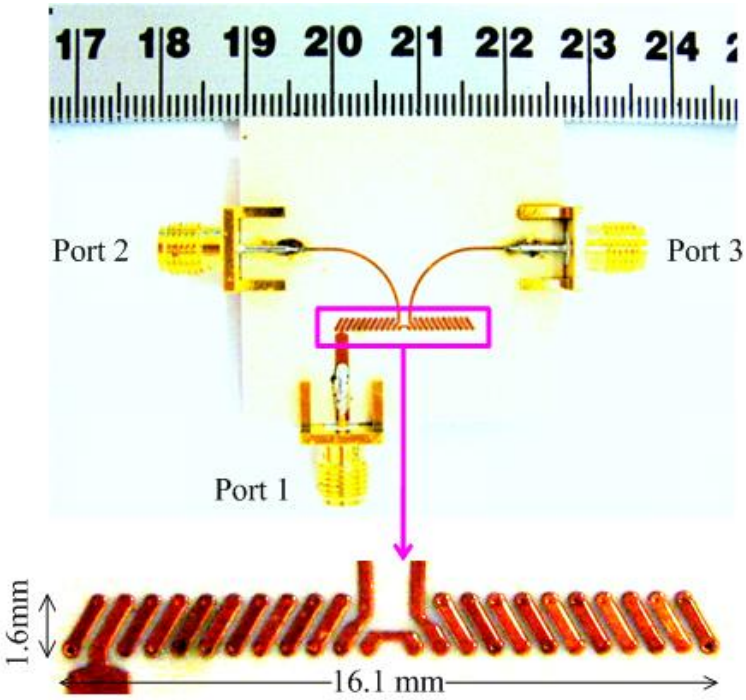

Figure 64: Prototype of the miniaturized Marchand balun.

Figure 64 shows the prototype photograph of a miniaturized Marchand balun. It is fabricated on a three-layer printed circuit board (PCB) with a microwave substrate consisting the core laminate of Rogers RO4003C (upper) and prepreg of RO4450B (lower) for multilayer implementation with 1oz copper cladding on each metal layer. Their dielectric constant and loss tangent are (ε_r=3.38, tanδ=0.0021) and (ε_r=3.54, tanδ=0.004), respectively. The finished balun only occupies a very compact planar area of 16.1mm by 1.6mm (including via sizes) in total, or equivalently, 0.1288λ_0 by 0.0128λ_0 at 2.4GHz (λ_0 is free-space wavelength).

Feeding lines are used to extend input/output ports of the balun to PCB board edges for purpose of measurements using SMA connectors. Very small extra strips are added to balun ports for terminal connections. Proper calibration and de-embedding are performed to remove effects from cables, connectors, and feeding line extensions. The three-port balun circuit is measured by Agilent Technologies N5230C PNA-L four-port network analyzer, while electromagnetic simulations are run by a full-wave solver (HFSS) from Ansys. Their results are shown in Figures 65-68. Good agreements are found between simulation and measurement results, which also helps to validate HFSS simulations.

A three-port *S*-parameter comparison between measurement (solid lines) and simulation (dashed lines) is shown in Figure 65 (a) for the developed miniaturized Marchand balun with all three ports in a single-ended configuration. The input (port 1) is terminated in 50 Ω and both outputs (port 2 and port 3) are terminated in 150 Ω. The measured 10dB return loss (RL) bandwidth (BW) ranges from 1.64 to 2.98 GHz with the center frequency of operation at 2.31GHz and a fractional bandwidth (FBW) of 58%. It is labeled in the figure. In this band (10dB RL BW), measured insertion losses are re-examined in Figure 65 (b). They are very close to ideal value of -3 dB, considering metallic and dielectric losses in practice. The measured input return loss is much better than 10dB and its dip locates at 1.93 GHz with 46.1 dB. Excellent in-band performances (S_{11}, S_{21}, and S_{31}) demonstrate that the proposed balun works well with an impedance transformation ratio of 1:3 from source to load impedances shown in Figure 61. There exists small shifts among the RL dip, operation center frequency (2.3GHz), and initial design frequency (2.4GHz), mainly because of the inexact-50Ω reference impedance of designed slow-wave coupled lines as well as practical fabrication tolerances.

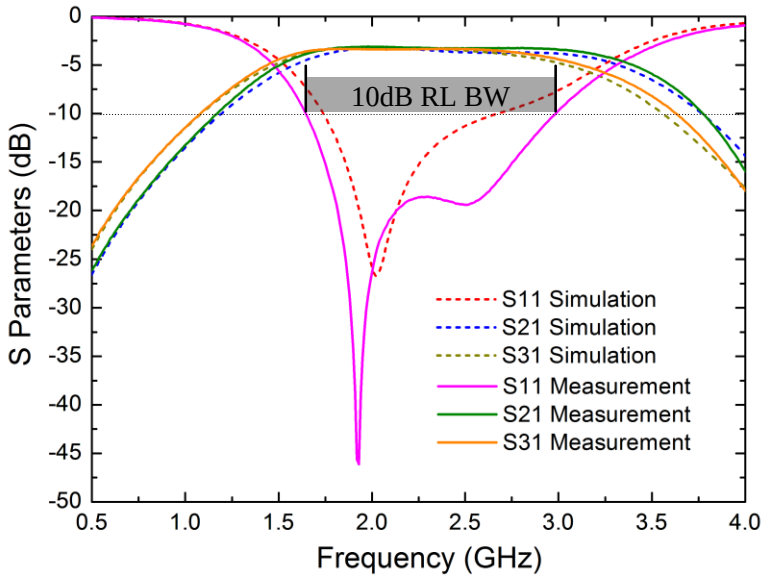

(a) S_{11}, S_{21}, and S_{31}

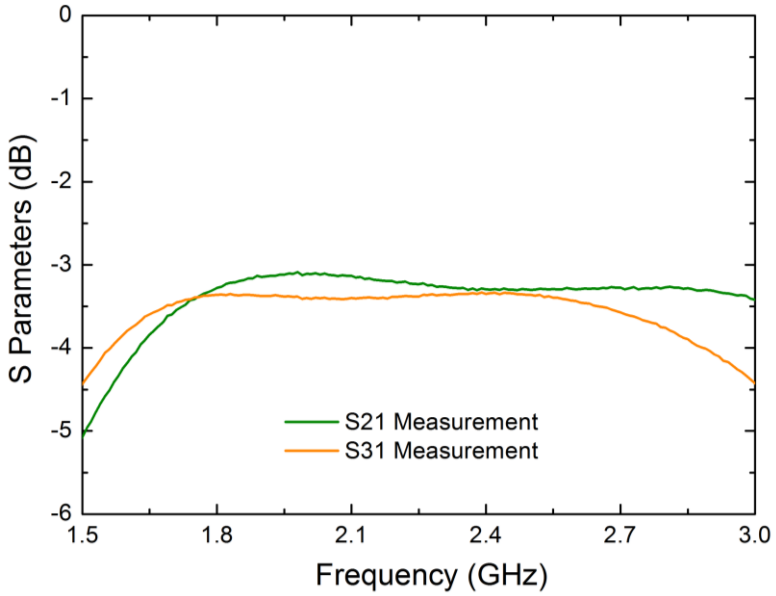

(b) Measured insertion losses

Figure 65: Measured (solid) and simulated (dashed) three-port scattering parameters of the miniaturized Marchand balun in a single-ended configuration (Z_s=50Ω and Z_L=150Ω). (a) S_{11}, S_{21}, and S_{31}; (b) Measured insertion losses in band.

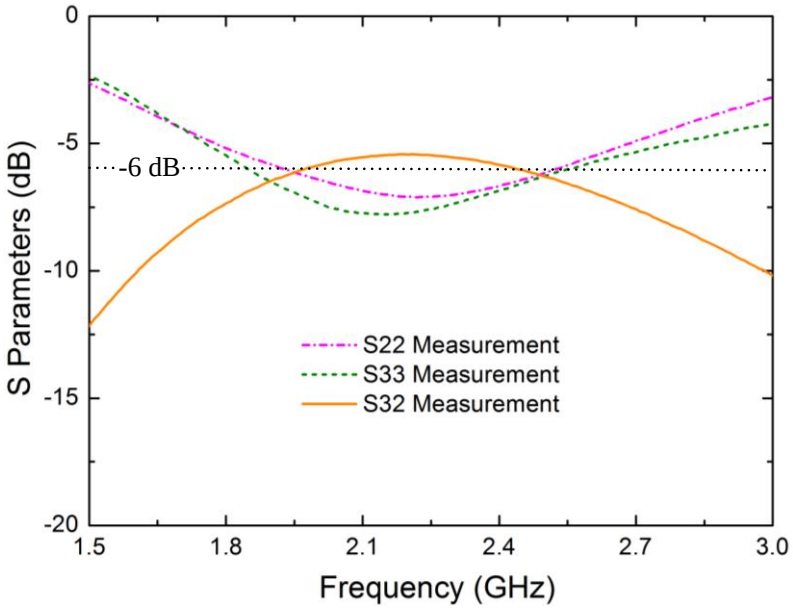

Figure 66: Measured output return losses and isolation (S_{22}, S_{33}, and S_{32}).

Figure 66 shows the measured output return losses and isolation between balanced outputs of the designed Marchand balun. Both output return losses and isolation are around -6 dB at operation center frequency with small variations, which is consistent with theoretical prediction by Equation (6.5). It makes sense as a general three-port passive network cannot be simultaneously guaranteed to be lossless, reciprocal, and matched at all ports. Furthermore, output return losses and isolation can be improved much by adding a resistive network to balun outputs [86, 93].

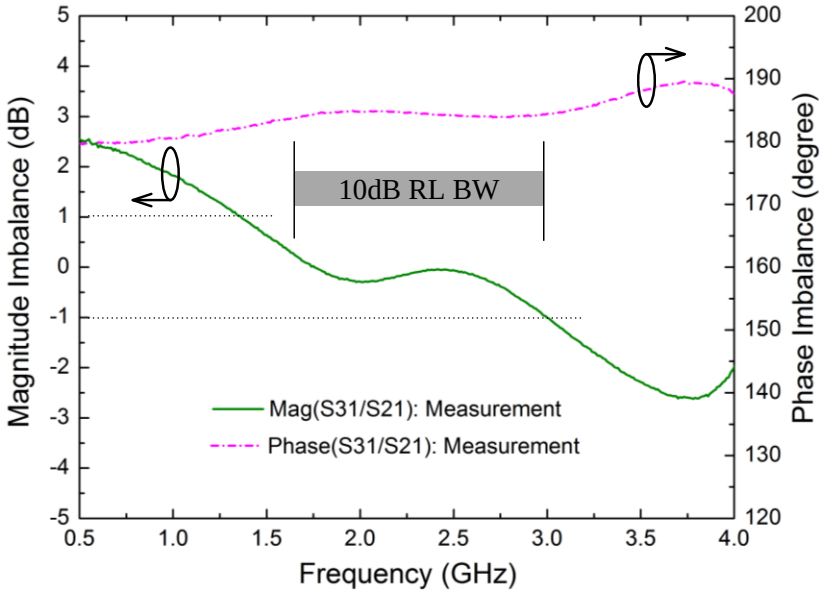

Figure 67: Measured amplitude and phase imbalances of the miniaturized Marchand balun.

Both measured amplitude and phase imbalances at two balanced outputs of the proposed balun are presented in Figure 67. Cumulative phases of S_{21} and S_{31} are used to calculate phase difference. In the 10dB input return loss bandwidth, phase balance is achieved well from 180^{o}+3.7^{o} to 180^{o}+4.9^{o}. Small phase imbalance could be attributed largely to both slight discrepancy between even- and odd-mode phase velocities of slow-wave coupled lines and the inserted non-ideal connection line with non-zero electrical length due to physical separation between balanced outputs. The in-band amplitude imbalance is less than 1dB. Other in-band measured performances are summarized in Table VIII.

The basic function of a balun is to generate differential-mode signals from a single-ended input excitation as well as to suppress common-mode signal. Figure 68 illustrates two-port *S* parameters of the proposed balun circuit with either differential or common outputs. It is found that the differential signal can be attained very well in the frequency band of concern. Jumps are observed in *S*-parameter curves probably due to quarter-wavelength resonances of coupled lines.

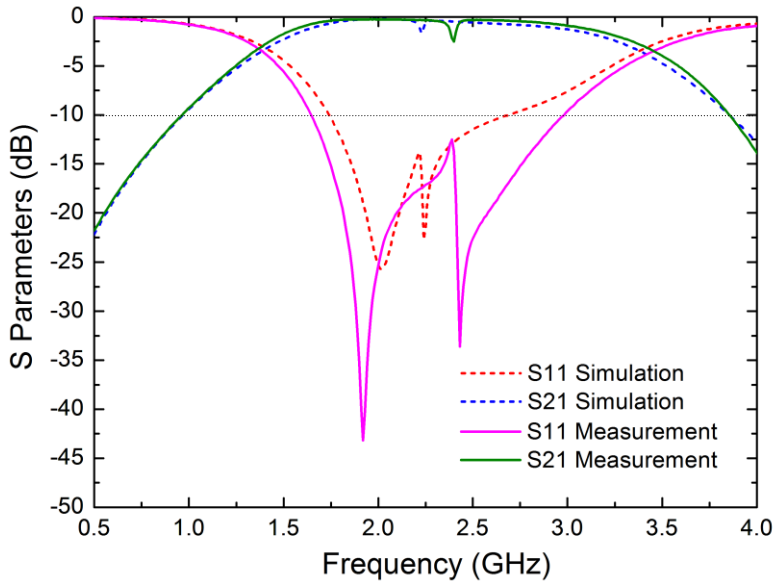

(a) Differential output

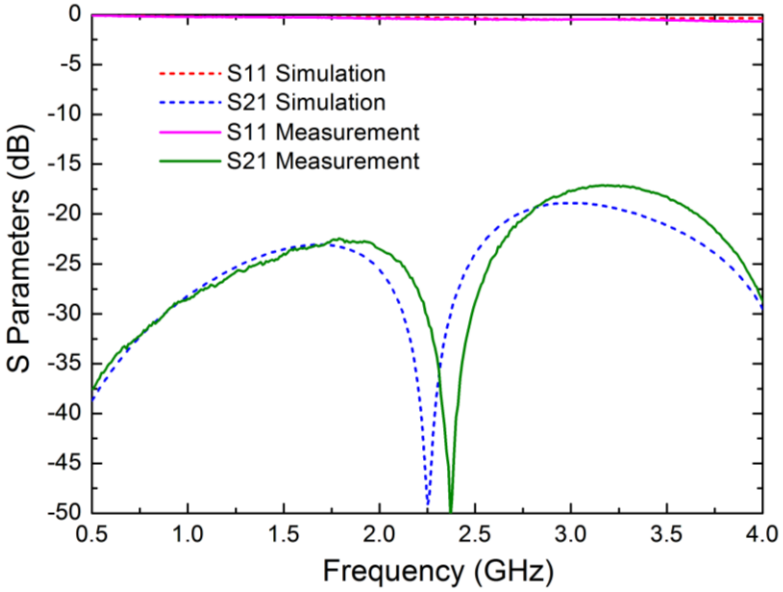

(b) Common output

Figure 68: Measured (solid) and simulated (dashed) two-port scattering parameters of the proposed balun. (a) Differential output; (b) Common output.

TABLE VIII: MEASURED IN-BAND[a] PERFORMANCES OF THE MINIATURIZED MARCHAND BALUN.

10dB RL BW	FBW	Max. RL	Amplitude imbalance	Phase imbalance	ITR
1.64~2.98GHz	58%	46.1 dB	< 1 dB	< 5^{o}	1:3

[a] 'In-band' is defined as the 10dB input return loss bandwidth

6.5 Concluding Remarks

A novel miniaturized impedance-transforming Marchand balun comprising two quarter-wave sections of slow-wave coupled lines has been analyzed, designed, and fabricated. Measured results agree well with full-wave simulations. Good amplitude and phase balances are found in a wide operation frequency region (covering 2.4GHz ISM band) with a fractional bandwidth of about 58%. The balun PCB prototype shows a planar area reduction of over 80%, compared to conventional microstrip implementations on the same circuit board. Advanced fabrication processes with higher line resolution, e.g. LTCC or silicon IC microelectronics, can be employed for similar compact Marchand baluns with better performances or circuit applications to the emerging 60GHz WiGig band.

7 MINIATURIZED COUPLED-LINE 180^{O} HYBRID COUPLER

7.1 Introduction

In recent years, compact mobile handsets have become prevalent in our daily lives, accordingly their demand has been ever increasing. It brings stringent design challenges to RF/microwave engineers. Size reduction and functional integration are regarded as two of key factors for success. Modern sophisticated fabrication processes enable the cost-effective implementation of high-performance miniaturized microwave circuits.

180^{o} hybrid is perhaps one of the most versatile components in microwave passive community for its multiple functionalities in signal splitting or combining. Ideally, it is a four-port circuit providing perfect matching at all ports and good isolation between either two input or two output ports. Depending on which input port is excited, a signal can be split evenly into two in-phase (equivalent to power divider) or 180^{o} out-of-phase (equivalent to a balun) components at two outputs. In turn, when two excitation signals are applied to the previous two 'output' ports, their sum and difference would be generated at the previous two 'input' ports, respectively. For those superb features, extensive applications of the 180^{o} hybrid can be found in various microwave circuits and systems, e.g., phase shifter [94], voltage-variable attenuator [95], push-pull configurations [96], mixers [97], power amplifiers [98-100], and monopulse radar system [101], as shown in Figure 69. In some applications (Figure 69 (a) and (c)), one of the four ports is not used and must be connected to a matched termination to maintain their proper operations.

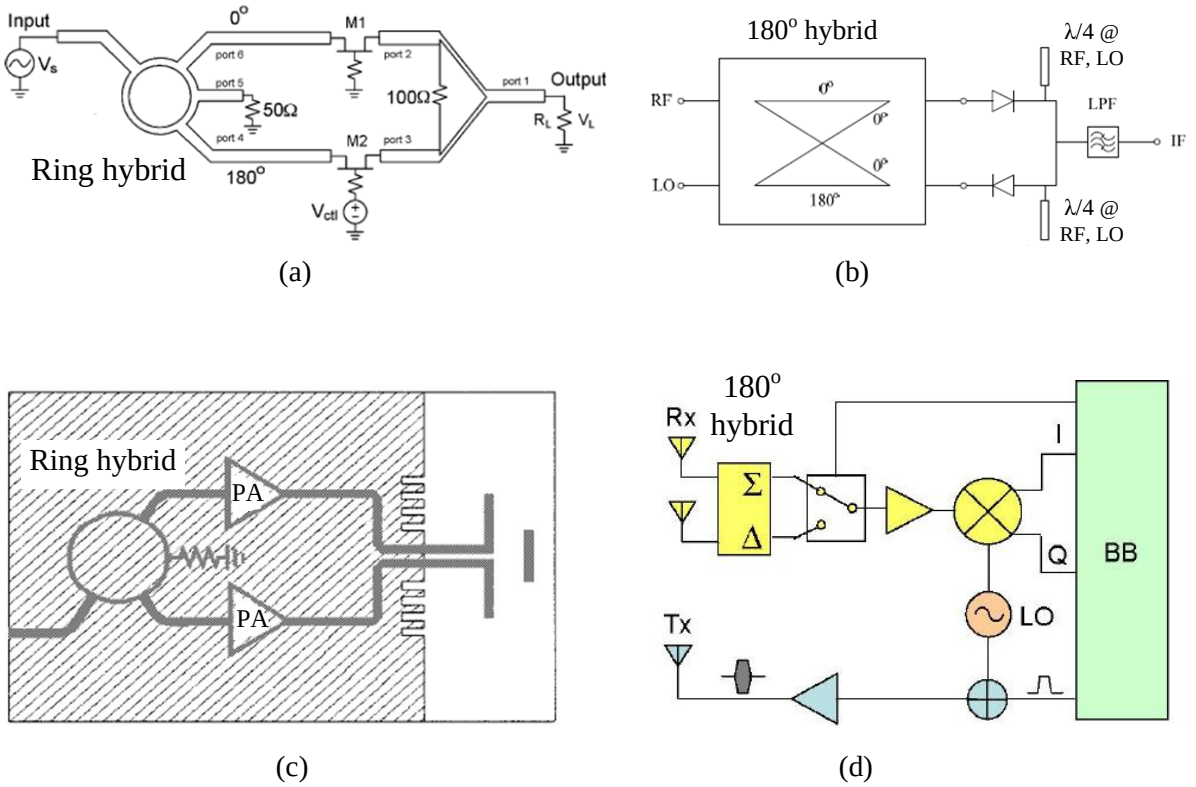

Figure 69: 180° hybrid applications: (a) Voltage-variable attenuator; (Source: reference [95] Fig. 1.). (b) Single-balanced diode mixer; (Source: reference [97] Fig. 1.). (c) Push-pull power amplifier to differentially feed Yagi antenna; (Source: reference [99] Fig. 1.). (d) Monopulse radar. (Source: reference [101] Fig. 3.).

So far, for its simple structure and easy realization, a great deal of attention have been given to 180° rat-race hybrid in the form of conventional ring or its branch-line variation with all ports interconnected physically based on the mechanism of multipath interferences. They are depicted in Figure 70. However, the traditional microstrip implementation often leads to considerable amount of planar area of hybrid couplers, which become more significant at low frequencies, because their dimensions depend on the guided wavelength. Numerous miniaturization techniques have been reported to develop small rat-race hybrids for compact wireless systems, such as slow-wave structure

[102-103], left-handed metamaterial [104-105], shunt stub loaded [106-107], folded/meandered lines [18, 108-109], fractal space filling [110], advanced multilayered LTCC [104, 111], etc. Nevertheless, rat-race hybrids often exhibit narrow-band performances.

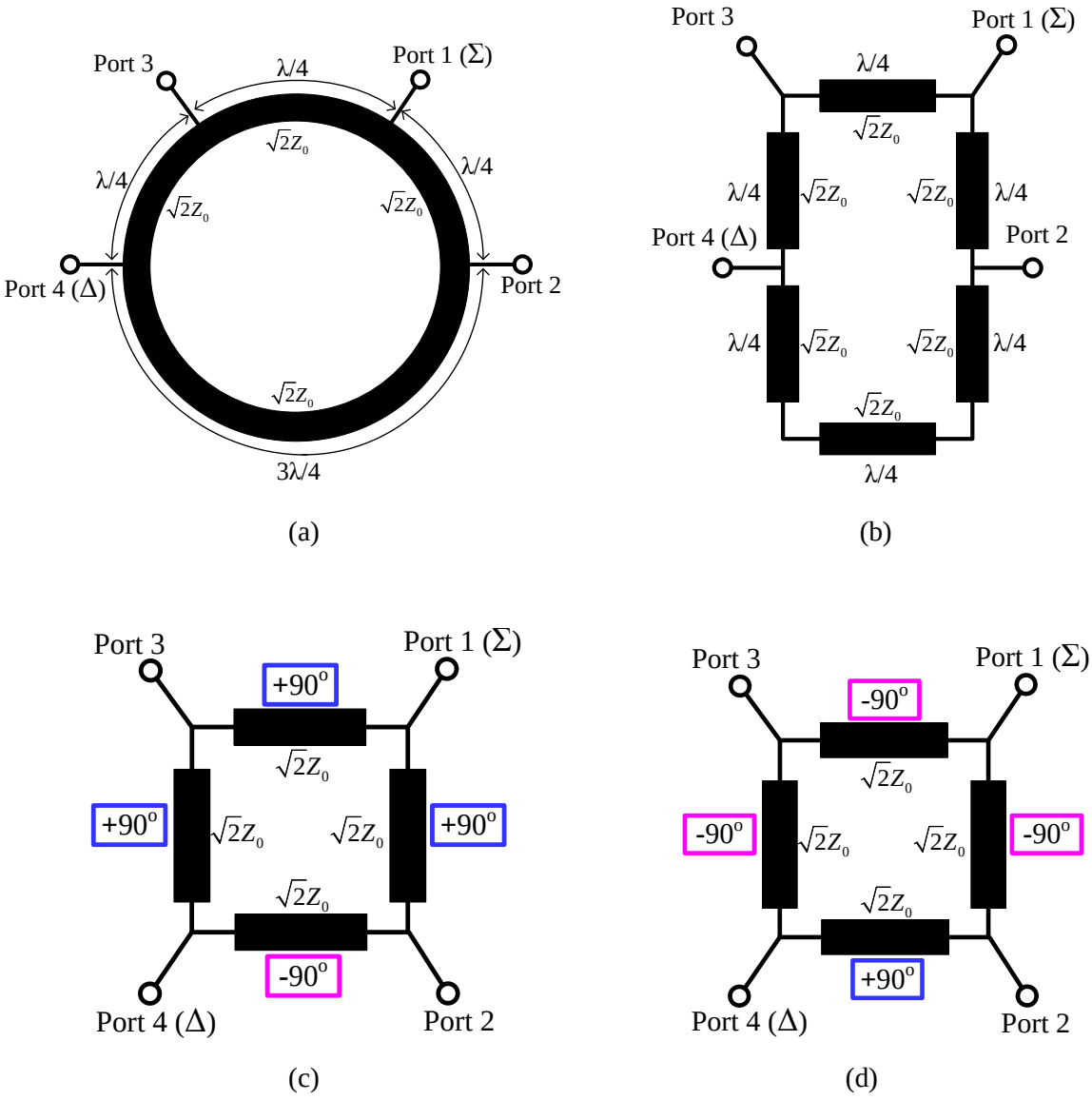

Figure 70: Rat-race 180° hybrids: (a) Conventional circular ring; (b) Its branch-line variation; (c) Metamaterial type I [104]; (d) Metamaterial type II [104]. (Termination impedances: Z_0)

A new circuit topology of 180^o coupled-line hybrids, as depicted in Figure 71 (a), was recently introduced [40-41, 112] based upon the mechanism of electromagnetic couplings. It consists of two quarter-wavelength coupled-line sections with a half-wave uncoupled-line section in between. Simple signal-flow analysis and elaborate theoretical study were performed, respectively, in [40] and [41] to investigate the characteristics of coupled-line 180^o hybrid. It shows wide-band performances in terms of return loss, but also provides DC isolation for coupled ports. This is preferred for circuits in practical RF front ends where parasitic DC signal components are always present, owing to DC biasing, even-order nonlinearities, self-mixing, etc.

In this section, we present a miniaturized coupled-line 180^o hybrid evolved from novel slow-wave structures of both $\lambda/4$ coupled and $\lambda/2$ isolated line sections through an innovative construction. Its concept is illustrated in Figure 71 (b). The periodically interleaved artificial coupled lines, based on 3D folded inductors with high density of vias, feature equal even- and odd-mode phase velocities, significant slow-wave factors, and proper line impedances as well as coupling enhancement. The periodic slow-wave isolated line, based on inverse mushroom structure, is meant to gear its characteristic impedance to the coupled-line reference impedance. Both coupled and isolated transmission lines exhibit least dispersion and attenuation over a broad frequency range. As for the miniaturized 180^o hybrid, sufficient coupling level and equal modal phase velocities of the synthesized coupled lines, respectively, help to facilitate equal power splitting and phase balances at outputs under both in-phase and out-of-phase operations.

A straightforward analysis, design, and synthesis procedure are provided. As proof-of-concept demonstration, a prototype is fabricated on a printed circuit board (PCB) with common microwave substrate of Rogers RO4003C based upon a three-layer microstrip implementation. Good agreements are found between full-wave simulation and measurement results. Moreover, excellent electrical

performances of the proposed coupled-line 180° hybrid are observed. Physically, it occupies merely 9% planar area over its conventional counterpart of microstrip ring hybrid on the same type of board.

7.2 Circuit Architecture, Analysis, and Synthesis

7.2.1 Circuit Architecture

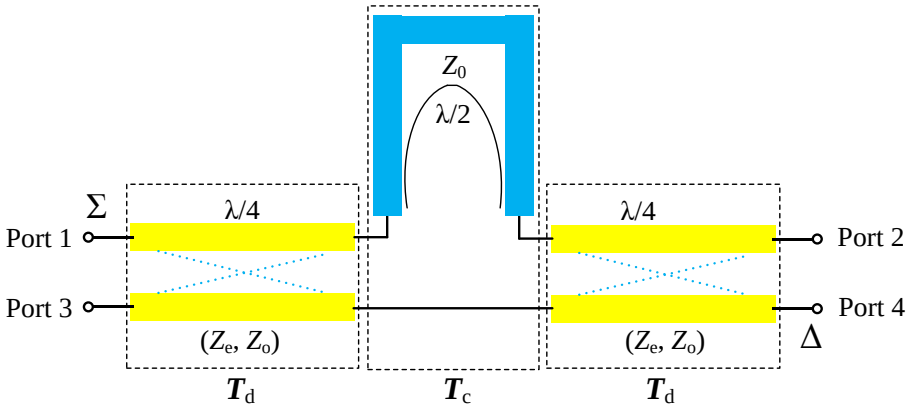

(a) Conventional microstrip coupled-line hybrid coupler

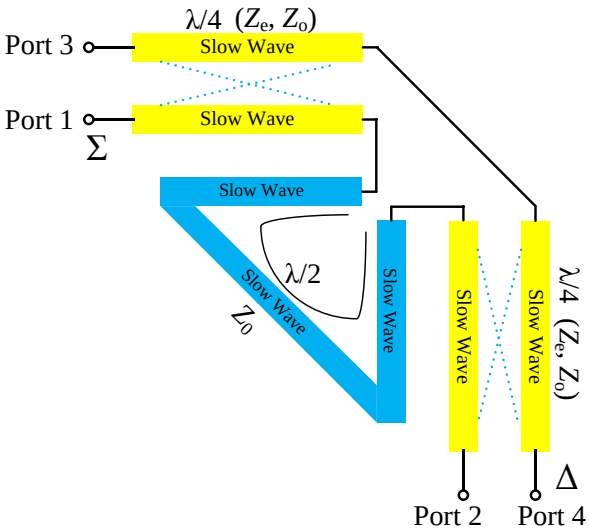

(b) Proposed slow-wave miniaturized hybrid coupler

Figure 71: Circuit architecture of microstrip coupled-line 180° hybrids: (a) Conventional coupled-line hybrid; (b) Proposed slow-wave miniaturized coupled-line hybrid. (Z_0: reference impedance; Z_e and Z_o are even- and odd-mode impedances of coupled lines).

The coupled-line 180^o hybrid is simple in configuration and thereby convenient for microstrip implementation. Its circuit architecture is depicted in Figure 71 (a). It comprises one half-wave isolated line section and two identical quarter-wave symmetric coupled line sections with equal even- and odd-mode phase velocities. Signal experiences 180 degree phase difference when it travels on upper and lower transmission paths. Coupled line reference impedance and isolated line characteristic impedance are meant to be the same as the system reference impedance Z_0, providing good impedance matching at four port terminations. In addition, the proposed hybrid should present wide-band performance in terms of return loss, originating from intrinsic broadband characteristics of impedance matching for coupled lines, which was indicated in the directional coupler design.

7.2.2 Analysis of Coupled-Line Hybrid

A signal flow graph analysis was presented in [40] to reveal the operation principle of coupled-line 180^o hybrid coupler. As it is constructed by cascading three four-port passive networks, a more general approach employing transmission (***T***) matrix was proposed to formulate the theoretical study on coupled-line hybrid [41]. It is briefly stated here for both completeness and further analysis to gain certain design insights.

Functionally, the hybrid coupler can be divided into three building blocks of 4-port circuits: two identical directional couplers ($\boldsymbol{T}_d$) and one connection block ($\boldsymbol{T}_c$) comprising a 180^o phase-shifting line and a direct connection. It is shown in Figure 71 (a). Symmetric coupled lines can be decomposed into even and odd modes to obtain their corresponding 2-port ***T*** matrices and then to form 4-port ***T*** matrix of the directional coupler. According to the network cascading rule, the 4-port ***T*** matrix of hybrid coupler ($\boldsymbol{T}_h$) can be derived by multiplying those of directional couplers ($\boldsymbol{T}_d$) and connection block ($\boldsymbol{T}_c$)

$$[\boldsymbol{T}_h]_{4\times4} = [\boldsymbol{T}_d]_{4\times4} \times [\boldsymbol{T}_c]_{4\times4} \times [\boldsymbol{T}_d]_{4\times4}.$$

Finally, it can be transformed to 4-port ***S*** matrix of hybrid. Only the results of scattering parameters [41] are presented here for limited space.

$$[\boldsymbol{S}]_{4\times4} = \begin{bmatrix} 0 & \frac{2Z_eZ_o}{Z_e^2+Z_o^2} & \frac{Z_e^2-Z_o^2}{Z_e^2+Z_o^2} & 0 \\ \frac{2Z_eZ_o}{Z_e^2+Z_o^2} & 0 & 0 & \frac{Z_e^2-Z_o^2}{Z_e^2+Z_o^2} \\ \frac{Z_e^2-Z_o^2}{Z_e^2+Z_o^2} & 0 & 0 & -\frac{2Z_eZ_o}{Z_e^2+Z_o^2} \\ 0 & \frac{Z_e^2-Z_o^2}{Z_e^2+Z_o^2} & -\frac{2Z_eZ_o}{Z_e^2+Z_o^2} & 0 \end{bmatrix} \tag{7.1}$$

It can be observed that the through and coupled output signals are either in phase or 180^o out of phase with excitation signal, depending on which port is chosen as input. However, for the ring hybrid, both two output signals are in quadrature phase with input. Likewise, coupled-line 180^o hybrids have two essential functions as power combining and power dividing with two operation modes of either in phase or 180^o out of phase. They are illustrated as follows.

1. Excitation (e.g. @ port 1) can be applied on one of coupled lines with the 180^o phase-shifting line as connection in between. Both the coupled (S_{31}) and transmitted (S_{21}) signals are positive real values and hence have the same phase as the input signal. Hence, the hybrid performs the function of in-phase power dividing at output ports 2 and 3.
2. Excitation (e.g. @ port 4) can be applied on another of coupled lines with direct connection in between. The coupled signal (S_{24}) has the same phase as input signal, while the transmission signal (S_{34}) is 180^o out of phase with both input and coupled signals. Hence, the 180^o hybrid performs the balun function of power splitting with 180^o out of phase at ports 2 and 3.
3. Two excitations can be simultaneously applied, e.g. at port 2 and port 3. Their sum and difference of input signals would be generated at port 1 (Σ) and port 4 (Δ), respectively.

Due to reciprocity and symmetry of the circuit architecture, the hybrid coupler maintains the same characteristics when other ports are excited as inputs.

7.2.3 Synthesis of Hybrid Circuit

The power splitting ratio (*PSR*) between outputs is another important measure to characteristics of the coupled-line 180^o hybrid. It is defined as the ratio of *coupled* power to *through* power

$$PSR = \left|\frac{S_{31}}{S_{21}}\right|^2 = \frac{2C_V}{1-C_V^2} \tag{7.2a}$$

where C_V is the voltage coupling factor of coupled lines for directional coupler, that is,

$$C_V = \frac{Z_e - Z_o}{Z_e + Z_o}. \tag{7.2b}$$

In turn, C_V can also be expressed as a function of the power splitting ratio

$$C_V = \frac{\sqrt{PSR^2+1}-1}{PSR}. \tag{7.3}$$

In addition, the voltage coupling level (C_h) of coupled-line hybrid coupler can be obtained as

$$C_h = |S_{31}| = \frac{2C_V}{1+C_V^2}. \tag{7.4}$$

It is well known that the even- and odd-mode characteristic impedances of coupled transmission lines can be synthesized as

$$Z_e = Z_0\sqrt{\frac{1+C_V}{1-C_V}}, \tag{7.5a}$$

$$Z_o = Z_0\sqrt{\frac{1-C_V}{1+C_V}} \tag{7.5b}$$

where Z_0 is the reference impedance for coupled line design. It is also the characteristic impedance of phase-shift line as well as hybrid termination impedances (50Ω is usually chosen for Z_0).

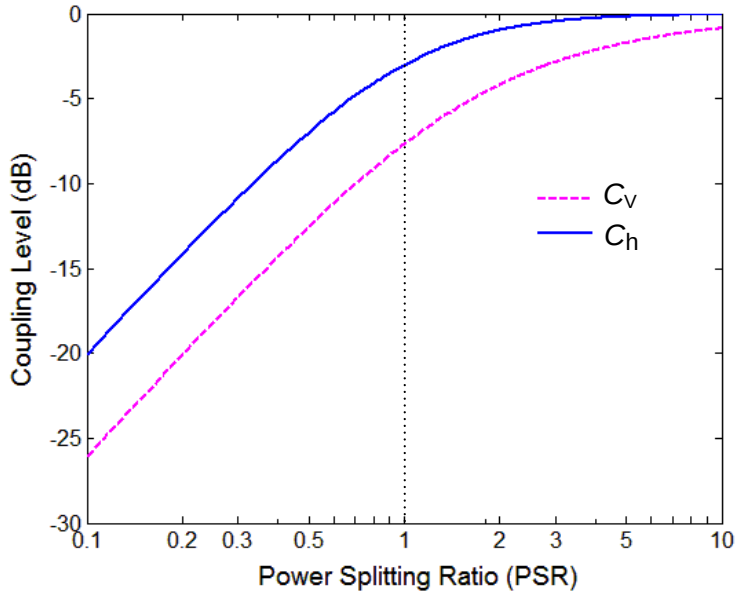

(a)

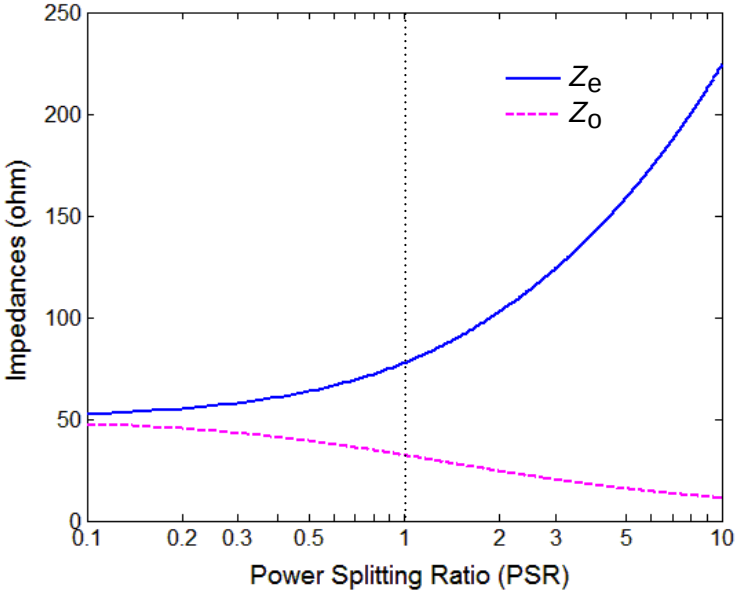

(b)

Figure 72: Circuit synthesis of coupled line 180° hybrid as a function of power splitting ratio: (a) Coupling levels of both coupled lines and hybrid coupler; (b) Even- and odd-mode impedances of the coupled line section (Z_0 =50Ω). (Semi-log plot with a logarithmic scale on the *x*-axis)

Based on Equations (7.3-7.5), it is straightforward to synthesize a coupled line 180^o hybrid circuit for a given power splitting ratio (*PSR*) or coupling level (C_h) with good impedance matching at terminations. Design curves are plotted in Figure 72 for the coupling levels of both hybrid (C_h) and coupled lines (C_V) with its even- and odd-mode characteristic impedances. It is found that the coupling level of coupled lines (C_V) is always considerably weaker than that of hybrid coupler (C_h). For a certain strong hybrid coupling level, it helps to relax the stringent coupling requirement of coupled lines, which is difficult to achieve for conventional microstrip implementation on a printed circuit board.

A few typical values of design parameters are listed in Table IX for synthesis of a hybrid coupler. Equal power splitting (*PSR* = 1:1, C_h = -3dB) is usually preferred in most practical applications. Its corresponding values are highlighted in the table with coupled-line parameters C_V of -7.7 dB, Z_e of 77.7 Ω, and Z_o of 32.2 Ω in a 50Ω system.

TABLE IX: TYPICAL VALUES OF CIRCUIT PARAMETERS FOR SYNTHESIS OF COUPLED LINE 180^O HYBRID (Z_0 =50Ω).

PSR	C_h (dB)	C_V (dB)	Z_e (Ω)	Z_o (Ω)
1:3	-10.1	-15.9	58.8	42.5
1:2	-7.0	-12.5	63.6	39.3
1:1	**-3.0**	**-7.7**	**77.7**	**32.2**
2:1	-0.97	-4.2	102.9	24.3
3:1	-0.46	-2.8	124.1	20.1

7.3 Design and Implementation

The coupled line 180^o hybrid comprises primarily of one λ/2 section of isolated transmission line and two identical λ/4 sections of coupled transmission lines. Coupling level and impedance matching of hybrid coupler rely on the proper impedances of both coupled and isolated lines. Their dimensions can be shrank by employing the slow wave methodology, which is to be implemented to design a miniaturized 180^o hybrid coupler with equal power splitting in this section. Apart from slow wave and impedance issues, particular attention must be directed to modal phase-velocity equalization of coupled lines to achieve certain performances for hybrid, e.g., phase and amplitude balances.

7.3.1 Slow-Wave EBG Isolated Line

A layout design example of artificial slow-wave isolated transmission line is depicted in Figure 73 (a)-(d). It is a right-handed electromagnetic bandgap (EBG) structure based on a three-layer setup with floating vias providing inter-layer interconnects between top and middle metal layers. They constitute a complex signal layer with respect to the ground layer where current return path exists. It offers design flexibility to individually synthesize serial inductance and shunting capacitance on top and middle layers, respectively. In addition, it helps to suppress the capacitive parasitics between dominant inductor and capacitor since potentials are about the same on top and middle layers in a small unit cell. We entitle this novel topology ***inverse*** *mushroom* structure.

In contrast, in typical *mushroom* topology shown in Figure 73 (e), there are inter-connecting vias sandwiched between lower and bottom metal layers to move part or whole of ground plane upwards for a standard circuit board with given thickness. They constitute a complex ground layer with respect to the top signal layer with both quasi-lumped inductors and capacitors. A slow-wave mushroom example was developed in [3], and is shown here in Figure 73 (f) for direct contrast to our inverse mushroom counterpart.

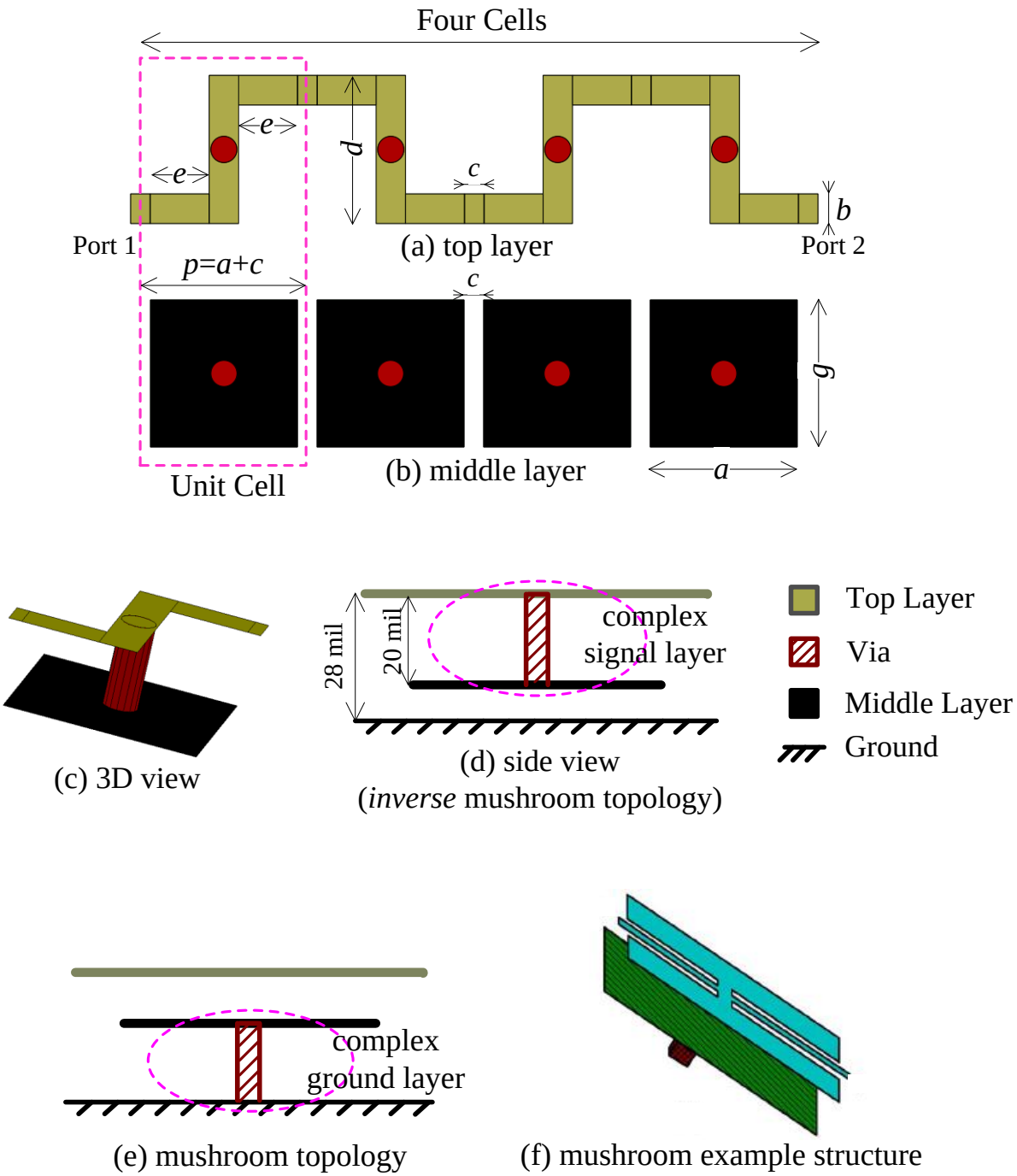

Figure 73: Layout of a slow-wave isolated transmission line based on three-layer setup of inverse mushroom topology. (a) top layer; (b) middle layer; (c) 3D view; (d) side view; (e) mushroom topology; (f) mushroom example structure (Source: reference [3] Fig. 5.). (Unit: 1mil = 25.4µm)

Basic idea is provided below for the layout design of slow-wave EBG periodic transmission line. Likewise, compressed, twisted, or fragmented (CTF) metal strips are spread out three-dimensionally (3D) into a multilayer dielectric substrate. High-density distributed metallic elements can help to enrich inductive and capacitive effects. Hence significant quasi-lumped inductor and capacitor could be synthesized within a small unit cell to enhance slow-wave factor (SWF) or effective dielectric constant. Both conventional and inverse mushroom topologies can help to increase shunting capacitances as well as to bring down characteristic impedance of an artificial EBG transmission line for the usual 50Ω system.

TABLE X: PHYSICAL DIMENSIONS OF THE UNIT CELL OF A SLOW-WAVE ISOLATED TRANSMISSION LINE*.

Parameters	*a*	*b*	*c*	*d*	*e*	*g*	*p*
Value	45 mil	9 mil	6 mil	45 mil	18 mil	45 mil	51 mil

* $e = (a-b)/2$; $d = g$; $g = a$; $p = a+c$; 1mil = 25.4μm

Our design example of a slow-wave unit cell is implemented on a three-layer setup using the inverse mushroom topology, as shown in Figure 73. It employs the microwave substrate Rogers RO4003C with electrical properties of $\varepsilon_r = 3.38$ and $\tan \delta = 0.0021$. Bottom metal layer is the regular uniform ground plane. A rectangular patch (*a* by *g*) is placed on the middle layer with height of 8 mils to provide shunting capacitance to the ground. Meandered thin wire with width *b* is used on the top layer, which is 20 mils above middle layer, to serve as serial inductance. Floating via is sandwiched to interconnect the top inductor and middle capacitor layers to form a complex signal layer. It is located at the center of a unit cell for symmetry to guarantee optimum signal transmission from the *LC* circuit. The extension of inductor trace outside the capacitor patch is *c* for cascading unit cells

with periodicity $p=a+c$. For design convenience, the relationships are assumed for $e = (a-b)/2$, $d = g$, $g = a$, and $c = 6$ mils, which leads to only two variables (a and b) left for tuning. Slow-wave effect and proper impedance can be achieved by adjusting the serial inductance and shunting capacitance through changing values of a and b. Full-wave electromagnetic solver (HFSS) is utilized to determine their values. A set of physical dimension parameters are listed in Table X.

It is worthwhile to mention that this slow-wave line is completed with no additional cost of sacrificing line width. The unit cell occupies only 51 mils in length by 45 mils in width, which is even narrower than a conventional uniform 50Ω microstrip line with width of 62 mils on the same substrate.

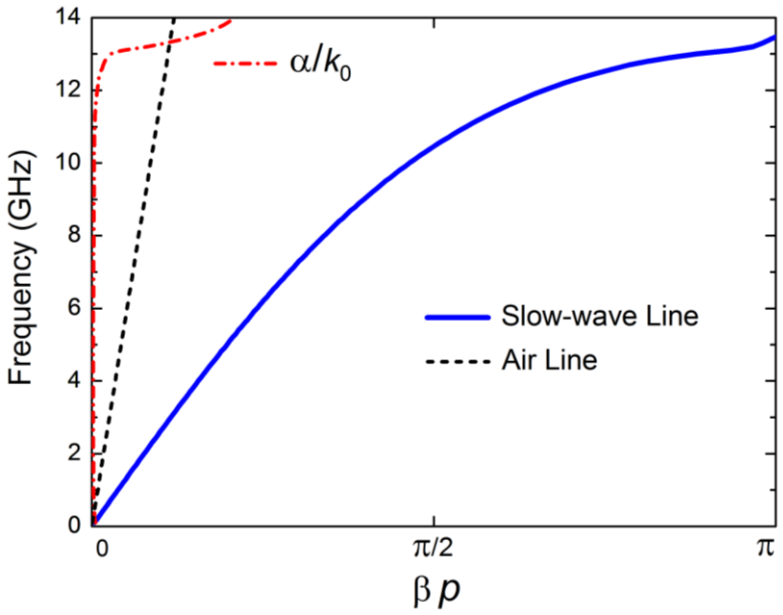

Figure 74: Dispersion diagram of the slow-wave EBG isolated-line unit cell.

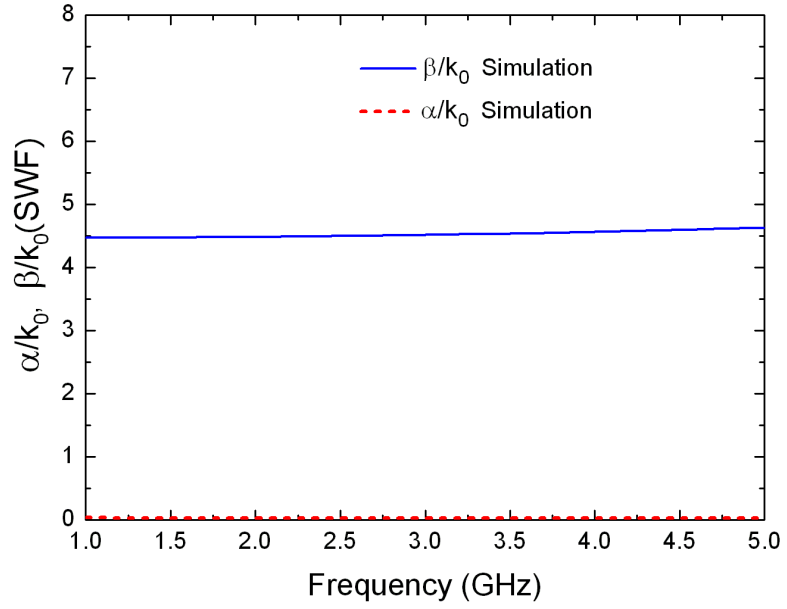

(a) Normalized propagation constant

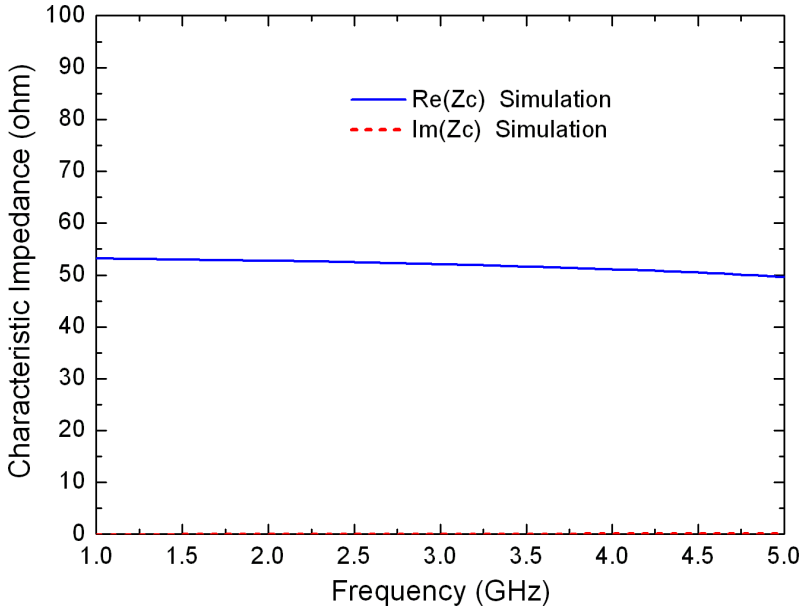

(b) Characteristic impedance

Figure 75: Propagation characteristics of the 50Ω slow-wave EBG isolated line. (a) Normalized attenuation and phase constants; (b) Characteristic impedance.

Dispersion characteristics are obtained from HFSS full-wave simulation results. They are rather interesting. Figure 74 shows the dispersion diagram of the artificial right-handed slow-wave line unit cell, along with its normalized attenuation constant to help identify the cut-off frequency. It is found that dispersion curve linearity is maintained quite well at frequencies much below the cut-off frequency of around 13 GHz. It is clear that this structure supports slow-wave propagation in the entire pass-band frequency region under investigation. More details of propagation characteristics are illustrated in Figure 75 in the frequency range of interest from 1 to 5GHz. It is found that the slow-wave factor (SWF) and real part of characteristic impedance are very stable with little dispersion. They are about 4.5 and 50Ω, respectively. In addition, losses seem negligible, as confirmed by the bottom curves of both normalized attenuation constant and imaginary impedance.

7.3.2 Slow-Wave Coupled Lines

A novel slow-wave coupled line structure based on a three-layer *inverse mushroom* topology was presented in chapter 5. Symmetry of this structure is ensured so both physically and electrically that even/odd-mode analysis can be applied to the slow-wave coupled lines. The enlarged 3D view of a coupled-line unit cell is shown in Figure 76 (d) for convenience. It was implemented on the highly metalized substrate of Rogers RO4003C. Parallel metal strips are interleaved on upper two different layers through high density of interconnecting vias, which somewhat resembles fence walls in substrate integrated waveguides (SIW), to constitute a complex signal layer. Hence 3D-folded coupled inductors are formed to enhance magnetic coupling and thereby total effective coupling level. Moreover, balanced inductive and capacitive couplings can be achieved by a proper design. It enables the equalization of even- and odd-mode phase velocities, large slow-wave factors, as well as the coupling enhancement for synthesizing artificial periodic coupled transmission lines with least dispersion and attenuation over a very broad frequency range. Preliminary results of the novel slow-

wave coupled lines, based on HFSS full-wave simulations, are repeated here in Table XI for completeness.

TABLE XI: FULL-WAVE SIMULATED CHARACTERISTIC PARAMETERS OF THE SLOW-WAVE COUPLED LINES @ 2.4GHz*.

Z_e	Z_o	Z_0	C_V	ε_{effe}	ε_{effo}	SWF_e	SWF_o
69 Ω	31 Ω	46 Ω	-8.4 dB	27.9	28.7	5.28	5.36

* ε_{eff}: effective dielectric constant; SWF: slow-wave factor

7.3.3 Miniaturized Coupled-Line 180° Hybrid

The schematic diagram in Figure 71 (b) depicts the proposed circuit scheme of miniaturized coupled-line 180° hybrid coupler by replacing conventional coupled and isolated microstrip lines with slow-wave ones through an innovative deployment. The half-wave isolated line section is bended as a triangle which is located in the inner rectangular area bounded by two perpendicular quarter-wave coupled line sections, which renders the resulted hybrid coupler more compact. It intends to work in a 50Ω system, which requires that both artificial slow-wave coupled line reference impedance and isolated line characteristic impedance be designed to target at 50 Ω.

The layout implementation of proposed hybrid coupler is illustrated in Figure 76 based on a three-metal-layer stack-up on Rogers RO4003C substrate based on an *inverse* mushroom configuration. Inter-layer connections between top and middle layers are realized using metal filled circular via-holes. All vias have the same dimensions, with 8mil-diameter hole and 5mil-width annular ring. Other strip width and spacing are above 6 mils, which would lead to cost-effective fabrication using present PCB processes.

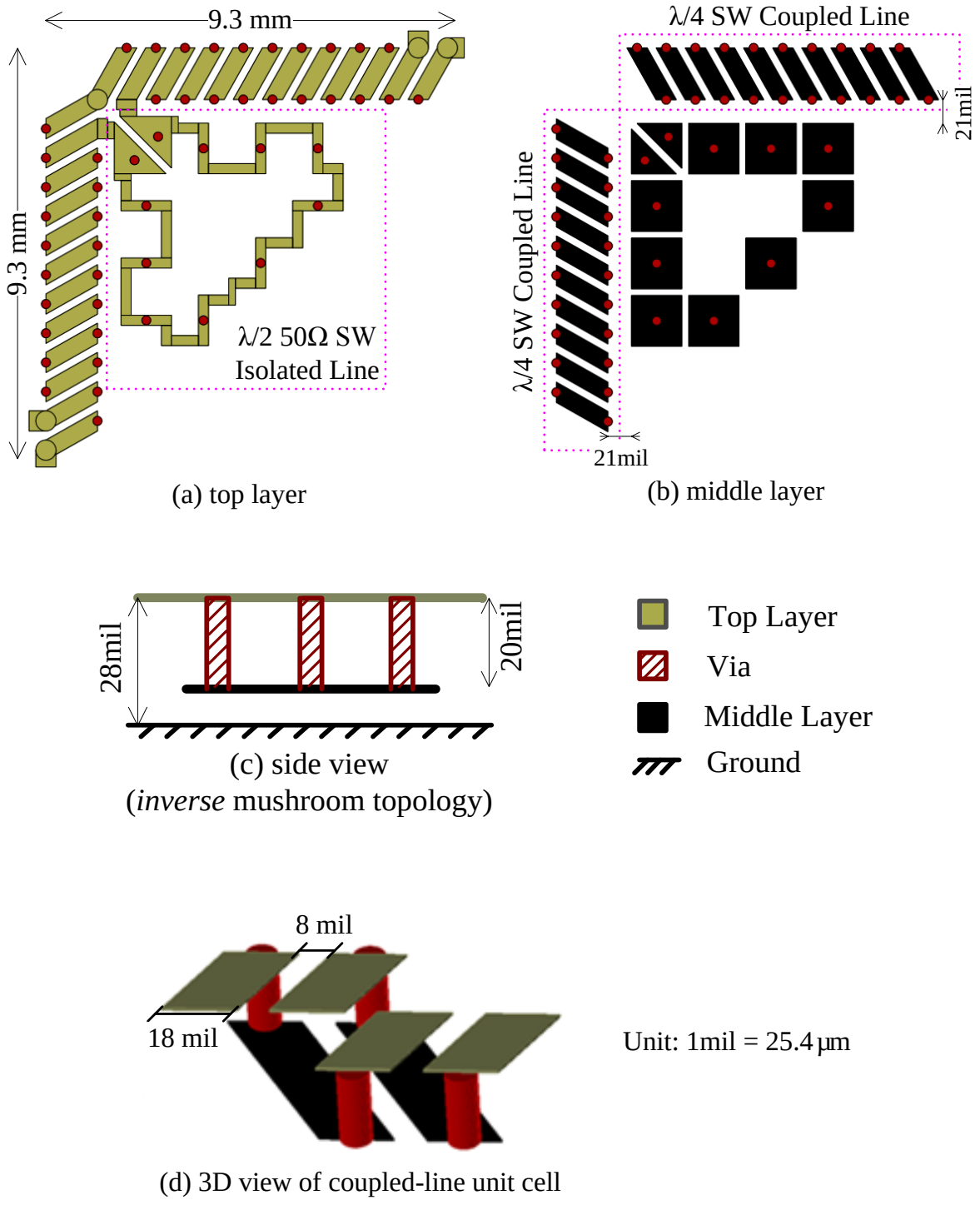

Figure 76: Layout of the miniaturized coupled-line 180° hybrid based on a three-layer setup. (a) top layer, (b) middle layer, (c) side view, (d) enlarged 3D view of coupled line unit cell.

Unit cells of slow-wave coupled and isolated lines were designed first. The 50Ω half-wavelength phase-shifting triangular line section consists of nine unit cells along with two half cells at ends, for purpose of both phase compensation and physical connections to each quarter-wave coupled line section of five cells. Array of high-density vias form electrical fence wall to suppress parasitic couplings between the neighboring coupled and isolated line subsections. A tuning and optimizing process is necessary while integrating the hybrid coupler from isolated and coupled line sections with small adjustments. The entire circuit layout is retuned finally through a full-wave electromagnetic solver (HFSS) for optimum hybrid performances. Detailed dimensions are labeled in Figure 76.

7.4 Experimental Results and Discussions

A photograph of prototype is shown in Figure 77 for the developed miniaturized coupled line 180^o hybrid coupler. It is fabricated on a three-layer printed circuit board (PCB) with 1oz copper cladding on each metal layer. As for board material, in addition to upper core laminate (RO4003C), the lower prepreg of Rogers RO4450B (ε_r=3.54, tanδ=0.004) has to be used for multilayer fabrication. The finished hybrid coupler occupies only a very compact rectangular planar area of 9.5mm by 9.5mm (including via sizes) in total, or equivalently, $0.076\lambda_0$ by $0.076\lambda_0$ at 2.4GHz (λ_0 is free-space wavelength). Feeding line extensions are employed for measurements using SMA connectors. The four-port hybrid circuit is tested by Agilent Technologies N5230C PNA-L 4-port network analyzer, while its full-wave simulations are performed by HFSS.

Coupled-line 180^o hybrid coupler has two essential functions: power combining and power dividing. The former is the reverse operation way of the latter which is hence emphasized here and demonstrated experimentally. The hybrid coupler performs the power dividing function under two operation modes of either in phase or 180^o out of phase, depending on which line is chosen for excitation.

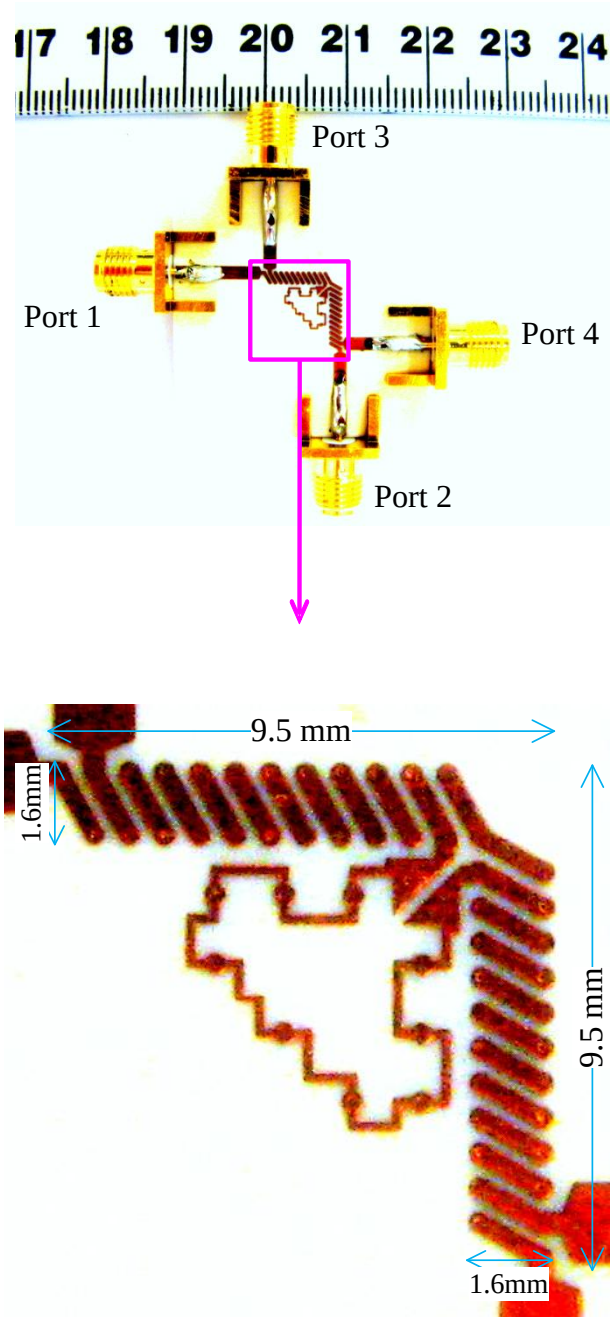

Figure 77: Photograph of fabricated miniaturized coupled-line 180^{o} hybrid.

7.4.1 In-Phase Operation

In-phase operation can be enforced by applying the excitation signal on one of the coupled lines with the half-wave phase-shifting connection line between two coupled-line sections. Proper synthesis of artificial coupled and isolated lines enables equal power splitting between coupled and through outputs of hybrid coupler.

Figure 78 shows the *S*-parameter comparison between measurement (solid lines) and full-wave simulation (dashed lines) for the developed miniaturized coupled line 180^o hybrid coupler with input excitation at port 1. It is found that both measured and simulated return losses (S_{11}) are far below -10dB over the whole frequency range under investigation (from 0.5 to 4GHz). It confirms the aforementioned wide-band characteristics in terms of impedance matching for coupled-line circuits. Excellent isolation is observed by the fact that both measured and simulated S_{41} are well below -20dB over the entire frequency region. Besides, magnitude and phase imbalances at coupled (port 3) and through (port 2) outputs are further examined in Figure 79 where cumulative phases of S_{21} and S_{31} are used. From measurement results, phase balance of $0^o \pm 10^o$ is achieved from 2.12 to 2.56 GHz, and amplitude balances of -3dB $\pm$ 1dB at coupled and through outputs are obtained from 1.93 to 2.53 GHz and 1.73 to 2.85 GHz, respectively.

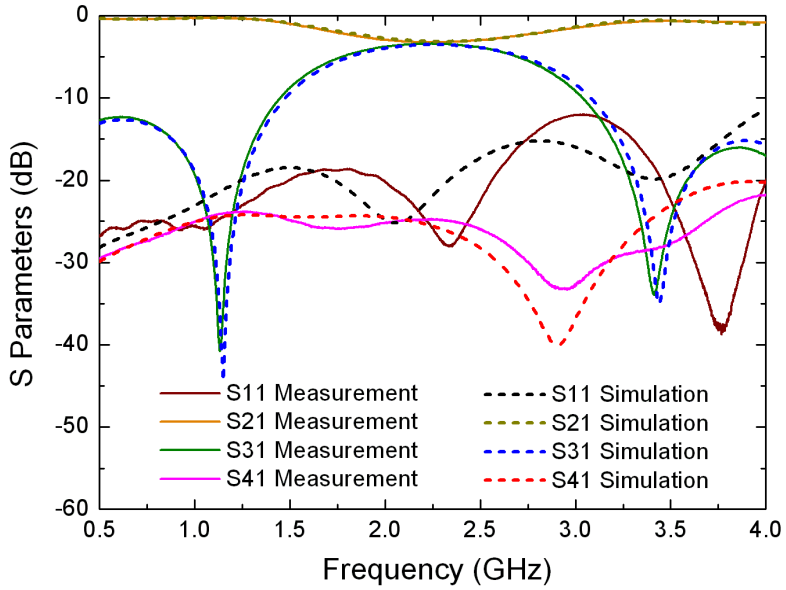

(a) Magnitude

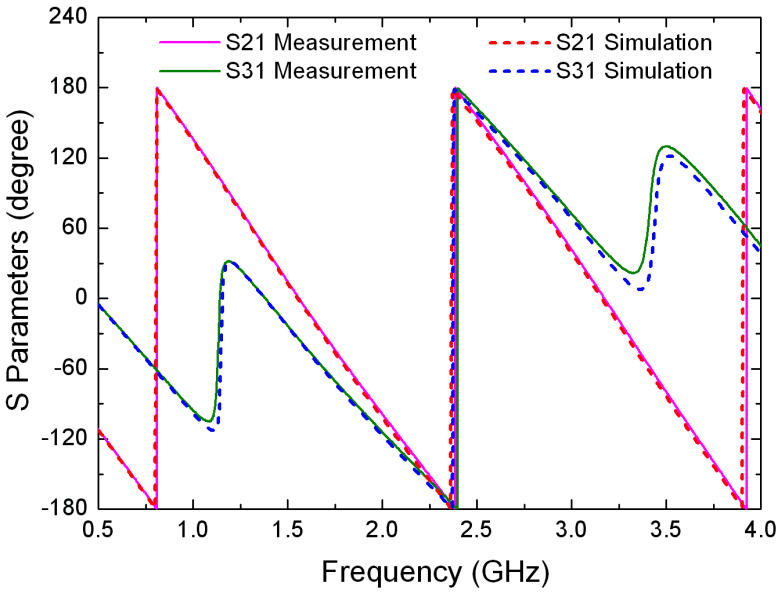

(b) Phase

Figure 78: Comparison of measured (solid) and simulated (dashed) scattering parameters for the miniaturized 180° hybrid coupler under in-phase operation with excitation at port 1. (a) Magnitudes of S_{11}, S_{21}, S_{31}, and S_{41}; (b) Phases of S_{21} and S_{31}.

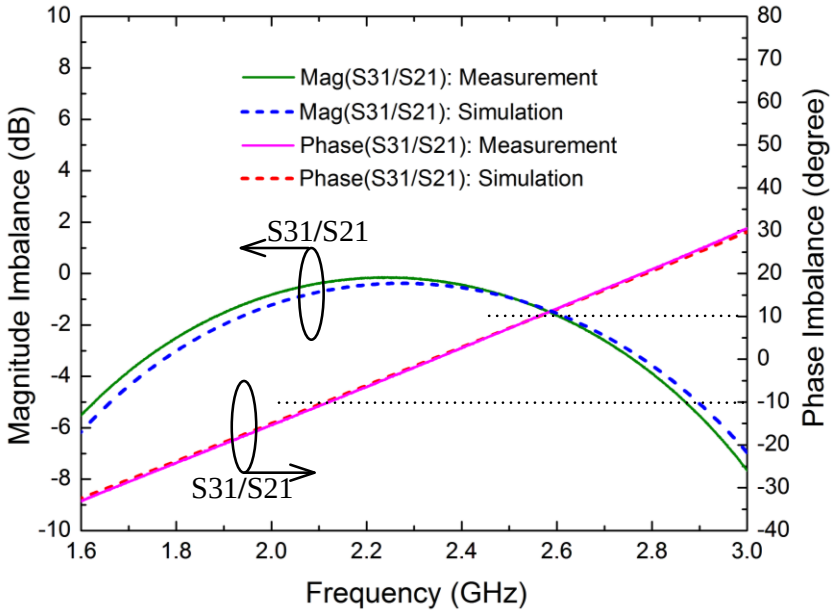

Figure 79: Measured (solid) and simulated (dashed) imbalances of magnitude and phase at hybrid outputs under in-phase operation with excitation at port 1.

7.4.2 180° Out-of-Phase Operation

A *S*-parameter comparison between measurement (solid lines) and simulation (dashed lines) is presented in Figure 80 for the proposed compact hybrid coupler with excitation at port 4. Wide-band features are found for measured/simulated return losses (S_{44}) and isolations (S_{14}). Both are much below -15dB and -20dB, respectively, over the entire frequency range under investigation. Equal power splitting (-3 dB) between coupled (S_{24}) and through (S_{34}) ports is achieved around 2.25 GHz. Figure 81 shows the magnitude and phase imbalances (S_{24}/S_{34}) at hybrid outputs under the out-of-phase operation mode. Phase balances of $180^{o}\pm10^{o}$ are observed from 2.12GHz to 2.59GHz based on measured frequency responses.

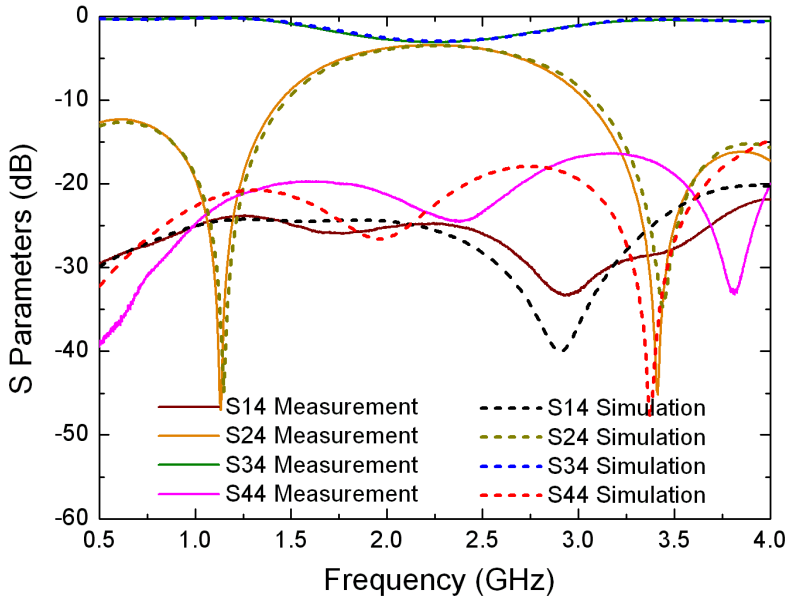

(a) Magnitude

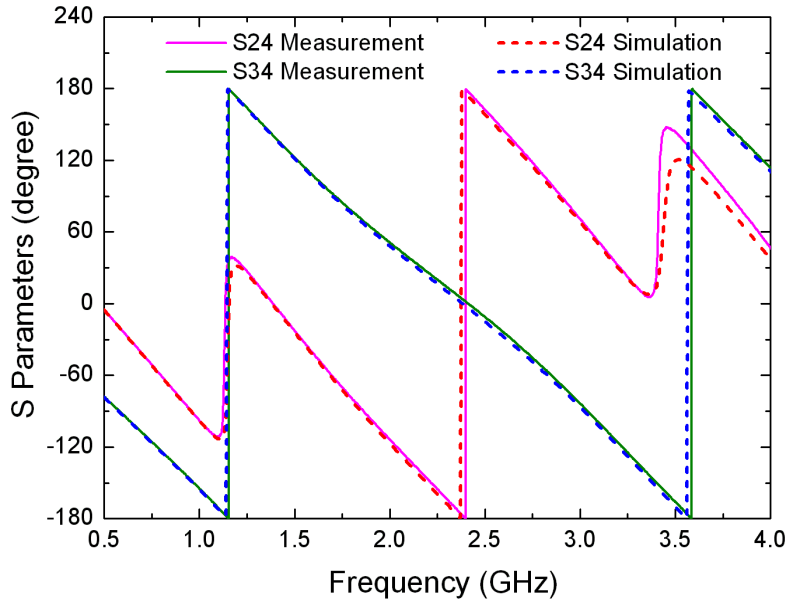

(b) Phase

Figure 80: Comparison of measured (solid) and simulated (dashed) scattering parameters for the miniaturized 180° hybrid coupler under 180° out-of-phase operation with excitation at port 4. (a) Magnitudes of S_{14}, S_{24}, S_{34}, and S_{44}; (b) Phases of S_{24} and S_{34}.

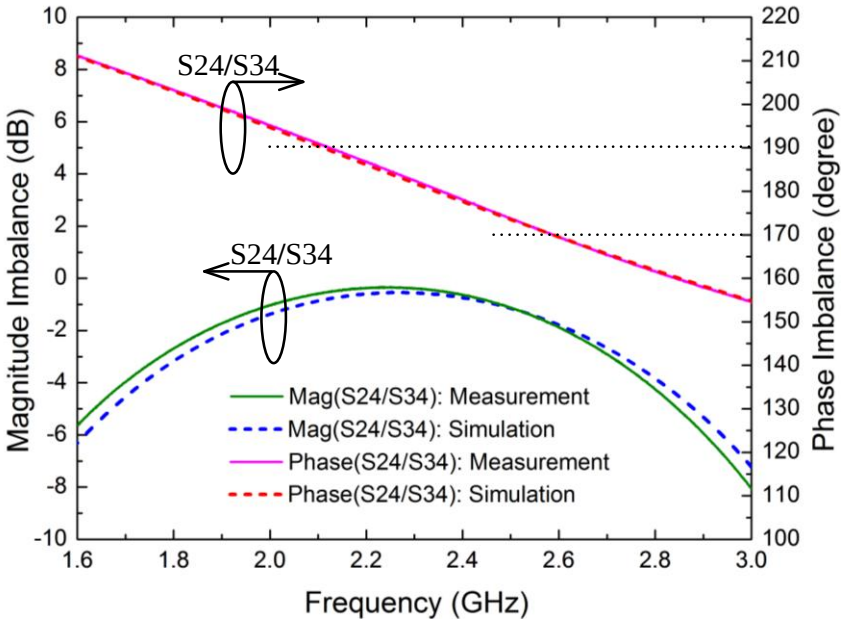

Figure 81: Measured (solid) and simulated (dashed) imbalances of magnitude and phase at hybrid outputs under 180^{o} out-of-phase operation with excitation at port 4.

TABLE XII: PERFORMANCES OF THE MINIATURIZED COUPLED-LINE 180^{O} HYBRID COUPLER.

Operation Mode	In Phase (Bandwidth: GHz)		180^{o} Out of Phase (Bandwidth: GHz)	
	Simulation	Measurement	Simulation	Measurement
Through (-3±1 dB)	1.78~2.83	1.73~2.85	1.82~2.76	1.76~2.75
Coupling (-3±1 dB)	1.98~2.53	1.93~2.53	1.99~2.53	1.94~2.53
Return loss (< -10 dB)	All[a]	All	All	All
Isolation (< -20 dB)	All	All	All	All
Phase balance (±10^{o})	2.11~2.56	2.12~2.56	2.11~2.59	2.12~2.59

[a] 'All' represents the entire frequency range from 0.5 to 4GHz under investigation

Performances are summarized in Table XII for the designed miniaturized coupled-line 180^o hybrid. In the table, words 'All' for return loss and isolation represent the entire frequency range (from 0.5 to 4GHz) under investigation, which shows broadband characteristics of coupled-line circuits. Parameters of return loss, through, coupling, and isolation correspond to (S_{11}, S_{21}, S_{31}, S_{41}) and (S_{44}, S_{34}, S_{24}, S_{14}) for the hybrid coupler under in-phase and 180^o out-of-phase operation modes with excitations at port 1 and port 4, respectively. In turn, when two excitation inputs are simultaneously applied to port 2 and port 3, their sum and difference would be generated at port 1 (Σ) and port 4 (Δ), respectively. Those performances are rather interesting and acceptable for the target 2.4GHz ISM band applications, although the center frequency of operation deviates a little bit to 2.25GHz or so. It could be attributed to practical fabrication tolerances as well as the corresponding adjustments in simulation.

In addition, good agreements are found between simulation and experimental results in Figures 78~81, which also helps to validate the HFSS full-wave simulation. Slight discrepancies between measured and simulated *S*-parameters of return loss and isolation might be due to parasitics associated with SMA connectors soldered on feeding line extensions at board edges for test, while they are not taken into account in simulations.

7.5 Concluding Remarks

A novel concept of miniaturized coupled-line 180^o hybrid coupler has been proposed by evolving from two quarter-wave slow-wave coupled-line sections with a half-wave slow-wave isolated line section in between. Circuit architecture, analysis, and synthesis are provided for the hybrid circuit. Artificial slow-wave coupled and isolated lines are properly designed based on a three-layer inverse mushroom topology. They present significant slow-wave factors with least dispersion and attenuation over a broad frequency range with very high cut-off frequencies. The resulted coupler structure does not demand prohibitively small trace width or spacing, thereby is cost-effective in fabrication.

As a proof-of-concept demonstration, a PCB prototype was fabricated and tested. Measured results show good agreement with simulations. The hybrid coupler performs in-phase or 180^{o} out-of-phase power dividing as well as power combining with sum and difference signals. Good amplitude and phase balances are found at hybrid outputs as well as equal power splitting at the operation frequency of interest. It is demonstrated that the occupied planar area of developed hybrid is reduced over 90%, in contrast to conventional rat-race microstrip ring hybrid on the same substrate, which makes it rather appealing to modern compact wireless systems. It is worthwhile to mention that the design methodology can also be extended to implementations on LTCC or silicon microelectronics.

8 FOLDED ELECTRICALLY SMALL INTEGRATED ANTENNAS

In previous chapters, artificial coupled transmission lines had been well studied, and a few circuit miniaturization examples were developed based on slow-wave coupled lines. Meanwhile, antennas still remain the bottleneck of passive modules miniaturization in compact RF front ends. This chapter presents a folding scheme to address fundamental issues of planar electrically small resonant antennas with small radiation resistance, low radiation efficiency, high *Q* factor, and narrow bandwidth by examining their impedance characteristics. Two printed folded helical antennas are investigated as examples of small antennas for GSM1800/1900 bands. Dramatic bandwidth enhancements of as much as 66% and 163% are found, respectively, for folded helical dipole and its monopole version over their non-folded counterparts. The proposed folding method facilitates the integrated antenna miniaturization with self resonance, sufficient bandwidth, and self impedance matching.

8.1 Introduction

Nowadays, the demand for compact mobile handsets has been ever increasing as more and more functionalities are integrated in a wireless system on a small circuit board. Hence the area reserved for the antenna part is usually much smaller than a wavelength [113]. There have been significant interests and efforts in electrically small antennas (ESA) [114-115]. Fundamental issues of shrinking antenna dimensions are placed on the radiation efficiency, impedance bandwidth, or quality factor *Q* which is limited by the overall antenna volume [116]. In addition to the necessary gain, impedance characteristics also play a key role in its performance.

Common integrated antenna elements are primarily in the forms of dipoles, monopoles, or their variations (e.g. straight or inverted F antenna) printed on dielectric substrate surfaces. Dipole is self-balanced with differential feeding, and majority of currents flow only on the antenna itself along with certain immunity to environmental perturbations. It shows stable performance when approaching to other

objects [117], and is therefore often preferred in some systems, such as for RFID applications. In addition, monopole antenna is actually an asymmetric dipole system [118] with one of its dipole halves replaced by a vicinity partial ground plane to provide current return path. In convention, the ground plane is usually not counted in the monopole antenna area since it is also necessary and shared with other circuits on board. But it does contribute to radiation from the antenna system, and offers an additional degree of freedom to control the radiation resistance and impedance bandwidth (or *Q* factor).

Miniaturized dipoles or monopoles can be implemented by compressing, twisting, or fragmenting (CTF) wire traces in *planar* or *volumetric* configurations on a single- or multi-layer substrate. For example, meandered-line antenna is a typical ESA in two dimensions [119]. Besides, helical antennas are formed by winding wires or traces in three dimensions, and they operate in the normal mode with radiation characteristics similar to those of dipoles/monopoles, as geometry dimensions of helix are much smaller than a wavelength. Normal-mode helical antennas are widely employed as small antennas in many mobile handsets. However, those typical ESAs usually suffer small radiation resistance and high *Q* factor. Folded dipoles had been well known for a long time to step up impedance by about four times [120]. Therefore, folding scheme provides a valuable solution to address aforementioned issues of electrically small dipole antennas or their monopole versions. This methodology had been demonstrated by a vertically two-arm folded meandered-line miniaturized planar dipole on a circuit board [119] and a four-arm folded cylindrical/spherical volumetric helix in air [121]. They are shown in Figure 82 (a) and (b), respectively.

In this Chapter, with the intention to develop integrated ESAs for mobile handsets, we investigate the miniaturized folded helical antennas printed on a circuit board. They are implemented on the common cost-effective FR4 substrate by winding traces on the top and bottom surfaces through vias for inter-layer connections. Miniaturized folded helical dipole and monopole antennas are designed as two examples for GSM1800/1900 frequency bands. Characteristics and performances are illustrated mainly through *Q*-

factor analysis. As a proof-of-concept demonstration, prototypes are fabricated and tested. Good agreements are observed between measured and full-wave simulated results. It shows that both folded helical dipole and monopole antennas are found to have dramatic *Q* reduction and bandwidth enhancement over their non-folded counterparts, along with self impedance tuning.

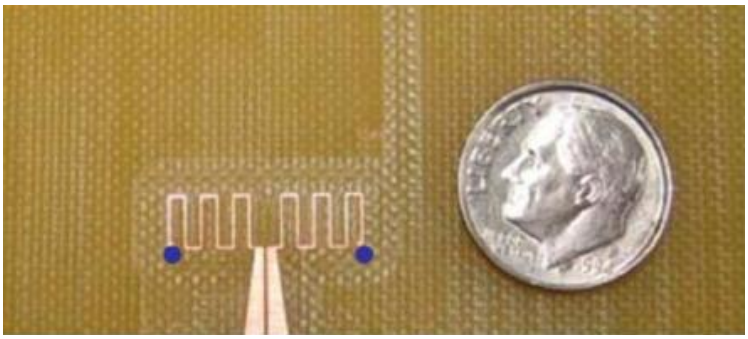

(a) Two-arm folded meandered planar dipole on PCB

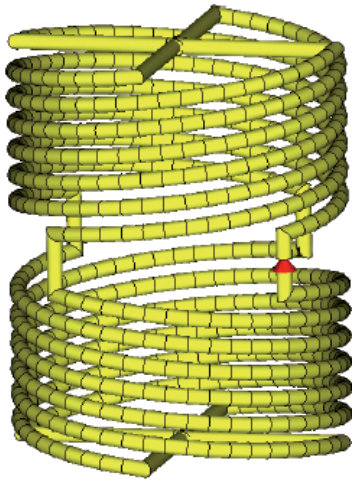

(b) Four-arm folded cylindrical volumetric helix in air

Figure 82: Folded electrically small dipoles. (a) Two-folded meandered planar dipole on PCB; (Source: reference [119] Fig. 2.). (b) Four-folded cylindrical volumetric helix in air. (Source: reference [121] Fig. 5.)

8.2 Theoretical Analyses of Printed ESAs

8.2.1 General Fundamental Issues

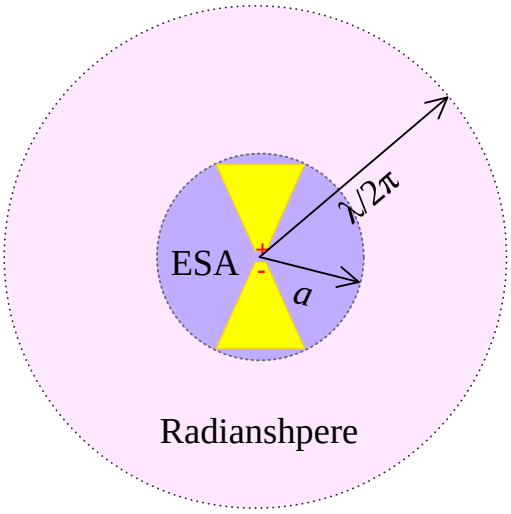

Figure 83: Electrically small antenna in free space.

As shown in Figure 83, an antenna is usually considered electrically small as it can be enclosed within a radian sphere with radius of $\lambda/2\pi$ [122], that is,

$$ka \le \frac{1}{2} \tag{8.1}$$

where $k=2\pi/\lambda$ is the wave number in free space and a is the largest dimension of antenna. In [122], a radiansphere was defined by Wheeler as a boundary to describe that the stored and radiated energies dominate the interior and exterior regions, respectively. Chu [123] derived the minimum radiation quality factor Q of an omni-directional antenna enclosed by a hypothetical sphere of radius a, as indicated by the inner circle in Figure 83. McLean [124] re-examined such limits and improved Chu's

work. It was found that fundamental physics places a strict lower bound on the radiation Q of electrically small antennas [124]

$$Q_{lb} = \eta_r \cdot \left[\frac{1}{(ka)^3} + \frac{1}{ka} \right] \tag{8.2}$$

where $\eta_r = R_{rad}/(R_{rad}+R_{loss})$ is the antenna radiation efficiency with R_{rad} and R_{loss} being the radiation and loss resistances, respectively.

It is known empirically that the bandwidth is inversely proportional to the quality factor. Antennas cannot have a Q smaller than its corresponding lower bound Q_{lb} given by Equation 8.2. Hence the minimum Q limit imposes an upper bound on the achievable impedance bandwidth [116]

$$FBW \approx \frac{s-1}{Q\sqrt{s}} \tag{8.3}$$

where *FBW* is the matched fractional bandwidth (FBW) and *s* denotes the voltage standing wave ratio (VSWR).

It is worthwhile to mention that the matched FBW could be obtained in two cases. Antennas are self-tuned to resonate with input impedance equal to 50 Ω, which is called self impedance matching. It is preferred in most practical applications. Another approach is to design an external lossless *LC* impedance matching network to transform antenna input impedance to 50 Ω. It should be noted that the bandwidth of matching network must be wide enough to cover antenna's intrinsic bandwidth. In addition, a simple way to check the matched FBW is to terminate the antenna with itself input impedance.

However, those fundamental issues were examined in free space or air, but also they are encountered in printed planar ESAs. As the effective antenna length is reduced for radiation, longer traces are necessary to maintain resonance at the design frequency. As a result, small radiation resistance (due to short radiating length), significant ohmic loss (due to long current path), and large stored energy

(confined in complicated structure) would lead to low radiation efficiency η_r and high Q factor as well as narrow bandwidth, as compared to regular straight wire antennas. Furthermore, small resonant resistance also imposes difficulty on impedance matching to standard 50Ω systems.

8.2.2 Q-Factor Calculation

As mentioned above, the Q factor is an important measure to characterize antenna's performances. It can be approximately calculated from the antenna input impedance through the formula [116]

$$Q_z(\omega) = \frac{\omega}{2R(\omega)}\sqrt{\left(\frac{dR(\omega)}{d\omega}\right)^2 + \left(\frac{dX(\omega)}{d\omega} + \frac{|X(\omega)|}{\omega}\right)^2} \tag{8.4}$$

where R and X represent the input resistance and input reactance, respectively, and ω is the angular frequency.

8.2.3 Principles of Folding Scheme

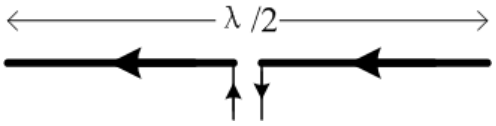

(a) Regular dipole

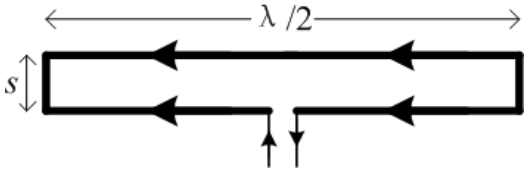

(b) Folded dipole

Figure 84: Straight wire half-wave dipoles. (a) Regular dipole. (b) Folded dipole.

Folded dipole is essentially a two-wire half-wave transmission line resonator which is short circuited at both ends and is fed at the center of one of two wires. It is shown in Figure 84 (b). The basic principle is to bend each dipole half backward to distribute radiating currents on the driven and parasitic arms in phase at resonance. It helps to enhance the radiated power and to improve the *Q* factor, bandwidth, and impedance characteristics. Therefore, folding scheme provides a possible solution to address fundamental issues of printed ESAs in forms of dipole, monopole, or their variations.

The operation of a folded dipole can be decomposed into antenna and transmission-line modes. Its input impedance is given as [120]

$$Z_{in} = \frac{4Z_t Z_d}{Z_t + 2Z_d} \tag{8.5a}$$

where

$$Z_t = j\, Z_c \tan\left(\beta l / 2\right) \tag{8.5b}$$

is the input impedance of half two-wire short-terminated transmission line with characteristic impedance Z_c and phase constant β. Besides, Z_d is the input impedance of regular non-folded dipole shown in Figure 84 (a). When the lines are about half-wavelength long where $Z_t \approx \infty$, the input impedance of folded dipole is stepped up by four times approximately, in contrast to non-folded dipole.

8.3 Miniaturized Printed Folded Helical Dipole

Small integrated antennas are favored in portable wireless systems. A main problem encountered in antenna miniaturization is the lack of effective radiating area, which results in small radiation resistance and high *Q* factor. Normal mode helix antennas are typical ESAs and found useful in many systems. Folding is a proper approach to improve their *Q* and impedance characteristics, which had been well investigated for antennas in free space [114, 121].

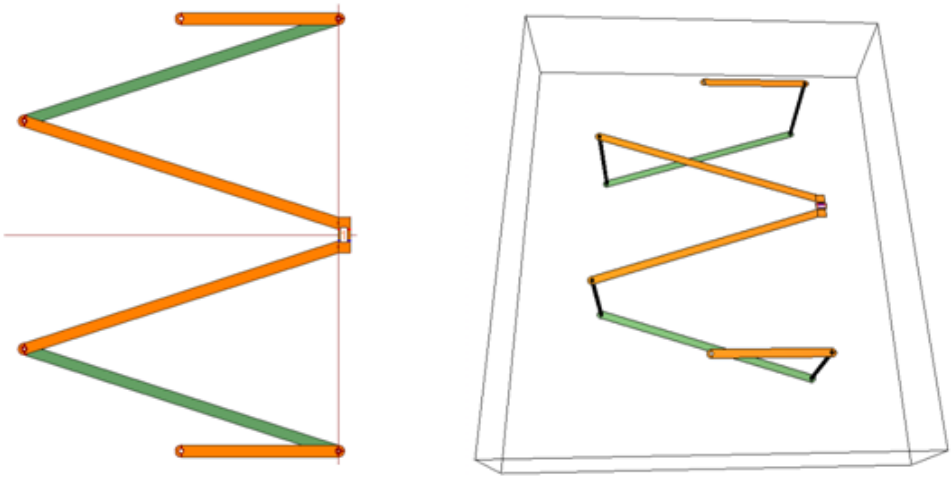

Top view 3D view

(a) Non-folded helical dipole

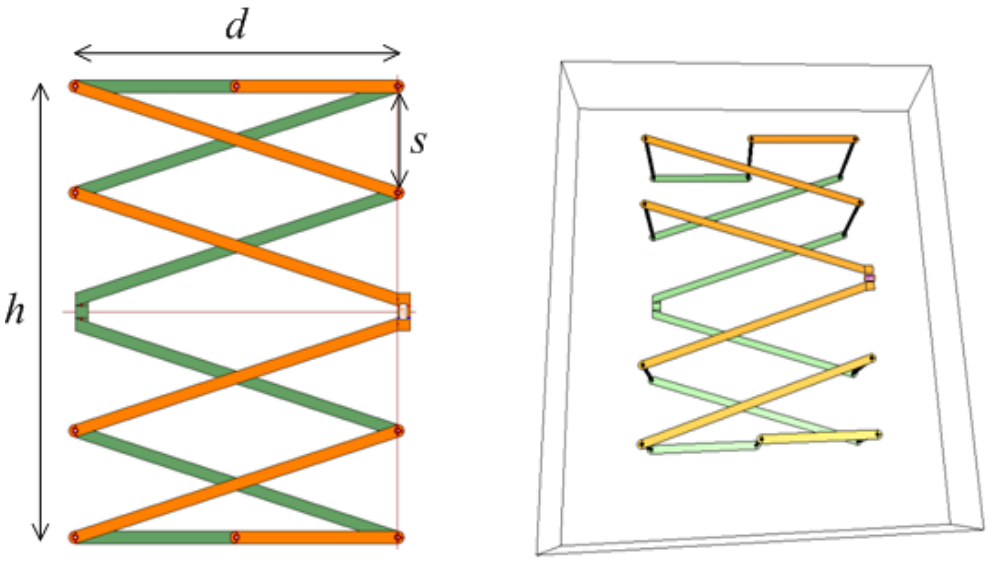

Top view 3D view

(b) Folded helical dipole

Figure 85: Printed helical dipole antennas. (a) Non-folded; (b) Two-folded.

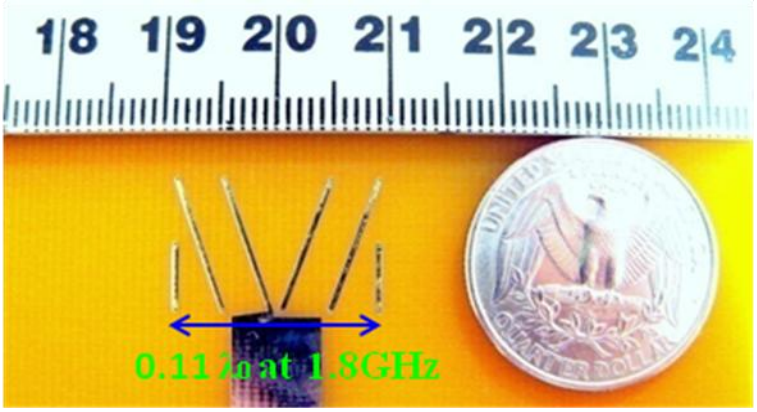

Figure 86: Photograph of the fabricated folded helical dipole.

In this section, an integrated helical dipole is proposed to be folded on a printed circuit board with the feed at the center of the driven arm. Traces are wound on the top (yellow color) and bottom (green) surfaces of a dielectric slab in between vias serve as inter-layer interconnects for each helical arm itself. An extra via is used to provide connections between two arms to form folded version at both ends of the dipole, where the final 1/4 turn is bended inward a little for additional antenna length reduction, as shown in Figure 85.

They are designed on the common FR4 substrate (ε_r=4.2, tanδ=0.02) of 125mil thickness with 0.5oz copper cladding for each metal layer. Trace width is about 0.5mm with very small variations which could be ignored in this case. Through-hole vias comprise 8mil-diameter hole with 6mil-width annular ring. Other geometry parameters are labeled in Figure 85 and their values are designated as s=3.8 mm, d=12.2 mm, and h=18.8 mm. Those parameters of the folded helical dipole are fine tuned for design frequency at GSM1800 MHz by full-wave simulations with Zeland IE3D and Ansys HFSS. A photograph is shown in Figure 86 for the fabricated prototype of a folded helical dipole. The total dipole length h is about only 11.3% of a free-space wavelength at 1.8GHz. Impedance characteristics are provided and shown in Figure 87 for both helical dipole and its folded version from IE3D simulation results.

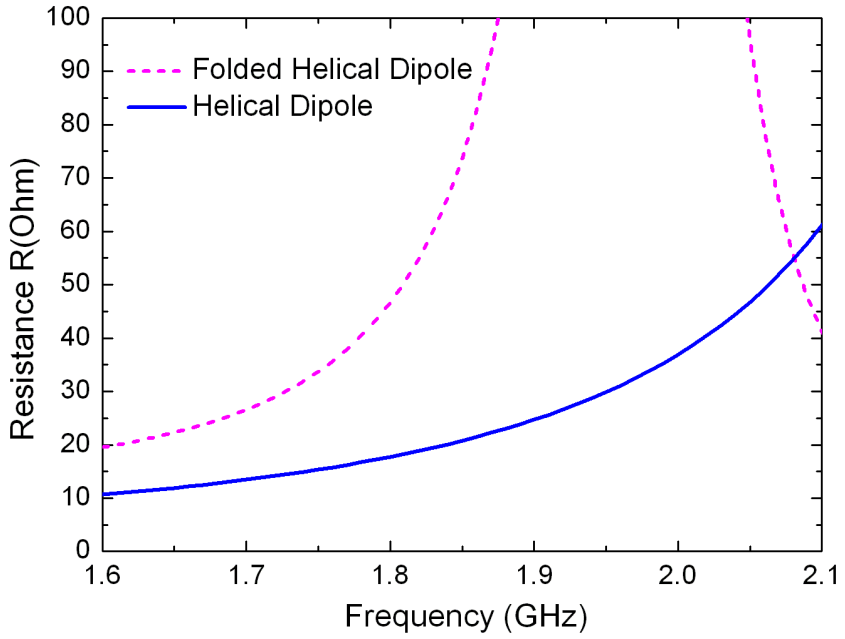

(a) Resistance

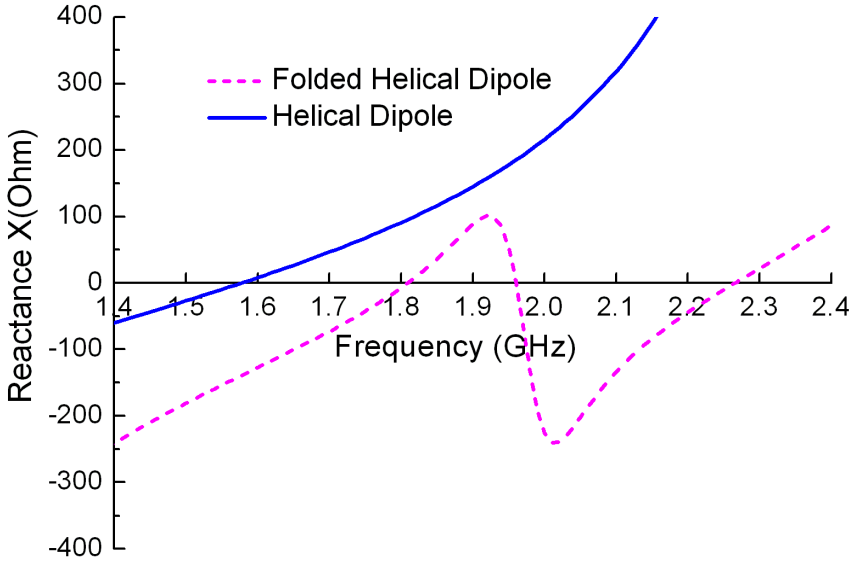

(b) Reactance

Figure 87: Input impedances of helical dipoles.

It is found from Figure 87 that the folded helical dipole resonates at the design frequency while its non-folded counterpart resonates around 1.58GHz, which deviates from the design point significantly. The main reason of this phenomenon is due to the fact that the even-mode phase velocity differs from that of an odd mode in an inhomogeneous dielectric medium, as the folded dipole can be decomposed into antenna (even) and transmission-line (odd) modes. Resonant resistance increases to almost four times as expected. In addition, the radiating currents are observed to add in phase in the driven and parasitic arms to increase the radiated power by a factor of 4 as compared to a regular $\lambda/2$ non-folded dipole. They are illustrated in Figure 88 based on IE3D simulation.

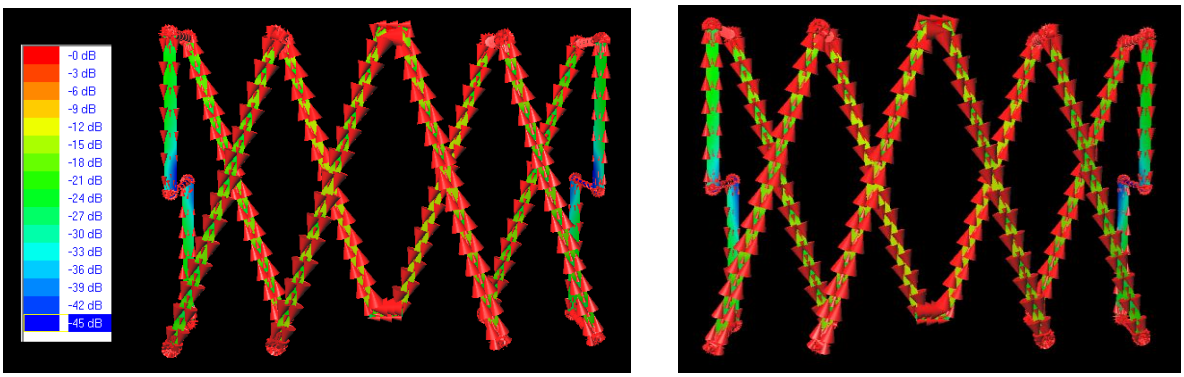

Figure 88: Current distributions of folded helical dipole at 1.81 GHz.

Figure 89 shows the *Q* factors of both folded and non-folded helical dipoles based on the impedance results in Figure 87. It presents a clear advantage of folded helical dipole to have about 40% *Q* reduction from 27.2 to 16.3 around design frequency, corresponding to 66% bandwidth enhancement over the non-folded counterpart, as indicated by Equation 8.3.

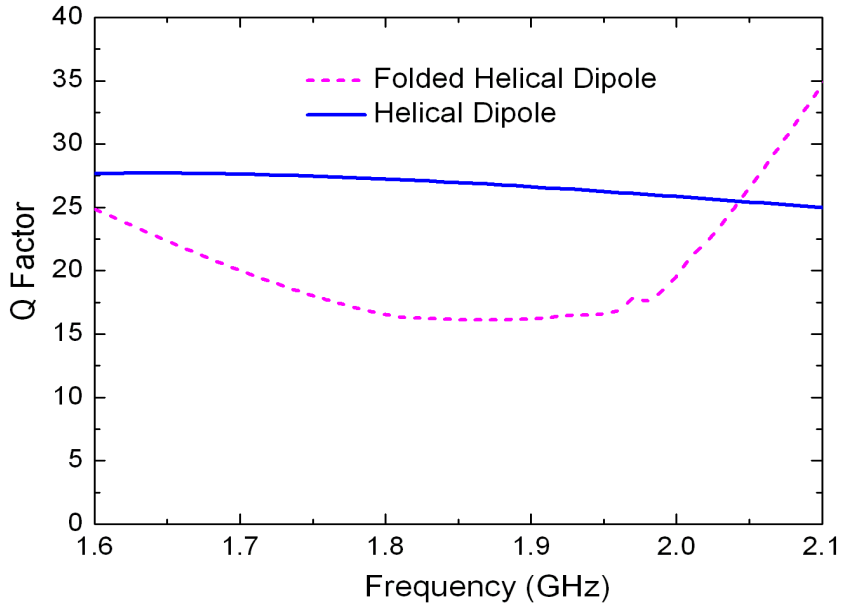

Figure 89: *Q* factors of helical dipole antennas.

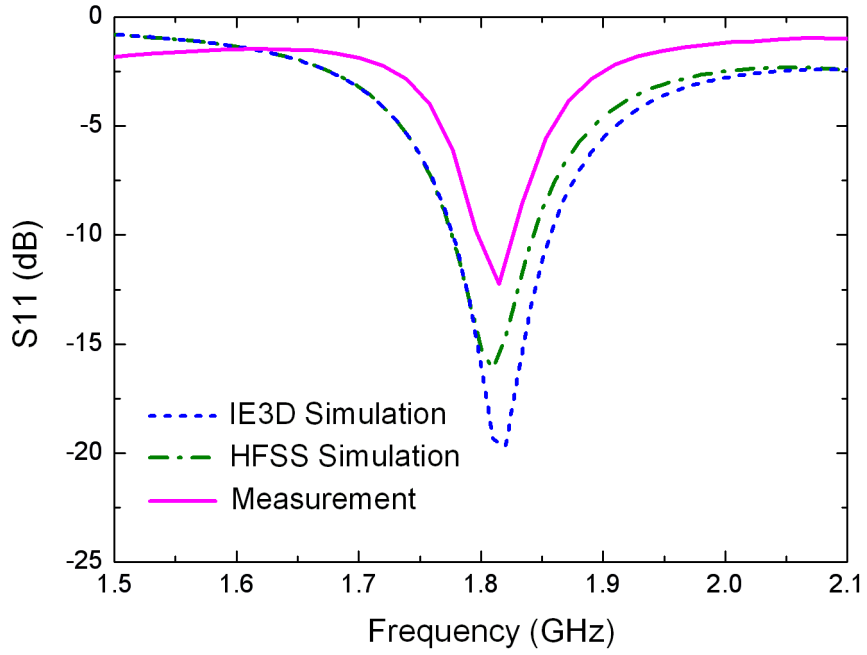

Figure 90: Return loss of the folded helical dipole antenna with feeding lines.

As for regular ESAs, the radiation resistance is very small and usually on the order of several ohms. It imposes certain difficulty on impedance matching to the nominal characteristic impedance of 50ohms. Folded dipoles intend to step up impedance by a factor of 4, and are expected to mitigate the above issue. Figure 90 presents the return loss of the designed folded helical dipole antenna, including broadside feeding lines. The folded helical dipole works as an integrated electrically small antenna to have impedance matching in band of interest.

8.4 Miniaturized Printed Folded Helical Monopole

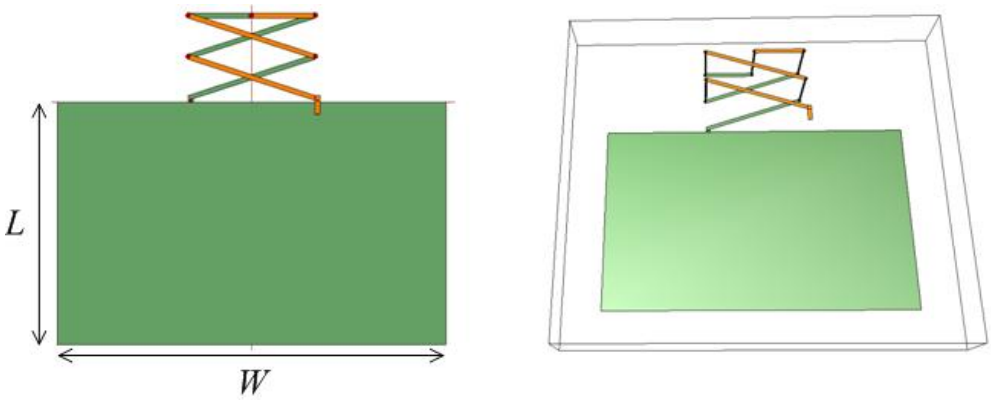

(a) Top view (b) 3D view

Figure 91: Printed folded helical monopole antenna.

It is well known that part of metal ground plane can be removed right underneath the antenna on the back side to broaden the bandwidth for monopoles. This truncated ground plane and monopole itself actually form an asymmetric dipole system [118]. In this section, a miniaturized folded helical monopole is evolved from the small folded helical dipole in Section 8.3 by replacing the dipole halves of driven and parasitic arms on one side with a partial ground plane on the bottom. The parasitic arm is connected back

to the bottom truncated ground plane. It is shown in Figure 91. The helical monopole part is exactly the same as its dipole counterpart in Section 8.3, except *W*=4cm and *L*=2.5cm for ground dimensions here. Hence the monopole length is about only 5.6% of a free-space wavelength at 1.8GHz. A photograph is shown in Figure 92 for the fabricated prototype of folded helical monopole.

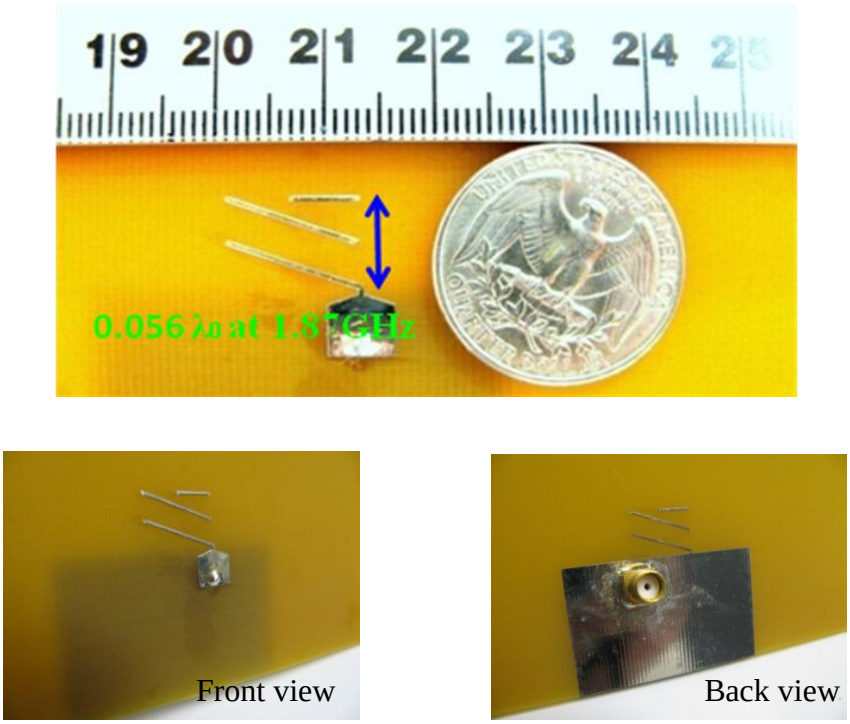

Figure 92: Photograph of the fabricated folded helical monopole.

Similar to a folded dipole, radiating currents add up in phase on driven and parasitic monopole arms as its length is ideally quarter guided wavelength. This mechanism improves the *Q* and impedance characteristics of antenna. *Q* factors can also be obtained from input impedances of helical monopoles by IE3D simulations. They are shown in Figure 93 for both folded and non-folded helical monopoles.

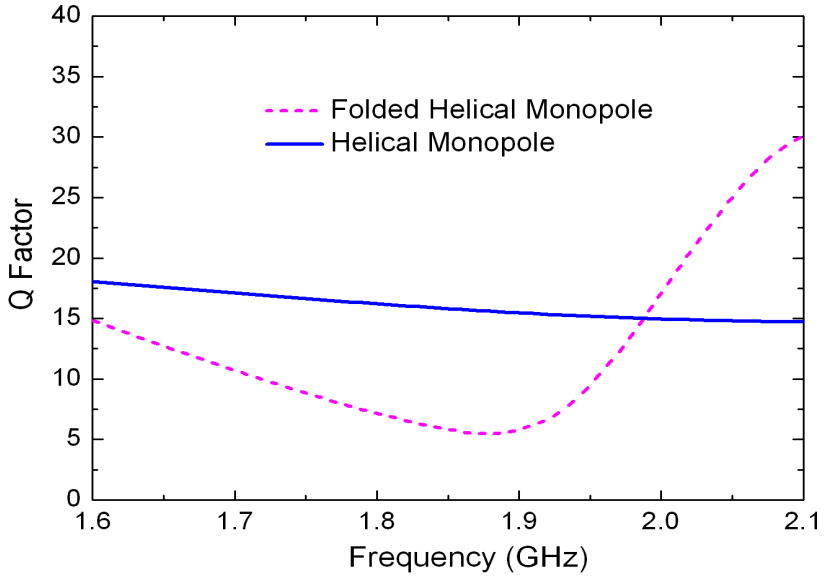

Figure 93: *Q* factors of helical monopole antennas.

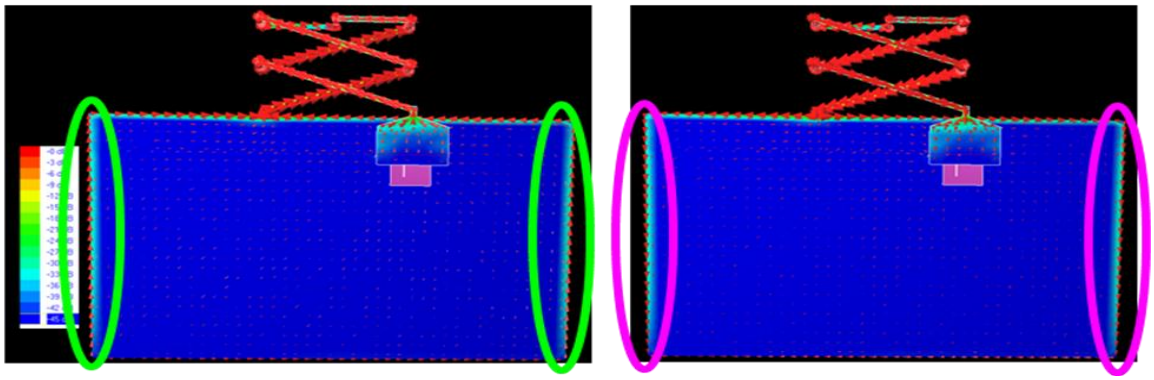

Figure 94: Current distributions on the monopole arms and ground plane.

Obiviously, as the helical monopole is folded, its *Q* value decreases from 15.9 to 6.1 with about 62% reduction, corresponding to about 163% bandwidth enhancement. Interestingly, it is observed that *Q* values of helical monopole and its folded version are, respectively, lower than those of their dipole

counterparts in the frequency range of interest (1700~2000MHz). The primary reason for monopoles' low *Q* feature is the radiation contributed from the truncated partial ground plane where significant current densities are found on ground edges, as shown in Figure 94. In turn, the partial ground plane could also be employed to control the *Q* and impedance charateristics for bandwidth enhancement and impedance matching. Good performance is obtained when the ground plane is tuned to have dimensions *W*=4cm and *L*=2.5cm. Return loss of the designed folded helical monopole antenna is illustrated in Figure 95, including feeding effects for both simulations and measurement.

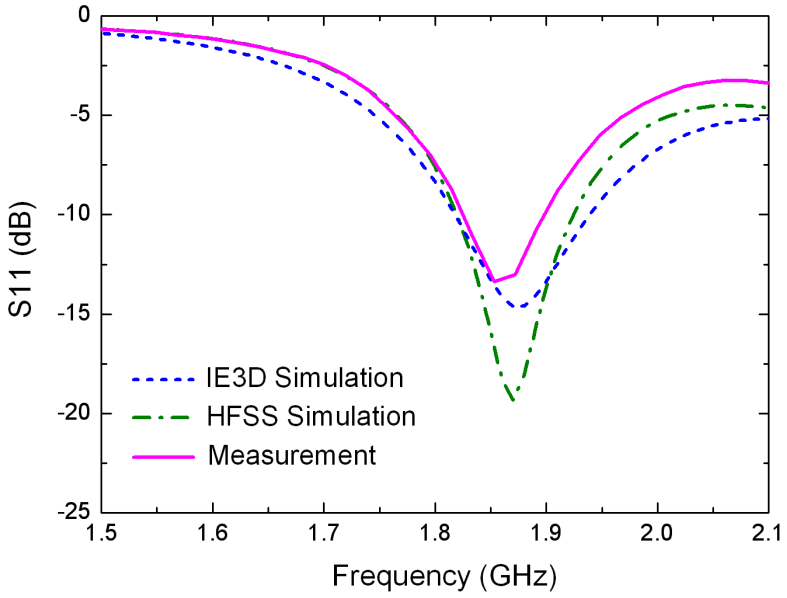

Figure 95: Return loss of the folded helical monopole antenna with feeding.

8.5 Concluding Remarks

It had been known for many decades that radiation resistance and *Q* factor are normally poor for electrically small antennas (ESA) as their effective radiating dimensions shrink downwards much smaller

than a wavelength. Folded antenna gains its renewed interest recently to address fundamental issues of ESAs. With a small spacing between driven and parasitic arms, radiating currents add up in phase on two arms to radiate more power. Therefore, folded ESAs become candidates for efficient radiators.

Normal-mode helixes are well-known small antennas and are employed in many portable wireless systems. Low-profile printed helical antennas are much favored as they could be integrated on the circuit board directly. This chapter investigates the characteristics (mainly through *Q* factor) of folded printed helical dipole as well as its monopole version. *Q*-factor reductions of about 40% and 62%, corresponding to dramatic bandwidth enhancements of as much as 66% and 163% were found, respectively, for folded helical dipole and folded helical monopole over their non-folded counterparts. Both integrated folded helical ESAs achieve good self impedance matching in bands of interest to standard 50Ω systems without external matching circuits.

9 CONCLUSIONS AND FUTURE WORK

In this chapter, a brief summary and main conclusions of this thesis study, featuring miniaturized RF/microwave passive circuits and antennas, are drawn based upon the author's Ph.D. research work that were presented in previous chapters. Furthermore, some interesting topics will be recommended and discussed for future potential investigations.

9.1 Summary and Conclusions

In this dissertation, novel practical RF/microwave slow-wave coupled-line circuits and antennas for compact wireless communication systems have been proposed, analyzed, designed, implemented, and demonstrated. Generally, artificial periodic *coupled* transmission lines can be divided into two types: right-handed and left-handed cases. In tradition, the former is usually referred to as electromagnetic band-gap (EBG) structure, while the latter falls into the category of metamaterial.

In details, intensive theoretical investigations were performed in chapter 3 for both right-handed and left-handed symmetric artificial coupled transmission lines based on their equivalent ideal circuit models. Dispersion characteristics (e.g. propagation constants and characteristic impedances) are examined, under both even- and odd-mode excitations, over the entire frequency range covering both pass band and stop band. In particular, modal phase-velocity equalization (*MPE*) and mode-selection characteristics (*MSC*) are highlighted in pass bands, respectively, for the right-handed and left-handed cases. It is found that positive inductive coupling is necessary for equal even- and odd-mode phase velocities over a broad frequency range in pass band for right-handed coupled lines, whereas equal modal phase velocities might only exist at a single frequency point in the pass band for left-handed coupled lines.

The complete theory offers a solid understanding to operations of artificial coupled transmission lines. However, due to the trend of rapid R&D processes in industry, simplified instructions can help

provide much direct design insights into circuit synthesis of artificial coupled lines with certain characteristics. Hence design criteria and their supplemental trade-offs were developed and illustrated in sections 4.2 and 5.2.1, respectively, for right-handed slow-wave coupled lines which could find extensive practical applications for low dispersion. They are discussed primarily through guided-wave characteristics, including propagation constants, line impedances, slow-wave factors, and cutoff frequencies, under even- and odd-mode excitations. In general, self inductance and capacitance contribute mainly to slow-wave effects and characteristic impedances, while mutual inductance and coupling capacitance can be utilized to alter dispersion characteristics to yield both equal modal phase velocities and substantial coupling level.

Subsequently, design guidelines were given for physical layout realization of slow-wave coupled lines with periodic inductive and/or capacitive loadings by using engineered artificial metallization. Compressed, twisted, or fragmented (CTF) metal strips are spread out three-dimensionally (3D) into a multilayer dielectric substrate. Those high-density distributed metallic elements can help to enrich inductive and capacitive effects within a small unit cell. It gives rise to slow-wave effects and desired impedances of each line. Meanwhile, particular attention must be directed to synthesizing proper coupling capacitance and inductance to have certain balanced electric and magnetic couplings.

With the tools of commercial full-wave electromagnetic solvers, various dimensions of physical layouts can be fine tuned for proper performances. A slow-wave structure of right-handed coupled lines was proposed in chapter 4 by using spiral-type inter-wound planar coupled inductors on the common FR4 substrate. It presents large slow-wave factors of about 8, cut-off frequencies of around 3.5 GHz, equal even- and odd-mode phase velocities, as well as similar coupling level of conventional coupled microstrip lines. As a result, a directional coupler is developed at 2.4 GHz as an application example with both dramatic 80% size reduction and comparable performances of the normal microstrip counterpart.

Furthermore, the coupling level of coupled transmission lines plays an important role in circuit applications. Accordingly, by employing a novel coupling mechanism that enhances the magnetic coupling significantly, a new slow-wave coupled line structure was investigated in chapter 5 based on three-layer *inverse mushroom* topology on the microwave substrate of Rogers RO4003C. Parallel metal strips are interleaved periodically on upper two different layers through high density of interconnecting vias, resembling fence walls in substrate integrated waveguides (SIW), to form 3D-folded coupled inductors. A series of full-wave parametric studies were conducted to determine geometry dimensions for desired characteristics. It is observed that symmetry of this structure is guaranteed very well both physically and electrically. It gains least dispersion, loss, proper line impedances, and equal modal phase velocities over a very broad frequency region of interest with both even- and odd-mode cutoff frequencies up to 17 GHz. In contrast to conventional microstrip counterpart on the same substrate, this new coupled-line structure has only half width but presents slow-wave factors of about 5.3 along with 3-4dB coupling enhancement. Consequently, many novel high-performance compact coupled-line circuits could be evolved from such intriguing structure. To demonstrate its circuit applications, a miniaturized directional coupler and two low-order coupled-line band-pass filters (BPF) in both regular and folded configurations were designed and implemented in chapter 5 as well.

It is well known that Marchand baluns are capable of performing the signal transformation from unbalanced to balanced modes, or vice versa, which involve differential operations favored for noise suppression. The detailed analysis, synthesis, and design procedures were illustrated in chapter 6. Its performances, in terms of bandwidth, amplitude/phase imbalances, and impedance transformation ratio, depend on the coupling level and directivity of each constituent directional coupler. A miniaturized impedance-transforming planar Marchand balun was developed there by using two quarter-wave sections of the slow-wave coupling-enhanced coupled lines which had been proposed in

chapter 5. The planar dimensions of balun are only 16.1mm by 1.6mm in total, or equivalently $0.1288\lambda_0$ by $0.0128\lambda_0$ at 2.4GHz (λ_0: free-space wavelength), with area reduction of over 80%. It gains an impedance transformation ratio of 1:3 from source to load impedances (Z_s=50Ω and Z_L=150Ω). The 10dB return loss (RL) bandwidth (BW) ranges from 1.64 to 2.98 GHz with a fractional bandwidth (FBW) of 58% and maximum RL of 46.1 dB. The in-band phase balance is achieved well from 180^o+3.7^o to 180^o+4.9^o and amplitude imbalance is less than 1dB.

In addition, a novel coupled-line 180^o hybrid coupler was introduced in chapter 7 based upon the mechanism of electromagnetic couplings, which is fundamentally different from conventional rat-race 180^o ring hybrid. The circuit architecture, analysis, synthesis, and design curves were elaborated to investigate the characteristics of hybrid coupler. A miniaturized coupled-line 180^o hybrid was evolved from slow-wave structures of two λ/4 coupling-enhanced coupled line sections and one λ/2 phase-shifting uncoupled line section in between through an innovative construction. As well, the 50Ω slow-wave isolated line presents a significant slow-wave factor of about 4.5 with least dispersion and attenuation over a broad frequency range with cutoff frequency up to 13 GHz. The finished hybrid coupler only occupies a very compact area of 9.5mm by 9.5mm (equivalently $0.076\lambda_0$ by $0.076\lambda_0$ at 2.4GHz) with over 90% planar area saving, in contrast to microstrip ring hybrid on the same substrate. It shows wide-band performances in terms of both return loss (< -10dB) and isolation (< -20dB) over the entire frequency range under investigation (from 0.5 to 4GHz). For both in-phase and 180^o out-of-phase operations, phase imbalances of less than 10^o is achieved from 2.12 to 2.56 GHz, and amplitude balances of -3dB ± 1dB are obtained from 1.94 to 2.53 GHz and 1.76 to 2.75 GHz at coupled and through outputs, respectively.

Finally, antennas still remain the bottleneck of passive modules miniaturization in compact RF front ends. Fundamental issues of shrinking antenna dimensions involve small radiation resistance, low radiation efficiency, high *Q* factor, and narrow bandwidth. Interestingly, the folding scheme is

found to provide a valuable solution. In chapter 8, miniaturized printed folded helical dipole and monopole antennas at GSM1800/1900 bands were investigated as two examples of electrically small antennas (ESA) with self resonance, sufficient bandwidth, and self impedance matching. They were designed on the common double-layer FR4 substrate by winding traces on the top and bottom surfaces through vias for inter-layer connections. *Q*-factor reductions of about 40% and 62%, corresponding to dramatic bandwidth enhancements of as much as 66% and 163% were observed, respectively, for folded helical dipole and folded helical monopole over their non-folded counterparts. The finished antenna sizes are about only $0.113\lambda_0$ and $0.056\lambda_0$ at 1.8 GHz for folded helical dipole and monopole, respectively.

In this thesis work, layout masks are implemented on conventional printed circuit boards (PCB) without stringent requirements for purpose of proof-of-concept demonstrations at low cost. Actual circuit prototypes were then fabricated and tested. Good agreements are found between measured and simulated results. As a result, the theoretical analyses and design criteria have been validated by full-wave EM simulations which are further verified by experiments.

9.2 Recommendations for Future Work

The comprehensive theory, design guidelines, and synthesis procedures have laid the groundwork for a good understanding of artificial coupled transmission lines. Consequently, a few typical examples of high-performance miniaturized coupled line circuits and antennas have been developed and demonstrated in this dissertation. However, there still exist certain room of natural extensions and improvements that would help strengthen this work for perfection, which could be a never-ending process. In this section, some interesting projects are hence suggested for future explorations in RF passive circuits and antennas.

1. Performance enhancements are often favored and pursued in modern wireless systems, but they are limited by manufacture constraints of standard PCB process. The proposed theory and

design methodology can also be applied to circuit implementations on low temperature co-fired ceramic (LTCC), silicon IC microelectronics, RF MEMS, or other advanced technologies. Multi-layer fabrication processes with fine line/spacing resolutions can facilitate more-compact circuits with better performances. In addition, the cutoff frequency of artificial transmission lines could be further pushed upwards for circuit applications at very high frequency bands, such as the emerging 60GHz WiGig band.

2. New artificial right-handed coupled line structures can be designed for certain purposes, e.g. slow-wave effects, more coupling enhancement, equal or different modal phase velocities, by using regular/advanced processes or with ground plane perturbations [70]. For instance, the feature of different even- and odd-mode phase velocities could be utilized to develop coupled-line quadrature hybrid couplers [42].
3. Variations can be made to existing circuit designs that have been presented in this thesis. For example, Marchand balun gains different impedance transformation ratio from source to load impedances, such as 1:1, which requires that the constituent couple lines have a coupling factor C_v= -4.77dB and even/odd-mode impedances of Z_e=96.5Ω and Z_o=25.9Ω in a 50Ω system. In addition, coupled line 180^o hybrid couplers are also possible for different power splitting ratio (*PSR*) between '*Through*' and '*Coupled*' outputs. *PSR*=1:2 would require the coupled lines of C_v= -12.5dB, Z_e=63.6Ω, and Z_o=39.3Ω, which could be realized by conventional uniform microstrip coupled lines on common PCB.
4. Other novel circuit applications can be developed by using artificial right-handed coupled transmission lines, e.g. hairpin filter [70] and single-band [37] or dual-band [38] coupled line Wilkinson power divider/combiner.
5. A complete theoretical analysis has been performed in section 3.3 on metamaterial (left-hand) coupled transmission lines, which provides a solid foundation for future work on developing

novel left-handed coupled line structures. Mode-selection characteristics (MSC) can be utilized to behave as a RF mode choker to generate either purely common mode signal or purely differential mode signal. The latter could be used to reduce EM emissions to suppress RF interferences for low noise circuits. In addition, both fast-wave and slow-wave regions are observed in left-handed coupled lines, which can be employed for antenna leak-wave radiation [55] and miniaturized coupled line circuits, respectively.

CITED LITERATURE

[1] G. V. Eleftheriades and R. Islam, "Miniaturized microwave components and antennas using negative-refractive-index transmission-line (NRI-TL) metamaterials," *Metamaterials*, vol. 1, pp. 53-61, 2007.

[2] C. Zhou and H. Y. D. Yang, "The Design of Miniaturized Printed Wire Antennas Using Double-Layer Periodic Metallization," *Antennas and Wireless Propagation Letters, IEEE*, vol. 6, pp. 11-14, 2007.

[3] Z. Chengzhi and H. Y. D. Yang, "Design Considerations of Miniaturized Least Dispersive Periodic Slow-Wave Structures," *Microwave Theory and Techniques, IEEE Transactions on*, vol. 56, pp. 467-474, 2008.

[4] Z. Yanyan and H. Y. D. Yang, "Ultra slow-wave periodic transmission line using 3D substrate metallization," *in Microwave Symposium Digest, 2008 IEEE MTT-S International*, 2008, pp. 891-894.

[5] P. V. Bijumon, et al., "High dielectric constant low loss microwave dielectric ceramics in the Ca5Nb2-xTaxTiO12 system," *Materials Letters*, vol. 57, pp. 1380-1384, 2003.

[6] D. J. Masse, et al., "A new low-loss high-k temperature-compensated dielectric for microwave applications," *Proceedings of the IEEE*, vol. 59, pp. 1628-1629, 1971.

[7] R. J. Cava, "Dielectric materials for applications in microwave communications," *Journal of Materials Chemistry*, vol. 11, pp. 54-62, 2001.

[8] R. K. Hoffmann, "*Handbook of microwave integrated circuits*," 1987.

[9] T. Nakatsuka, et al., "A highly miniaturized receiver front-end hybrid IC using on-chip high-dielectric constant capacitors for mobile communication equipment," in *Microwave and Millimeter-Wave Monolithic Circuits Symposium, 1995. Digest of Papers., IEEE 1995*, 1995, pp. 85-88.

[10] H. Matsumoto, et al., "A miniaturized dielectric monoblock duplexer matched by the buried impedance transforming circuit," in *Microwave Symposium Digest, 1995., IEEE MTT-S International*, 1995, pp. 1539-1542 vol.3.

[11] S. J. Fiedziuszko, et al., "Dielectric materials, devices, and circuits," *Microwave Theory and Techniques, IEEE Transactions on*, vol. 50, pp. 706-720, 2002.

[12] Y. P. Zhang, et al., "A dielectric-loaded miniature antenna for microcellular and personal communications," in *Antennas and Propagation Society International Symposium, 1995. AP-S. Digest, 1995*, pp. 1152-1155 vol.2.

[13] H. Jantunen, et al., "Design aspects of microwave components with LTCC technique," *Journal of the European Ceramic Society*, vol. 23, pp. 2541-2548, 2003.

CITED LITERATURE (Continued)

[14] A. E. Fathy, "Low Temperature Co-fired Ceramic (LTCC) Technology for RF Multi-layer Circuit Applications-Technology and Modeling."

[15] A. J. Piloto and K. America, "Integrated Passive Components: A Brief Overview of LTCC Surface Mount & Integral Options," *ADVANCING MICROELECTRONICS*, vol. 26, pp. 24-28, 1999.

[16] M. Nguyen, "Multilayer Design Techniques for Extremely Miniaturized CMOS Microwave and Millimeter-Wave Distributed Passive Circuits," *IEEE Transactions on Microwave Theory and Techniques*, vol. 54, pp.4218-4224, 2006.

[17] L. Yo-Shen, et al., "Design of an LTCC tri-band transceiver module for GPRS mobile applications," *Microwave Theory and Techniques, IEEE Transactions on*, vol. 52, pp. 2718-2724, 2004.

[18] C. Chih-Chiang and C. K. C. Tzuang, "Synthetic quasi-TEM meandered transmission lines for compacted microwave integrated circuits," *Microwave Theory and Techniques, IEEE Transactions on*, vol. 52, pp. 1637-1647, 2004.

[19] C. Meng-Ju, et al., "A CMOS 3-dB directional coupler using edge-coupled meandered synthetic transmission lines," in *Microwave Symposium Digest, 2008 IEEE MTT-S International*, 2008, pp. 771-774.

[20] M. Esa, et al., "Miniaturized Microwave Meander Coupled-Line Two-Way Wilkinson Power Divider."

[21] H. Chen and Y. Zhang, "A novel compact planar six-way power divider using folded and hybrid-expanded coupled lines," *Progress In Electromagnetics Research*, vol. 76, pp. 243-252, 2007.

[22] S. M. Wang, et al., "A study of meandered microstrip coupler with high directivity," 2003, pp. 63-68.

[23] J. M. Gonzalez-Arbesu, et al., "Are space-filling curves efficient small antennas," *Antennas and Wireless Propagation Letters, IEEE*, vol. 2, pp. 147-150, 2003.

[24] E. E. Altshuler, "Electrically small self-resonant wire antennas optimized using a genetic algorithm," *Antennas and Propagation, IEEE Transactions on*, vol. 50, pp. 297-300, 2002.

[25] C. Hosung, et al., "Design of electrically small wire antennas using a pareto genetic algorithm," *Antennas and Propagation, IEEE Transactions on*, vol. 53, pp. 1038-1046, 2005.

[26] Z. Yanyan and H. Y. D. Yang, "A miniaturized printed wire antenna utilizing 3D substrate metallization for wireless communications," in *Antennas and Propagation Society International Symposium, 2008. AP-S 2008. IEEE*, 2008, pp. 1-4.

CITED LITERATURE (Continued)

[27] Y. Ishikawa, et al., "A miniaturized low-spurious 1.9 GHz MSW band-pass filter using YIG resonators with multi metal rings," in *Microwave Symposium Digest, 1992., IEEE MTT-S International*, 1992, pp. 1403-1406 vol.3.

[28] H. Ogawa and T. Itoh, "Slow-Wave Characteristics of Ferromagnetic Semiconductor Microstrip Line," *Microwave Theory and Techniques, IEEE Transactions on*, vol. 34, pp. 1478-1482, 1986.

[29] R. Mongia, et al., *RF and microwave coupled-line circuits*: Artech House Norwood, MA, 1999.

[30] A. Eroglu and L. Jay Kyoon, "The Complete Design of Microstrip Directional Couplers Using the Synthesis Technique," *Instrumentation and Measurement, IEEE Transactions on*, vol. 57, pp. 2756-2761, 2008.

[31] A. Podell, "A high directivity microstrip coupler technique," 1970, pp. 33-36.

[32] S. L. March, "Phase Velocity Compensation in Parallel-Coupled Microstrip," in *Microwave Symposium Digest, MTT-S International*, 1982, pp. 410-412.

[33] R. Phromloungsri and M. Chongcheawchamnan, "A high directivity coupler design using an inductive compensation technique," in *Microwave Conference Proceedings, 2005. APMC 2005. Asia-Pacific Conference Proceedings*, 2005, p. 4 pp.

[34] L. Li, et al., "Slow-Wave Line Coupler With Interdigital Capacitor Loading," *IEEE Transactions on Microwave Theory and Techniques*, vol. 55, pp. 2427-2433, 2007.

[35] N. Marchand, "Transmission line conversion transformers," *Electronics*, vol. 17, pp. 142-145, 1944.

[36] M. Shimozawa, et al., "A parallel connected Marchand balun using spiral shaped equal length coupled lines," in *Microwave Symposium Digest, 1999 IEEE MTT-S International*, 1999, pp. 1737-1740 vol.4.

[37] T. Xinyi and K. Mouthaan, "Analysis and design of compact two-way Wilkinson power dividers using coupled lines," in *Microwave Conference, 2009. APMC 2009. Asia Pacific*, 2009, pp. 1319-1322.

[38] P. Myun-Joo, "Two-Section Cascaded Coupled Line Wilkinson Power Divider for Dual-Band Applications," *Microwave and Wireless Components Letters, IEEE*, vol. 19, pp. 188-190, 2009.

[39] C. Jui-Chieh, et al., "A Novel Planar Three-Way Power Divider," *Microwave and Wireless Components Letters, IEEE*, vol. 16, pp. 449-451, 2006.

CITED LITERATURE (Continued)

[40] M. J. Park and B. Lee, "Coupled-line 180o hybrid coupler," *Microwave and Optical Technology Letters*, vol. 45, pp. 173-176, 2005.

[41] V. Napijalo and B. Kearns, "Multilayer 180o Coupled Line Hybrid Coupler," *Microwave Theory and Techniques, IEEE Transactions on*, vol. 56, pp. 2525-2535, 2008.

[42] Z. L. Weikle and Rm, II, "A compact quadrature coupler based on coupled artificial transmission lines," *IEEE Microwave and Wireless Components Letters*, vol. 15, pp. 889-891, 2005.

[43] J. L. Allen, "Inhomogeneous Coupled-Line Filters with Large Mode-Velocity Ratios," *Microwave Theory and Techniques, IEEE Transactions on*, vol. 22, pp. 1182-1186, 1974.

[44] J. L. Allen, "Multi-Section Inhomogeneous Coupled-Line Filters with Large Mode-Velocity Ratios," in *Microwave Symposium Digest, MTT-S International*, 1975, pp. 113-115.

[45] C. C. Chen, et al., "A fully planar microstrip coupled-line coupler with a high coupling level," *Microwave and Optical Technology Letters*, vol. 46, pp. 170-171, 2005.

[46] G. Prigent, et al., "A design method for improvement of λg/4 coupled-line narrow bandpass filter response," *Microwave and Optical Technology Letters*, vol. 39, pp. 121-125, 2003.

[47] E. M. T. Jones, "Coupled-strip-transmission-line filters and directional couplers," *Microwave Theory and Techniques, IRE Transactions on*, vol. 4, pp. 75-81, 1956.

[48] S. E. Melais, et al., "A low-profile broadband strip-line balun," 2005.

[49] J. F. Mao, et al., "Synthesis of coupled transmission lines," *IEEE Transactions on Circuits and Systems I: Fundamental Theory and Applications*, vol. 44, pp. 327-337, 1997.

[50] A. Lai, et al., "Composite right/left-handed transmission line metamaterials," *Microwave Magazine, IEEE*, vol. 5, pp. 34-50, 2004.

[51] C. Caloz, "Dual Composite Right/Left-Handed (D-CRLH) Transmission Line Metamaterial," *Microwave and Wireless Components Letters, IEEE*, vol. 16, pp. 585-587, 2006.

[52] G. Siso, et al., "Generalized Model for Multiband Metamaterial Transmission Lines," *Microwave and Wireless Components Letters, IEEE*, vol. 18, pp. 728-730, 2008.

[53] W. Shu-Jung, et al., "A Novel Wideband Common-Mode Suppression Filter for Gigahertz Differential Signals Using Coupled Patterned Ground Structure," *Microwave Theory and Techniques, IEEE Transactions on*, vol. 57, pp. 848-855, 2009.

CITED LITERATURE (Continued)

[54] M. R. Hashemi and T. Itoh, "Dual-mode leaky-wave excitation in symmetric composite right/left-handed structure with center vias," in *Microwave Symposium Digest (MTT), 2010 IEEE MTT-S International*, 2010, pp. 9-12.

[55] M. R. M. Hashemi and T. Itoh, "Coupled Composite Right/Left-Handed Leaky-Wave Transmission Lines Based on Common/Differential-Mode Analysis," *Microwave Theory and Techniques, IEEE Transactions on*, vol. 58, pp. 3645-3656, 2010.

[56] N. G. Alexopoulos and C. M. Krowne, "Characteristics of Single and Coupled Microstrips on Anisotropic Substrates," *Microwave Theory and Techniques, IEEE Transactions on*, vol. 26, pp. 387-393, 1978.

[57] D. D. Paolino, "MIC Overlay Coupler Design Using Spectral Domain Techniques," *Microwave Theory and Techniques, IEEE Transactions on*, vol. 26, pp. 646-649, 1978.

[58] S. Luo, et al., "Design of an Overlay Directional Coupler by a Full-Wave Analysis," *Microwave Theory and Techniques, IEEE Transactions on*, vol. 31, pp. 1017-1022, 1983.

[59] M. Dydyk, "Accurate design of microstrip directional couplers with capacitive compensation," in *Microwave Symposium Digest, 1990., IEEE MTT-S International*, 1990, pp. 581-584 vol.1.

[60] M. Dydyk, "Microstrip directional couplers with ideal performance via single-element compensation," *Microwave Theory and Techniques, IEEE Transactions on*, vol. 47, pp. 956-964, 1999.

[61] L. Seungku and L. Yongshik, "An Inductor-Loaded Microstrip Directional Coupler for Directivity Enhancement," *Microwave and Wireless Components Letters, IEEE*, vol. 19, pp. 362-364, 2009.

[62] D. M. Pozar, *Microwave Engineering*, 3rd ed. New York: Wiley, 2005.

[63] W. R. Eisenstadt and Y. Eo, "S-parameter-based IC interconnect transmission line characterization," *Components, Hybrids, and Manufacturing Technology, IEEE Transactions on*, vol. 15, pp. 483-490, 1992.

[64] T. I. Christophe Caloz, *Electromagnetic Metamaterials: Transmission Line Theory and Microwave Applications: The Engineering Approach*. Hoboken: John Wiley & Sons, 2006.

[65] F. Capolino, *Theory and Phenomena of Metamaterials*. Boca Raton: CRC Press, 2009.

[66] W. Ching-Kuo, et al., "Electric-magnetic-electric slow-wave microstrip line and bandpass filter of compressed size," *Microwave Theory and Techniques, IEEE Transactions on*, vol. 50, pp. 1996-2004, 2002.

CITED LITERATURE (Continued)

[67] H. Ma and H. Y. D. Yang, "Novel slow-wave coupled lines with coupling enhancement," in *Microwave Symposium Digest (MTT), 2011 IEEE MTT-S International*, 2011, pp. 1-4.

[68] Z. Lei and W. Ke, "Multilayered coupled-microstrip lines technique with aperture compensation for innovative planar filter design," in *Microwave Conference, 1999 Asia Pacific*, 1999, pp. 303-306 vol.2.

[69] M. C. Velazquez-Ahumada, et al., "Parallel coupled microstrip filters with ground-plane aperture for spurious band suppression and enhanced coupling," *Microwave Theory and Techniques, IEEE Transactions on*, vol. 52, pp. 1082-1086, 2004.

[70] L. Cheng-Hsien, et al., "Enhanced Coupling Structures for Tight Couplers and Wideband Filters," *Microwave Theory and Techniques, IEEE Transactions on*, vol. 59, pp. 574-583, 2011.

[71] M. C. Velazquez-Ahumada, et al., "Parallel coupled microstrip filters with floating ground-plane conductor for spurious-band suppression," *Microwave Theory and Techniques, IEEE Transactions on*, vol. 53, pp. 1823-1828, 2005.

[72] D. E. Bockelman and W. R. Eisenstadt, "Combined differential and common-mode scattering parameters: theory and simulation," *Microwave Theory and Techniques, IEEE Transactions on*, vol. 43, pp. 1530-1539, 1995.

[73] W. Fan, et al., "Mixed-mode S-parameter characterization of differential structures," in *Electronics Packaging Technology, 2003 5th Conference (EPTC 2003)*, 2003, pp. 533-537.

[74] W. R. Brinlee, et al., "A novel planar double-balanced 6-18 GHz MMIC mixer," in *Microwave Symposium Digest, 1994., IEEE MTT-S International*, 1994, pp. 9-12 vol.1.

[75] S. A. Maas and Y. Ryu, "A broadband, planar, monolithic resistive frequency doubler," in *Microwave Symposium Digest, 1994., IEEE MTT-S International*, 1994, pp. 443-446 vol.1.

[76] L. Chin-Shen, et al., "Analysis of Multiconductor Coupled-Line Marchand Baluns for Miniature MMIC Design," *Microwave Theory and Techniques, IEEE Transactions on*, vol. 55, pp. 1190-1199, 2007.

[77] M. Chongcheawchamnan, et al., "A Push-Pull Power Amplifier Using Novel Impedance-Transforming Baluns," in *Microwave Conference, 2000. 30th European*, 2000, pp. 1-4.

[78] J. Hyeong Tae, et al., "Design of the Doherty amplifier with push-pull structure using balun transformer," in *Microwave Symposium Digest, 2004 IEEE MTT-S International*, 2004, pp. 851-854 Vol.2.

[79] P. C. Hsu, et al., "Uniplanar broad-band push-pull FET amplifiers," *Microwave Theory and Techniques, IEEE Transactions on*, vol. 45, pp. 2150-2152, 1997.

CITED LITERATURE (Continued)

[80] T. Rutkowski, et al., "Wideband coaxial balun for antenna application," in *Microwaves and Radar, 1998. MIKON '98., 12th International Conference on*, 1998, pp. 389-392 vol.2.

[81] F. Chen and J. Qian, "A novel infinite balun used in folded dipole," in *Antennas and Propagation Society International Symposium, 1990. AP-S. Merging Technologies for the 90's. Digest*., 1990, pp. 547-548 vol.1.

[82] J. R. Brianeze, et al., "Tridimensional Yagi Antenna," in *Microwave and Optoelectronics Conference (IMOC), 2009 SBMO/IEEE MTT-S International*, 2009, pp. 432-436.

[83] J. R. Brianeze, et al., "Tridimensional Yagi antenna: shaping radiation pattern with a non-planar array," *Microwaves, Antennas & Propagation, IET*, vol. 4, pp. 1434-1441, 2010.

[84] S. Jwo-Shiun and L. Tsung-Lin, "Design of a planar balun," in *Microwave Conference, 2001. APMC 2001. 2001 Asia-Pacific*, 2001, pp. 535-538 vol.2.

[85] C. Y. Ng, et al., "Analysis and design of a high-performance planar Marchand balun," in *Microwave Symposium Digest, 2002 IEEE MTT-S International*, 2002, pp. 113-116.

[86] A. Kian Sen and I. D. Robertson, "Analysis and design of impedance-transforming planar Marchand baluns," *Microwave Theory and Techniques, IEEE Transactions on*, vol. 49, pp. 402-406, 2001.

[87] A. Kian Sen, et al., "Analysis and design of miniaturized lumped-distributed impedance-transforming baluns," *Microwave Theory and Techniques, IEEE Transactions on*, vol. 51, pp. 1009-1017, 2003.

[88] W. M. Fathelbab and M. B. Steer, "New classes of miniaturized planar Marchand baluns," *Microwave Theory and Techniques, IEEE Transactions on*, vol. 53, pp. 1211-1220, 2005.

[89] Y. X. Guo, et al., "LTCC Full-Matching Marchand Balun," in *Microwave Conference, 2006. 36th European*, 2006, pp. 76-78.

[90] M. Tzyh-Ghuang, et al., "Miniaturized Distributed Marchand Balun Using Coupled Synthesized CPWs," *Microwave and Wireless Components Letters, IEEE*, vol. 21, pp. 188-190, 2011.

[91] M. Tzyh-Ghuang and C. Yu-Ting, "A Miniaturized Multilayered Marchand Balun Using Coupled Artificial Transmission Lines," *Microwave and Wireless Components Letters, IEEE*, vol. 19, pp. 446-448, 2009.

[92] S. Y. Zheng, et al., "Size reduced Marchand balun with integrated microstrip to CPW transition," in *Microwave Conference Proceedings (APMC), 2010 Asia-Pacific*, 2010, pp. 1236-1239.

CITED LITERATURE (Continued)

[93] M. Chongcheawchamnan, et al., "On miniaturization isolation network of an all-ports matched impedance-transforming Marchand Balun," *Microwave and Wireless Components Letters, IEEE*, vol. 13, pp. 281-283, 2003.

[94] M. E. Khaldi, et al., "Improvement of performance of optically controlled microstrip phase shifters," *Microwaves, Antennas & Propagation, IET*, vol. 1, pp. 427-432, 2007.

[95] C. E. Saavedra and Z. You, "Ring-hybrid microwave voltage-variable attenuator using HFET transistors," *Microwave Theory and Techniques, IEEE Transactions on*, vol. 53, pp. 2430-2434, 2005.

[96] M. Miyagi, "Parallel Push-Pull Hybrid Circuit," *Microwave Theory and Techniques, IRE Transactions on*, vol. 10, pp. 34-40, 1962.

[97] Z. Zhen-Yu, et al., "180-degree substrate integrated waveguide hybrid and its application to broadband millimeter-wave single balanced mixer design," in *Microwave Conference Proceedings (APMC), 2010 Asia-Pacific*, 2010, pp. 1649-1652.

[98] K. W. Eccleston, "Design considerations for the dual-fed distributed power amplifier," in *Microwave Conference, 2000 Asia-Pacific*, 2000, pp. 205-208.

[99] C. Y. Hang, et al., "High-efficiency push-pull power amplifier integrated with quasi-Yagi antenna," *Microwave Theory and Techniques, IEEE Transactions on*, vol. 49, pp. 1155-1161, 2001.

[100] N. Tanzi, et al., "A 1-Watt doubly balanced 5GHz flip-chip SiGe power amplifier," in *Radio Frequency Integrated Circuits (RFIC) Symposium, 2003 IEEE*, 2003, pp. 141-144.

[101] V. Cojocaru, et al., "A 24GHz Low-Cost, Long-Range, Narrow-Band, Monopulse Radar Front End System for Automotive ACC Applications," in *Microwave Symposium, 2007. IEEE/MTT-S International*, pp. 1327-1330, 2007.

[102] S. Kam Man, et al., "A novel microstrip ring hybrid incorporating a PBG cell," *Microwave and Wireless Components Letters, IEEE*, vol. 11, pp. 258-260, 2001.

[103] W. Chao-Wei, et al., "A New Planar Artificial Transmission Line and Its Applications to a Miniaturized Butler Matrix," *Microwave Theory and Techniques, IEEE Transactions on*, vol. 55, pp. 2792-2801, 2007.

[104] T. Chao-Hsiung, "Compact LTCC Rat-Race Couplers Using Multilayered Phase-Delay and Phase-Advance T-Equivalent Sections," *Advanced Packaging, IEEE Transactions on*, vol. 33, pp. 543-551, 2010.

CITED LITERATURE (Continued)

[105] H. Okabe, et al., "A compact enhanced-bandwidth hybrid ring using an artificial lumped-element left-handed transmission-line section," *Microwave Theory and Techniques, IEEE Transactions on*, vol. 52, pp. 798-804, 2004.

[106] C. Ming-Lin, "Miniaturized ring coupler of arbitrary reduced size," *Microwave and Wireless Components Letters, IEEE*, vol. 15, pp. 16-18, 2005.

[107] T. Chao-Hsiung and C. Hsiang-Ju, "Compact Rat-Race Coupler Using Shunt-Stub-Based Artificial Transmission Lines," *Microwave and Wireless Components Letters, IEEE*, vol. 18, pp. 734-736, 2008.

[108] R. K. Settaluri, et al., "Compact folded line rat-race hybrid couplers," *Microwave and Guided Wave Letters, IEEE*, vol. 10, pp. 61-63, 2000.

[109] C. Meng-Ju, et al., "Design of Synthetic Quasi-TEM Transmission Line for CMOS Compact Integrated Circuit," *Microwave Theory and Techniques, IEEE Transactions on*, vol. 55, pp. 2512-2520, 2007.

[110] H. Ghali and T. A. Moselhy, "Miniaturized fractal rat-race, branch-line, and coupled-line hybrids," *Microwave Theory and Techniques, IEEE Transactions on*, vol. 52, pp. 2513-2520, 2004.

[111] S. Tze-Ming, et al., "Multilayer 180^{o} hybrid in LTCC," in *Microwave Conference, 2008. APMC 2008. Asia-Pacific*, pp. 1-4, 2008.

[112] V. Napijalo, "Multilayer 180o hybrid coupler in LTCC technology for 24GHz applications," in *Microwave Conference, 2007. European*, 2007, pp. 552-555.

[113] C. Soras, et al., "Analysis and design of an inverted-F antenna printed on a PCMCIA card for the 2.4 GHz ISM band," *Antennas and Propagation Magazine, IEEE*, vol. 44, pp. 37-44, 2002.

[114] S. R. Best, "A discussion on the quality factor of impedance matched electrically small wire antennas," *Antennas and Propagation, IEEE Transactions on*, vol. 53, pp. 502-508, 2005.

[115] H. Y. D. Yang, "Miniaturized printed wire antenna for wireless communications," *Antennas and Wireless Propagation Letters, IEEE*, vol. 4, pp. 358-361, 2005.

[116] A. D. Yaghjian and S. R. Best, "Impedance, bandwidth, and Q of antennas," *Antennas and Propagation, IEEE Transactions on*, vol. 53, pp. 1298-1324, 2005.

[117] H. Morishita, et al., "Performance of balance-fed antenna system for handsets in the vicinity of a human head or hand," *Microwaves, Antennas and Propagation, IEE Proceedings* -, vol. 149, pp. 85-91, 2002.

CITED LITERATURE (Continued)

[118] H. Y. D. Yang and Y. Y. Zhang, "A wideband miniaturized dipole antenna on a printed circuit board," *Progress In Electromagnetics Research C*, vol. 10, pp. 175-185, 2009.

[119] Z. Yanyan and H. Y. D. Yang, "Bandwidth-Enhanced Electrically Small Printed Folded Dipoles," *Antennas and Wireless Propagation Letters, IEEE*, vol. 9, pp. 236-239, 2010.

[120] C. A. Balanis, *Antenna Theory: Analysis and Design*, 3rd ed. Chichester, U. K.: Wiley, 2005.

[121] S. R. Best, "The Quality factor of the folded cylindrical helix," *Radioengineering*, vol. 18, pp. 343-347, 2009.

[122] H. A. Wheeler, "Fundamental Limitations of Small Antennas," *Proceedings of the IRE*, vol. 35, pp. 1479-1484, 1947.

[123] L. J. Chu, "Physical Limitations of Omni-Directional Antennas," *Journal of Applied Physics*, vol. 19, pp. 1163-1175, 1948.

[124] J. S. McLean, "A re-examination of the fundamental limits on the radiation Q of electrically small antennas," *Antennas and Propagation, IEEE Transactions on*, vol. 44, p. 672, 1996.

VITA

NAME: Haijiang Ma

EDUCATION: B.S., Electrical Engineering, Zhejiang University, 2004

M.S., Electrical Engineering, Zhejiang University, 2006

Ph.D., Electrical and Computer Engineering, University of Illinois at Chicago, 2012

PROFESSIONAL MEMBERSHIP: Graduate student member of Institute of Electrical and Electronic Engineers Microwave Theory and Technique Society (MTT)

HONOR & AWARDS: Finalist for Student Paper Competition on MTT-IMS, June 2011

Finalist for Student Paper Competition on MTT-IMS, May 2010

Honor Graduate Student of Zhejiang University, June 2004.

PUBLICATIONS: Haijiang Ma and H. Y. David Yang, "Miniaturized Integrated Folded Helical Antennas", *IEEE International Symposium on Antennas and Propagation*, pp.753-756, July 2011, Spokane, WA.

Haijiang Ma and H. Y. David Yang, "Novel Slow-Wave Coupled Lines with Coupling Enhancement", *IEEE MTT-S International Microwave Symposium*, pp.1-4, June 2011, Baltimore, MD.

Haijiang Ma and H. Y. David Yang, "Dispersion Characteristics of Metamaterial Slow-Wave Coupled Lines", *IEEE MTT-S International Microwave Symposium*, pp.1-4, May 2010, Anaheim, CA.

H.Y. David Yang, Vamsee K. Chekka, and Haijiang Ma, "Slow-Wave Transmission Line Transformers/Baluns", *IEEE MTT-S International Microwave Symposium*, pp.1536-1539, May 2010, Anaheim, CA.

JOURNAL PAPERS IN PREPARATION: Haijiang Ma and H. Y. David Yang, "Novel Slow-Wave Coupling-Enhanced Coupled Lines for Circuit Applications".

Haijiang Ma and H. Y. David Yang, "A 2.4GHz Miniaturized Impedance-Transforming Marchand Balun".

Haijiang Ma and H. Y. David Yang, "A 2.4GHz Miniaturized Coupled-Line 180^{o} Hybrid Coupler".